LBNL-40841

ERNEST ORLANDO LAWRENCE
BERKELEY NATIONAL LABORATORY

Two-Dimensional Nuclear Magnetic Resonance of Quadrupolar Systems

Shuanhu Wang

Materials Sciences Division

September 1997

Ph.D. Thesis

LBNL-40841

Two-Dimensional Nuclear Magnetic Resonance of Quadrupolar Systems

Shuanhu Wang
Ph.D. Thesis

Department of Chemistry
University of California, Berkeley

and

Materials Sciences Division
Ernest Orlando Lawrence Berkeley National Laboratory
University of California
Berkeley, CA 94720

September 1997

This work was supported by the Director, Office of Energy Research, Office of Basic Energy Sciences, Materials Sciences Division, of the U.S. Department of Energy under Contract No. DE-AC03-76SF00098.

LBNL 40841

Two-Dimensional Nuclear Magnetic Resonance of Quadrupolar Systems

by

Shuanhu Wang

Two-Dimensional Nuclear Magnetic Resonance of Quadrupolar Systems

by

Shuanhu Wang

Doctor of Philosophy in Chemistry

University of California at Berkeley

Professor Alexander Pines, Chair

Abstract

This dissertation describes two-dimensional nuclear magnetic resonance theory and experiments which have been developed to study quadrupoles in the solid state. The technique of multiple-quantum magic-angle spinning (MQMAS) is extensively reviewed and expanded upon in this thesis. Specifically, MQMAS is first compared with another technique, dynamic-angle spinning (DAS). The similarity between the two techniques allows us to extend much of the DAS work to the MQMAS case. Application of MQMAS to a series of aluminum containing materials is then presented. The superior resolution enhancement through MQMAS is exploited to detect the five- and six-coordinated aluminum in many aluminosilicate glasses. Combining the MQMAS method with other experiments, such as HETCOR, greatly expands the possibility of the use of MQMAS to study a large range of problems and is demonstrated in Chapter 5. Finally, the technique switching-angle spinning (SAS) is applied to quadrupolar nuclei to fully characterize a quadrupolar spin system in which all of the 8 NMR parameters are accurately determined. This dissertation is meant to demonstrate that with the combination of two-dimensional NMR concepts and new advanced spinning technologies, a series of multiple-dimensional NMR techniques can be designed to allow a detailed study of quadrupolar nuclei in the solid state.

Contents

List of Tables

List of Figures

Acknowledgements

A Chinese proverb says that three of the most enjoyable things in life are: To achieve a career goal successfully, to marry somebody that you love, and to meet old friends when you are far away from home. This is a very good summary of my graduate life at Berkeley.

Getting a Ph.D. at Berkeley was not even in my wildest dream. Born in a small village in China, my career could simply end after high school. Without the encouragements and supports from my parents, sisters, brothers and my teachers in high school, I would not have been to a top university in China, let alone to come to Berkeley later. I would like to thank Professor Alexander Pines, who has created a very active researching environment that attracts so many smart people around the world to the group. Working with these people is the greatest thing one can imagine. I am greatly indebted to Dr. Jay Shore, who led a new graduate student into the field of NMR, and spent so much time and put so much effort to help me out whenever I had trouble with the experiments. Professor Alexis Bell was another great mentor that taught me how to decompose, analyze and attack each hard problem in my first year at Berkeley. I would like also to thank Dr. Jeff Yarger, who is not only a great collaborator, but also a computer lover whom I can share my computer experience with. While it is hard to list all of the people that have been so helpful to me, I want to give my heartful thanks to Dr. Russell Larsen, Andrew Kolbert, Yungya Lin, Susan De Paul, and Matthias Ernst.

I should not forget my collaborators at Stanford and Santa Barbara. Without Dr. Zhi Xu and Prof. Jonathan Stebbins, who constantly provide me interesting samples, I could not have finished my work now. Dr. Lucy Bull and Susan De Paul are my collaborators on the MQMAS/HETCOR project. Without their experience

on cross-polarization and probe design, the project would last much longer. Dr. Jay Baltisberger deserves my special thanks for his help in setting up many of the experiments.

It is during my graduate school time that I met my wife and got married. Being a Berkeley man has made my life much easier. I do not need to take special efforts to convince my wife to marry me; Instead, I only need to let her know my shortcomings.

My life at Berkeley would have been really tough if not for the help of all my good friends here. It is not possible for me to use more space than just list some of their names: Zhan Chen, Jiulong Meng, Weiling Wang, Bin He, Yulin Lou, Wenzhong Xiao, Qian Fu, Suli Fei, Meihong, Baohua Huang, Xiaodong Sun.

Chapter 1

Introduction

More than 60% of the isotopes in the periodic table have an uneven distribution of nuclear charges, and thus an electric quadrupole moment. The coupling between the nuclear quadrupole moment and the electric field gradient (EFG) generated at the center of the nucleus gives an electric quadrupolar interaction that dominates all other internal spin interactions (such as chemical shift and dipolar interactions) that a quadrupolar nucleus experiences. The nuclear magnetic resonance (NMR) spectra of quadrupoles are often broadened by this interaction, whose second-order effect can not be efficiently removed by the conventional sample rotation method magic-angle spinning (MAS). The low resolution of the resultant spectra greatly limits the applicability of NMR to various important materials, and requires novel techniques to give liquid-like resolution in the solid-state.

Dynamic-angle spinning (DAS) [1, 2] and multiple-quantum magic-angle spinning (MQMAS) [3] are two of the most important developments that overcome the resolution problem. DAS, first realized at Berkeley in 1990, has evolved into a relatively mature technique by now; the MQMAS method proposed by L. Frydman in 1995, however, is showing great promise and has some intrinsic advantages over DAS. This thesis describes the MQMAS and DAS experiments I performed at Berkeley that represent some newer contributions to high-resolution NMR of quadrupoles. Even though my research has been focusing on MQMAS, the great similarity between DAS and MQMAS makes it desirable to present both techniques in parallel, and compare them when possible.

Following this short introduction, chapter 2 presents some basic NMR theories

that are used throughout this thesis. In chapter 3, DAS and MQMAS are discussed and compared to each other in great detail. The similarities between the two techniques are clearly demonstrated and various developments based on DAS are shown to be equally applicable to MQMAS. Chapter 4 applies MQMAS to ^{27}Al-containing minerals and zeolites. The advantages of MQMAS over MAS is illustrated in both crystalline and glass samples. Preliminary application of MQMAS to ^{17}O is also given. Chapter 5 shows another interesting experiment that utilizes MQMAS to give high-resolution HETCOR spectra for quadrupoles.

The last chapter in this thesis focuses on the switching-angle spinning (SAS) technique that allows the determination of chemical shift parameters along with the relative orientation between the chemical shift and quadrupolar principal axis systems (PAS). Compared to conventional one-dimensional techniques, this method is more accurate and reliable, when the magnitude of chemical shift interaction is moderate.

Since MQMAS is now a hot topic in the NMR community, great advances have been achieved in the past two years. A brief review of this area is given in the appendix. With this review , the thesis becomes a complete reference for high-resolution NMR of quadrupoles.

Chapter 2

Basic NMR Theory

The wealth of structural and dynamic information in NMR experiments comes from the combination of various nuclear spin interactions and the external perturbations applied to the system. The nuclear spin interactions affect the eigenstates of the system, therefore change the experimental NMR spectra. The external perturbations generated by RF fields can be manipulated with arbitrary flexibility to selectively utilize or average out specific interaction(s), leaving us with spectra manifesting different aspects of the system. There have been many good books that provide general discussions of the principles of nuclear magnetic resonance [4, 5, 6, 7] and its application to solid state materials [8, 9]. In the current chapter, I will only include some fundamentals of NMR theory that are used in the later chapters to describe the more advanced NMR experiments.

2.1 Rotations

All techniques used for selective averaging in NMR rely on rotations of one or another kind of the internal Hamiltonians. The behavior of any physical property under rotation can be studied more easily when the property is expressed in terms of irreducible tensor operators [10]. The reason is that the transformation of the tensors under rotation is well known.

Rotations in NMR take two distinct forms: rotations in spin space and rotations in real space. Each NMR Hamiltonian can be written as a summation of product of

spin and spatial tensors as shown below.

$$H_\lambda = \sum_l \sum_{m=-l}^{l} (-1)^m R^\lambda_{l,-m} T^\lambda_{lm} \tag{2.1}$$

The tensor components R^λ_{lm} and T^λ_{lm} are the spatial and spin tensor components, respectively. The rotations in each space only affect the variables in that space, thus by writing the Hamiltonians in the above form, the spin and real spaces are decoupled and handled separately.

A rotation is often specified by three Euler angles (α, β, γ) between the two reference frames before and after rotation, as shown in Figure 2.1. An lth-rank tensor then transforms in the following way.

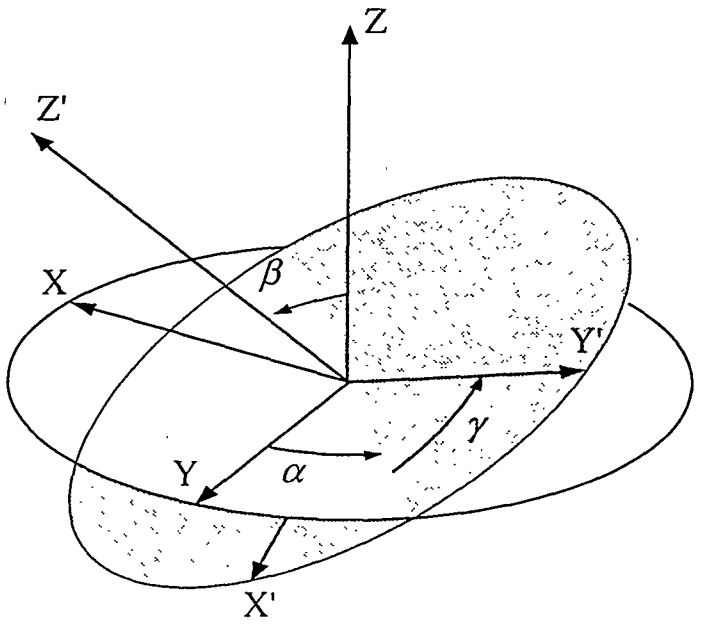

Figure 2.1: The Euler angles α, β, γ that describe the transformation between two reference frames.

$$A'_{lm} = \sum_{n=-l}^{l} D^{(l)}_{nm}(\alpha, \beta, \gamma) A_{ln} \tag{2.2}$$

Here, A and A' are tensors in the original and new frames. The evaluation of tensor

$D^{(l)}$ is facilitated by the reduced Wigner rotation matrix elements $d^{(l)}_{nm}$.

$$D^{(l)}_{nm}(\alpha,\beta,\gamma) = e^{-i(m\alpha+n\gamma)} d^{(l)}_{nm}(\beta) \tag{2.3}$$

For most of the work in this thesis, I will deal primarily with second-order tensors in the spin and spatial spaces. Therefore, a table of second-order Wigner matrices is included here for further references.

n \ m	2	1	0	-1	-2
2	$(\frac{1+\cos\beta}{2})^2$	$-\frac{1+\cos\beta}{2}\sin\beta$	$\sqrt{\frac{3}{8}}\sin^2\beta$	$-\frac{1-\cos\beta}{2}\sin\beta$	$(\frac{1-\cos\beta}{2})^2$
1	$\frac{1+\cos\beta}{2}\sin\beta$	$\cos^2\beta - \frac{1-\cos\beta}{2}$	$-\sqrt{\frac{3}{8}}\sin 2\beta$	$\frac{1+\cos\beta}{2} - \cos^2\beta$	$-\frac{1-\cos\beta}{2}\sin\beta$
0	$\sqrt{\frac{3}{8}}\sin^2\beta$	$\sqrt{\frac{3}{8}}\sin 2\beta$	$\frac{3\cos^2\beta-1}{2}$	$-\sqrt{\frac{3}{8}}\sin 2\beta$	$\sqrt{\frac{3}{8}}\sin^2\beta$
-1	$\frac{1-\cos\beta}{2}\sin\beta$	$-\cos^2\beta + \frac{1+\cos\beta}{2}$	$\sqrt{\frac{3}{8}}\sin 2\beta$	$-\frac{1-\cos\beta}{2} + \cos^2\beta$	$-\frac{1+\cos\beta}{2}\sin\beta$
-2	$(\frac{1-\cos\beta}{2})^2$	$\frac{1-\cos\beta}{2}\sin\beta$	$\sqrt{\frac{3}{8}}\sin^2\beta$	$\frac{1+\cos\beta}{2}\sin\beta$	$(\frac{1+\cos\beta}{2})^2$

Table 2.1: Reduced Wigner rotation matrix elements $d^{(2)}_{nm}(\beta)$

2.2 Perturbation Theory

Static perturbation theory [11, 12] is used throughout this thesis to analyze the effects of the nuclear spin Hamiltonians on the resultant NMR spectra. The theory is useful when the Hamiltonian can be written as

$$H = H_0 + \lambda V, \tag{2.4}$$

where $V \ll H_0$ and $0 \leq \lambda \leq 1$. Assuming that the eigenstates and eigenvalues of H_0 are $|n>$ and ε_n, that is

$$H_0|n> = \varepsilon_n|n>, \tag{2.5}$$

perturbation theory makes the assumption that the eigenstates and eigenvalues of H are obtained by adding higher order correction terms to those of the unperturbed

system.

$$|N> = |n> + \lambda|N^{(1)}> + \lambda^2|N^{(2)}> + \cdots \quad (2.6)$$

$$\varepsilon_N = \varepsilon_n + \lambda\varepsilon_N^{(1)} + \lambda^2\varepsilon_N^{(2)} + \cdots \quad (2.7)$$

Here, $|N^{(i)}>$ and $\varepsilon_N^{(i)}$ are a series of correction terms to the eigenstate $|n>$ and eigenvalue ε_n. Inserting Eqns 2.6 and 2.7 into

$$H|N> = (H_0 + \lambda V)|N> = \varepsilon_N|N>, \quad (2.8)$$

and collecting terms on both side of the equation with the same power of λ, the first- and second-order energy corrections can be obtained.

$$E_N^{(1)} = < n|V|n > \quad (2.9)$$

$$E_N^{(2)} = \sum_{n \neq m} \frac{< n|V|m >< m|V|n >}{\varepsilon_n - \varepsilon_m} \quad (2.10)$$

The result on the first-order energy correction states that we need merely to calculate eigenvalue corrections using the original basis set. This is equivalent to ignoring all the terms in V that do not commute with the basis Hamiltonian H_0 (non-secular terms). Using a matrix representation, this means that all the non-diagonal matrix elements in V are neglected and the Hamiltonian $H_0 + V$ is approximated by a diagonal Hamiltonian. This process of truncating Hamiltonians has proved essential in the treatment of internal spin Hamiltonians in NMR.

2.3 Nuclear Spin Hamiltonians

The nuclear spin Hamiltonians consist of a number of terms that describe physically different interactions of the nuclear spins.

$$H = H_Z + H_{RF} + H_Q + H_{CS} + H_D \quad (2.11)$$

The first two terms, H_Z and H_{RF}, reflect the coupling of the nuclear magnetic dipole moment with the external static and RF magnetic fields. These fields are controlled by the experimenter. The last three terms are determined by the local environment around the nucleus instead. Of all the spin interactions mentioned here, only the electric quadrupolar interaction will be discussed in any details, as the thesis is mainly concerned with half-interger quadrupolar nuclei.

2.3.1 Zeeman Interaction

The single strongest interaction in high-field NMR experiment is the Zeeman interaction, whose magnitude is proportional to the static magnetic field strength B_0. This direction of B_0 also defines the z-axis of the laboratory frame.

$$H_Z = -\hbar\gamma B_0 I_0 = -\hbar\omega_0 I_0 \tag{2.12}$$

In this equation, γ is a ratio between the nuclear dipole moment and the nuclear angular momentum (gyromagnetic ratio), and ω_0 is the Larmor frequency. The spin operator

$$I_0 = I_Z \tag{2.13}$$

is one of the three spherical operators making up the complete spin operator set. The other two are defined below.

$$I_\pm = \pm\frac{1}{\sqrt{2}}(I_X \pm iI_Y) \tag{2.14}$$

The eigenstates of the dominating Zeeman Hamiltonian form a basis set for the perturbative treatment of other nuclear spin interactions. A nuclear spin with quantum number I will have $2I + 1$ eigenstates, each denoted as $|Im>$ where $-I \leq m \leq I$. In the basis set formed by these eigenstates, the matrix elements

of the spin operators are given below.

$$I_0|Im> = m \tag{2.15}$$

$$I_\pm|Im> = \pm\frac{1}{\sqrt{2}}\sqrt{(I \mp m)(I \pm m + 1)}|I, m \pm 1> \tag{2.16}$$

2.3.2 Quadrupolar Interaction

While the nuclear charge distribution for a spin-$\frac{1}{2}$ nucleus is spherical, the distribution is uneven for a quadrupolar nucleus. The reorientation of the nucleus therefore affects the energy of the nucleus and the electric interaction of the nucleus with its surrounding becomes important when dealing with a quadrupolar nucleus. Classically, the interaction between a charge distribution $\varrho(\vec{r})$ and an electric field potential $V(\vec{r})$ is

$$E_Q = \int_V \varrho(\vec{r})V(\vec{r})d\vec{r} \tag{2.17}$$

integrated over the three-dimensional space. Since $V(\vec{r})$ often takes a quite complex form dependent on the spatial distribution of all the electronic and nuclear charges, a Taylor series expansion is used instead to simplify Eqn 2.17.

$$V(\vec{r}) = V(0) + \sum_{\alpha=x,y,z} \alpha\frac{\partial V}{\partial \alpha}|_{\vec{r}=0} + \frac{1}{2!}\sum_{\alpha,\beta=x,y,z} \alpha\beta\frac{\partial^2 V}{\partial\alpha\partial\beta}|_{\vec{r}=0} + \ldots \tag{2.18}$$

The expansion is about the center of mass of the nucleus, which coincides with the center of charge of the nucleus. Substituting Eqn 2.18 into Eqn 2.17 yields the following expression.

$$E_Q = ZeV(0) + \sum_{\alpha=x,y,z} P_\alpha\frac{\partial V}{\partial \alpha}|_{\vec{r}=0} + \frac{1}{2!}\sum_{\alpha,\beta=x,y,z} Q'_{\alpha\beta}\frac{\partial^2 V}{\partial\alpha\partial\beta}|_{\vec{r}=0} + \ldots \tag{2.19}$$

Here, Ze is the total charge density of a nucleus, which is constant and of little interest; the α component of the electric dipole moment

$$P_\alpha = \int_V \alpha \varrho(\vec{r}) d\vec{r} \tag{2.20}$$

equals to zero since the center of mass and center of charge for a nucleus coincide. The third term is the product of two second-rank tensors. The $\alpha\beta$ component of the electric quadrupole moment $Q'_{\alpha\beta}$ is defined below.

$$Q'_{\alpha\beta} = \int_V \alpha\beta \varrho(\vec{r}) d(\vec{r}) \tag{2.21}$$

The $\alpha\beta$ components of the electric field gradient (EFG) tensor is defined as

$$V_{\alpha\beta} = \frac{\partial^2 V}{\partial\alpha\partial\beta} \mid_{\vec{r}=0} . \tag{2.22}$$

It is more convenient to express the EFG tensor in its principal axis system (PAS) with its three eigenvalues V_{XX}, V_{YY} and V_{ZZ}. These eigenvalues fulfill the following relationship.

$$|V_{ZZ}| \geq |V_{YY}| \geq |V_{XX}| \tag{2.23}$$

Since the EFG tensor is traceless, two parameters (eq and η_Q) are actually enough to define it uniquely.

$$eq = V_{ZZ} \tag{2.24}$$

$$\eta_Q = \frac{V_{XX} - V_{YY}}{V_{ZZ}} \tag{2.25}$$

The second parameter η_Q is the asymmetric parameter of the electric field gradient and takes a value between 0 and 1. This parameter reflects the local symmetry around the nucleus, and equals to zero when the surrounding of the nucleus is axial symmetric.

The derivation of the quantum mechanical Hamiltonian for a quadrupolar nucleus then becomes quite complicated [4, 6], but the final result has the following form.

$$H_Q = \hbar\omega_Q \sum_{m=-2}^{2} A^Q_{2,-m} T^Q_{2m} \tag{2.26}$$

where

$$\omega_Q = \frac{eq \cdot eQ}{2I(2I-1)\hbar} = \frac{e^2qQ}{2I(2I-1)\hbar}. \tag{2.27}$$

The nuclear quadrupole moment eQ is derived from Q' in Eqn 2.21. A quadrupolar coupling constant C_Q is now introduced to report the coupling between the nuclear quadrupole moment and the electric field gradient.

$$C_Q = \frac{e^2qQ}{\hbar} \tag{2.28}$$

The different spin tensor components in Eqn 2.26 have the following meanings.

$$T^Q_{20} = \frac{1}{\sqrt{6}}(3I_0^2 - I^2) \tag{2.29}$$

$$T^Q_{2,\pm1} = \frac{1}{\sqrt{2}}(I_0 I_\pm + I_\pm I_0) \tag{2.30}$$

$$T^Q_{2,\pm2} = I_\pm^2 \tag{2.31}$$

The spatial tensor component

$$A^Q_{2m} = \sum_{n=-2}^{2} D^{(2)}_{nm}(\alpha^Q, \beta^Q, \gamma^Q)\rho^Q_{2n} \tag{2.32}$$

is expressed in the laboratory frame. The spatial tensor ρ^Q in the quadrupole principal axis frame (PAS) is defined as

$$\rho^Q_{20} = \sqrt{\frac{3}{2}} \tag{2.33}$$

$$\rho^Q_{2,\pm1} = 0 \tag{2.34}$$

$$\rho^Q_{2,\pm2} = \eta_Q/2. \tag{2.35}$$

These two tensors relate to each other through a general rotation with three Euler angles α^Q, β^Q and γ^Q between the two frames.

The magnitude of quadrupolar interaction is often in the megahertz range, and quadrupolar interaction dominates all other nuclear spin interactions except for the Zeeman interaction. Perturbative treatment for this interaction needs to be carried out to the second-order to fully account for its influence on the NMR spectra. On the other hand, C_Q and η_Q contain invaluable information about the local geometry around the nucleus that experimental extraction of them has proved essential in the determination of structure and dynamics of many classes of materials.

2.3.3 Chemical Shift Interaction

Chemical shift interaction is a magnetic interaction deriving from the coupling between the nuclear dipole moment and the local magnetic field created by the motions of the surrounding electrons. The Hamiltonian is expressed here in the laboratory frame using a spherical tensor representation.

$$H_{CS} = \hbar\gamma(A_{00}^{CS}T_{00}^{CS} + \delta_{CS}\sum_{m=-2}^{2}(-1)^m A_{2m}^{CS}T_{2,-m}^{CS}) \tag{2.36}$$

In this equation, the spin space tensors are given below in Eqn 2.37 to Eqn 2.40.

$$T_{00}^{CS} = B_0 I_0 \tag{2.37}$$

$$T_{20}^{CS} = \sqrt{\frac{2}{3}} B_0 I_0 \tag{2.38}$$

$$T_{2,\pm1}^{CS} = \frac{1}{\sqrt{2}} B_0 I_\pm \tag{2.39}$$

$$T_{2,\pm2}^{CS} = 0 \tag{2.40}$$

Similar to the quadrupole case, it is more convenient to define chemical shift parameters in its principal axis system (PAS). The three eigenvalues of the tensor

are δ_{XX}, δ_{YY} and δ_{ZZ}. The isotropic chemical shift is then the trace of the chemical shift tensor.

$$\delta_{iso} = \frac{\delta_{XX} + \delta_{YY} + \delta_{ZZ}}{3} \tag{2.41}$$

The assignment of δ_{XX}, δ_{YY} and δ_{ZZ} needs to fulfill the following condition.

$$|\delta_{ZZ} - \delta_{iso}| \geq |\delta_{YY} - \delta_{iso}| \geq |\delta_{XX} - \delta_{iso}| \tag{2.42}$$

The chemical shift anisotropy (CSA) and asymmetric parameter are defined by

$$\delta_{CS} = \frac{3}{2}(\delta_{ZZ} - \delta_{iso}) \tag{2.43}$$

$$\eta_{CS} = \frac{\delta_{XX} - \delta_{YY}}{\delta_{ZZ} - \delta_{iso}}, \tag{2.44}$$

where δ_{CS} characterizes the size of CSA and η_{CS} reflects the local symmetry around the nucleus.

Using the above definitions, the spatial tensor components ρ_{ij}^{CS} in the chemical shift PAS are described as

$$\rho_{00}^{CS} = \delta_{iso} \tag{2.45}$$

$$\rho_{20}^{CS} = \sqrt{\frac{3}{2}} \tag{2.46}$$

$$\rho_{2,\pm 1}^{CS} = 0 \tag{2.47}$$

$$\rho_{2,\pm 2}^{CS} = \eta_{CS}/2. \tag{2.48}$$

The spatial tensor A^{CS} in the laboratory frame is obtained from the PAS frame tensor ρ^{CS} through a general rotation.

$$A_{lm}^{CS} = \sum_{n=-l}^{l} D_{nm}^{(l)}(\alpha^{CS}, \beta^{CS}, \gamma^{CS}) \rho_{ln}^{CS} \tag{2.49}$$

Here, α^{CS}, β^{CS} and γ^{CS} are Euler angles between the CSA PAS and the laboratory frame.

Chemical shift anisotropy is usually in the range of kilohertz and is more conveniently reported in the units of parts per million (ppm). Perturbative treatment of this interaction only needs to be done to the first-order. Like C_Q and η_Q, $\delta_{iso}, \delta_{CS}$ and η_{CS} probe the local structure and dynamics near to the nucleus that a series of NMR applications are solely dependent on the accurate measurement of these parameters.

2.3.4 Dipolar Interaction

Dipolar Interaction (DI) between two spins I_i and I_j is described by following equation.

$$H_{D_{ij}} = -\hbar\omega_{D_{ij}} \sum_{m=-2}^{2} (-1)^m T_{2m}^{D_{ij}} A_{2,-m}^{D_{ij}} \tag{2.50}$$

Here, $\omega_{D_{ij}}$ is the magnitude of the dipolar interaction that ranges from zero to tens of kilohertz for different spin pairs.

$$\omega_{D_{ij}} = \frac{\gamma_i \gamma_j}{r_{ij}^3} \tag{2.51}$$

The spin tensor components are given by

$$T_{20}^{D_{ij}} = \frac{1}{\sqrt{6}}(3I_{z,i}I_{z,j} - I_i \cdot I_j) \tag{2.52}$$

$$T_{2,\pm1}^{D_{ij}} = \frac{\sqrt{2}}{2}(I_{z,i}I_{\pm,j} + I_{\pm,i}I_{z,j}) \tag{2.53}$$

$$T_{2,\pm2}^{D_{ij}} = I_{\pm,i}I_{\pm,j} \tag{2.54}$$

The lab frame tensor $A^{D_{ij}}$ is defined based on tensor $\rho^{D_{ij}}$ in the dipolar principal axis system (PAS). The conversion between the two tensors involves only one Euler

angle ($\beta^{D_{ij}}$) since only the z-axis of the dipolar PAS frame is fixed.

$$A_{2m}^{D_{ij}} = \sum_{n=-2}^{n=2} D_{nm}^{(2)}(0, \beta^{D_{ij}}, 0)\rho_{2n}^{D_{ij}} \tag{2.55}$$

where

$$\rho_{20}^{D_{ij}} = \sqrt{\frac{3}{2}} \tag{2.56}$$

$$\rho_{2,\pm 1}^{D_{ij}} = 0 \tag{2.57}$$

$$\rho_{2,\pm 2}^{D_{ij}} = 0. \tag{2.58}$$

The strong dependence of $\omega_{D_{ij}}$ on the distance between the two spins makes the dipolar interaction a unique probe on internuclear distances. This thesis, however, will not consider dipolar interaction in much detail. The readers can consult with other references to see how the dipolar interaction is utilized to enhance NMR signal [13, 14], to do spectral editing [15] and to establish connectivities among complex spin networks [5, 16].

2.4 Perturbative Treatment of Spin Hamiltonians

We now start to look at how the internal spin interactions affect the NMR spectra using perturbation theory. As mentioned before, first-order perturbative treatment is needed for all three of the interactions (CSA, QI and DI), while second-order expansion is also needed when dealing with the quadrupolar interaction. As long as the first-order perturbation theory is concerned, only the secular part of the Hamiltonians that commute with the Zeeman Hamiltonian remains and all other terms can be safely dropped.

2.4.1 Static Sample

The part of the chemical shift Hamiltonian that commutes with the Zeeman Hamiltonian is given below.

$$\begin{aligned} H_{CS} &= h\gamma(A_{00}^{CS}T_{00}^{CS} + \delta_{CS}A_{20}^{CS}T_{20}^{CS}) \\ &= h\omega_0\delta_{iso}I_0 + h\gamma\delta_{CS}T_{20}^{CS}A_{20}^{CS} \\ &= h\omega_0(\delta_{iso}I_0 + \sqrt{\frac{2}{3}}\delta_{CS}I_0A_{20}^{CS}) \end{aligned} \tag{2.59}$$

In terms of the energy correction, Eqn 2.9 is used and

$$\begin{aligned} \omega_{m\leftrightarrow n}^{CS} &= (< Im|H_{CS}|Im > - < In|H_{CS}|In >)/h \\ &= (m-n)\omega_0(\delta_{iso} + \sqrt{\frac{2}{3}}\delta_{CS}A_{20}^{CS}) \end{aligned} \tag{2.60}$$

The factor $(m-n)$ here suggests that the $3/2 \leftrightarrow -3/2$ transition would have a chemical shift tripled that of the $1/2 \leftrightarrow -1/2$ transition.

Truncation of the quadrupolar Hamiltonian to the first-order gives

$$H_Q = \frac{h\omega_Q}{\sqrt{6}}.A_{20}^Q(3I_0^2 - I(I+1)). \tag{2.61}$$

The first-order energy correction to state $|Im>$ is again calculated by inserting this equation into Eqn 2.9.

$$< Im|H_Q|Im >= \frac{h\omega_Q}{\sqrt{6}}.A_{20}^Q(3m^2 - I(I+1)) \tag{2.62}$$

It is insightful to work out the energy differences for various transitions of a half-integer quadrupolar nucleus.

$$\Delta E_{m\leftrightarrow m-1}^{1Q} = \frac{3h\omega_Q}{\sqrt{6}}.A_{20}^Q(2m-1) \tag{2.63}$$

$$\Delta E_{m\leftrightarrow -m}^{1Q} = 0 \tag{2.64}$$

For the $m \leftrightarrow m-1$ transition with $m \neq \frac{1}{2}$, the correction is in the order of ω_Q (megahertz) and can hardly be observed in most experiments (for opposite examples, see [17, 18, 19]). The most commonly observed central transition ($1/2 \leftrightarrow -1/2$ transition), together with other symmetric multiple-quantum transitions ($m \leftrightarrow -m$ transitions), is however, not affected to the first-order by the quadrupolar interaction. Second-order perturbation theory is thus used, and the final results are described below [20].

$$\begin{aligned} \Delta E^{2Q}_{m\leftrightarrow -m} &= \frac{\hbar\omega_Q^2}{\omega_0}((4I(I+1)-8m^2-1)A^Q_{21}A^Q_{2,-1} + \\ &\quad (2I(I+1)-2m^2-1)A^Q_{22}A^Q_{2,-2}) \end{aligned} \tag{2.65}$$

This equation reduces to the more commonly used expression for the central transition.

$$\Delta E^{2Q}_{1/2\leftrightarrow -1/2} = \frac{\hbar\omega_Q^2}{2\omega_0}(I(I+1)-3/4)(2A^Q_{21}A^Q_{2,-1} + A^Q_{22}A^Q_{2,-2}) \tag{2.66}$$

Figure 2.2 shows schematically how the energy levels of a spin $I = \frac{3}{2}$ nucleus are shifted by the quadrupolar interaction. Without the quadrupolar interaction, four $(2I+1)$ equally spaced energy levels are observed. The first-order quadrupolar interaction changes the energy of each level by an amount in the order of the quadrupolar interaction (megahertz). However, the m and -m energy levels are shifted in the same direction, and the $m \leftrightarrow -m$ transition frequency is not affected to the first-order. The second-order quadrupolar interaction, however, does affect the transition frequencies and the frequency shifts are described by Eqns 2.65 and 2.66.

2.4.2 Spinning Samples

To yield better resolution, most solid-state NMR experiments are carried out under spinning condition. Sample spinning introduces extra rotations in the real

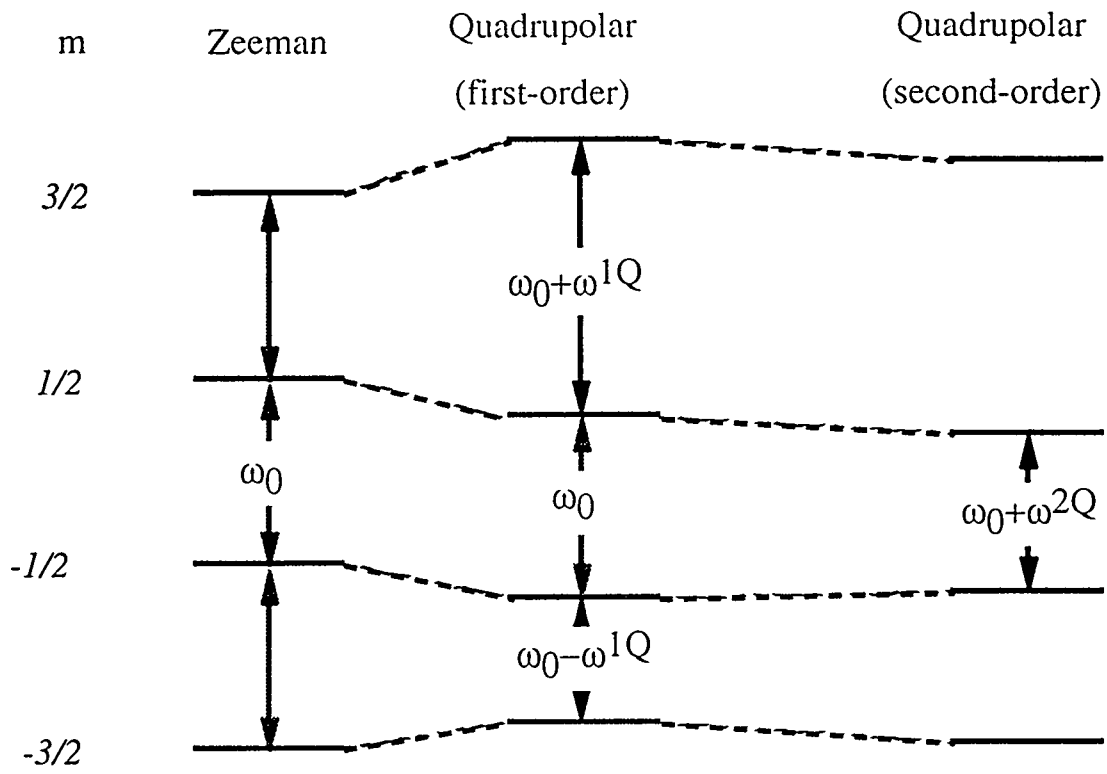

Figure 2.2: Zeeman, first- and second-order energy splittings for $I = \frac{3}{2}$ nucleus.

space (but does not change the spin space tensors), so the format of the energy correction expressions is not changed (Eqn 2.60 and Eqn 2.65), except that the spatial tensors A^Q and A^{CS} now involve another rotation in the real space.

Figure 2.3 demonstrates the transformations we need to perform on a spatial tensor A^λ in a rotating sample. The tensor is first transformed from its principal axis frame (PAS) to the rotor frame, and then to the laboratory frame. The Euler angles involved in the two transformations are (α, β, γ) and $(\omega_r t, \theta, 0)$ respectively. Here ω_r is the spinning speed and θ is the angle between the spinner axis and the static field B_0. According to Eqn 2.2,

$$A^\lambda_{lm} = \sum_{k=-l}^{l} \sum_{n=-l}^{l} D^{(l)}_{nk}(\alpha, \beta, \gamma) D^{(l)}_{km}(\omega_r t, \theta, 0) \rho^\lambda_{ln}. \tag{2.67}$$

As a comparison, there is only one rotation involved in the static case (see Eqn 2.32

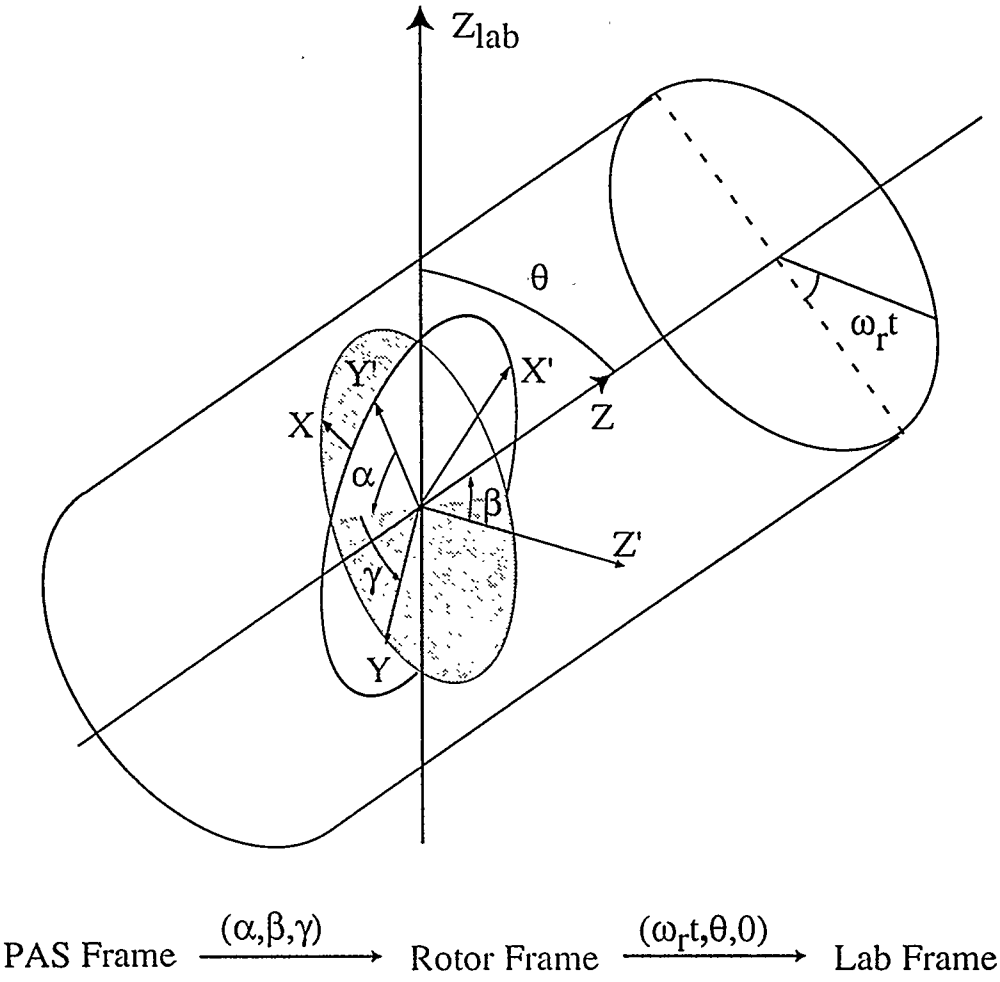

Figure 2.3: PAS to rotor to lab frame. The Euler angles used in the transformation are indicated.

and Eqn 2.49). The above expression is now time-dependent and can be written as the sum of the time-independent and time-dependent terms. The time-dependent terms result in extra peaks (sidebands) in an NMR spectrum, and will not be discussed in detail [21, 22]. Here, we consider only the time-independent ($k = 0$) terms, which suffice for the derivation of high-resolution NMR theory.

For chemical shift interaction, the important spatial tensor is A_{20}^{CS} (Eqn 2.60).

According to Eqn 2.67,

$$A_{20}^{CS} = \sum_{k=-2}^{2} D_{k0}^{(2)}(\omega_r t, 0, 0) \sum_{n=-2}^{2} D_{nk}^{(2)}(\alpha^{CS}, \beta^{CS}, \gamma^{CS}) \rho_{2n}^{CS}. \tag{2.68}$$

The $k \neq 0$ terms in the summation can be dropped since they are time-dependent. The remaining $k = 0$ terms give the following expression for A_{20}^{CS}.

$$A_{20}^{CS} = \sqrt{\frac{3}{2}} P_2(\cos\theta)\left(\frac{3\cos^2\beta^{CS} - 1}{2} + \frac{\eta_{CS}}{2}\sin^2\beta^{CS}\cos 2\alpha^{CS}\right) \tag{2.69}$$

Here, $P_2(\cos\theta)$ is the second-order Legendre polynomial.

$$P_2(\cos\theta) = \frac{3\cos^2\theta - 1}{2} \tag{2.70}$$

A similar result is obtained for the first-order quadrupolar interaction.

$$A_{20}^{1Q} = \sqrt{\frac{3}{2}} P_2(\cos\theta)\left(\frac{3\cos^2\beta^{Q} - 1}{2} + \frac{\eta_{Q}}{2}\sin^2\beta^{Q}\cos 2\alpha^{Q}\right) \tag{2.71}$$

The expressions for a static sample can be derived by setting $P_2(\cos\theta) = 1$ (or $\theta = 0.0°$). Applying Eqn 2.69 to Eqn 2.60, a more often used version of the chemical shift frequency is written as.

$$\omega^{CS} = \omega_{iso} + A_2^{CS}(\alpha^{CS}, \beta^{CS}) P_2(\cos\theta), \tag{2.72}$$

where

$$\omega_{iso} = \omega_0 \delta_{iso} \tag{2.73}$$

and

$$A_2^{CA} = \sqrt{\frac{2}{3}} \delta_{CS} A_{20}^{CS} / P_2(\cos\theta). \tag{2.74}$$

Eqn 2.72 contains an isotropic term that is independent of crystalline orientation, and an anisotropic term that is dependent on the crystalline orientation. The latter needs

to be averaged out if high-resolution is desired. Similar expression can be obtained for the first-order quadrupolar interaction.

For the second-order quadrupolar interaction, the product of two second-rank tensors ($A^Q_{2m}A^Q_{2,-m}$) needs to be expanded. There are two ways of calculating the expansion. The first one works well when the time-dependent terms in the expansion are not important and can be dropped (which is the fast-spinning case). The tensor product is first explicitly written out as follows.

$$A^Q_{2m}A^Q_{2,-m} = \sum_{l,n=-2}^{2} D^{(2)}_{nl}(\alpha^Q,\beta^Q,\gamma^Q)D^{(2)}_{lm}(\omega_r t,0,0)\rho^Q_{2n} \times \sum_{k,p=-2}^{2} D^{(2)}_{pk}(\alpha^Q,\beta^Q,\gamma^Q)D^{(2)}_{k,-m}(\omega_r t,0,0)\rho^Q_{2p} \tag{2.75}$$

Only the $l = k = 0$ terms in the above equation are time-independent and are separated out.

$$A^Q_{2m}A^Q_{2,-m} = \sum_{n=-2}^{2} D^{(2)}_{n0}(\alpha^Q,\beta^Q,\gamma^Q)D^{(2)}_{0m}(\omega_r t,0,0)\rho^Q_{2n} \times \sum_{p=-2}^{2} D^{(2)}_{p0}(\alpha^Q,\beta^Q,\gamma^Q)D^{(2)}_{0,-m}(\omega_r t,0,0)\rho^Q_{2p} \tag{2.76}$$

For the central transition, the expression $2A^Q_{21}A^Q_{2,-1} + A^Q_{22}A^Q_{2,-2}$ expands as below.

$$2A^Q_{21}A^Q_{2,-1} + A^Q_{22}A^Q_{2,-2} = \frac{1}{8}\sum_{i,j=0}^{2} a'_{ij}(\eta_Q)\cos 2i\alpha^Q \cos 2j\beta^Q \tag{2.77}$$

where

$$a'_{ij} = a^{(0)}_{ij} + a^{(2)}_{ij}P_2(\cos\theta) + a^{(4)}_{ij}P_4(\cos\theta). \tag{2.78}$$

Here,

$$P_4(\cos\theta) = \frac{1}{8}(35\cos^4\theta - 30\cos^2\theta + 3) \tag{2.79}$$

is the 4th-order Legendre polynomial. The η_Q-dependent a_{ij} elements are given in table 2.2 [23, 24]. Using these parameters, static and MAS spectra of quadrupolar nuclei can be simulated (simulating the sidebands requires extra effort).

i	j	$a_{ij}^{(0)}$	$a_{ij}^{(2)}$	$a_{ij}^{(4)}$
0	0	$-\frac{12}{5}(1+\frac{1}{3}\eta_Q^2)$	$-\frac{12}{7}(1-\frac{1}{3}\eta_Q^2)$	$\frac{81}{1120}(18+\eta_Q^2)$
0	1	0	$-\frac{36}{7}(1-\frac{1}{3}\eta_Q^2)$	$\frac{9}{56}(18+\eta_Q^2)$
0	2	0	0	$\frac{9}{32}(18+\eta_Q^2)$
1	0	0	$\frac{24}{7}\eta_Q$	$\frac{81}{56}\eta_Q$
1	1	0	$-\frac{24}{7}\eta_Q$	$\frac{27}{14}\eta_Q$
1	2	0	0	$-\frac{27}{8}\eta_Q$
2	0	0	0	$\frac{27}{32}\eta_Q^2$
2	1	0	0	$-\frac{9}{8}\eta_Q^2$
2	2	0	0	$\frac{9}{32}\eta_Q^2$

Table 2.2: Coefficients in the anisotropic cosine expansion for second-order quadrupolar correction.

Substituting Eqn 2.77 into Eqn 2.66, the energy splitting due to second-order quadrupolar interaction is

$$\Delta E_{1/2\leftrightarrow -1/2}^{2Q} = \frac{hC_Q^2(I(I+1)-3/4)}{4I^2(2I-1)^2\omega_0}(2A_{21}^Q A_{2,-1}^Q + A_{22}^Q A_{2,-2}^Q), \tag{2.80}$$

which after rearrangement, leads to the following form for the transition frequency.

$$\omega^{2Q} = \omega_{iso}^{2Q} + A_2^Q(\alpha^Q,\beta^Q)P_2(\cos\theta) + A_4^Q(\alpha^Q,\beta^Q)P_4(\cos\theta) \tag{2.81}$$

Here,

$$\omega_{iso}^{(2Q)} = -\frac{3(I(I+1)-3/4)}{40\omega_0 I^2(2I-1)^2}C_Q^2(1+\frac{\eta_Q^2}{3}) \tag{2.82}$$

is the isotropic second-order quadrupolar shift. The last two terms, being anisotropic, depend on the crystalline orientation and the relative orientation between the rotor axis and the laboratory frame z-axis. These two terms are to be averaged out when high-resolution spectra are desired.

If Eqn 2.65 instead of Eqn 2.66 is combined with Eqn 2.77, the second-order quadrupolar frequency shift for the $m \leftrightarrow -m$ transition is obtained.

$$\omega^{2Q}_{m\leftrightarrow -m} = C_0(I,m)\omega^{2Q}_{iso} + C_1(I,m)A^Q_2(\alpha^Q,\beta^Q)P_2(\cos\theta) + C_2(I,m)A^Q_4(\alpha^Q,\beta^Q)P_4(\cos\theta) \tag{2.83}$$

Compared to Eqn 2.81, three constants dependent on the transition and the spin quantum number are introduced. These values are shown in table 2.3.

I	m	C_0	C_1	C_2
3/2	1/2	1	1	1
	3/2	-3	0	-21/27
5/2	1/2	1	1	1
	3/2	6/8	60/32	114/72
	5/2	-50/8	-20/32	-150/72
7/2	1/2	1	1	1
	3/2	27/15	144/60	303/135
	5/2	-1	2	165/135
	7/2	-147/15	-168/60	-483/185
9/2	1/2	1	1	1
	3/2	54/24	252/96	546/216
	5/2	30/24	300/96	570/216
	7/2	-84/24	168/96	84/216
	9/2	-324/24	-216/96	-1116/216

Table 2.3: Coefficients C_0, C_1 and C_2 in Eqn 2.83.

Another way of expanding the product of second-rank tensors takes the advantage that the product of two second-rank tensors is a sum of rank 0, 2, 4 tensors.

$$A^Q_{2m}A^Q_{2,-m} = \sum_{l=0,2,4} < l0|22m,-m > a_{l0} \tag{2.84}$$

In this equation, a_{l0} is the tensor element of an lth-rank tensor.

$$a_{l0} = \sum_{n=-l}^{l} D^{(l)}_{n0}(\omega_r t, 0, 0) \sum_{k=-l}^{l} D^{(l)}_{kn}(\alpha^Q, \beta^Q, \gamma^Q)\sigma_{lk} \tag{2.85}$$

Here

$$\sigma_{lk} = \sum_{j=-2}^{2} < lk|22j, k-j > \rho_{2j}\rho_{2,k-j}, \tag{2.86}$$

and $< l0|22m, -m >$ and $< lk|22j, k-j >$ are Glebsh-Gordon coefficients [12].

Of all the terms in Eqn 2.85, only the $n = 0$ components are time-independent. Neglecting all the terms with $n \neq 0$,

$$A^Q_{2m}A^Q_{2,-m} = \sum_{l=0,2,4} d^{(l)}_{00} \sum_{k=-l}^{l} < l0|22m, -m > D^{(l)}_{k0}(\alpha^Q, \beta^Q, \gamma^Q)\sigma_{lk}. \tag{2.87}$$

Notice that

$$d^{(l)}_{00}(\cos\theta) = P_l(\cos\theta), \tag{2.88}$$

Eqn 2.81 is reached after inserting Eqn 2.87 into Eqn 2.80.

2.5 Evolution of Spin System

After a brief discussion of the eigenstates and eigenvalues of a single spin, we now start to look at how these eigenstates and eigenvalues evolve in an NMR experiment. The evolution corresponds to rotations in the spin space, and is better described with the concepts of density matrix and density operator introduced as follows [11, 12].

2.5.1 Density Operator

For a given spin ensemble, if all of the spins are in the same state (pure state), described by the state function $|\Psi(t) >$ in an orthonormal basis $\{|In >\}$ with coeffi-

cients $C_m(t)$, the density operator $\rho(t)$ is defined by

$$\rho(t) = |\Psi(t) >< \Psi(t)| = \sum_{m,n=-I}^{I} C_m(t)C_n^*(t)|Im >< In| \tag{2.89}$$

If on the other hand, not all of the spins are in the same state (mixed state), the density operator is described by the ensemble average over all the spins.

$$\rho(t) = \overline{|\Psi(t) >< \Psi(t)|} = \sum_{m,n=-I}^{I} \overline{C_m(t)C_n^*(t)}|Im >< In| \tag{2.90}$$

The density matrix A is the matrix representation of the density operator, and is used to facilitate the numerical calculation of the evolution of the density operator.

$$A_{mn}(t) = \overline{C_m(t)C_n^*(t)} \tag{2.91}$$

The equation of motion of the density operator is described by the Liouville-von Neumann equation

$$\frac{d}{dt}\rho(t) = -i[H(t), \rho(t)], \tag{2.92}$$

whose solution is given by

$$\rho(t) = U(t)\rho(0)U(t)^{-1}. \tag{2.93}$$

Here,

$$U(t) = Texp(-i\int_0^t H(t')dt') \tag{2.94}$$

and T is the Dyson time-ordering operator [25]. When $H(t)$ is time-independent, the evolution of the density matrix can be simply represented as

$$\rho(t) = e^{-iHt}\rho(0)e^{iHt}. \tag{2.95}$$

In a real system where sample is spinning, H is often time-dependent even in the rotating frame (the reference frame that rotates around the laboratory z-axis at the

Larmor frequency. In this frame, the effect of the static field on the NMR spectra is removed. It is also the NMR detection frame). The general approach to calculate the density matrix at time t is to break up the time axis into small intervals, during each of which the Hamiltonian is constant (Figure 2.4). The density operator is then the cascaded evolutions in all the time intervals.

$$\rho(t) = e^{-iH_n t_n} e^{-iH_{n-1} t_{n-1}} \cdots e^{-iH_1 t_1} \rho(0) e^{iH_1 t_1} \cdots e^{iH_{n-1} t_{n-1}} e^{iH_n t_n} \tag{2.96}$$

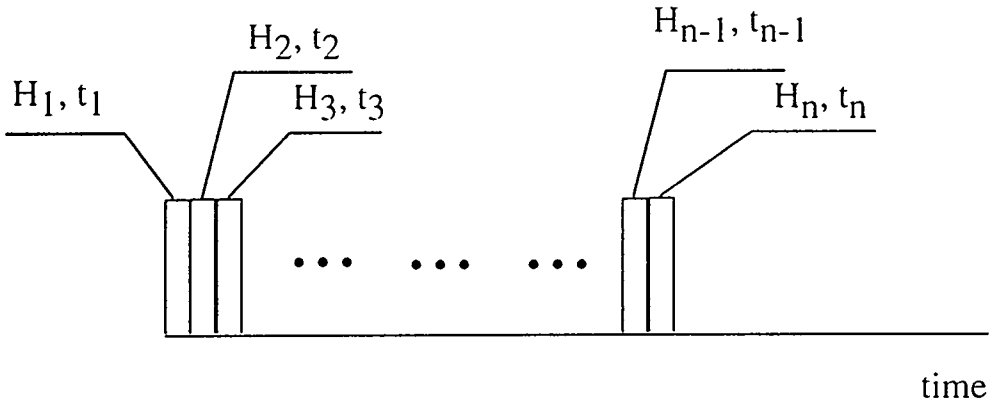

Figure 2.4: Treatment of a time-dependent Hamiltonian. The time axis is divided into small intervals, during each of which the spin Hamiltonian is time-independent.

The observable in an NMR experiment is I_+ , and the detection is achieved by using a single coil capable of collecting data in quadrature (both the real and imaginary components of the signal). Using the density operator representation, the expectation value of the operator I_+ is expressed as

$$< I_+ >= Tr(\rho(t) I_+) = \sum_{r=-I}^{I} < Ir|\rho(t) I_+|Ir >. \tag{2.97}$$

$< I_+ >$ is time-dependent and induces an electric signal that is picked up by a detection coil. The detected signal is the free induction decay (FID) of the system.

In most experiments, the phase of the receiver (ϕ_r) may be controlled to arbitrary accuracy in the computer, so the actual signal is described as

$$S(t) = e^{-i\phi_r} < I_+ >= e^{-i\phi_r} Tr(\rho(t) I_+). \tag{2.98}$$

By inserting Eqn 2.90 into Eqn 2.97, we get

$$\begin{aligned} < I_+ > &= \sum_{m,n,r=-I}^{I} \overline{C_m(t) C_n^*(t)} < Ir|Im >< In|I_+|Ir > \\ &= \sum_{m,n,r=-I}^{I} \overline{C_m(t) C_n^*(t)} \delta_{mr} \delta_{n,r+1} \\ &= \sum_{n,m=-I}^{I} \overline{C_m(t) C_n^*(t)} \delta_{n,m+1} = \sum_{m=-I}^{I} A_{m-1,m}. \end{aligned} \tag{2.99}$$

This suggests that only single-quantum transitions ($m \leftrightarrow m-1$) are directly observable, whereas multiple-quantum transitions have to be detected indirectly. This also brings about the concept of coherence, which is specified by a variable number p, and corresponds to the off-diagonal elements A_{mn} ($m \neq n$) in the density matrix. Usually, a non-zero off-diagonal element in the density matrix means that there is a connection between the two energy levels. A coherence phase factor then exists in the density matrix element, which evolves as the system evolves. At equilibrium, however, only diagonal elements exist and the density matrix is

$$\rho(0) = \frac{e^{-H_Z/kT}}{Z}, \tag{2.100}$$

where Z is a normalization prefactor and H_Z is the Zeeman Hamiltonian. With H_Z being much smaller than kT, ρ_0 is approximated as

$$\rho(0) \approx \frac{\hbar \gamma B_0}{(2I+1)kT} I_0 \rightarrow \rho(0) = I_0 \tag{2.101}$$

after dropping the constant prefactors. This gives the initial state of an NMR system. The linear dependence of $\rho(0)$ on γ means that a larger γ often gives a larger population difference and stronger NMR signal.

2.5.2 Evolution Under RF pulses

Radio frequency pulses of a well-defined length (τ), amplitude (B_1) and phase (ϕ) are used to rotate nuclear spin states by creating and destroying coherences or changing populations of the different energy levels. The strength of the pulse is defined by

$$\omega_1 = \gamma B_1. \tag{2.102}$$

The frequency ω of the pulse is often set very close to the Larmor frequency ω_0, so the Hamiltonian corresponds to the RF pulse is described as

$$H_{RF} = \hbar\omega I_Z + \hbar\omega_1(I_X\cos(\omega\tau+\phi) + I_Y\cos(\omega\tau+\phi)). \tag{2.103}$$

In the rotating frame, the Larmor frequency no longer enters the expression,

$$H_{RF}^{eff} = \hbar\Delta\omega I_Z + \hbar\omega_1(I_X\cos\phi + I_Y\sin\phi) \tag{2.104}$$

and the pulse acts as if it is a static field in the transverse $x-y$ plane at an angle ϕ with respect to the x-axis. Here, $\Delta\omega$ includes the chemical shift contribution and the frequency offset in an experiment. Notice that this Hamiltonian is no longer time-dependent in the rotating frame, one can easily calculate the density operator at time t.

$$\rho(t) = e^{-iH_{RF}^{eff}t}\rho(0)e^{iH_{RF}^{eff}t} \tag{2.105}$$

For a spin-$\frac{1}{2}$ nucleus under RF irradiation with phase ϕ, the evolution of different initial states is shown in the following equations.

$$U_{RF}(I_\phi)I_Z U_{RF}^{-1}(I_\phi) = I_Z\cos\omega_1 t + \sin\omega_1 t(I_X\sin\phi - I_Y\cos\phi) \tag{2.106}$$

$$U_{RF}(I_\phi) I_X U_{RF}^{-1}(I_\phi) = I_X(\cos^2\phi + \sin^2\phi\cos\omega_1 t) + I_Y\frac{\sin 2\phi}{2}(1-\cos\omega_1 t) - I_Z\sin\phi\sin\omega_1 t \quad (2.107)$$

$$U_{RF}(I_\phi) I_Y U_{RF}^{-1}(I_\phi) = I_Y(\sin^2\phi + \cos^2\phi\cos\omega_1 t) + I_X\frac{\sin 2\phi}{2}(1-\cos\omega_1 t) + I_Z\cos\phi\sin\omega_1 t \quad (2.108)$$

Here, $U_{RF}(I_\phi) = e^{-iH_{RF}^{eff}}$ and ϕ is the phase of the pulse. These equations are more useful when they are expressed in the spherical tensor basis set.

$$U_{RF} I_0 U_{RF}^{-1} = I_0\cos\omega_1 t + \frac{i\sin\omega_1 t}{\sqrt{2}}(I_+ e^{-i\phi} + I_- e^{i\phi}) \quad (2.109)$$

$$U_{RF} I_\pm U_{RF}^{-1} = \frac{1}{2}I_\pm(1+\cos\omega_1 t) + \frac{i}{\sqrt{2}}I_0 e^{\pm i\phi}\sin\omega_1 t - \frac{1}{2}I_\mp e^{\pm 2i\phi}(1-\cos\omega_1 t) \quad (2.110)$$

Some important points are worth noting:

I. A 90° pulse ($\omega_1 t = \pi/2$) generates a 90° rotation in the spin space. It rotates I_0 into $x-y$ plane and creates both I_+ and I_- coherences (we assign each coherence I_+ (or I_-) a coherence number 1(-1), and give it a variable name p). The coherences after the pulse have well-defined phases. For example, a 90°_x pulse creates magnetization along the $-y$ direction.

II. When

$$[H_{RF}^{eff}, \rho(0)] = 0, \quad (2.111)$$

the density matrix does not evolve since

$$e^{-iH_{RF}^{eff}}\rho(0)e^{iH_{RF}^{eff}} = \rho(0). \quad (2.112)$$

For example, after a 90°_y pulse, if another pulse is applied along the y-direction, The density matrix does not evolve and the system is in a spin-locked state. The second pulse is called a spin-locking pulse.

III. A single pulse causes the mixing of elements in the density matrix. For instance, if $\rho(0) = I_+$ and another RF pulse is applied for a time t, $\rho(t)$ is a mixture of three coherences: +1, 0 and -1. The change of coherence order under RF pulse is called coherence transfer.

IV. The phase factor ($\Delta\phi$) experienced by each coherence after a pulse with phase ϕ is proportional to the coherence number change (Δp) during coherence transfer.

$$\Delta\phi = -\Delta p\phi \tag{2.113}$$

Thus different phase factors are experienced for different final coherences. This is the key to the selection of coherence pathway, which is introduced later.

The existence of more than two energy levels for a quadrupolar nucleus in high-field greatly complicates the effect of an RF pulse on the spin system [26, 27]. In this case, the relative magnitude of ω_Q and ω_1 determines the exact effect of the pulse on the spin system. In one extreme, when $\omega_1 \gg \omega_Q$, the RF pulse is a hard pulse and a nuclear spin nutates just like a non-quadrupolar spin. On the other hand, if $\omega_1 \ll \omega_Q$, the pulse is a soft pulse and only the central transition is excited. The spin then nutates $I + \frac{1}{2}$ times as fast as a non-quadrupolar spin. In this respect, it is not unique to define 90° pulse length for a quadrupolar nucleus. When a soft pulse is used, the 90° pulse length reported is the solid-state pulse length; When a hard pulse is instead used, the pulse length is the liquid-state pulse length (since in the liquid state, the averaged quadrupolar coupling constant is zero), which is $I + \frac{1}{2}$

times as long as the solid-state pulse length. The different definitions of pulse length sometimes cause confusion. We shall go back to the excitation problem in chapter 3 when multiple-quantum experiments are involved.

2.5.3 Free Induction Decay

Free induction decay (FID) is the evolution of the spin system after or between RF pulses. The evolution is governed by the total Hamiltonian of the system, which may consist of many internal spin Hamiltonians.

$$H_{FID}^{eff} = H_{CS} + H_Q + H_D \tag{2.114}$$

The evolution of the density operator is described by

$$\rho(t) = e^{-iH_{FID}^{eff}t}\rho(0)e^{iH_{FID}^{eff}t}, \tag{2.115}$$

if H_{FID}^{eff} is time-independent.

Free induction decay does not cause the creation and destroy of coherences, thus no coherence transfer is involved. However, a phase factor is still experienced for each coherence.

$$U_{FID}I_0U_{FID}^{-1} = I_0 \tag{2.116}$$

$$U_{FID}I_\pm U_{FID}^{-1} = I_\pm e^{\mp i\Omega t} \tag{2.117}$$

In these equations,

$$U_{FID} = e^{-iH_{FID}^{eff}}, \tag{2.118}$$

and Ω is a sum of the shift frequencies due to chemical shift and 2nd-order quadrupolar interaction.

$$\Omega = \omega^{CS} + \omega^{2Q} \tag{2.119}$$

Some important points are worth noting here:

I. If the spin system is in I_0 state, it does not evolve when there is no pulse applied. As a result, when a 90° pulse is applied to the magnetization in the $x-y$ plane, the final density matrix has an I_0 component that does not evolve after the pulse. This component can be kept for a short time (tens of milliseconds to many seconds) and restored by another 90° pulse. The pair of 90° pulses separated by a short delay used for storing magnetization is called a z-filter. The stored magnetization actually decays slowly during the delay between the pulses. The decay is the result of exchanging energy between the spin reservoir and its environment, and can be characterized by an exponential decay with time constant T_1 (spin-lattice relaxation) [28, 29].

$$M_0 - M_Z = M_{0e}^{-t/T_1} \tag{2.120}$$

Here M_Z is the remaining magnetization in the z-direction and M_0 is the magnetization when the system is at equilibrium. z-filter is used in DAS to store magnetization along the z-axis during the reorientation of spinner axis.

II. The phase factor that is accumulated during FID is dependent on the resonance frequency Ω. This is where the chemical shift and quadrupolar interactions come into play to affect the NMR spectra.

III. The shift frequencies for the +1 and -1 coherences have opposite signs. If the +1 and -1 coherences are both detected, mirror image of the real peaks is expected. This is not a problem in a simple one-dimensional NMR experiment, as the detector records only the signal from I_+ coherence. In a two-dimensional experiment, this does cause problems that need to be treated carefully.

2.5.4 Example: A Simple 1D NMR Experiment

As an example, let us consider the evolution of the density matrix of a spin system in a simple one-dimensional NMR experiment shown in Figure 2.5. We also assume

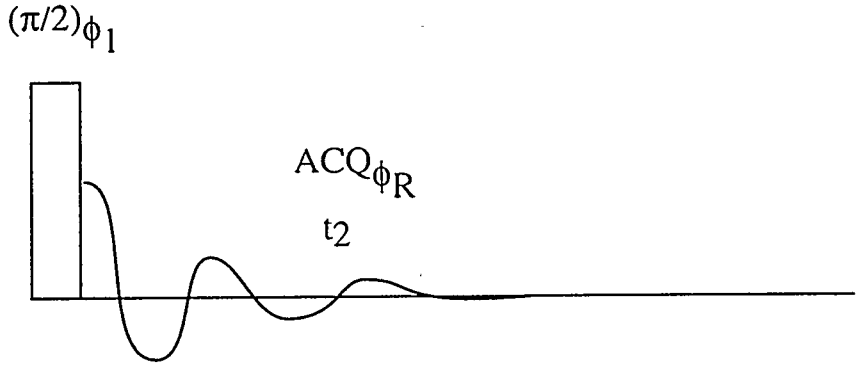

Figure 2.5: Pulse sequence for a simple one-dimensional NMR experiment.

that all of the spins have the same resonance frequency Ω. The experiment has only one 90°_x pulse ($\phi = 0$), which is followed by quadrature detection with $\phi_r = 90°$. The density matrix at equilibration is I_0, which after the pulse becomes a mixture of I_+ and I_- (Eqn 2.109).

$$I_0 \longrightarrow \frac{i}{\sqrt{2}}(I_+ + I_-) \tag{2.121}$$

This mixed state after delay t becomes (Eqn 2.117)

$$\frac{i}{\sqrt{2}}(I_+ + I_-) \longrightarrow \frac{i}{\sqrt{2}}.(I_+ e^{-i\Omega t} + I_- e^{i\Omega t}) \tag{2.122}$$

The signal is then expressed as

$$S(t) = e^{-i\pi/2} Tr(\rho(t) I_+) = exp(i\Omega t), \tag{2.123}$$

which after complex Fourier transformation, gives a δ-function in the frequency domain.

The line observed in a real NMR experiment is never a δ-function but has a finite linewidth. Since the sample has a finite volume, different parts of the sample have slightly different resonance frequencies due to the field inhomogeneity. This frequency difference broadens the NMR spectrum. Impurities in a sample may contribute to the broadening as well. Even if all of these factors do not exist, the spin-spin relaxation dephases the coherences and still broadens the spectra. Notice that a nuclear spin is not isolated in the system, its interaction with environment could add a random phase factor to the coherence. This causes the dephasing of the magnetization whose net effect can often be approximated by an exponential decay with a time constant T_2 (spin-spin relaxation time) [30]. Including this decay in Eqn 2.123 gives the experimentally detected signal.

$$S(t) = e^{-t/T_2} e^{i\Omega t} \tag{2.124}$$

Fourier transformation of this signal results in a Lorentzian-shape peak at frequency Ω.

2.5.5 Coherence Pathway

It is common in NMR that multiple pulses are used. Since an RF-pulse creates and mixes coherences of different orders and each coherence evolves with different frequencies, after many pulses, the resultant density matrix may be very complicated. Even though the detector only picks up the -1 coherence, the signal still comes from spins followed different paths and is quite complex. The coherence orders that the nuclear spins follow can be specified by writing out the coherence numbers along the path sequentially (coherence pathway). For example, in Figure 2.6, the coherence pathway designated by the bolded line is the $0 \rightarrow -1 \rightarrow 0 \rightarrow -1$ pathway, whereas the dotted line is the $0 \rightarrow +1 \rightarrow 0 \rightarrow -1$ pathway.

In a multiple-pulse NMR experiment, the desired signal often comes from a specific

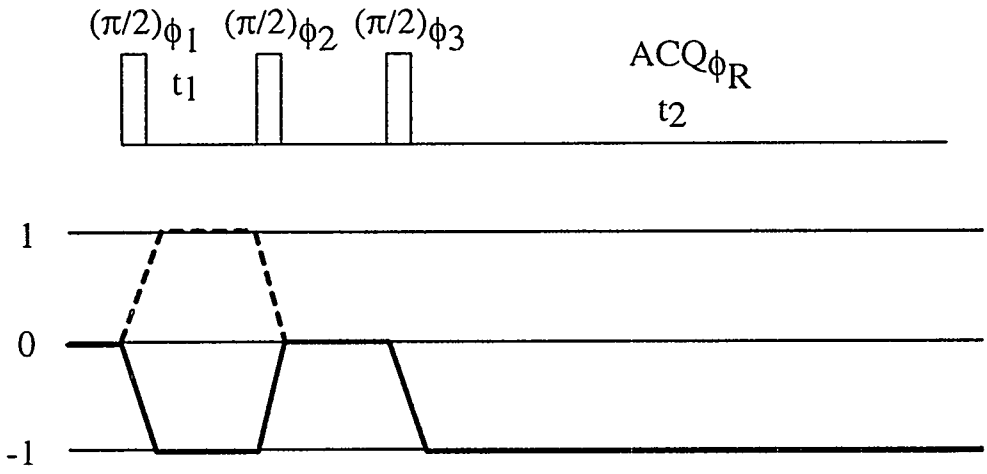

Figure 2.6: The coherence pathway for a simple DAS experiment. The bolded and dashed lines are the desired signal.

coherence pathway. To get rid of the signal from other pathways, we can add up signal from many different experiments in which the phases of the pulses and the receivers are systematically incremented (phase cycle). Some empirical rules that are used to design correct phase cycles are listed below [31, 32, 33].

I. The last pulse needs no phase cycle since the detection ensures that the -1 coherence is selected.

II. If a pulse is changed in phase by ϕ, then a coherence undergoing a change in coherence order of Δp experiences a phase shift of $-\Delta p \cdot \phi$.

III. If the coherence order changes along a desired coherence pathway is $(\Delta p_1, \Delta p_2, \cdots \Delta p_n)$. the receiver phase should be set to

$$\phi_r = -\sum_{i=1}^{n} \Delta p_i \cdot \varphi_i, \tag{2.125}$$

to ensure the selection of this pathway. Here, φ_i is the phase of the ith RF pulse.

IV. To restrict the coherence transfer under a pulse to a particular change Δp in coherence order, we may perform $m(m > |\Delta p|)$ experiments with the RF phase

$$\phi_i = 2k_i\pi/m, \tag{2.126}$$

where $k_i = 0, 1, \cdots, m-1$.

V. The above procedure retains not only the coherence undergoes a change Δp, but also those with changes equal to $\Delta p \pm nm$, where n is an integer.

As an example, consider the coherence pathway of a simple DAS experiment (Figure 2.6). Here, both the bolded and the dashed pathways are to be retained. The first pulse induces coherence transfer with $\Delta p = \pm 1$. According to rule IV, this pulse need to be cycled through at least two phases (0°, 180°). According to rule V, the phase cycle retains all the odd-order coherences, and rejects the even-order coherences. Similarly, the second pulse is cycled through two phases (0°, 180°) to guarantee coherence transfer with $\Delta p = \pm 1$. The third pulse can be left uncycled since receiver picks up the -1 coherence order. Using Eqn 2.125, the receiver phases can be determined and the following 4-step phase cycle is obtained.

$$\begin{aligned} \phi_1 &= 0°, 0°, 180°, 180° \\ \phi_2 &= 0°, 180°, 0°, 180° \\ \phi_3 &= 0°, 0°, 0°, 0° \\ \phi_r &= 0°, 180°, 180°, 0° \end{aligned} \tag{2.127}$$

In an experiment that involves a lot of pulses, it may be possible to leave some pulses uncycled. In the above DAS experiment, the delay between the second and third pulses is 30-60msec, which is long enough that coherences other than the zeroth order (the I_0 state) disappear due to relaxation. This means that the long delay kills

all the unwanted coherences and phase cycle of the second pulse is unnecessary. The simplified two-step phase cycle is given below.

$$\begin{aligned} \phi_1 &= 0°, 180° \\ \phi_2 &= 0°, 0° \\ \phi_3 &= 0°, 0° \\ \phi_r &= 0°, 180° \end{aligned} \tag{2.128}$$

More examples of how to construct correct phase cycles are discussed in chapter 3.

2.6 Two-Dimensional NMR

2.6.1 Basics

A two-dimensional NMR experiment has two distinct free evolution periods, usually separated by RF pulses to enhance the information content of the spectra. The basic scheme of the experiment is shown in Figure 2.7 and four different intervals exist in the experiment. During the preparation period, the spin system is prepared in a coherent state from the equilibrated state I_0 through RF pulses. In the course of evolution period, the spin system is allowed to undergo free evolution under the effective Hamiltonian $H^{(1)}_{FID}$. The superscipt designates that this Hamiltonian is the Hamiltonian during the first evolution period. The evolution period is made variable in a two-dimensional experiment, allowing the sampling of I_1-evolution. The mixing period may consist of one or more pulses, separated by constant intervals. For example, in the DAS experiment shown in Figure 2.6, the second and third pulses separated by a time interval (z-filter) comprises the mixing period. The mixing process introduces perturbation to the spin system so that the effective Hamiltonian after mixing period ($H^{(2)}_{FID}$) is often different from $H^{(1)}_{FID}$. The detection period is similar to that in a one-dimensional experiment.

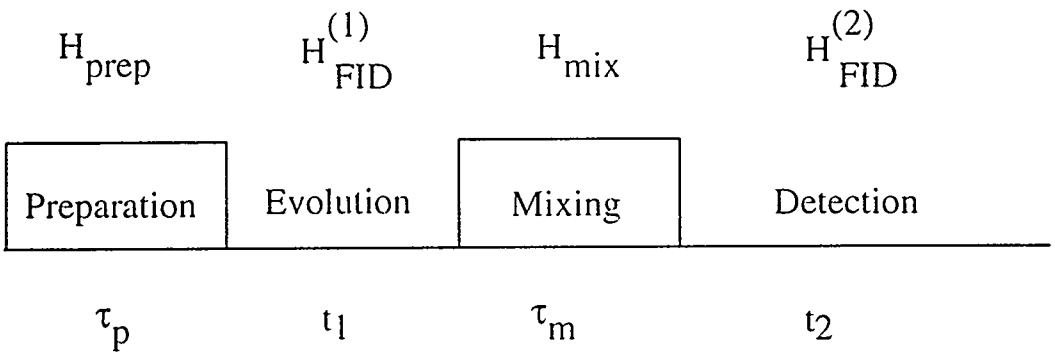

Figure 2.7: A schematic diagram of a two-dimensional NMR experiment.

Assuming that the frequency shifts in the evolution period and the detection period are Ω_1 and Ω_2 respectively, the signal from a two dimensional experiment can often be described by the product of two free induction decay signals.

$$S(t_1, t_2) = e^{-t_1/T_2} e^{i\Omega_1 t} e^{-t_2/T_2} e^{i\Omega_2 t} \tag{2.129}$$

After two-dimensional Fourier transformation, frequency domain spectrum is obtained which reflects the correlation between the two frequency domains.

2.6.2 Pure-Absorption Phase 2-D NMR Lineshape

Fourier transformation of Eqn 2.129 actually does not give a spectrum with best resolution. The frequency spectrum contains negative intensity (dispersive) and does not have pure phase. To see the problem clearly, consider the Fourier transformation of the t_2 dimension of Eqn 2.129.

$$S(t_1, \omega_2) = e^{-t_1/T_2} e^{i\Omega_1 t_1} (A(\omega_2, \Omega_2) + iD(\omega_2, \Omega_2)) \tag{2.130}$$

Here $A(\omega, \Omega)$ and $D(\omega, \Omega)$ are the absorptive and dispersive lineshape functions with a peak at Ω in the ω dimension.

$$A(\omega, \Omega) = \frac{T_2}{1 + (\omega - \Omega)^2 T_2^2} \tag{2.131}$$

$$D(\omega,\Omega) = \frac{(\omega-\Omega)T_2^2}{1+(\omega-\Omega)^2T_2^2} \tag{2.132}$$

After a second Fourier transformation, the signal in the frequency domain is then

$$\begin{aligned} S(\omega_1,\omega_2) &= (A(\omega_1,\Omega_1)+iD(\omega_1,\Omega_1))(A(\omega_2,\Omega_2)+iD(\omega_2,\Omega_2)) \\ &= A(\omega_1,\Omega_1)A(\omega_2,\Omega_2) - D(\omega_1,\Omega_1)D(\omega_2,\Omega_2) \\ &\quad + i(A(\omega_1,\Omega_1)D(\omega_2,\Omega_2) + D(\omega_1,\Omega_1)A(\omega_2,\Omega_2)) \end{aligned} \tag{2.133}$$

The imaginary component can be dropped now and the real component is displayed. The real component contains the $-D(\omega_1,\Omega_1)D(\omega_2,\Omega_2)$ term which leads to a phase-twisted lineshape. The desired signal is $A(\omega_1,\Omega_1)A(\omega_2,\Omega_2)$ only.

One of the solutions (States method) [34] is to acquire the data in a hypercomplex fashion. Instead of recording a single dataset, two datasets $S_c(t_1,t_2)$ and $S_s(t_1,t_2)$ are recorded separately. Mathematically, the two signals correspond to the cosine and sine portions of the signal in the t_1 dimension.

$$S_c(t_1,t_2) = \cos(\Omega_1 t_1)e^{-(t_1+t_2)/T_2}e^{i\Omega_2 t_2} \tag{2.134}$$

$$S_s(t_1,t_2) = \sin(\Omega_1 t_1)e^{-(t_1+t_2)/T_2}e^{i\Omega_2 t_2} \tag{2.135}$$

Fourier transformation about t_2 is then separately done on both datasets.

$$S_c(t_1,\omega_2) = \cos(\Omega_1 t_1)e^{-t_1/T_2}(A(\omega_2,\Omega_2)+iD(\omega_2,\Omega_2)) \tag{2.136}$$

$$S_s(t_1,\omega_2) = \sin(\Omega_1 t_1)e^{-t_1/T_2}(A(\omega_2,\Omega_2)+iD(\omega_2,\Omega_2)) \tag{2.137}$$

The imaginary components of both datasets are then dropped and the real components are combined appropriately to form a dataset

$$S(t_1,\omega_2) = A(\omega_2,\Omega_2)e^{-t_1/T_2}e^{-i\Omega_1 t_1}. \tag{2.138}$$

The Fourier transformation of this dataset with respect to t_1 is

$$S(\omega_1,\omega_2) = A(\omega_2,\Omega_2)(A(\omega_1,\Omega_1)+iD(\omega_1,\Omega_1)). \tag{2.139}$$

Only the real channel of this signal is showed and the spectrum is of pure-absorption phase lineshape.

In the simple DAS experiment shown in Figure 2.6, the bolded line gives the signal in Eqn 2.129. In order to get S_c and S_s, it is essential to retain the coherence pathway designated by the dashed line. The signal corresponding to the dashed line is

$$S'(t_1, t_2) = e^{-t_1/T_2} e^{-i\Omega_1 t} e^{-t_2/T_2} e^{i\Omega_2 t}. \tag{2.140}$$

The detected signal is then

$$S_c(t_1, t_2) = S + S' = 2\cos(\Omega_1 t_1) e^{-t_1/T_2} e^{-t_2/T_2} e^{i\Omega_2 t_2}. \tag{2.141}$$

For the last equality,

$$\cos(\Omega t) = \frac{e^{-i\Omega t} + e^{i\Omega t}}{2} \tag{2.142}$$

is used.

The sine part of the signal can be obtained by phase shifting the first pulse by -90°, and keeping the phases of all other pulses unchanged. The detected signal is thus

$$\begin{aligned} S_s(t_1, t_2) &= e^{-i\pi/2} S + e^{i\pi/2} S' \\ &= 2\sin(\Omega_1 t_1) e^{-t_1/T_2} e^{-t_2/T_2} e^{-i\Omega_2 t_2}. \end{aligned} \tag{2.143}$$

Chapter 3

High-Resolution NMR of Quadrupoles

In the preceding chapter, the orientational dependence of the chemical shift and quadrupolar interactions were derived. Conventional sample spinning techniques (magic-angle spinning (MAS) and variable-angle spinning (VAS)) are first introduced in this chapter and are shown to be ineffective to average out the 2nd-order quadrupolar interaction. Dynamic-angle spinning (DAS) and multiple-quantum magic-angle spinning (MQMAS) methods are then presented which reconstruct high-resolution isotropic spectra for quadrupolar nuclei. Experimental results with both techniques are shown and compared in detail.

3.1 Magic-Angle and Variable-Angle Spinning

Magic-angle spinning (MAS) was first developed by Andrew [35, 36] to remove heteronuclear dipolar coupling and chemical shift anisotropy that a spin-$\frac{1}{2}$ nucleus experiences. Combined with cross polarization (CP) [13], it allows routine rapid collection of proton-enhanced ^{13}C spectra with liquid-like resolution in most solid-state NMR laboratories [14]. The principles of the MAS technique were discussed in chapter 2, where the 1st-order frequency shift due to chemical shift was written as

$$\omega^{CS}(\alpha^{CS}, \beta^{CS}) = \omega_{iso} + A_2^{CS}(\alpha^{CS}, \beta^{CS}) P_2(\cos\theta) \tag{3.1}$$

The symbols all have their common meanings. It is instantaneously clear that spinning the sample at the magic-angle (MAS, $\theta = 54.74°$) averages out the orientation-dependent terms in the above equation ($P_2(\cos\theta) = 0$).

Figure 3.1 is the simulated static and MAS spectra of a spin-$\frac{1}{2}$ nucleus at two

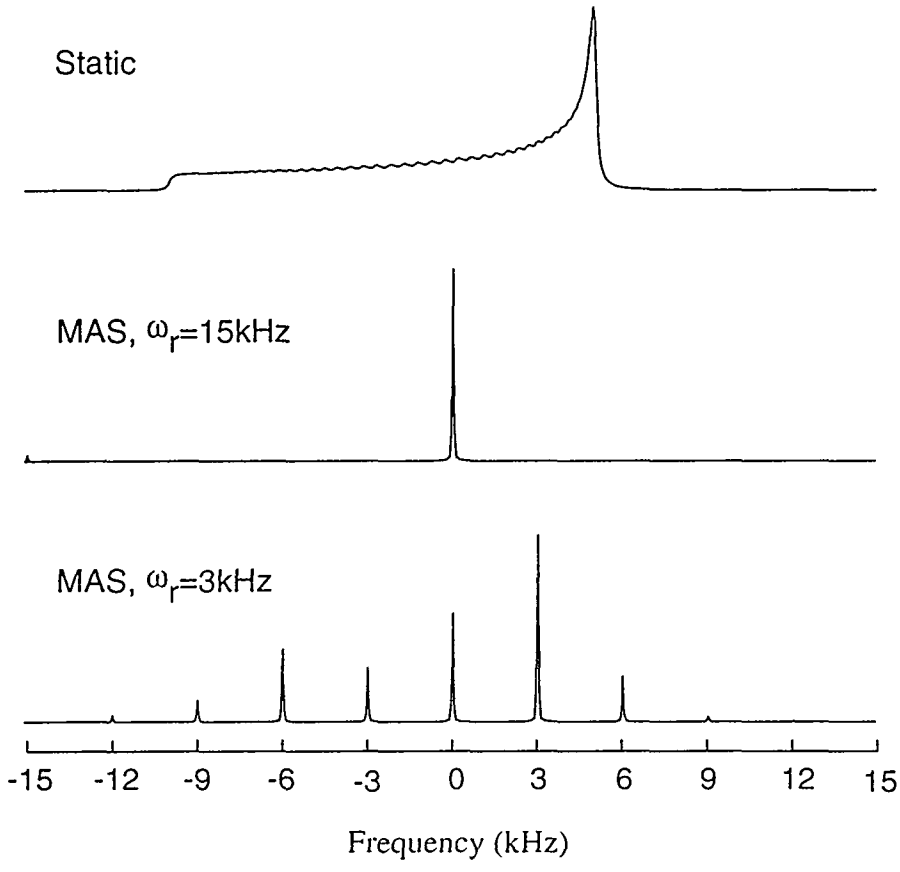

Figure 3.1: Simulated static and MAS spectra of a spin-$\frac{1}{2}$ nucleus. The parameters used for simulation are $\delta_{iso} = 0.0$ppm, $\delta_{CS} = 100$ppm, $\eta_{CS} = 0.0$, $\omega_0 = 100$MHz.

spinning rates. As expected, MAS removes the anisotropy of chemical shift interaction, leading to a sharp peak at the isotropic chemical shift position. It is also clear that additional lines may appear at $\delta_{iso} + n\omega_r$ when the spinning speed ω_r low. These lines are spinning sidebands that come from the modulation of the free evolution by the sample rotation. The modulation originates from the time-dependent terms we neglected in Eqns 2.68 and 2.76, and will not be considered in detail in this thesis [21, 22, 37]. For now, we consider only the isotropic sites (centerbands) in the spectra. Experimentally, discriminating centerbands from sidebands is overcome by performing measurements at two spinning rates and the peaks that do not shift will be the isotropic sites.

MAS is also efficient in removing the 1st-order quadrupolar interaction. Again,sidebands

are expected [19].

$$\omega^{1Q}_{m\leftrightarrow m-1} = \frac{3(2m-1)\hbar C_Q}{4I(2I-1)} P_2(\cos\theta)(\frac{3\cos^2\beta^Q - 1}{2} + \frac{\eta_Q}{2}\sin^2\beta^Q\cos 2\alpha^Q) \qquad (3.2)$$

The difficulty is, however, that the 1st-order quadrupolar interaction is often so large that the satellite transitions ($m \leftrightarrow m-1$ transitions , $m \neq \frac{1}{2}$) that are broadened by the 1st-order interaction are not observable (see [17, 18, 19]) for opposite examples). The central transition is further broadened by 2nd-order quadrupolar interaction, which has scalar and P_2-, P_4-dependent terms that give the frequency expression below (see also, Eqn 2.81).

$$\omega^{2Q}(\alpha^Q,\beta^Q) = \omega^{2Q}_{iso} + A^Q_2(\alpha^Q,\beta^Q)P_2(\cos\theta) + A^Q_4(\alpha^Q,\beta^Q)P_4(\cos\theta) \qquad (3.3)$$

The dependences of $P_2(\cos\theta)$ and $P_4(\cos\theta)$ on the spinning angle θ is shown in Figure 3.2. It is obvious that $P_2(\cos\theta) = 0$ and $P_4(\cos\theta) = 0$ have no common roots. This means that spinning the sample at the magic-angle (MAS) or at an angle other than 54.74° (variable-angle spinning, VAS) is not effective for the removal of the 2nd-order quadrupolar anisotropy. As an example, Figure 3.3 shows the ^{23}Na 9.4T static and MAS spectra of $Na_2C_2O_4$. The MAS spectrum is narrower than the static spectrum by a factor of 5, but is still broadened to 4kHz by the residue 2nd-order quadrupolar interaction.

To further demonstrate the effect of sample spinning on the quadrupolar lineshapes, Figure 3.4 shows the simulated spectra with different quadrupolar asymmetric parameters (η_Q) and spinning angles (θ) [38, 39]. It is interesting that when $\eta_Q \approx 0$, spinning the sample at 79.19° or 37.38° gives better resolution than MAS [40, 41]. Nevertheless, this is not true when η_Q approaches unity, and the spectra are rarely as sharp as the MAS spectra of spin-$\frac{1}{2}$ nuclei. Dynamic-angle spinning (DAS) and multiple-quantum magic-angle spinning (MQMAS) are two of the solutions that over-

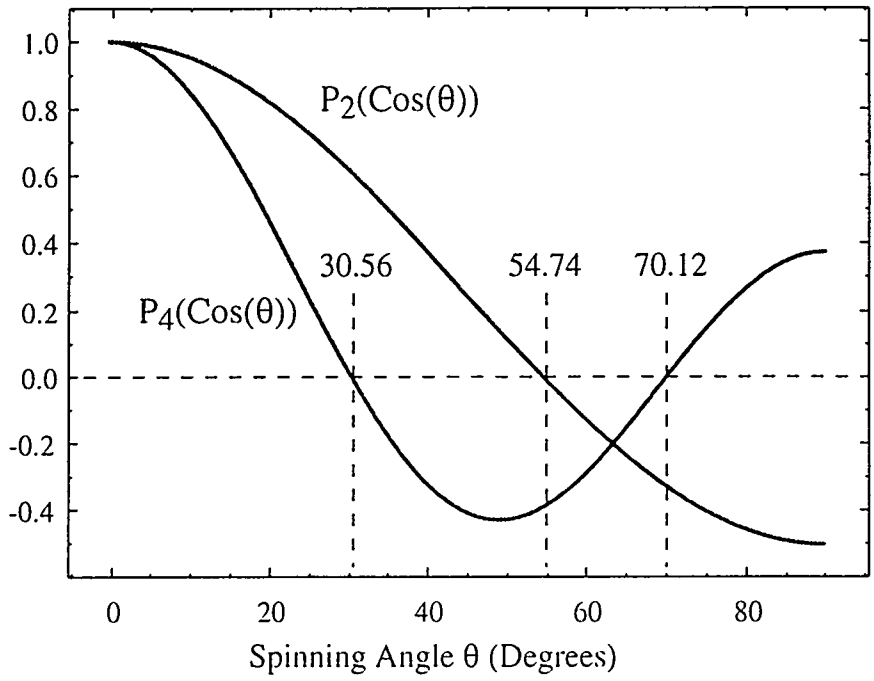

Figure 3.2: 2nd and 4th order Legendre polynomials as a function of spinner angle. There is no single angle at which both polynomials are zero.

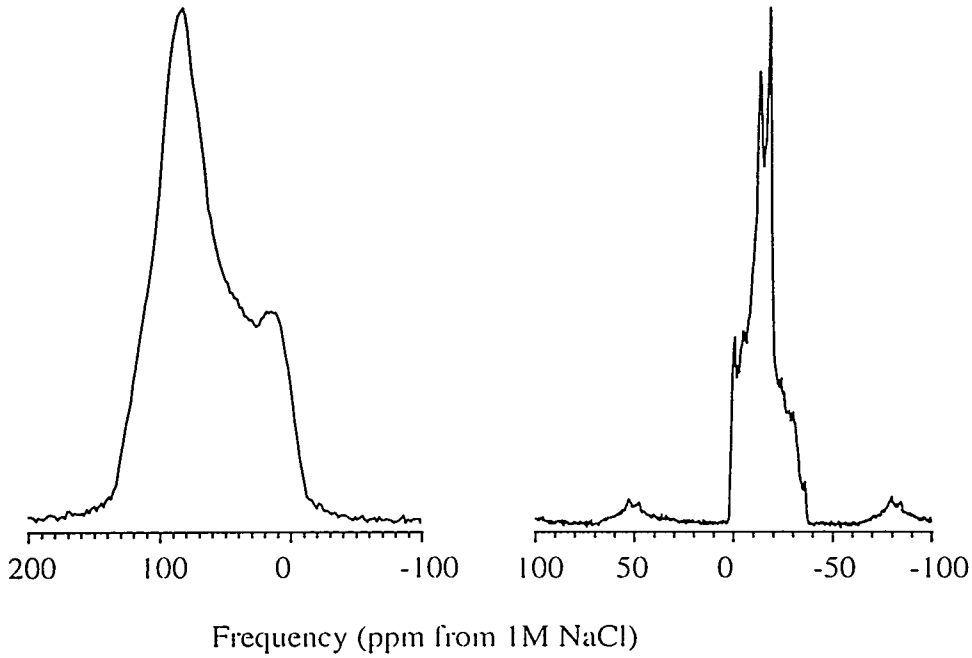

Figure 3.3: ^{23}Na static and MAS spectra of $Na_2C_2O_4$ at 9.4T. The MAS spectrum is narrower than the static spectrum, but is still broadened to about 4 kilohertz.

come this resolution problem and will be discussed primarily in this chapter. Alternative solutions such as double rotation (DOR) and dynamic-angle hopping (DAH) are also briefly discussed at the end of this chapter.

3.2 2nd-order Averaging: Theory

The analysis in section 3.1 reveals a major problem to overcome in the NMR of half-integer quadrupolar spins. The central transition, which are not broadened to the 1st-order by quadrupolar interaction, remains broad under MAS or VAS since the frequency expression for 2nd-order quadrupolar interaction contains two anisotropic terms that depend on $P_2(\cos\theta)$ and $P_4(\cos\theta)$ respectively (Eqn 2.83).

$$\omega^{2Q}_{m\leftrightarrow -m} = C_0(I,m)\omega^{2Q}_{iso}+C_1(I,m)A^Q_2(\alpha^Q,\beta^Q)P_2(\cos\theta)+C_2(I,m)A^Q_4(\alpha^Q,\beta^Q)P_4(\cos\theta) \tag{3.4}$$

3.2.1 Hahn-Echo Experiment

The simplest experiment that removes the 2nd-order quadrupolar broadening, is the Hahn-echo experiment. The experiment consists of a 90° (ϕ_1) pulse followed by a delay $t_1/2$ followed by an 180° (ϕ_2) pulse followed by another delay $t_1/2$ and then acquisition with receiver phase ϕ_r (Figure 3.5). When t_1 is incremented in a two-dimensional fashion, this experiment allows the measurement of the intrinsic T_2 relaxation time.

The observed signal in this experiment may be calculated as follow. The initial density matrix I_0 evolves during the first pulse into a mixture of two states.

$$I_0 \xrightarrow{90^\circ_{\phi_1}} \frac{i}{\sqrt{2}}(I_+e^{-i\phi_1} + I_-e^{i\phi_1}) \tag{3.5}$$

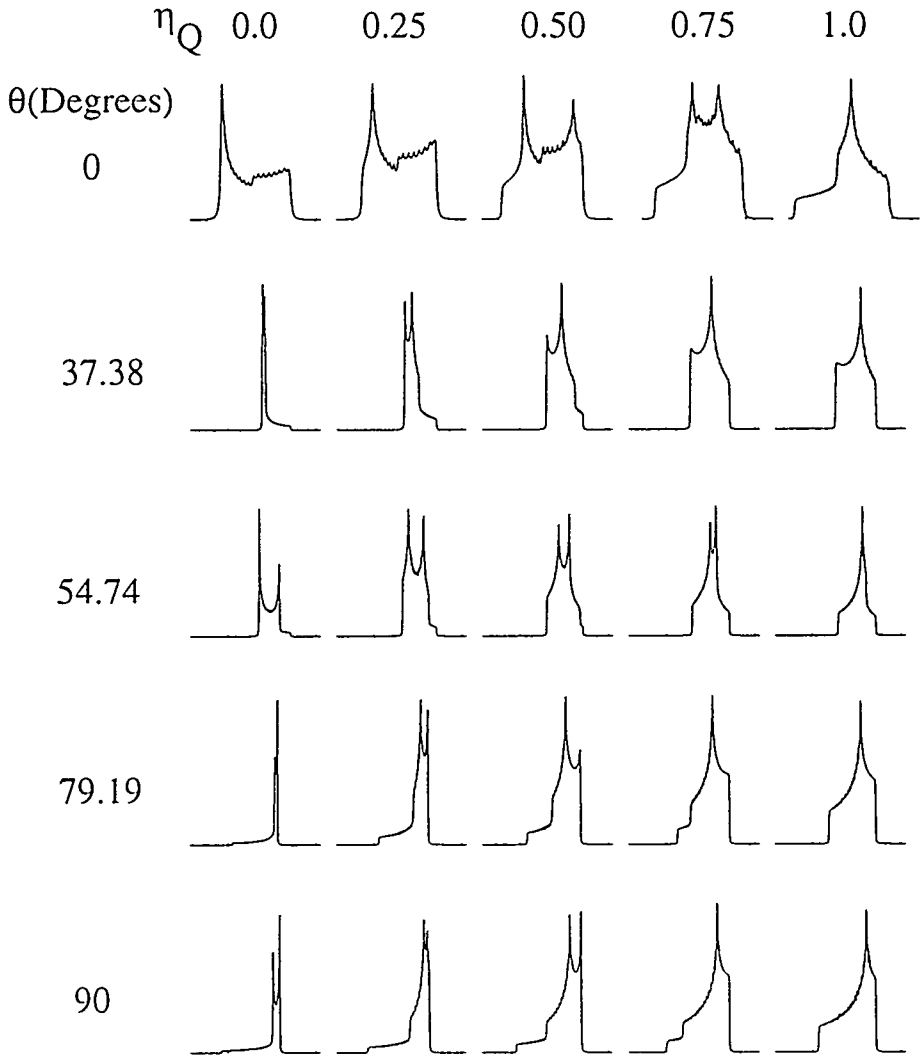

Figure 3.4: Simulated quadrupolar variable-angle spinning (VAS) spectra assuming infinite spinning rate. The vertical scale is not the same for different spectra.

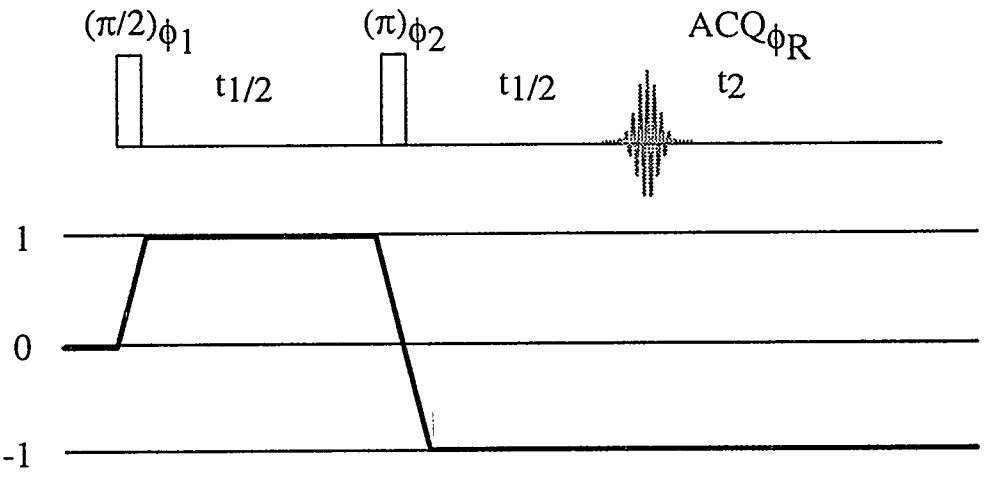

Figure 3.5: 90°-180° Hahn-echo sequence and coherence pathway. This sequence allows the measurement of intrinsic spin-spin relaxation time T_2. The sequence refocuses the 2nd-order quadrupolar interaction, together with the isotropic chemical shift and 2nd-order quadrupolar shift.

The states continue to evolve under the effective FID Hamiltonian for a time $t_1/2$.

$$\frac{i}{\sqrt{2}}(I_+e^{-i\phi_1} + I_-e^{i\phi_1}) \xrightarrow{FID} \frac{i}{\sqrt{2}}(I_+e^{-i(\phi_1+\Omega t_1/2)} + I_-e^{i(\phi_1+\Omega t_1/2)}) \tag{3.6}$$

When the 180° pulse is applied, the system evolves into

$$\frac{i}{\sqrt{2}}(I_+e^{-i(\phi_1+\Omega t_1/2)} + I_-e^{i(\phi_1+\Omega t_1/2)}) \xrightarrow{180^\circ_{\phi_2}}$$

$$-\frac{i}{\sqrt{2}}(I_-e^{-i(\phi_1-2\phi_2+\Omega t_1/2)} + I_+e^{i(\phi_1-2\phi_2+\Omega t_1/2)}), \tag{3.7}$$

which then evolves for a time $t_1/2$ before final detection is done. Since evolution does not result in any coherence transfer, the only coherence we need to consider here is the -1 coherence.

$$-\frac{i}{\sqrt{2}}I_-e^{-i(\phi_1-2\phi_2+\Omega t_1/2)} \xrightarrow{FID} -\frac{i}{\sqrt{2}}I_-e^{-i(\phi_1-2\phi_2+\Omega t_1/2-\Omega t_1/2)} \tag{3.8}$$

$$S(t_1,t_2) = -\frac{i}{\sqrt{2}}e^{-(t_1+t_2)/T_2}e^{-i(\phi_1-2\phi_2+\phi_r)}e^{i\Omega t_2}Tr[I_-I_+]$$

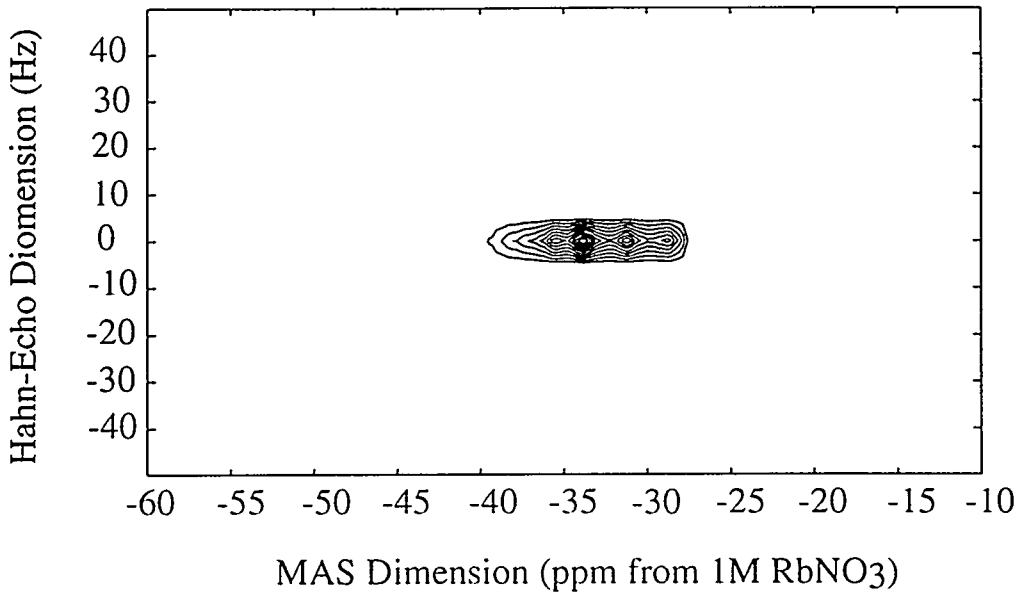

Figure 3.6: Hahn-echo spectrum of ^{87}Rb in $RbNO_3$ at 11.7T. Notice that only one zero-frequency peak is observed even though there are three distinct rubidium sites in the salt.

$$= -\frac{i}{2\sqrt{2}} e^{-(t_1+t_2)/T_2} e^{-i(\phi_1-2\phi_2+\phi_r)} e^{i\Omega t_2} \tag{3.9}$$

Except for the T_2 decay, this signal has no t_1 dependence. The dephasing due to the chemical shift and quadrupolar interactions in the t_1 dimension is refocused, and an echo forms at the start of the acquisition. An isotropic peak is expected in the t_1 dimension (Figure 3.6) as all of the anisotropies are removed.

This method is in fact, not suitable for practical applications since it does not discriminate chemical sites with different isotropic shifts or quadrupolar coupling constants. The 180° pulse refocuses the evolution under isotropic shifts and a single zero-frequency peak is observed in the isotropic dimension (Fig 3.6). The desired technique would in principle, refocus the dephasing due to the anisotropic terms in Eqn 3.3, but would not refocus the evolution under the isotropic shifts. Both DAS and MQMAS achieve this goal. DAS accomplishes this selective averaging spatially, by spinning the sample at two angles sequentially; MQMAS, instead, combines sample

spinning and multiple-quantum transitions to achieve this purpose. In DAS, the isotropic evolution is not disturbed so the observed shifts in the isotropic dimension are the same as those observed in DOR or DAH; MQMAS, however, partially refocuses the isotropic evolution so the observed shifts, only after correct transformation, give the DAS shifts. In this respect, both DAS and MQMAS are special types of echo experiments.

Two points are worth noting here about the echo experiment. First, the above derivation assumes that the 90° and 180° pulses are ideal so that no signal from other coherence pathways is observed. Experimentally, phase cycle must be exploited to ensure that the correct pathway ($0 \rightarrow +1 \rightarrow -1$) is selected. A four-step phase cycle is given below.

$$\begin{aligned} \phi_1 &= 0°, 0°, 0°, 0° \\ \phi_2 &= 0°, 90°, 180°, 270° \\ \phi_r &= 0°, 180°, 0°, 180° \end{aligned} \tag{3.10}$$

Second, the t_1 dimension in a two-dimensional experiment can be broken up into many intervals. This gives us more freedom to prepare the spin system to achieve desired averaging. In fact, the t_1 dimensions of DAS and MQMAS are both broken up into two separated time intervals.

3.2.2 DAS

Figure 3.7 shows the DAS experiment, the pulse sequence and the corresponding coherence pathway [1]. In this experiment, the sample undergoes free precession after a 90° pulse with the sample spinning at a first angle θ_1 for $\frac{t_1}{1+k}$. Here, k is a constant that is defined later. A second 90° pulse stores half of the magnetization along the z-axis, after which the spinner axis is flipped to θ_2. A third 90° pulse then brings the

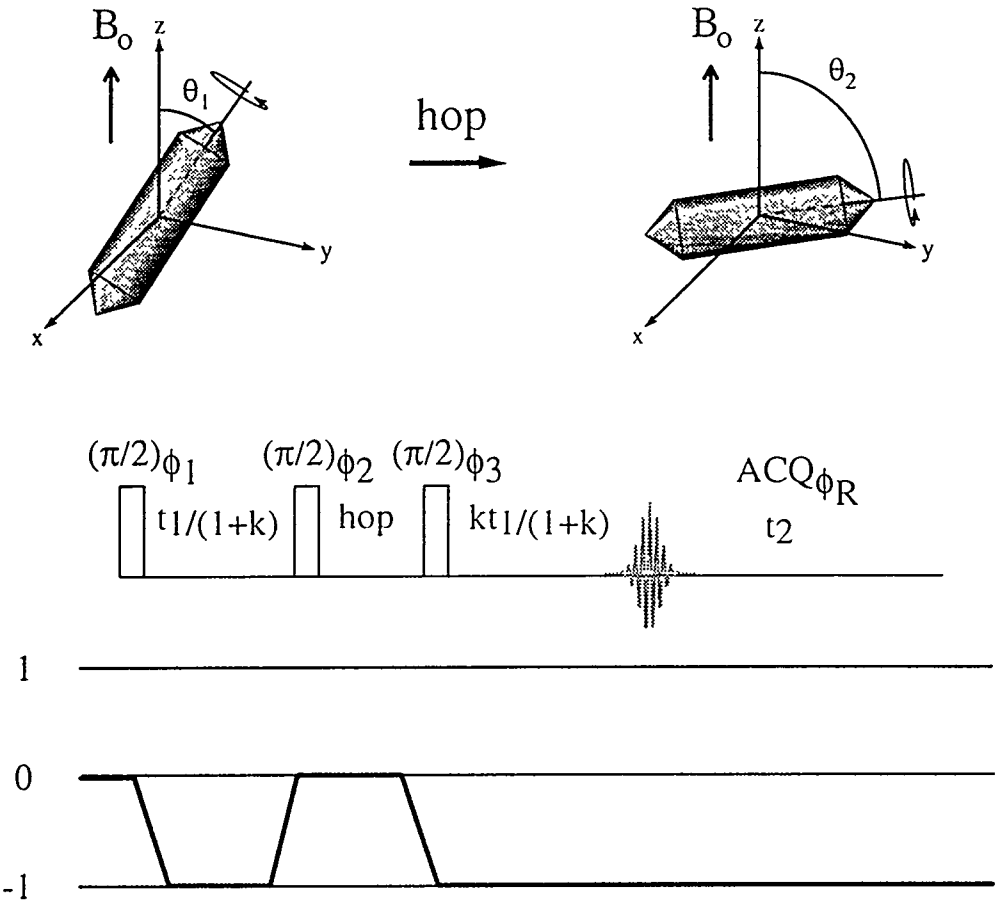

Figure 3.7: DAS experiment and pulse sequence. In this experiment, the value t_1 is incremented in a two-dimensional fashion. During the time interval between the z-filter pulses, the spinning angle is flipped from θ_1 to θ_2. The t_1 dimension gives the isotropic DAS spectrum.

stored magnetization to the transverse plane (This pair of 90° pulses separated by a time interval is termed as a z-filter. It behaves as if the density matrix were the same before and after the z-filter. This is true when appropriate phase cycle is performed). A DAS-echo is formed at $\frac{kt_1}{1+k}$ after the third pulse and acquisition starts exactly on the echo top. By incrementing t_1 in a two-dimensional fashion, a two-dimensional dataset is acquired which, after Fourier transform, has an isotropic t_1 dimension.

To see how the DAS-echo is formed, consider the 2nd-order quadrupolar frequency

expressions at two angles.

$$\omega_1^{2Q}(\alpha^Q,\beta^Q) = \omega_{iso}^{2Q} + A_2^Q(\alpha^Q,\beta^Q)P_2(\cos\theta_1) + A_4^Q(\alpha^Q,\beta^Q)P_4(\cos\theta_1) \quad (3.11)$$

$$\omega_2^{2Q}(\alpha^Q,\beta^Q) = \omega_{iso}^{2Q} + A_2^Q(\alpha^Q,\beta^Q)P_2(\cos\theta_2) + A_4^Q(\alpha^Q,\beta^Q)P_4(\cos\theta_2) \quad (3.12)$$

Unlike the Hahn-echo experiment, in both parts of the echo time, the -1 coherence pathway is selected and the isotropic evolution due to 2nd-order quadrupolar shift and the isotropic chemical shift is preserved. To get rid of the anisotropic terms, θ_1 and θ_2 are chosen to have opposite signs for $P_2(\cos\theta_1)$ and $P_2(\cos\theta_2)$, and for $P_4(\cos\theta_1)$ and $P_4(\cos\theta_2)$.

$$P_2(\cos\theta_1) = -k_1 P_2(\cos\theta_2) \quad (3.13)$$

$$P_4(\cos\theta_1) = -k_2 P_4(\cos\theta_2). \quad (3.14)$$

It is interesting to see what happens when $k_1 = k_2 = k > 0$. In this special case, if another function on α^Q and β^Q is defined as

$$A^Q(\alpha^Q,\beta^Q) = A_2^Q(\alpha^Q,\beta^Q)P_2(\cos\theta_2) + A_4^Q(\alpha^Q,\beta^Q)P_4(\cos\theta_2), \quad (3.15)$$

Eqn 3.11 and Eqn 3.12 can be rewritten as

$$\omega_1^{2Q}(\alpha^Q,\beta^Q) = \omega_{iso}^{2Q} - kA^Q(\alpha^Q,\beta^Q) \quad (3.16)$$

$$\omega_2^{2Q}(\alpha^Q,\beta^Q) = \omega_{iso}^{2Q} + A^Q(\alpha^Q,\beta^Q). \quad (3.17)$$

The phase factor experienced by a quadrupolar spin at the start of the acquisition time is

$$\phi^{2Q}(t_1) = \int_0^{\frac{t_1}{k+1}} \omega_1^{2Q}(\alpha^Q,\beta^Q)dt + \int_0^{\frac{kt_1}{k+1}} \omega_2^{2Q}(\alpha^Q,\beta^Q)dt \quad (3.18)$$

$$= \omega_{iso}^{2Q}\left(\frac{t_1}{1+k} + \frac{kt_1}{1+k}\right) - A(\alpha^Q,\beta^Q)\left(\frac{kt_1}{1+k} - \frac{kt_1}{1+k}\right)$$

$$= \omega_{iso}^{2Q} t_1. \quad (3.19)$$

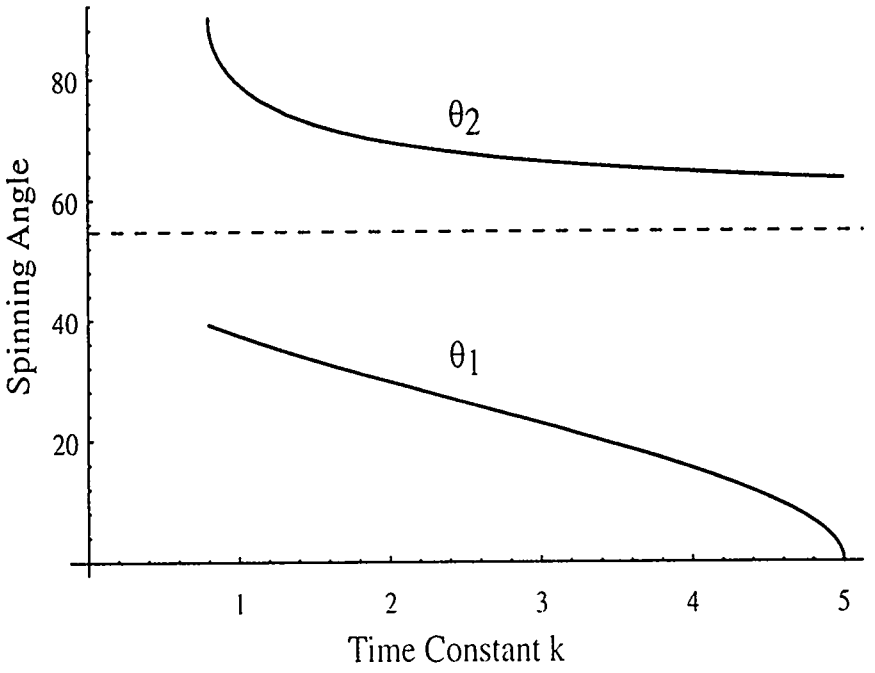

Figure 3.8: DAS angle pairs as a function of k. The angle θ_1 and θ_2 are solutions to Eqn 3.20.

The derivation assumes that the z-filter does nothing but restore the density matrix.

The assumption that $k_1 = k_2 = k$ leads to,

$$\frac{P_2(\cos\theta_2)}{P_2(\cos\theta_1)} = \frac{P_4(\cos\theta_2)}{P_4(\cos\theta_1)}, \tag{3.20}$$

whose solution gives $0.8 \leq k \leq 5$. Figure 3.8 shows the DAS angle pairs as a function of parameter k. The most popularly used pairs are the $k = 1$ (37.38° and 79.19°) and the $k = 5$ (0.00° and 63.43°) pairs [42, 43]. The chemical shift anisotropy (CSA) is also averaged out by DAS. To see this, consider the evolved phase due to the chemical shift interaction.

$$\begin{aligned}
\phi^{CS}(t_1) &= \int_0^{\frac{t_1}{k+1}} \omega_1^{CS}(\alpha^{CS},\beta^{CS})dt + \int_0^{\frac{kt_1}{k+1}} \omega_2^{CS}(\alpha^{CS},\beta^{CS})dt \\
&= \omega_{iso}\left(\frac{t_1}{1+k} + \frac{kt_1}{1+k}\right) - A_2^{CS}(\alpha^{CS},\beta^{CS})\left(\frac{kt_1}{1+k} - \frac{kt_1}{1+k}\right) \\
&= \omega_{iso}t_1.
\end{aligned} \tag{3.21}$$

The evolution under the anisotropic chemical shift is refocused at t_1. The total phase that a quadrupolar spin experiences after t_1 evolution is

$$\phi^{DAS}(t_1) = (\omega_{iso} + \omega_{iso}^{2Q})t_1, \tag{3.22}$$

and the observed shift in DAS (in the unit of ppm) is

$$\delta^{DAS} = \delta_{iso} + \delta_{iso}^{2Q}. \tag{3.23}$$

Here,

$$\delta_{iso}^{2Q} = \frac{10^6 \cdot \omega_{iso}^{2Q}}{\omega_1}. \tag{3.24}$$

A DAS-spectrum of $RbNO_3$ is shown in Figure 3.9. There are three different rubidium environments in this salt, corresponding to the three isotropic peaks in the DAS spectrum [44]. Also shown here is the one-dimensional projections in the isotropic (1-D DAS spectrum) and the anisotropic dimensions (VAS spectrum). The projection in the anisotropic dimension matches the VAS spectrum at 79.19°. Since the three rubidium sites are well-resolved in the DAS dimension, we can even add up the intensity for each site respectively. This gives us three VAS spectra in Figure 3.9, each of which can be separately simulated to give quadrupolar parameters.

3.2.3 MQMAS

In DAS, only the spinning angle is rendered to achieve high-resolution. There is another degree of freedom in Eqn 3.4 that is not well-exploited. The quadrupolar Hamiltonian associated with the symmetric multiple-quantum transition also has a similar format to that of the central transition, and can be utilized to construct isotropic spectra.

In MQMAS, the sample is continuously spun around the magic-angle. Strong RF pulses (usually with the highest achievable power level, and the pulse is termed as excitation pulse) are applied to create a triple-quantum coherence from the equilibrated

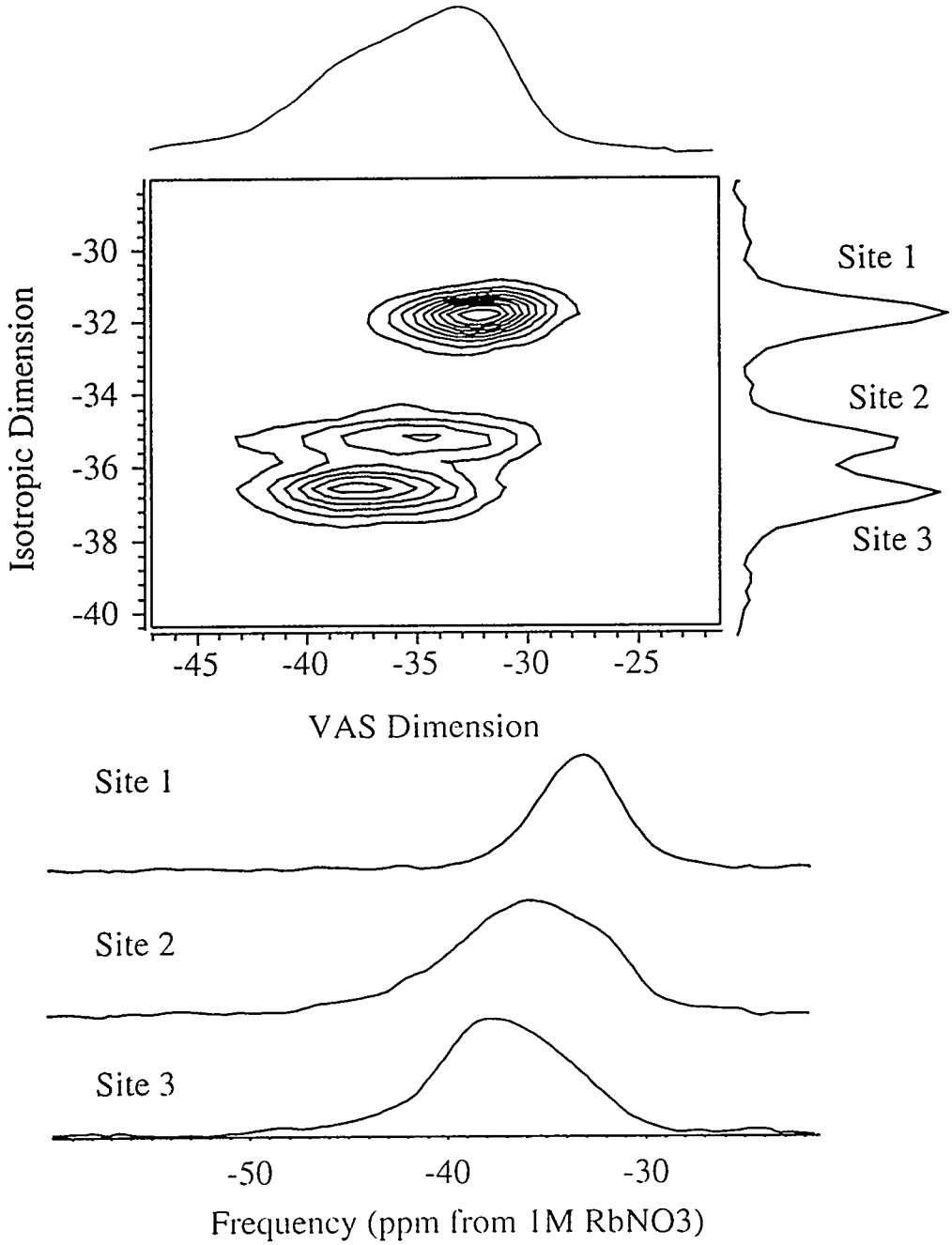

Figure 3.9: Two-dimensional ^{87}Rb DAS spectrum of $RbNO_3$ and the projections in both dimensions. Single site VAS spectra for each isotropic peak in the DAS dimension have been extracted and shown at the bottom of the contour plot.

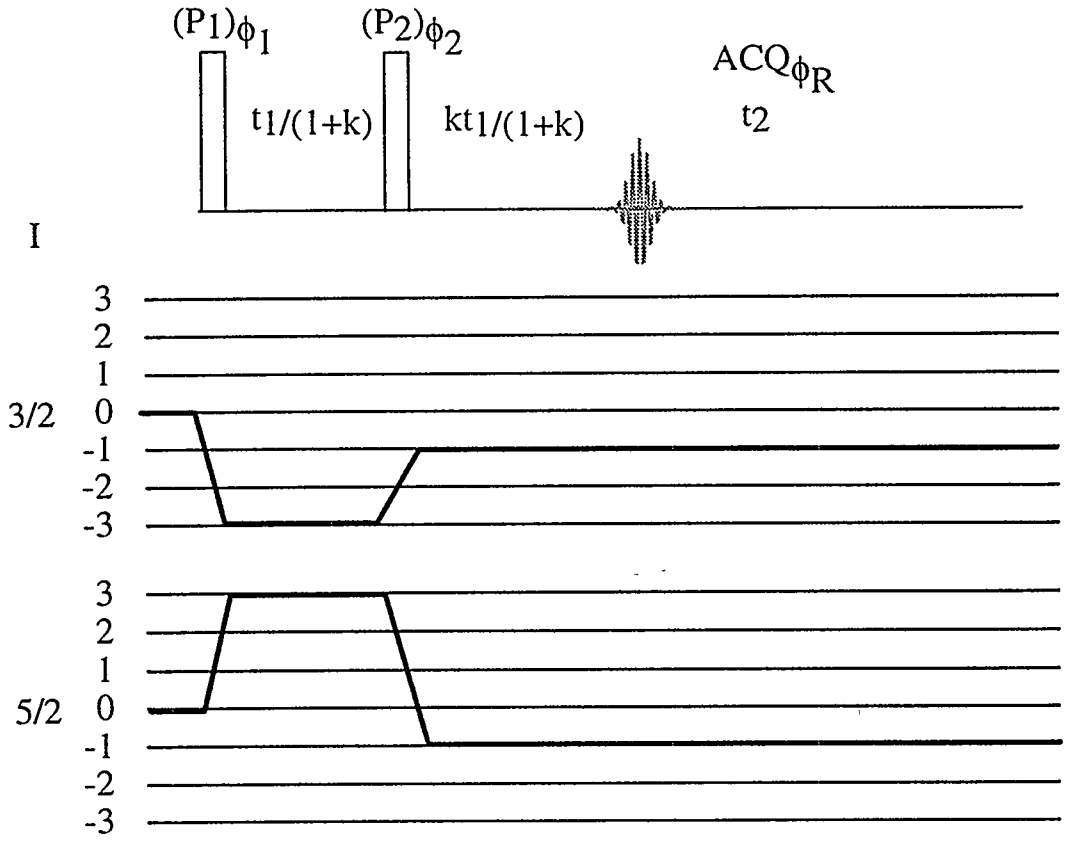

Figure 3.10: MQMAS experiment, pulse sequence and coherence pathway. In this experiment, the value t_1 is incremented in a two-dimensional fashion. The t_1 dimension reconstructs the isotropic MQMAS spectrum. For spin-$\frac{3}{2}$ nuclei, the $0 \rightarrow -3 \rightarrow -1$ pathway is selected; For spin-$\frac{5}{2}$ nuclei, the $0 \rightarrow 3 \rightarrow -1$ pathway is selected.

spin state I_0. Such a coherence evolves under the triple-quantum Hamiltonian for $\frac{t_1}{k+1}$, before another pulse (reconversion pulse) is applied to transfer the triple-quantum coherence into single-quantum coherence. Like DAS, an MQMAS echo is formed at $\frac{kt_1}{k+1}$ after this pulse. The experiment, pulse sequence and coherence pathway are shown in Figure 3.10 for $I = \frac{3}{2}$ and $I = \frac{5}{2}$ nuclei.

To see how an MQMAS-echo is formed, assume $I = \frac{3}{2}$ and $\theta = 54.74°$. The P_2-dependent term in Eqn 3.4 is dropped and the frequency expressions for the single-

and triple-quantum coherences are

$$\omega^{2Q}_{1/2\leftrightarrow -1/2}(\alpha^Q,\beta^Q,\gamma^Q) = C_0(I,1/2)\omega^{2Q}_{iso} + C_2(I,1/2)A^Q_4(\alpha^Q,\beta^Q)P_4(\cos\theta) \quad (3.25)$$

$$\omega^{2Q}_{3/2\leftrightarrow -3/2}(\alpha^Q,\beta^Q,\gamma^Q) = C_0(I,3/2)\omega^{2Q}_{iso} + C_2(I,3/2)A^Q_4(\alpha^Q,\beta^Q)P_4(\cos\theta) \quad (3.26)$$

Assuming that

$$k = \left|\frac{C_2(I,3/2)}{C_2(I,1/2)}\right|, \quad (3.27)$$

that $C_2(I,\frac{3}{2})$ and $C_2(I,\frac{1}{2})$ have different signs (which is true when $I = \frac{3}{2}$), and that the $-3 \rightarrow -1$ coherence pathway is selected, the phase factor experienced by a quadrupolar spin at the start of the acquisition is

$$\begin{aligned}
\phi^{2Q}(t_1) &= \int_0^{\frac{t_1}{k+1}} \omega^{2Q}_{3/2\leftrightarrow -3/2}(\alpha^Q,\beta^Q)dt + \int_0^{\frac{kt_1}{k+1}} \omega^{2Q}_{1/2\leftrightarrow -1/2}(\alpha^Q,\beta^Q)dt \\
&= \omega^{2Q}_{iso}\left(\frac{C_0(I,3/2)t_1}{1+k} + \frac{C_0(I,1/2)kt_1}{1+k}\right) \quad (3.28) \\
&\quad + P_1(\cos\theta)A^Q_1(\alpha^Q,\beta^Q)\left(\frac{kC_2(I,1/2)t_1}{1+k} + \frac{C_2(I,3/2)t_1}{1+k}\right) \\
&= \frac{C_0(I,3/2) + C_0(I,1/2)k}{1+k}\omega^{2Q}_{iso}t_1 \\
&= k_2\omega^{2Q}_{iso}t_1. \quad (3.29)
\end{aligned}$$

For the second to last equality,

$$k = -\frac{C_2(I,3/2)}{C_2(I,1/2)} \quad (3.30)$$

is used. Similar to DAS, the anisotropic phase is cancelled out at t_1 and an echo is formed. It is however, worth noting that the evolved phase of a quadrupolar spin at t_1 is no longer $\omega^{2Q}_{iso}t_1$, but is $\omega^{2Q}_{iso}t_1$ scaled by a factor k_2 defined by

$$k_2 = \frac{C_0(I,3/2) + C_0(I,1/2)k}{1+k}. \quad (3.31)$$

The removal of chemical shift anisotropy (CSA) by MQMAS is obvious since the sample is rotating around the magic-angle. The frequency shift due to chemical shift interaction is however, different from that in DAS.

$$\begin{aligned}\phi^{CS}(t_1) &= \int_0^{\frac{t_1}{k+1}} \omega^{CS}_{m\leftrightarrow -m}(\alpha^{CS},\beta^{CS})dt + \int_0^{\frac{kt_1}{k+1}} \omega^{CS}_{1/2\leftrightarrow -1/2}(\alpha^{CS},\beta^{CS})dt \\ &= (\frac{-2m}{k+1} + \frac{k}{k+1})\omega_{iso}t_1 \\ &= k_1\omega_{iso}t_1 \end{aligned} \tag{3.32}$$

The fact that the chemical shift of $m \leftrightarrow -m$ transition is $2m$ times as large as that of the central transition is used in the above equation. The scaling factor k_1 is defined by

$$k_1 = \frac{-2m+k}{k+1}. \tag{3.33}$$

The experimentally observed shift in the isotropic dimension of MQMAS is a combination of the isotropic chemical shift and the 2nd-order quadrupolar shift.

$$\delta^{MQMAS} = k_1\delta_{iso} + k_2\delta^{Q}_{iso} \tag{3.34}$$

This shift is different from the DAS shift.

Figure 3.11 shows the MQMAS spectrum of $RbNO_3$, together with the 1D projections (1D MQMAS and MAS spectra). Compared to Figure 3.9, the observed chemical shifts for the three sites are different in both experiments, as a result of the scaling factors (k_1 and k_2).

The assumption that $C_2(I,3/2)$ and $C_2(I,1/2)$ have opposite signs can be dropped without changing the principles of the MQMAS experiment. If they instead have same sign ($I > \frac{3}{2}$), the $0 \rightarrow +3 \rightarrow -1$ coherence pathway can be chosen, to remove the anisotropic part of the 2nd-order quadrupolar interaction. This is shown in Figure 3.10. The phase cycle that selects the appropriate coherence pathway is discussed in the next section.

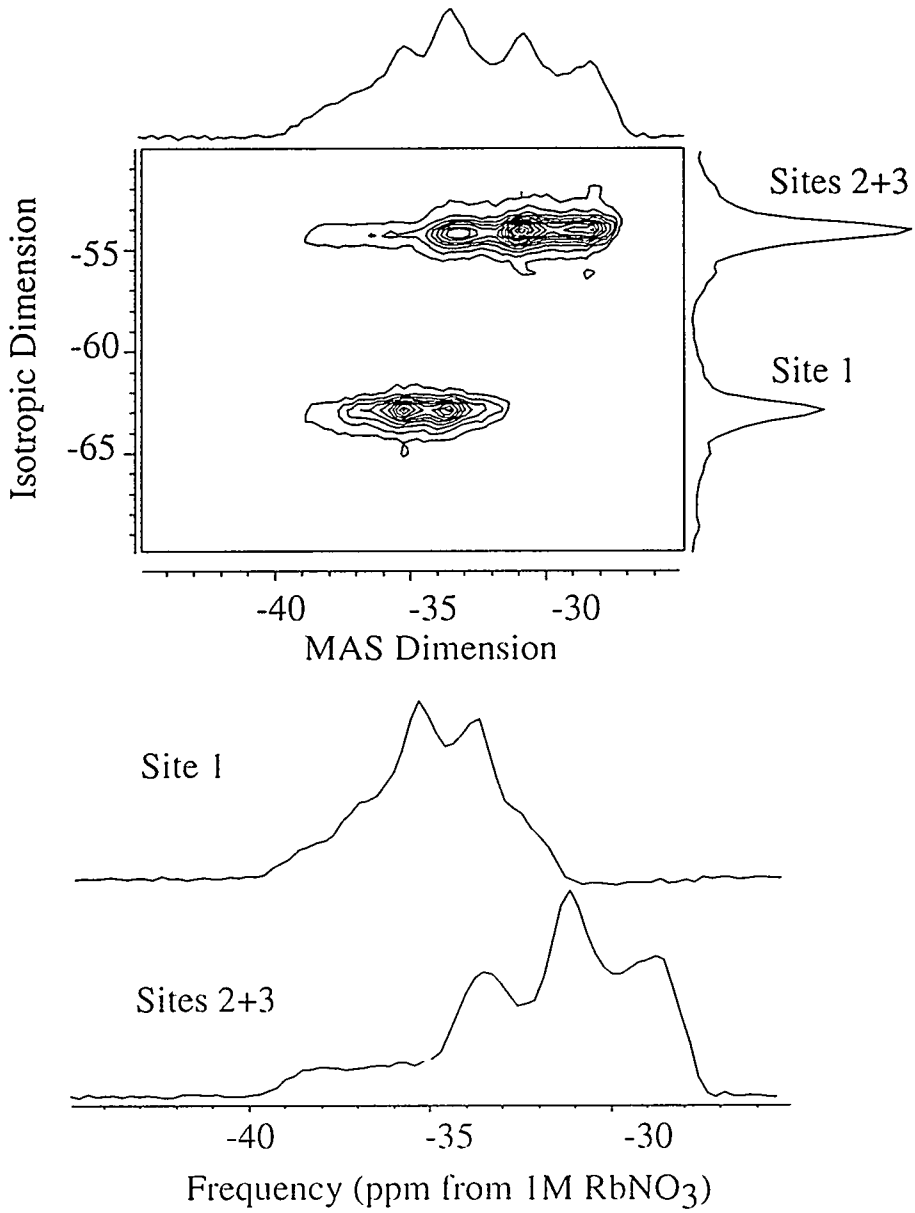

Figure 3.11: Two-dimensional ^{87}Rb 3QMAS spectrum of $RbNO_3$ and the projections in both dimensions. Single site MAS spectra for each isotropic peak in the MQMAS dimension have been extracted and shown at bottom of the contour plot. Notice that site 2 and 3 in the DAS spectrum are not resolved in the MQMAS spectrum.

I	m	Coherence Pathway	k	k_1	k_2
3/2	1/2	-	-	-	-
	3/2	$0 \rightarrow -3 \rightarrow -1$	7/9	17/8	-5/4
5/2	1/2	-	-	-	-
	3/2	$0 \rightarrow 3 \rightarrow -1$	19/12	-17/31	10/31
	5/2	$0 \rightarrow -5 \rightarrow -1$	25/12	85/37	-50/37
7/2	1/2	-	-	-	-
	3/2	$0 \rightarrow 3 \rightarrow -1$	101/45	-17/73	10/73
	5/2	$0 \rightarrow 5 \rightarrow -1$	11/9	-17/10	1
	7/2	$0 \rightarrow -7 \rightarrow -1$	161/45	148/103	-140/103
9/2	1/2	-	-	-	-
	3/2	$0 \rightarrow 3 \rightarrow -1$	91/36	-17/127	10/127
	5/2	$0 \rightarrow 5 \rightarrow -1$	95/36	-13/131	50/131
	7/2	$0 \rightarrow 7 \rightarrow -1$	7/18	-47/25	14/5
	9/2	$0 \rightarrow -9 \rightarrow -1$	31/6	79/55	-50/37

Table 3.1: Coherence pathway and different scaling values for different spins.

Even though the above discussion focuses on the combination of triple- and single-quantum transitions, other multiple-quantum transitions ($5/2 \leftrightarrow -5/2$, etc.) can also be exploited. The k (Eqn 3.27), k_1 (Eqn 3.33) and k_2 (Eqn 3.31) values are different for different transitions. These values, together with the relevant coherence pathways that are chosen to achieve selective average are shown in Table 3.1 [45].

3.3 Phase Cycle

The acquisition schemes shown in Figures 3.7 and 3.10 do not lead to pure-absorption phase DAS or MQMAS spectra even if hypercomplex datasets are acquired. Recall from chapter 2 that mirror image coherence pathways are required to give pure-absorption phase two-dimensional spectra. For DAS, the ± 1 pathways are to be retained in both halves of the t_1 evolution time. For MQMAS, the ± 3 pathways

are to be retained in the first half, and the ±1 pathways are necessary in the second half of the t_1 evolution. In the original sequences, the receiver detects only the -1 coherence during the second half, thus the detected signal is [1]

$$S_c(t_1,t_2) = e^{-(t_1+t_2)/T_2}\cos(\Omega_1 t_1/2)e^{i\Omega_2 t_1/2}e^{i\Omega_2 t_2} \quad (3.35)$$

$$S_s(t_1,t_2) = e^{-(t_1+t_2)/T_2}\sin(\Omega_1 t_1/2)e^{i\Omega_2 t_1/2}e^{i\Omega_2 t_2}. \quad (3.36)$$

It is not possible to get pure-absorption phase spectra from these two datasets.

The first modification to DAS to overcome this problem is to have a z-filter at the time the DAS-echo forms [46, 47]. The filter mixes I_+ and I_- coherences and stores the magnetization along z-axis and later restores it. This allows the retention of ±1 coherences in both halves of the t_1 period. The method has also been applied to MQMAS by Amoureux [48] and Wimperis [49]. While pure-absorption phase lineshape is obtained, one half of the signal is lost due to the use of z-filter. A better approach that is used in our experiment was first proposed by Grandenetti [50] to get pure-phase DAS spectra; a similar approach is also useful for MQMAS [51]. Figure 3.12 shows the modified DAS and MQMAS sequences. The major difference between the new sequences and the original ones is that the acquisition starts right after the last pulse. This corresponds to a redefinition of t_1 and t_2. For DAS, the evolution at the first angle is now t_1 and the evolution at the second angle is t_2. For MQMAS, the evolution under the triple-quantum Hamiltonian is t_1 and that under the single-quantum Hamiltonian is t_2. This definition places a shifting DAS (MQMAS) echo in the t_2 dimension at time kt_1. When the data is processed like other two-dimensional data without modification, a peak with a slope k is observed. This peak correlates the frequencies in two dimensions. A conventional DAS (MQMAS) spectrum can be obtained by shearing this spectrum with angle θ [52, 53, 54].

$$\theta = \tan^{-1} k \quad (3.37)$$

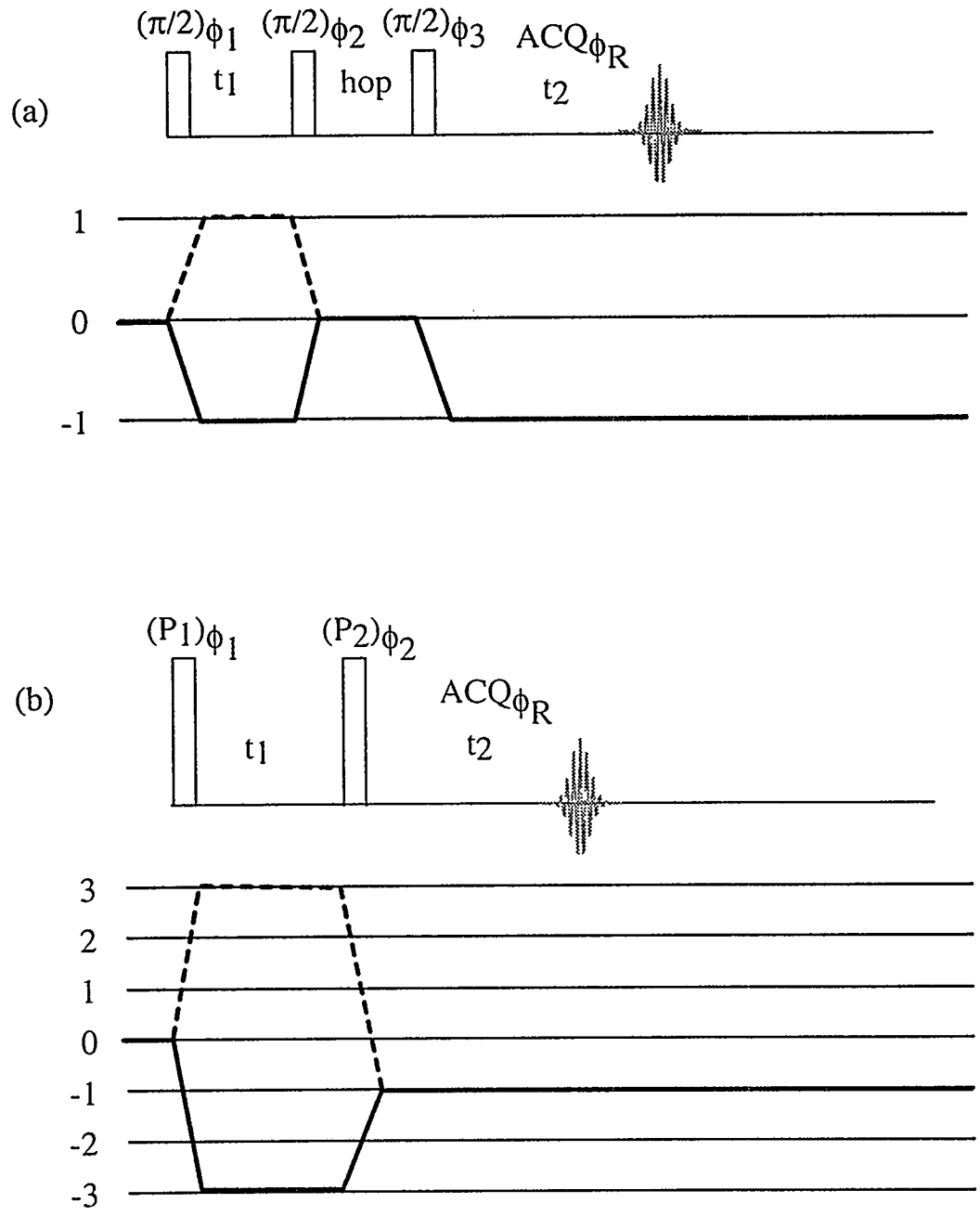

Figure 3.12: Hypercomplex DAS and MQMAS experiment. Coherence pathways designated by the bolded and dashed lines are both retained.

DAS cosine				
ϕ_1	0°	0°	180°	180°
ϕ_2	0°	180°	0°	180°
ϕ_3	0°	0°	0°	0°
ϕ_r	0°	180°	180°	0°
DAS sine				
ϕ_1	90°	90°	270°	270°
ϕ_2	0°	180°	0°	180°
ϕ_3	0°	0°	0°	0°
ϕ_r	0°	180°	180°	0°

Table 3.2: Hypercomplex DAS phase cycle with redefinition of t_1 and t_2.

This definition of the time axes is very similar to the definitions in other two-dimensional experiments. Using the rules in chapter two, phase cycles for DAS and MQMAS can be derived (Tables 3.2 and 3.3). For DAS, the derivation has already been worked out in chapter 2 for the cosine part of the signal (Eqn 2.127). The sine part of the signal is obtained by adding a 90° phase shift to the first pulse, and keeping all other pulses with their original phases. The phase cycle is shown in Table 3.2. For MQMAS, the change of the coherence order Δp is ± 3 during the first pulse thus a six-step phase cycle is needed to select these two coherences. The last pulse is left uncycled so the total number of steps in a cycle is 6. The receiver phase is set by

$$\phi_r = -3\phi_1 + 1\phi_2. \tag{3.38}$$

The first-pulse needs to be phase shifted by 30° (instead of 90°) to get the sine portion of the signal because the triple-quantum coherence experiences a phase shift three times that of the single-quantum coherence after a pulse applied to I_0. The phase cycle is shown in Table 3.3.

Most of the spectra presented in this thesis, are however, obtained using whole-

3QMAS cosine						
ϕ_1	0°	60°	120°	180°	240°	300°
ϕ_2	0°	0°	0°	0°	0°	0°
ϕ_r	0°	180°	0°	180°	0°	180°
3QMAS sine						
ϕ_1	30°	90°	150°	210°	270°	330°
ϕ_2	0°	0°	0°	0°	0°	0°
ϕ_r	0°	180°	0°	180°	0°	180°

Table 3.3: Hypercomplex MQMAS phase cycle with redefinition of t_1 and t_2.

echo acquisition [50, 51, 55] in which a pulse sequence of the form

$$\pi/2 - t_e - \pi - acq. \tag{3.39}$$

is used to refocus the signal and produce an echo. Here t_e is an echo time set to many milliseconds so the acquisition follows both the formation and decay of the echo. Notice that in an ordinary echo experiment, only the decay of the echo is recorded. The two-dimensional signal is of the form

$$S(t_1, t_2) = e^{-t_1/T_2} e^{i\Omega_1 t_1} e^{-(t_2-t_e)^2/T_2^2} e^{i\Omega_2(t_2-t_e)}. \tag{3.40}$$

When this signal is Fourier transformed with respect to t_2 and then phase corrected by a time t_e to the ω_2 dimension, the following signal is obtained,

$$S(t_1, \omega_2) = e^{-t_1/T_2} e^{i\Omega_1 t_1} A_{sr}(\omega_2, \Omega_2) \tag{3.41}$$

where

$$A_{sr}(\omega_2, \Omega_2) = e^{-(\omega_2-\Omega_2)^2 T_2^2/4}. \tag{3.42}$$

When the t_1 dimension is also Fourier transformed, pure-absorption mode 2D-spectrum is obtained.

$$S(\omega_1, \omega_2) = A_{sr}(\omega_2, \Omega_2)(A(\omega_1, \Omega_1) + iD(\omega_1, \Omega_1)) \tag{3.43}$$

HyperSEDAS cosine								
ϕ_1	0°	0°	0°	0°	180°	180°	180°	180°
ϕ_2	0°	0°	0°	0°	0°	0°	0°	0°
ϕ_3	0°	90°	180°	270°	0°	90°	180°	270°
ϕ_r	0°	270°	180°	90°	180°	90°	0°	270°
HyperSEDAS sine								
ϕ_1	90°	90°	90°	90°	270°	270°	270°	270°
ϕ_2	0°	0°	0°	0°	0°	0°	0°	0°
ϕ_3	0°	90°	180°	270°	0°	90°	180°	270°
ϕ_r	0°	270°	180°	90°	180°	90°	0°	270°

Table 3.4: Hypercomplex SEDAS phase cycle with redefinition of t_1 and t_2.

The advantage of whole-echo acquisition is that it does not require the additional dataset like the States method. It thus has a factor of $\sqrt{2}$ improvement in signal-to-noise ratio. Shifted-echo DAS (SEDAS) and shifted-echo MQMAS (SEMQMAS) were discussed in [50] and [51], respectively. The experiments can be further modified to combine with the States method to give HyperSEDAS and HyperSEMQMAS sequences, which collect also the mirror image coherence in the first half of the t_1 period and have another factor of $\sqrt{2}$ improvement in signal-to-noise ratio.

The sequences and coherence pathways for the HyperSEDAS and HyperSEMQMAS experiments are shown in Figure 3.13. The phase cycles for these two experiments are given in Table 3.4 and Table 3.5. For DAS, the first pulse is cycled through two-steps to select the ± 1 coherences. The third pulse is cycled through 4-steps to select the $+1$ coherence. For MQMAS, the first pulse is cycled through six-steps to select the ± 3 coherences. The third pulse is cycled through 8-steps to select the $+1$ coherence.

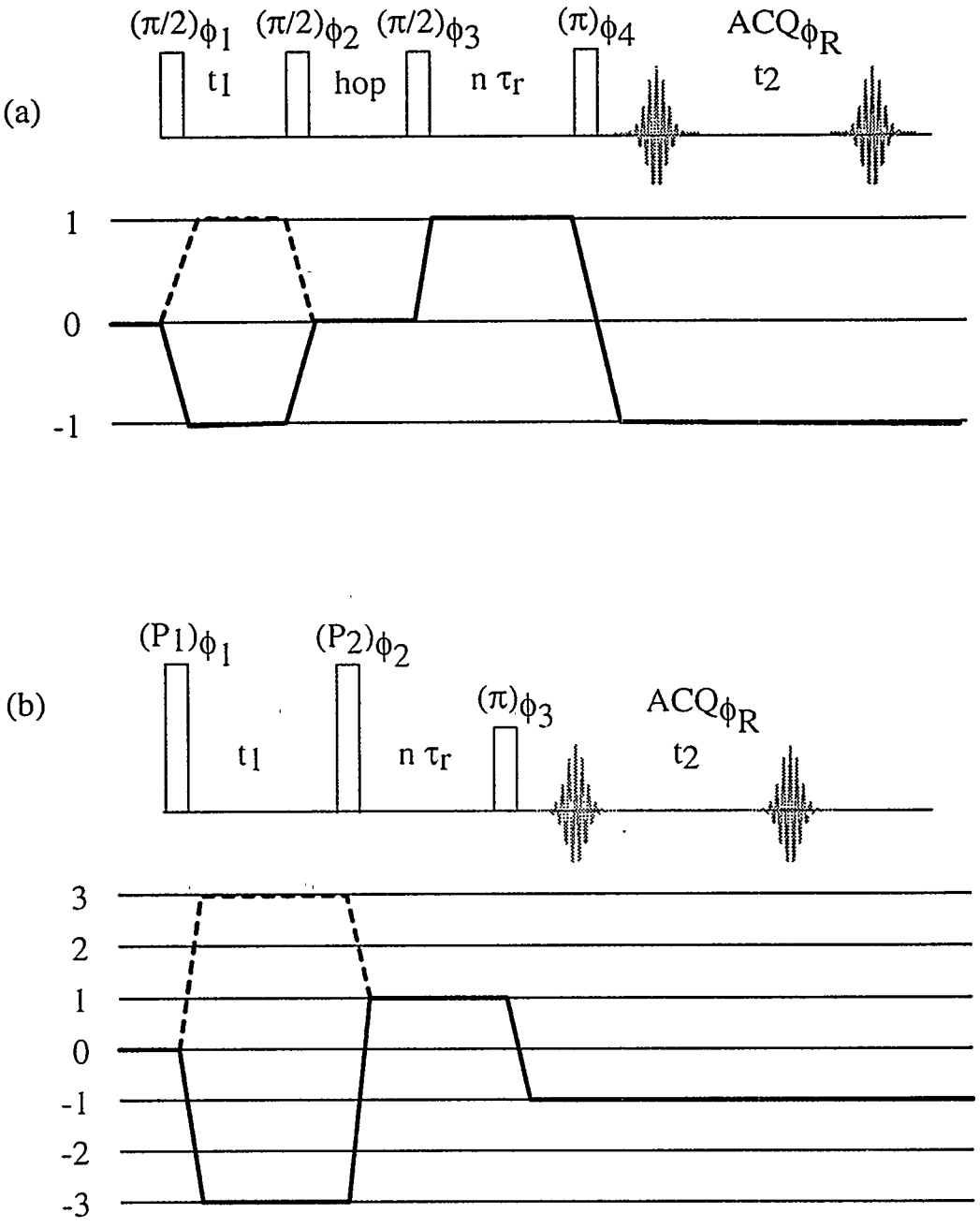

Figure 3.13: HyperSEDAS and HyperSEMQMAS experiments which acquire whole DAS or MQMAS echo in the t_2 dimension.

HyperSEMQMAS cosine												
ϕ_1	0°	60°	120°	180°	240°	300°						
ϕ_2	0°											
ϕ_3	0°	0°	0°	0°	0°	0°	45°	45°	45°	45°	45°	45°
	90°	90°	90°	90°	90°	90°	135°	135°	135°	135°	135°	135°
	180°	180°	180°	180°	180°	180°	225°	225°	225°	225°	225°	225°
	270°	270°	270°	270°	270°	270°	315°	315°	315°	315°	315°	315°
ϕ_r	0°	180°	0°	180°	0°	180°	90°	270°	90°	270°	90°	270°
	180°	0°	180°	0°	180°	0°	270°	90°	270°	90°	270°	90°
HyperSEMQMAS sine												
ϕ_1	30°	90°	150°	210°	270°	330°						
ϕ_2	0°											
ϕ_3	0°	0°	0°	0°	0°	0°	45°	45°	45°	45°	45°	45°
	90°	90°	90°	90°	90°	90°	135°	135°	135°	135°	135°	135°
	180°	180°	180°	180°	180°	180°	225°	225°	225°	225°	225°	225°
	270°	270°	270°	270°	270°	270°	315°	315°	315°	315°	315°	315°
ϕ_r	0°	180°	0°	180°	0°	180°	90°	270°	90°	270°	90°	270°
	180°	0°	180°	0°	180°	0°	270°	90°	270°	90°	270°	90°

Table 3.5: Hypercomplex SEMQMAS phase cycle with redefinition of t_1 and t_2.

3.4 Excitation and Reconversion Pulses

The preceding section on MQMAS made an assumption that a single-RF pulse applied on resonance is capable of exciting multiple-quantum coherence and transferring it back to single-quantum coherence for detection. In fact, the behavior of the quadrupolar spin system subject to strong RF pulses needs to be carefully reconsidered here to see how the excitation and reconversion happen. Some important questions to be answered are:

I. With what efficiency can multiple-quantum coherence be excited?

II. How efficiently can multiple-quantum coherence be reconverted into single-quantum coherence?

III. How do multiple-quantum coherences evolve?

IV. How do the phases of the RF-pulses affect the phase of the signal?

V. For a powder sample, are the excitation and reconversion processes homogeneous? That is, are crystallites with different orientations equally excited? As a result, is the resultant lineshape in the MAS dimension the same as ordinary MAS lineshapes?

VI. Is MQMAS quantitative?

Experimental answers to the above questions are summarized here. Relatively good signal-to-noise ratios can be achieved for nuclei with high γ, high abundance and short spin-lattice relaxation time [45, 56, 57, 58, 59, 60, 61, 62]. The Excitation and reconversion are expected to be inhomogeneous, but experimental results seem to disagree with this since good quadrupolar lineshapes are often observed in the MAS dimension when the quadrupolar coupling constant are not too large [58]. MQMAS is not quantitative, at least for the case that a single pulse is used for excitation. Relatively quantitative results, however, were presented recently by Griffin et al. [63].

3.4.1 Fictitious Spin-$\frac{1}{2}$ Operators

For the description of a spin-$\frac{1}{2}$ system (or the central transition of a quadrupolar nuclear spin system), three special operators I_0, $I_\pm$ are introduced. Together with the unity operator 1, the four operators form a complete basis that the density matrix can be expressed as

$$\rho(t) = a_0(t)I_0 + a_1(t)I_+ + a_{-1}(t)I_- + a_2 1. \tag{3.44}$$

The commutation relations among these operators often allow the analytical solution of the evolution of the density matrix of the system. More importantly, the effects

of RF-pulses and free induction decay on the spin system can be described in an intuitive way (See section 2.5.2).

In the general case of $I > 1/2$ spins, there are $2I + 1$ eigenstates and other operators are needed. Suppose that we have N Hermitian operators A_n, the density matrix and Hamiltonian are then expressed as

$$\rho(t) = \sum_{n=1}^{N} a_n(t) A_n + a_0 1 \tag{3.45}$$

$$H = \sum_{n=1}^{N} h_n(t) A_n, \tag{3.46}$$

analogous to the spin-$\frac{1}{2}$ case. The N operators should be chosen to fulfill certain Cartesian commutation relations which facilitate the calculation of the evolution of the system.

$$\rho(t) = e^{-iHt} \rho(0) e^{iHt} \tag{3.47}$$

One way of choosing the operators is to define fictitious spin-$\frac{1}{2}$ operators for a quadrupolar system. When $I = \frac{3}{2}$, the eigenstates $|\frac{3}{2}>$, $|\frac{1}{2}>$, $|-\frac{1}{2}>$, $|-\frac{3}{2}>$ can be renamed as $|4>, |3>, |2>$ and $|1>$. For each pair of the eigenstates, we introduce three operators according to the three Pauli matrices σ_x, σ_y and σ_z.

$$I_X^{rs} = \frac{1}{2}(|r><s| + |s><r|) \tag{3.48}$$

$$I_Y^{rs} = -\frac{i}{2}(|r><s| - |s><r|) \tag{3.49}$$

$$I_Z^{rs} = \frac{1}{2}(|r><r| - |s><s|), \tag{3.50}$$

where

$$< r|I_X^{rs}|s> = \frac{1}{2} \tag{3.51}$$

$$< r|I_Y^{rs}|s > \;=\; -\frac{i}{2} \tag{3.52}$$

$$< r|I_Z^{rs}|s > \;=\; \frac{1}{2}. \tag{3.53}$$

The commutation relations among these operators are described below.

$$[I_X^{rs}, I_Y^{rs}] = iI_Z^{rs} \tag{3.54}$$

$$[I_X^{rs}, I_X^{st}] = \frac{i}{2} I_Y^{rt} \tag{3.55}$$

$$[I_Y^{rs}, I_Y^{st}] = -\frac{i}{2} I_Y^{rt} \tag{3.56}$$

$$[I_Z^{rs}, I_Z^{st}] = 0 \tag{3.57}$$

$$[I_X^{rs}, I_Y^{st}] = -\frac{i}{2} I_X^{rt} \tag{3.58}$$

Other commutation relations can be found in [64, 65]. The above relations can be generalized as

$$[P, Q] = i\kappa R \tag{3.59}$$

where P, Q, and R are three operators in Eqns 3.54 through 3.58. Notice that these operators are not totally independent. For example,

$$I_Z^{rs} = I_Z^{rt} + I_Z^{ts}. \tag{3.60}$$

In principle, only $(2I+1)^2 - 1$ independent operators are needed for a spin-I system.

The observable operators I_X, I_Y, I_Z can be expressed as the summation of the above operators. For a spin-I system,

$$I_{X,Y} \;=\; \sum_{rs} \sqrt{c^{(rs)}} I_{X,Y}^{rs} \tag{3.61}$$

$$I_Z \;=\; \sum_{rs} c^{(rs)} I_Z^{rs} \tag{3.62}$$

and

$$c^{(rs)} = I(I+1) - m_r m_s. \tag{3.63}$$

Rotations in the spin space by RF pulses are then described by

$$e^{-i\theta P} Q e^{i\theta P} = Q\cos\kappa\theta + R\sin\kappa\theta. \tag{3.64}$$

For example, from Eqn 3.56, we get

$$U_Y^{rs}(-\theta) I_V^{st} U_Y^{rs}(\theta) = I_V^{st}\cos(\theta/2) - I_V^{rt}\sin(\theta/2) \tag{3.65}$$

with

$$U_p^{rs}(\theta) = e^{i\theta I_p^{rs}}, \tag{3.66}$$

where $p = X, Y, Z$.

3.4.2 Excitation by Single Pulse

The Hamiltonian of a spin-$\frac{3}{2}$ system is expressed by

$$\begin{aligned} H &= H_{off} + H_Q + H_{RF} \\ &= -\Delta\omega(3I_Z^{14} + I_Z^{23}) + \omega_Q(I_Z^{12} - I_Z^{34}) - \omega_1(\sqrt{3}I_X^{12} + 2I_X^{23} + \sqrt{3}I_X^{34}), \end{aligned} \tag{3.67}$$

where H_{off} is the frequency offset and includes the chemical shift. We have used Eqns 3.61 and 3.62 for spin-$\frac{3}{2}$ nucleus.

$$I_X = \sqrt{3}(I_X^{12} + I_X^{34}) + 2I_X^{23} \tag{3.68}$$

$$I_Y = \sqrt{3}(I_Y^{12} + I_Y^{34}) + 2I_Y^{23} \tag{3.69}$$

$$I_Z = 3I_Z^{14} + I_Z^{23} \tag{3.70}$$

Here, the 2nd-order quadrupolar interaction has been neglected. If we also take $\Delta\omega = 0$ and assume $\omega_1 \ll \omega_Q$, we get

$$H = \omega_Q I_Z^{12} - \sqrt{3}\omega_1 I_X^{12} - \omega_Q I_Z^{34} - \sqrt{3}\omega_1 I_X^{34} - 2\omega_1 I_X^{23}, \tag{3.71}$$

where the first two terms commute with the next two terms. We can transform the above Hamiltonian into a tilted frame by the following operator,

$$U_Y^{12}(\theta)U_Y^{34}(-\theta) \tag{3.72}$$

where

$$\theta = \tan^{-1}(\sqrt{3}\omega_1/\omega_Q). \tag{3.73}$$

The resultant Hamiltonian is then

$$\begin{aligned} H_T &= \omega_c(I_Z^{12} - I_Z^{34}) - 2\omega_1 U_Y^{12}(-\theta)U_Y^{34}(\theta)I_X^{23}U_Y^{34}(-\theta)U_Y^{12}(\theta) \\ &= \omega_c(I_Z^{12} - I_Z^{34}) - 2\omega_1(\cos^2\frac{\theta}{2}I_X^{23} + \sin^2\frac{\theta}{2}I_X^{14} + \frac{1}{2}\sin\theta(I_X^{24} + I_X^{13})), \end{aligned} \tag{3.74}$$

where

$$\omega_c = \frac{1}{\sqrt{\omega_Q^2 + 3\omega_1^2}} \tag{3.75}$$

and H_T is the Hamiltonian in the tilted frame. If we also neglect the last term in the equation for H_T and assume $\omega_1 \ll \omega_Q$, the tilted Hamiltonian becomes

$$H_T \approx \omega_Q(I_Z^{12} - I_Z^{34}) - 2\omega_1 I_X^{23} - \frac{3\omega_1^3}{2\omega_Q^2}I_X^{14}. \tag{3.76}$$

Clearly, the last two terms correspond to the single- and triple-quantum transition operators. The separation of the last two terms has the advantage that rotations in single-quantum and triple-quantum subspaces are independent. The equilibrated density matrix

$$\rho(0) \propto I_Z^{23} + 3I_Z^{14} \tag{3.77}$$

then evolves under H_T according to

$$\begin{aligned} \rho(t) &= e^{-iH_Tt}\rho(0)e^{iH_Tt} \\ &= (I_Z^{23}\cos 2\omega_1 t + I_Y^{23}\sin 2\omega_1 t) \\ &\quad + 3(I_Z^{14}\cos(\frac{3\omega_1^3}{2\omega_Q^2}t) + I_Y^{14}\sin(\frac{3\omega_1^3}{2\omega_Q^2}t)). \end{aligned} \tag{3.78}$$

This equation can now be used to describe the effect of an RF-pulse on a spin-$\frac{3}{2}$ system.

I. The terms in the first parenthesis describe the effect of the pulse on the central transition. This expression is almost the same compared to the spin-$\frac{1}{2}$ case except for the extra factor of 2. It suggests that the central transition behaves like an isolated fictitious spin-$\frac{1}{2}$ nucleus with a doubled nutation frequency. More generally, for a spin-I nucleus, scaling factor for the nutation frequency is $I + \frac{1}{2}$.

II. The terms in the second parenthesis describes the effect of the pulse on the triple-quantum transition. It suggests that an RF-pulse generates a rotation in the triple-quantum subspace. The nutation frequency is ω_1 scaled by a factor $(\frac{3}{2}\frac{\omega_1}{\omega_Q})^2$. The magnitude of the nutation, however, is two times larger than that of the central transition. This means that if the triple-quantum coherence is fully excited, its intensity is even stronger than that of the central transition. Experimentally, this is hardly true due to the inefficiency of the excitation.

III. The triple-quantum nutation frequency is dependent on the quadrupolar frequency,

$$\omega_Q = \frac{C_Q}{2I(2I-1)}\left(\frac{3\cos^2\beta^Q - 1}{2} + \frac{\eta_Q}{2}\sin^2\beta^Q\cos 2\alpha^Q\right) \qquad (3.79)$$

which is orientation-dependent. This means that a 90° pulse for one crystallite is not the 90° pulse for other crystallites and a triple-quantum 90° pulse for a powder sample can not be defined. As a result, the triple-quantum excitation is inhomogeneous.

The nutation behavior of a single crystal sample with $\omega_Q = 400$kHz is calculated as a function of RF-pulse length and shown in Figure 3.14a. From the sinusoidal dependence of the excitation efficiency on the pulse length, it is clear that the excitation is very inhomogeneous. When an average over the whole sample is taken, Figure 3.14b is obtained, where the triple-quantum signal builds up initially and fluctuates with longer pulses. The maximum of the excitation occurs when $\omega_1 t \approx 3\pi$ from this simple model.

It seems that for a spinning sample, the derivation above is still qualitatively correct, especially when the spinning speed is not very high and the RF power is high (see Figure 3.15). Assuming that $\omega_1 = 100$kHz and $\omega_r = 10$kHz, a solid state 3π pulse for $I = \frac{3}{2}$ nucleus is about 7.5μs, which takes 7.5% of a rotor period and the spinning effect may be neglected. The assumption that $\omega_1 \ll \omega_Q$ is not often true, because ω_Q is orientation-dependent. Nevertheless, the experimental data in Figure 3.15a suggests that spinning effect is not crucial and can be neglected in a qualitative analysis.

3.4.3 Reconversion by Single Pulse

To calculate the reconversion efficiency, we assume that the initial density matrix is I_y^{14} and calculate the evolution of the system under RF-pulse. we then have

$$a_x^{23} = \frac{1}{4}\sin^2\theta(\cos\omega^{13}t + \cos\omega^{24}t - 2) \tag{3.80}$$

$$a_y^{14} = 0. \tag{3.81}$$

where

$$\omega^{13} = (3\omega_1^2 + (\omega_Q - \omega_1)^2)^{1/2} \tag{3.82}$$

$$\omega^{24} = -(3\omega_1^2 + (\omega_Q + \omega_1)^2)^{1/2}. \tag{3.83}$$

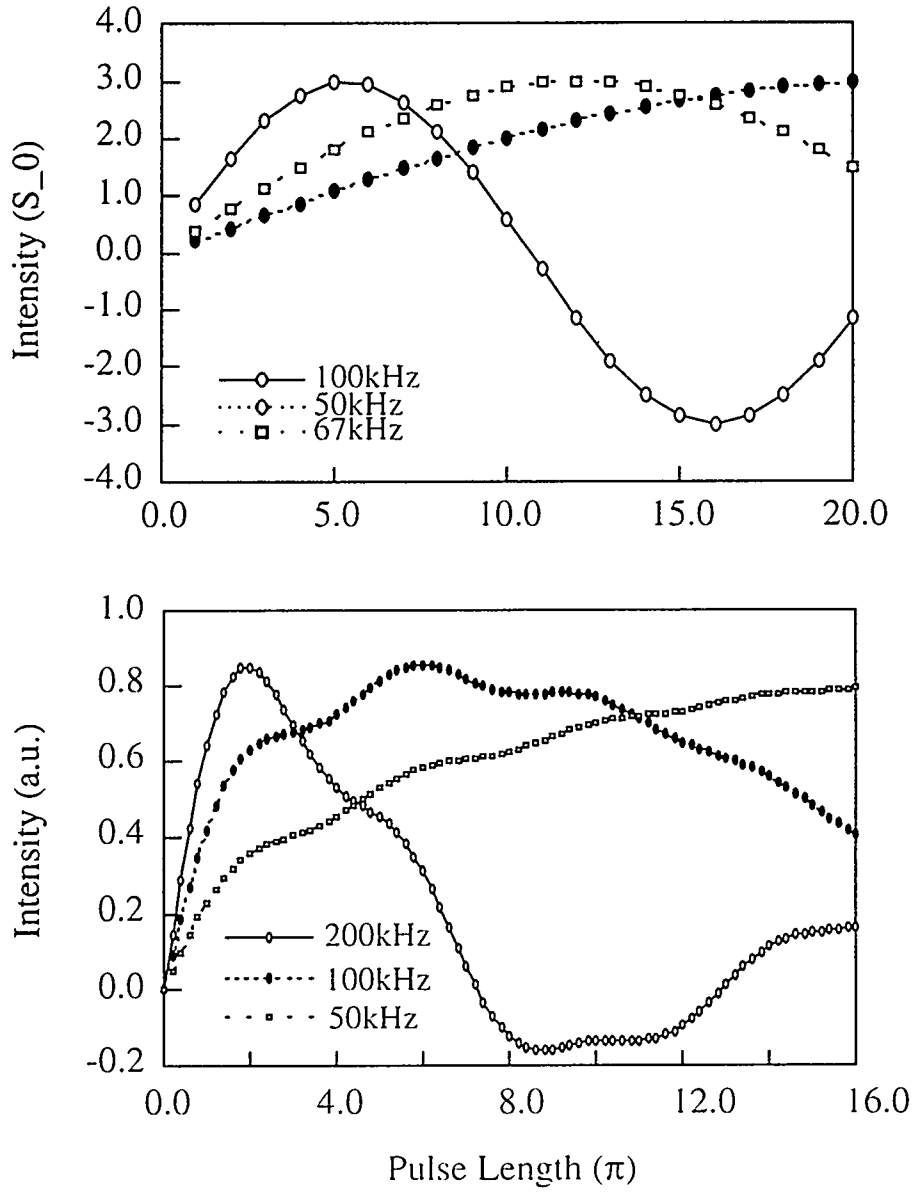

Figure 3.14: Calculated triple-quantum excitation efficiency for single crystal (upper) and powder (lower) samples as a function of pulse length. The magnitude of the RF field strength (ω_1) is shown as legends. The calculation assumes that $\omega_Q = 400$kHz. S_0 is the maximum signal intensity for the single-quantum transition.

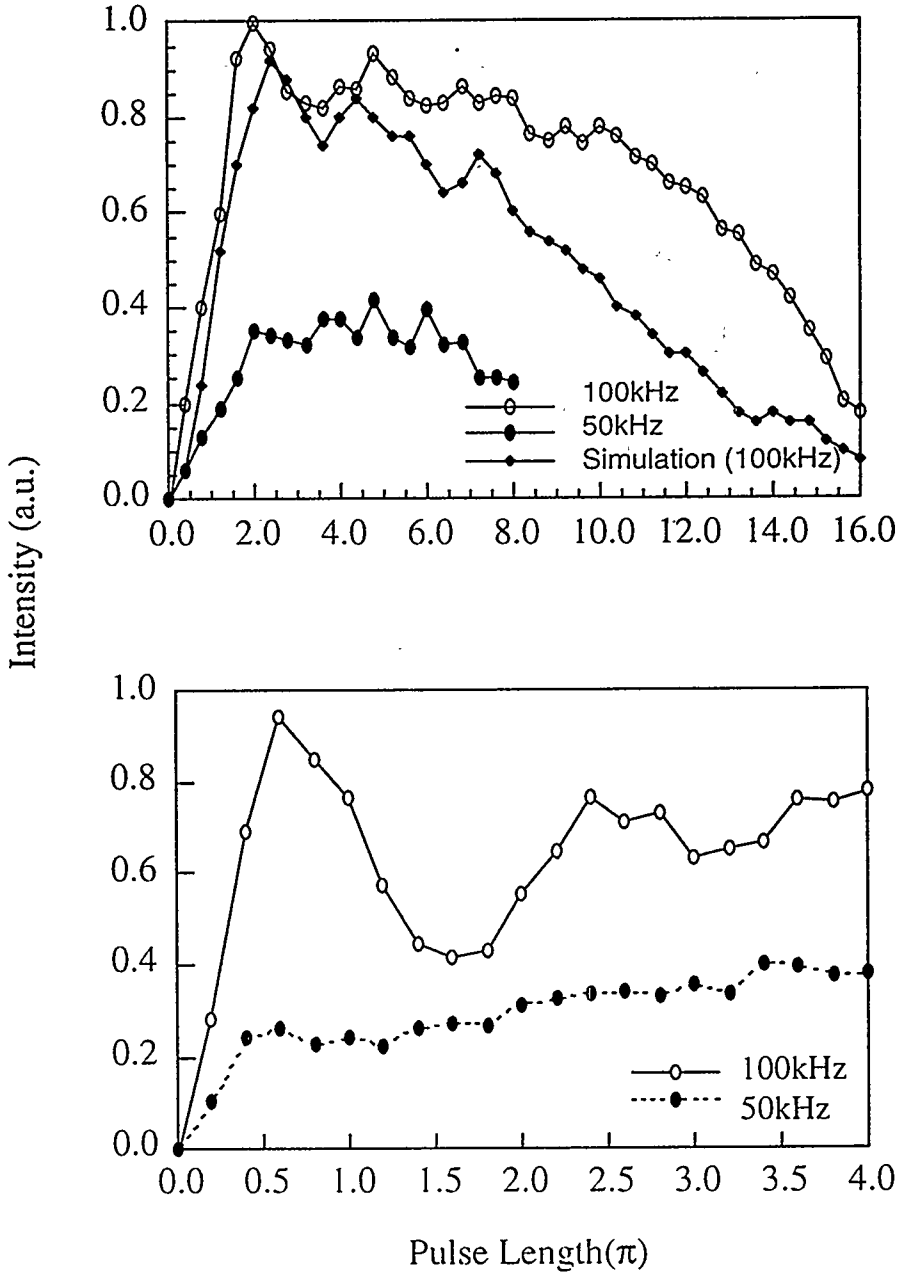

Figure 3.15: Experimental data on triple-quantum excitation (upper) and reconversion (lower) efficiency as a function of pulse length. The magnitude of the RF field strength (ω_1) is shown as legends. The calculation assumes that $\omega_Q = 400$kHz. Computer simulated result is also shown in the upper graph.

Unfortunately, a_x^{23} quickly drops to zero as the ratio between the quadrupolar frequency and the RF-pulse strength increases. To see this, notice that when $\omega_1 \ll \omega_Q$,

$$a_x^{23} < \sin^2\theta \approx \tan^2\theta = 3(\frac{\omega_1}{\omega_Q})^2. \tag{3.84}$$

This suggests that the reconversion efficiency is proportional to the square of the ratio between the RF field strength and the quadrupolar frequency, which is often very small. As a result, the reconversion problem is more serious than the excitation problem.

In Figure 3.16, the dependence of the reconversion efficiency on the reconversion pulse length is presented. Again, one sees the buildup of the single-quantum signal in a short period of time ($\omega_1 t = 0.8\pi$). However, the magnitude of the signal is very small. Neglecting spinning effect in this case is appropriate since the pulse length takes only about 2% of a rotor cycle (See Figure 3.15).

3.4.4 Excitation and Reconversion: Computer Simulation

To fully understand the excitation and reconversion processes under spinning condition, computer simulation has to be exploited [8, 66]. This is because the Hamiltonians of the system at time t and $t + \delta t$ do not commute to each other and the evolution of the density matrix has to be solved numerically by calculating

$$\rho(t) = e^{-iH_1\Delta t_1} e^{-iH_2\Delta t_2} \cdots e^{-iH_n\Delta t_n} \rho(0) e^{iH_n\Delta t_n} \cdots e^{iH_2\Delta t_2} \cdots e^{iH_1\Delta t_1}. \tag{3.85}$$

The calculation is often facilitated by the diagonalization of each Hamiltonian in the equation [8]. The calculation on the excitation efficiency is shown in Figure 3.15 (upper). The results qualitatively match those obtained by Amoureux [67] and Wu [68], that is, a relatively long pulse is needed for excitation. The discrepancy may be due to the slightly different parameters we used in the simulation. The simulation

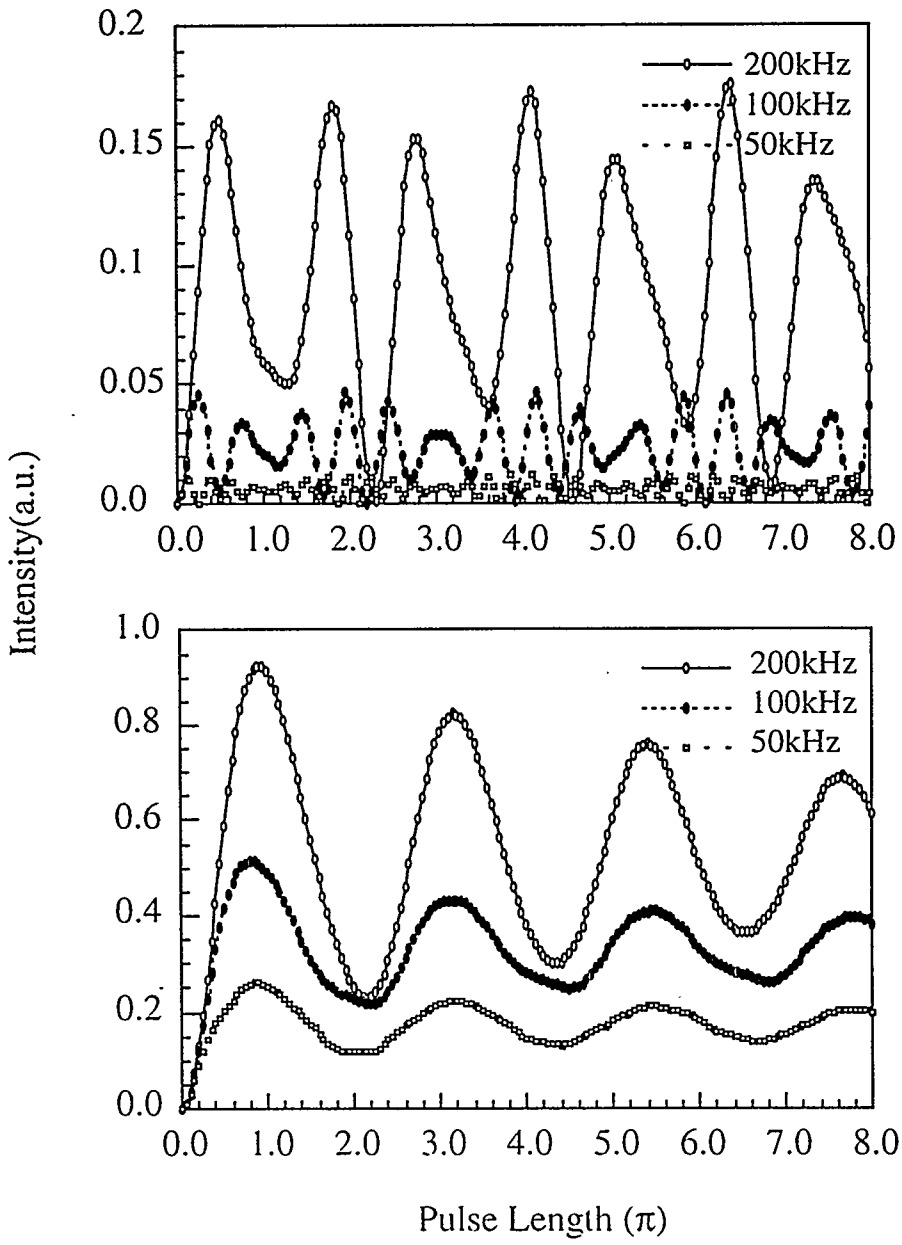

Figure 3.16: Calculated triple-quantum to single-quantum reconversion efficiency for single crystal (upper) and powder (lower) samples as a function of pulse length. The magnitude of the RF field strength (ω_1) is shown as legends. The calculation assumes that $\omega_Q = 400$kHz.

	Pulse length(μs)			
Exct./Recov.	3/2	5/2	7/2	9/2
Excitation	$\frac{8}{3}\pi$	3π	$\frac{8}{3}\pi$	$\frac{5}{2}\pi$
Reconversion	$\frac{2}{3}\pi$	π	π	π

Table 3.6: Pulse lengths that maximize the excitation and reconversion efficiency.

also reproduces the short-term behavior of the experimental data. The interested readers should consult other references [67, 68]. The best pulse lengths for excitation and reconversion are however, summarized in Table 3.6. Notice that the pulse lengths here are solid-state pulse lengths, and the result qualitatively agrees with the numbers obtained by the simple model which neglects the spinning effect.

3.4.5 Excitation and Reconversion by Spin-Locking

Another interesting method that is reported for excitation and reconversion was proposed by Wu et al. [63]. The pulse sequence and phase cycle are shown in Figure 3.17 and Table 3.7, respectively. Instead of using a single long pulse for excitation, two pulses (without time interval in between) are used. The first pulse is a solid-state 90° pulse, and the second pulse is a spin-locking pulse phase shifted by 90° with respect to the first pulse. The length of this second-pulse is set to $\tau_r/4$, where τ_r is the rotor period. The reconversion pulse is a single pulse whose length is again set to $\tau_r/4$. This pulse is much longer than the optimal pulse length suggested by Amoureux [67]. The efficiency of the sequence has been illustrated both by experiments and simulations. The most significant advantage of the sequence is that it is more quantitative.

The key idea behind this new sequence is that when the sample is spinning, the eigenstates of the spin Hamiltonian change with time. If initially the spin system is in I_X^{23} state, part of the coherence is converted into triple-quantum coherence I_X^{14} at

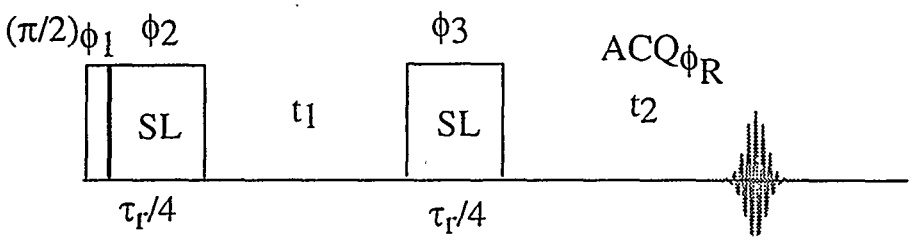

Figure 3.17: Spin-Locking pulse sequence for the excitation of triple-quantum coherence and its conversion back to single-quantum coherence.

Spin-Locking 3QMAS cosine						
ϕ_1	0°	60°	120°	180°	240°	300°
ϕ_2	90°	150°	210°	270°	330°	30°
ϕ_3	0°	0°	0°	0°	0°	0°
ϕ_r	0°	180°	0°	180°	0°	180°
spin-Locking 3QMAS sine						
ϕ_1	30°	90°	150°	210°	270°	330°
ϕ_2	120°	180°	240°	300°	0°	60°
ϕ_3	0°	0°	0°	0°	0°	0°
ϕ_r	0°	180°	0°	180°	0°	180°

Table 3.7: The spin-locking 3QMAS phase cycle with redefinition of t_1 and t_2.

$\tau_r/2$ and returns to I_X^{23} after a full rotor cycle when a spin-locking pulse is applied [69, 70, 71]. Also, part of the coherence is converted into I_X^{14} at $\tau_r/4$ and returns to I_X^{23} at $\tau_r/2$. If this is true, the first 90° pulse in the sequence shown in Figure 3.17 creates coherence I_X^{23}, which evolves into I_X^{14} at $\tau_r/4$. The third pulse, similarly transfer the coherence back into a single-quantum coherence.

Even though the authors have shown that their sequence is far more quantitative than the two-pulse sequence, the sequence has not been widely used untill now. One of the reasons may be that the sequence is only efficient for spin-$\frac{3}{2}$ nuclei. Another reason is probably that the sequence is still not well-understood. According to Vega, the spin-locking efficiency for quadrupolar nuclei is low and only under adiabatic conditions is the transfer of coherence by spin-locking possible [70]. It seems controversial that the spin-locking sequence gives good results since the adiabatic condition is expected to be hard to fulfill. People with further interests should read other references [69, 70, 71].

3.5 Comparison of DAS and MQMAS

This section addresses several complementary aspects of MQMAS and compares MQMAS with DAS [45]. Issues such as feasibility, linewidth, resolution are discussed. The chemical shift effect on the resultant spectra is then presented in great detail. It is also demonstrated here that CSA parameters can be extracted for quadrupoles using the multiple-quantum strategy.

3.5.1 Experiments

Most of the spectra presented in this chapter were obtained at 9.4T or 11.7T using a home-built 5mm DAS probe [72]. The spinning axis was initially set to 54.74° by maximizing the observed sideband intensity using KBr (^{81}Br) or deuterated HMB

(^{2}H) as standards. The ^{27}Al spectra were collected using a Doty Scientific 5mm high-speed MAS probe [73]. Spinning speeds greater than 7.5kHz were exploited in all experiments except for the one designed to give the intense $Na_2C_2O_4$ sideband pattern. The RF power level in the DAS experiments was set to ensure selective excitation of the central transition, and a typical 90° pulse length was about 7μs. In the MQMAS experiments, high power (35-40kHz for ^{17}O, 50-60kHz for other nuclei) was used to achieve efficient excitation.

The shifted-echo DAS sequence ($\frac{\pi}{2} - t_1 - \frac{\pi}{2} - hop - \frac{\pi}{2} - \tau_e - \pi$—acq.) [50] and shifted-echo MQMAS [51] sequence used in our experiments were described in Section 3.3. The echoes were typically shifted out by twenty to thirty rotor cycles (many milliseconds if possible) to achieve high sensitivity and undistorted signal. If the sensitivity was a problem due to T_2 relaxation during echo formation, the simple two-pulse MQMAS sequence (Figure 3.12) was used. 540° solid-state pulses were applied for the excitation and reconversion, which according to the results of Amoureux [67], do not give the maximum multiple-quantum excitation and reconversion efficiency. The data were processed according to the method suggested by Grandinetti [50, 51]. RMN software was used and can be downloaded from the following URL: http://www.chemistry.ohio-state.edu/ grandinetti/RMN/rmn.html.

All of the inorganic compounds used in the experiment were obtained from commercial sources, typically with a stated purity of at least 98%. The anorthite and ^{17}O enriched stilbite were made at Stanford university and characterized by X-ray diffraction (XRD) and ^{29}Si NMR.

3.5.2 Feasibility

MQMAS spectra of ^{23}Na (I=$\frac{3}{2}$), ^{87}Rb (I=$\frac{3}{2}$), ^{27}Al (I=$\frac{5}{2}$), ^{17}O (I=$\frac{5}{2}$) and ^{45}Sc (I=$\frac{7}{2}$) in some model compounds are shown in Figure 3.18. The typical recycle delay varies

between 0.5 and 1 second for different samples, resulting in an acquisition time no longer than 12 hours. This suggests that MQMAS spectrum can be acquired in a reasonable time period for these nuclei (also for ^{11}B, I=$\frac{3}{2}$ [62]) when the T_1 of the sample is not very long. The quadrupolar coupling constants (C_Q) are 3.6MHz for ^{87}Rb in $RbClO_4$ [24], 2.4MHz for ^{23}Na in $Na_2C_2O_4$ [58], about 5MHz for the ^{45}Sc sites in $Li_3Sc_2(PO_4)_3$, 2.8-8.4MHz for ^{27}Al sites in anorthite [60] and 3.4MHz and 4.8MHz for the two types of oxygen sites in stilbite. The MAS dimension of these spectra usually show well-defined MAS powder patterns, suggesting a relatively even excitation of the triple-quantum coherence.

The single-hop DAS spectra for the above ^{87}Rb, ^{23}Na and ^{17}O samples were also recorded. However, acquisition of the ^{11}B, ^{27}Al and ^{45}Sc DAS spectra was far less successful because of the short T_1. Typically, 30-50 milliseconds are needed to flip the spinner axis in a DAS experiment which means it can only be applied to samples with T_1 longer than 100-150ms. Another limiting factor for DAS is the homonuclear dipolar coupling, which creates coherences that may not be restored following axis reorientation [42]. There is no such limitation for MQMAS because a hopping period is not necessary between the two correlated evolution periods.

The major limiting factor for MQMAS is the magnitude of the quadrupolar interaction. Since the triple-quantum transition is forbidden to 1st-order, the MQMAS experiment is currently limited to sites with C_Q less than 4MHz for spin-$\frac{3}{2}$ nuclei. As a comparison, C_Q of up to 6.5MHz for I=$\frac{3}{2}$ nuclei does not lead to extra experimental difficulties for DAS [24]. In the extreme, Massiot et al. have obtained a ^{71}Ga (I=$\frac{3}{2}$) DAS spectrum of β-Ga_2O_3 with a C_Q of 12MHz [74].

As shown earlier in this chapter, the excitation efficiency of the triple-quantum coherence is determined by $\frac{\omega_Q}{\omega_1}$. To achieve maximum excitation efficiency, highest power level is usually used. When the RF strength is fixed, the quantity that de-

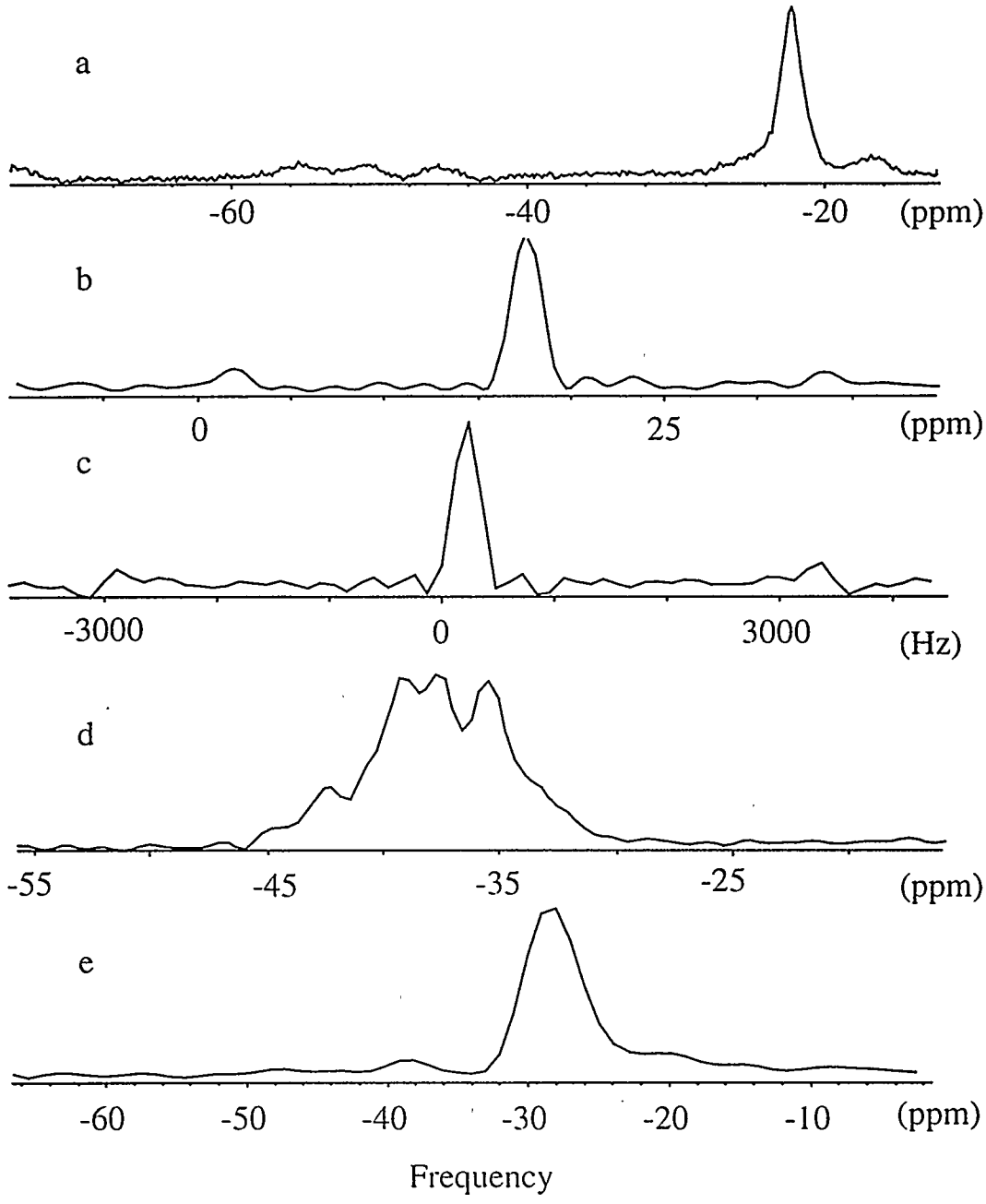

Figure 3.18: 3QMAS spectra of (a) $^{87}RbClO_4$ (b) $^{23}Na_2C_2O_4$ (c) ^{45}Sc in $Li_3Sc_2(PO_4)_3$ (d) ^{27}Al in anorthite (e) ^{17}O in stilbite. Spectra (a), (b), (d) were taken at 11.7T while the other two were taken at 9.4T. Frequencies are referenced to 1M $RbNO_3$ for ^{87}Rb, 1M NaCl for ^{23}Na, 1M $Al(NO_3)_3$ for ^{27}Al and H_2O for ^{17}O. Spectrum (d) is a slice taken along the isotropic dimension, which has better resolution than the isotropic projection.

termines the excitation efficiency is ω_Q which is defined as

$$\omega_Q = \frac{C_Q}{2I(2I-1)}, \tag{3.86}$$

and smaller ω_Q usually means better excitation unless ω_Q is vanishingly small. It is thus not surprising to see the efficient excitation for ^{27}Al (Figure 3.18d, anorthite, with C_Q up to 8.4MHz), but the inferior excitation for ^{87}Rb (Figure 3.18a, $RbClO_4$, C_Q=3.6MHz). The smaller scaling factor for I> $\frac{3}{2}$ nuclei suggests that the observation of C_Q up to 10MHz for ^{27}Al is feasible, based on the relatively efficient excitation of the triple-quantum coherence for ^{23}Na (e.g. $Na_2C_2O_4$, I=$\frac{3}{2}$, C_Q=2.4MHz). This is actually demonstrated by our experiment on kyanite (see next chapter), which contains ^{27}Al site with C_Q up to 10.0MHz. The fact that the single pulse excitation scheme is relatively efficient for spin-$\frac{5}{2}$ nuclei is important because C_Q for ^{27}Al and ^{17}O (both spin-$\frac{5}{2}$) are smaller than 10MHz in a lot of commonly used technological materials. However, care must be taken in the use of this technique for the study of site quantification.

3.5.3 Linewidth

The DAS and MQMAS linewidths (full width at half maximum, FWHM) of some model compounds are compared in Table 3.8. Also shown in this table is the linewidth data from MAS and Hahn-echo experiments (T_2-linewidth). In addition, the DAS linewidths for ^{11}B in D_3BO_3 [72], ^{27}Al in $LiAlSi_4O_{10}$ [75] and ^{17}O in diopside [46] are also included.

The DAS linewidth increases from about 200Hz for ^{87}Rb to 1.2kHz for ^{27}Al, consistent with the increasing homonuclear dipolar coupling strength. The MQMAS linewidth, on the other hand, is largely nucleus-independent, spanning the range between 170Hz and 270Hz. While the DAS and MQMAS lines are usually an order

Nucleus/compound	Linewidth(Hz)			
	DAS	MQMAS	Hahn-Echo	MAS
$^{87}RbNO_3$	160	180	10	2500
$^{87}RbClO_4$	250	270	10	5000
$^{23}Na_2C_2O_4$	500	260	25	3500
$D_3{}^{11}BO_3$ [72]	1100	-	-	4500
^{27}Al Kyanite [60]	-	170	30	7300
^{27}Al $LiAlSi_4O_{10}$ [76]	1200	-	-	4200
^{17}O Diopside [75]	120	100	-	3800
^{17}O Stilbite	600	270	30	4500

Table 3.8: Comparison of the DAS, MQMAS, echo and MAS linewidths for some model compounds.

of magnitude narrower than the MAS lines, they are an order of magnitude broader than the echo-linewidth. This is not a surprise, since magnetic field inhomogeneity as well as inhomogeneous broadenings is refocused by an echo sequence, leaving only the intrinsic T_2 relaxation under MAS. To understand completely why the MQMAS lines are so much wider than the echo lines requires more detailed and careful measurements to evaluate the contribution of each broadening mechanism. The residue dipolar coupling, the defects in the crystal and the field inhomogeneity can all be the dominating broadening mechanism.

The DAS linewidth can be related to the magnitude of the homonuclear dipolar interaction in the system [42]. The bilinear terms in the density matrix arising from the dipolar Hamiltonian can not be retained through a DAS angle change. Thus the dipolar Hamiltonian acts purely as a relaxation superoperator and it is not refocused at the DAS echo maximum. The independence of the MQMAS linewidth on the nucleus of interest at least suggests that homonuclear dipolar coupling is not a crucial factor for the implementation of the MQMAS experiment, which is a major advantage of MQMAS over DAS.

Strong heteronuclear dipolar coupling may render the MQMAS spectra broad

too. The problem seems serious only when ^{1}H is involved and can be overcome by ^{1}H decoupling [77].

3.5.4 Resolution

As shown in Eqn 3.34, the observed MQMAS shifts are scaled by two factors k_1 and k_2 and different from DAS (k_1=k_2=1) shifts. This makes the resolution of a MQMAS spectrum dependent not only on δ_{iso} and ω_{iso}^{2Q}, but also on k_1 and k_2. Some general conclusions about resolution can be drawn, but for a specific sample, care must be taken in spectral interpretation.

Eqn 3.34 indicates that two chemically different sites having the same quadrupolar coupling constant will have a frequency separation proportional to k_1 in the MQMAS spectrum. If $|k_1|$ is greater than 1.0, better resolution is expected for MQMAS; on the other hand, if $|k_1|$ is smaller than 1.0, DAS has better resolution. The factor k_2 has a similar effect on resolution, when the chemical shift of the two sites is the same. In the case that I=$\frac{3}{2}$, MQMAS has better resolution than DAS according to Table 3.1, and the opposite is true for I> $\frac{3}{2}$ nuclei. For I=$\frac{3}{2}$ nuclei, the enhanced resolution of MQMAS over DAS is readily seen in Figures 3.9 and 3.11 where the separation of the two MQMAS peaks in $RbNO_3$ (9ppm) is twice that in the DAS spectrum (5ppm). For I=$\frac{5}{2}$ nuclei, an example is given in Figure 3.19, which is an ^{17}O stilbite spectrum taken at 9.4T. In this case, DAS gives two partially resolved peaks, whereas only one peak is observed in the MQMAS spectrum. Similar resolution limitation was also seen for ^{45}Sc (I=$\frac{7}{2}$).

Despite the small scaling factors ($k_1 = -17/31, k_2 = 10/31$) for spin-$\frac{5}{2}$ nuclei, ^{27}Al is an ideal nucleus for MQMAS, as will be demonstrated in the next chapter [60]. MAS spectra for ^{27}Al are usually too broad to take advantage of the improved spectral dispersion. The moderate coupling constants for ^{27}Al in most materials [78]

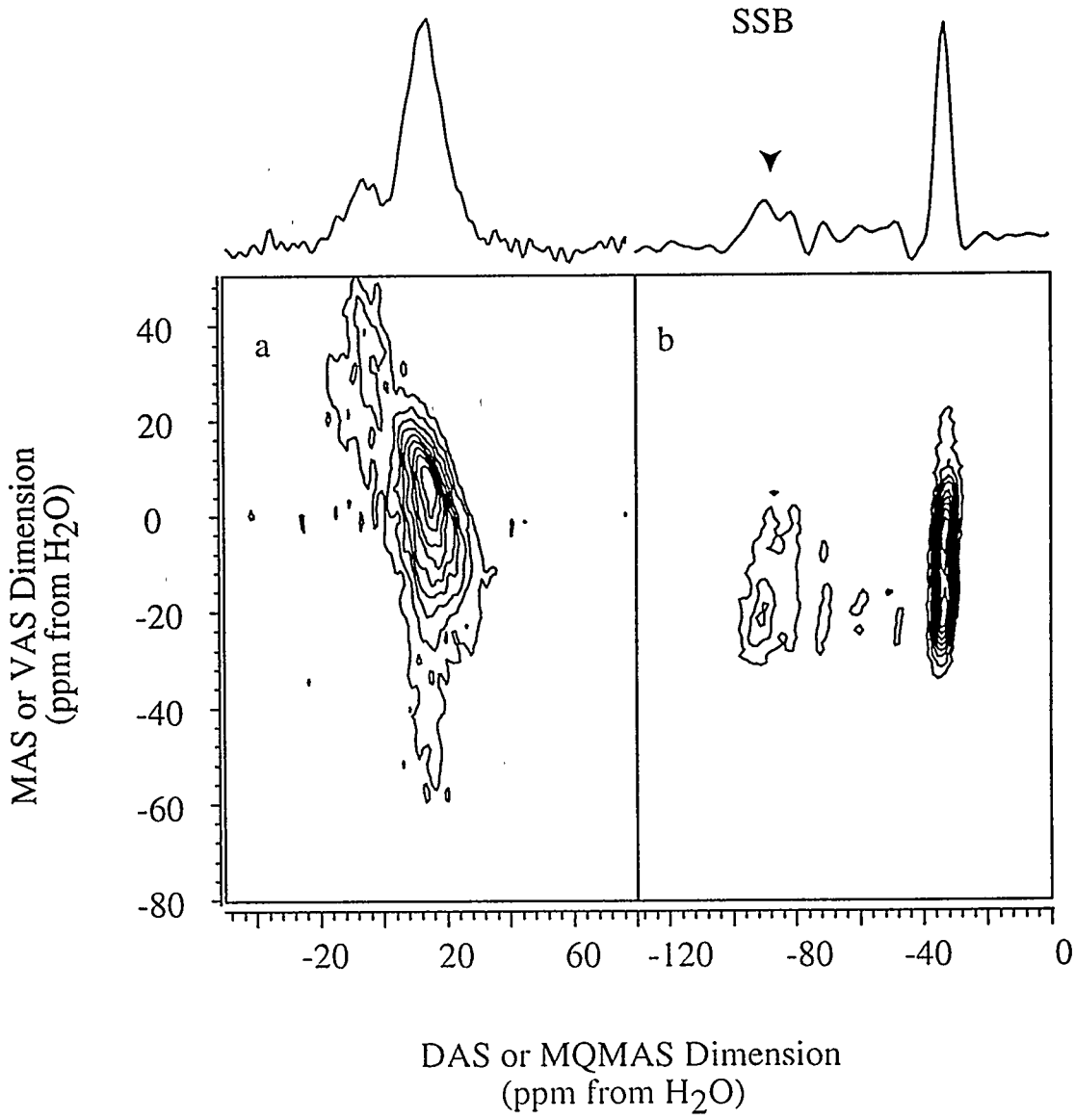

Figure 3.19: 9.4T DAS (a) and MQMAS (b) spectra of ^{17}O labeled stilbite. Two DAS peaks are discernible, but only one peak is observed in the MQMAS spectrum (the left hand side intensity is from spectral distortion and sideband).

make it very suitable for MQMAS studies. In addition, the decreased resolution in the 3QMAS spectrum can be overcome by correlating the quintuple-quantum coherence with the single-quantum coherence [79].

3.5.5 Chemical Shift Effect

It is somewhat interesting to see that two of the three rubidium sites in $^{87}RbNO_3$ collapse together in the 11.7T MQMAS spectrum. At the same field strength, three peaks exist in the DAS spectrum even though the MQMAS spectrum is expected to have better resolution. This problem happens also in the $RbNO_3$ DAS spectrum at 7.0T [24], whereas at that field strength, the MQMAS spectrum has three well-resolved peaks [51]. This overlap indicates that sites with different chemical shifts and quadrupolar interactions can appear at the same frequency in a DAS or MQMAS spectrum. Such an accidental overlap is a result of the cancellation of the chemical shift difference and the 2nd-order quadrupolar shift difference.

For well-crystallized samples, the accidental overlap can be overcome by multiple-field experiments. One can also perform both DAS and MQMAS experiments on the same sample at only one field, since the overlap conditions are different for these two experiments. In this respect, the combination of DAS and MQMAS removes the possibility of spectral misinterpretation.

For materials with a continuous distribution of chemical shifts and quadrupolar coupling constants (as in many amorphous and glassy materials), the problem of overlapping peaks limits the applicability of DAS and MQMAS. To see this, I will give a brief description of the general features of the ^{17}O DAS spectra for silicate glasses [80, 81]. DAS spectra of these materials are broadened usually from one to twenty kilohertz by the distribution of chemical sites (which have a distribution of chemical shift and quadrupolar parameters). Because DAS gives a two-dimensional

spectrum correlating the isotropic DAS shifts and the anisotropic interactions, an anisotropic slice taken perpendicular to the DAS dimension corresponds to a VAS spectrum and can be simulated to provide a set of quadrupolar (C_Q and η_Q) and chemical shift (δ_{iso}) parameters (See Figure 3.9). These parameters are related to structural information such as the Si-O-Si bond angles for bridging oxygen in ^{17}O glass (Eqn 4.1). The above approach assumes that each slice that is taken out corresponds to only one type of site. Because it is possible that sites with different chemical environments show up at the same frequency, this assumption does not necessarily hold.

As an example, consider the amorphous $Si^{17}O_2$ DAS data obtained by Baltisberger et al. [82] Using the quadrupolar and chemical shift parameters they obtained, the isotropic shifts in DAS, triple-quantum MAS and quintuple-quantum MAS spectra were calculated using Eqn 3.23 and 3.34. The results are shown in Figure 3.20a, where 100ppm is first subtracted from the 5QMAS shifts and then plotted. The data points on the left side of the figure are characterized by substantial error bars, which is mainly a result of simulation errors. The observed DAS shifts increase monotonically as a function of the slice number whereas the multiple-quantum shifts do not vary monotonically over the corresponding slices. What is also noted is that the spread of MQMAS shifts is much smaller for the same sites as in DAS as a result of the scaling factors in Eqn 3.34. For many of the ^{17}O inorganic glasses, the quadrupolar coupling constants (C_Q) decrease with the increase of the isotropic chemical shifts over a wide range of the Si-O-Si bond angles [82, 81]. The effect of a decreasing C_Q is to shift the MQMAS spectra to higher frequency (more positive ppm values). This effect is partially undone by the simultaneous increase of the isotropic chemical shift (note that $k_1 < 0$). The net result is a smaller spread of shifts in MQMAS spectra of ^{17}O glasses than one would get from a similar DAS experiment. The reason for the

difference between DAS and MQMAS is that k_1 and k_2 in DAS have the same sign (both plus), but they have opposite signs in MQMAS.

While Figure 3.20a shows that glassy samples may have a potential problem with overlap, it is worth considering a crystalline ^{17}O sample where C_Q and η_Q are better defined. Figure 3.20b shows similar calculations for the five ^{17}O sites in well-crystallized coesite [47]. All five sites are clearly separated in DAS, but sites 3, 4 and 5 are expected to overlap in the 3QMAS spectrum, and sites 4 and 5 are expected to overlap in the 5QMAS spectrum. This sort of overlap is possible in any sample depending on the relative sizes of the coupling constants and shifts. In this regard, performing all three experiments (DAS, 3QMAS and 5QMAS) would provide useful overall information as the overlap conditions for these techniques are different.

3.5.6 Chemical Shift Anisotropy

As discussed in the theory part of MQMAS, the CSA effect is magnified by a factor of $2m$ for the $m \leftrightarrow -m$ transition, which allows it to dominate the triple-quantum spectrum when its magnitude is comparable to that of the 2nd-order quadrupolar interaction in a single-quantum spectrum. In this case, anisotropic 2nd-order quadrupolar effect may be neglected in the triple-quantum dimension. Simulation of the 1D MQMAS spectrum then directly yields the CSA parameters. Carefully checking Table 2.3 suggests that this approach is only valid for I=$\frac{3}{2}$ nuclei (as long as 3QMAS is involved). When $I \neq \frac{3}{2}$, the 2nd-order quadrupolar effect is also amplified. However, when $I = \frac{3}{2}$ the magnitude of the 2nd-order quadrupolar interaction for the triple-quantum coherence is scaled down (by a factor of $\frac{7}{9}$), compared to that for the single-quantum coherence.

Figure 3.21 is the one- and two-dimensional 11.7T ^{87}Rb MQMAS (ω_r=8.9kHz) spectra of Rb_2CrO_4. Two sites exist in this compound, but only the one with smaller

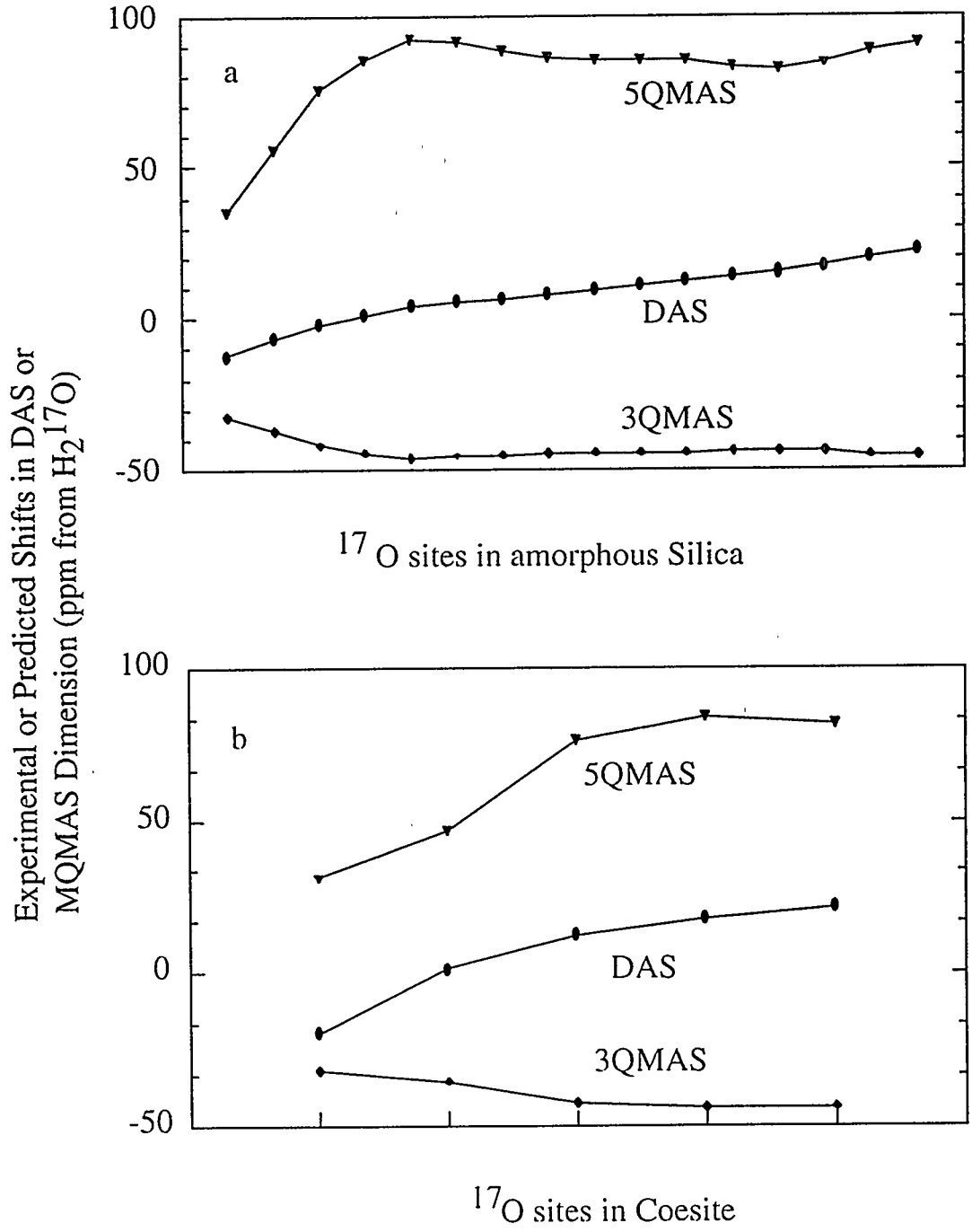

Figure 3.20: Comparison of the resonance frequencies of DAS, 3QMAS and 5QMAS for amorphous $Si^{17}O_2$ (a) and coesite (b). The Larmor frequency is 67.7MHz corresponding to ^{17}O at 11.7T. The isotropic chemical shift and quadrupolar coupling constant values are taken from [82] for SiO_2 glass, and from [47] for coesite. 100 ppm is subtracted from the 5QMAS shifts and then plotted in the figure.

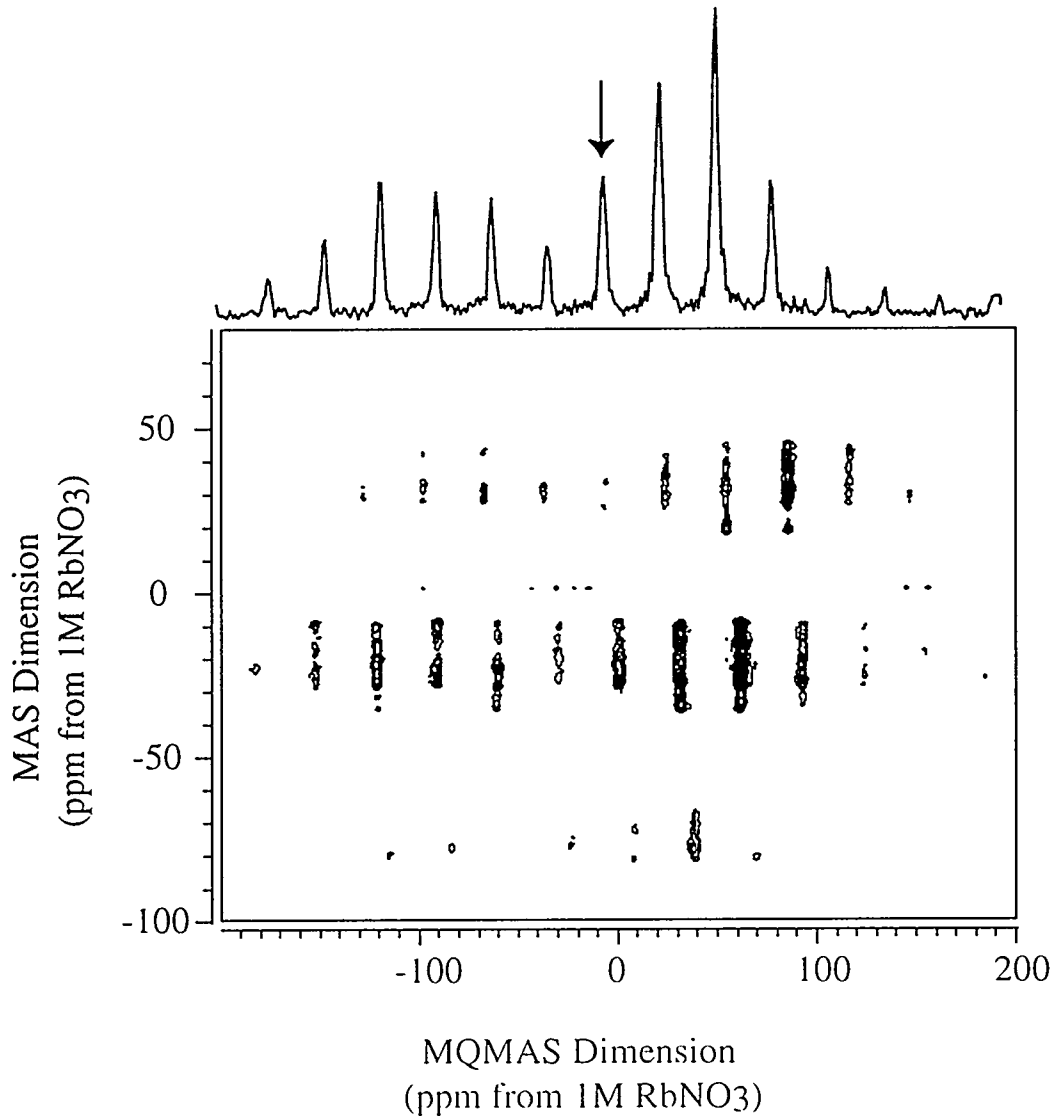

Figure 3.21: 11.7 T MQMAS spectrum of ^{87}Rb in Rb_2CrO_4. The projection of the centerband is shown above the contour plot. Due to the phase distortion, a magnitude spectrum is shown and the arrow points to the centerband. The simple two-pulse sequence is used.

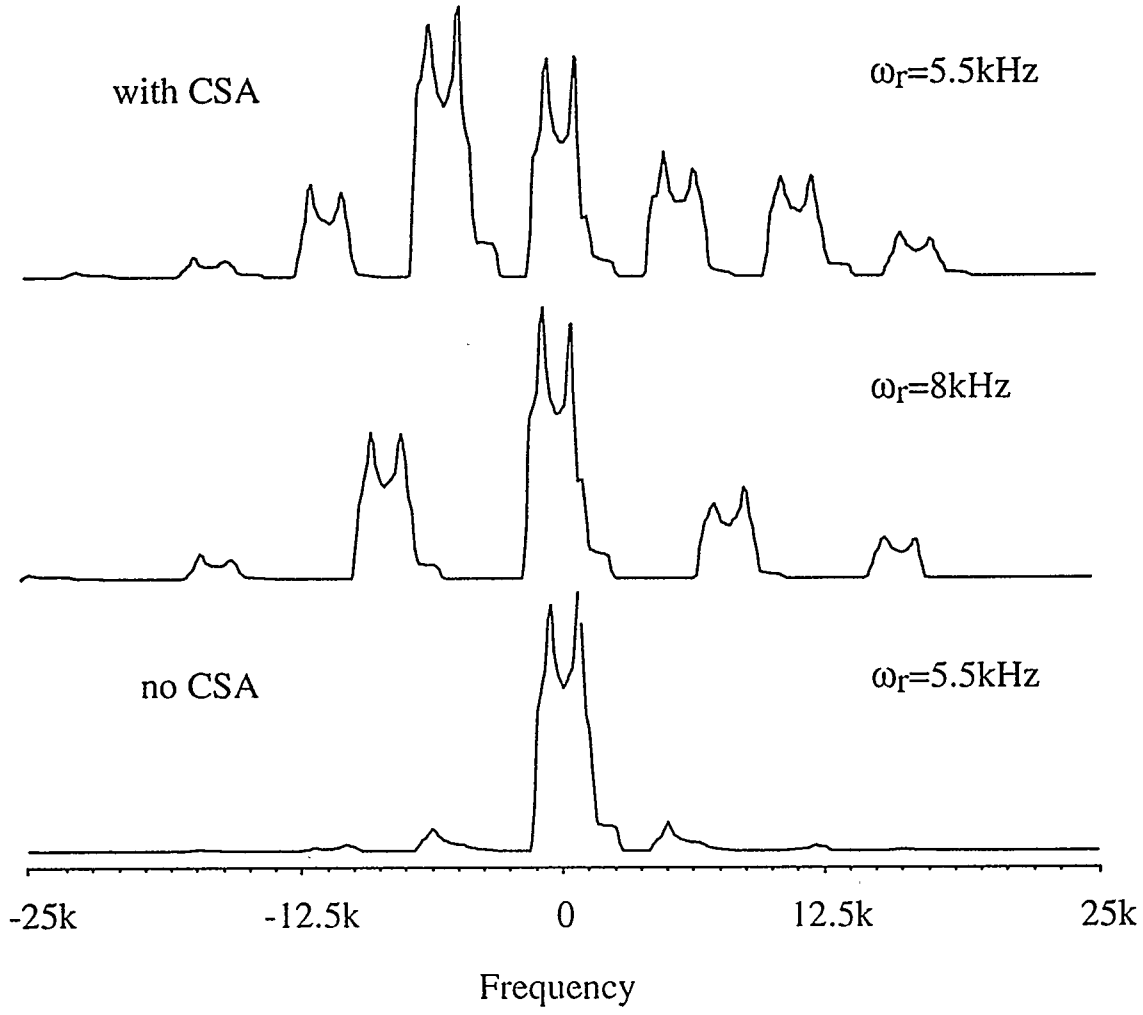

Figure 3.22: Simulated 11.7T MAS spectrum of ^{87}Rb in Rb_2CrO_4. Experimental spectrum (not shown) can not be reproduced if CSA is neglected.

C_Q is observed. The spectrum has a lot of sidebands ($\frac{mk+n}{1+k}\omega_r, n\omega_r$) away from the centerband in the two-dimensional frequency space, confirming the conclusions on the MQMAS sideband pattern [45, 83]. The simulated MAS spectra that either considers, or does not consider, the chemical shift anisotropy are shown in Figure 3.22.. It is clear that chemical shift anisotropy plays an important role in interpreting the data.

Figure 3.23 shows and compares the 1D DAS and MQMAS spectra of ^{87}Rb in Rb_2CrO_4. The MQMAS projection shows well-defined sideband pattern that is sim-

ulated in Figure 3.23c. The CSA and the 2nd-order quadrupolar broadening for Rb_2CrO_4 at 11.7T are 27kHz ($\delta_{CS} = -110$ppm) and 13kHz ($C_Q = 3.5$MHz), respectively [84]. Since they are somewhat comparable, the combined effect of CSA and quadrupolar interaction is complicated, and the DAS and MAS spectra are not sensitive to variations in the CSA parameters. It is then very difficult to obtain CSA information from either the DAS or MAS spectra. However, as CSA is amplified to 75kHz in the MQMAS dimension, the MQMAS spectrum of Rb_2CrO_4 covers a much larger frequency range and neglecting the 2nd-order quadrupolar interaction in simulating the MQMAS sideband intensities is possible. From Figure 3.23c, the magnitude and asymmetry parameter of CSA are determined ($\delta_{CS} = -110$ppm, $\eta_{CS} = 0.0$). These values are in good agreement with those determined by a switching-angle spinning (SAS) approach [84](chapter 6) but do not agree with other numbers found in the literature [85]. The Rb_2CrO_4 spectrum here also serves as an example to demonstrate that relatively large CSA does not limit the implementation of MQMAS.

3.6 Multiple-Quantum Variable-Angle Spinning

The concept of multiple-quantum NMR can be extended to the case that the sample is spinning at angles other than the magic-angle. To see how this can lead to other information not accessible through MQMAS, consider a spin-$\frac{3}{2}$ nucleus spinning at 70.12° or 30.56°, where $P_1(\cos\theta) = 0$. Since $C_1(3/2, 3/2) = 0$ (Table 2.3), Eqn 2.83 reduces to

$$\omega^{2Q}_{3/2\leftrightarrow -3/2} = C_0(\frac{3}{2}, \frac{3}{2})\omega^{2Q}_{iso}. \tag{3.87}$$

This means that anisotropic 2nd-order quadrupolar interaction does not broaden the triple-quantum spectrum. The spectrum is however, not a high-resolution spectrum

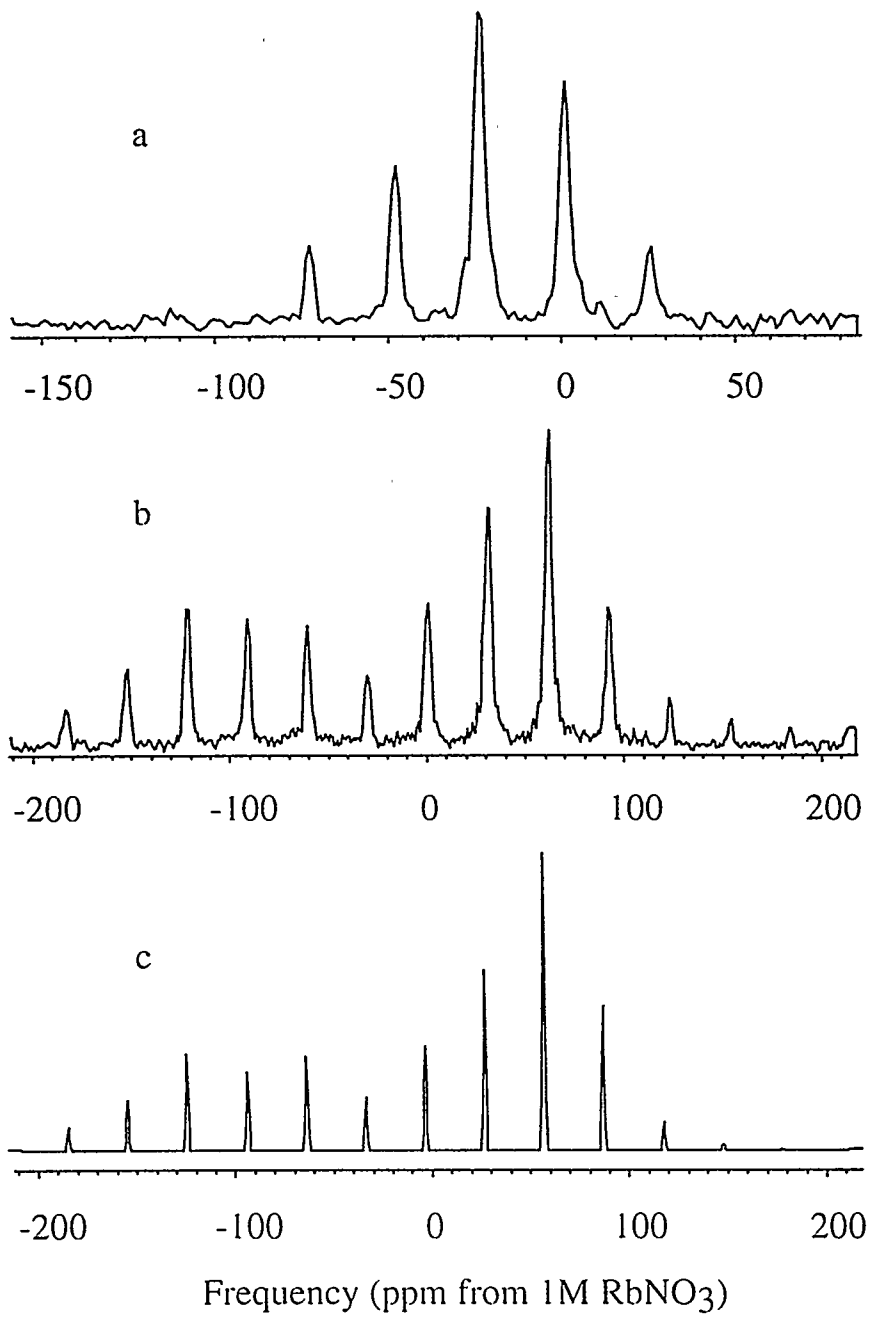

Figure 3.23: 11.7T DAS (a), MQMAS (b) and simulated MQMAS (c) spectra for ^{87}Rb in Rb_2CrO_4. The simulation neglects the anisotropic 2nd-order quadrupolar interaction.

since chemical shift anisotropy (CSA) still influences the spectrum.

$$\omega^{CS}_{3/2\leftrightarrow -3/2} = 3(\omega_{iso} + A^{CS}_2(\alpha^{CS}, \beta^{CS})P_4(\cos\theta)) \tag{3.88}$$

The pure CSA dimension (triple-quantum dimension) allows one to determine chemical shift anisotropy (CSA) directly, even if it is too small to be separated from the quadrupolar interaction in a single-quantum spectrum. The method would also be more sensitive to small chemical shift anisotropy since the CSA effect on a triple-quantum spectrum is magnified by a factor of three, compared to its effect on a single-quantum spectrum. Experimentally, the MQVAS data can be collected using the MQMAS sequences and processed accordingly. A shearing transformation is not needed since redefinition of the evolution time is not necessary here.

As an example, Figure 3.24 shows the 11.7T $RbNO_3$ 3QVAS spectrum acquired with sample rotated at 70.12°. The quadrupolar parameters for each of the three sites in this salt have been determined by DAS and MQMAS [51, 24]: $\delta_{iso} = -27.4$ppm, C_Q=1.68MHz, $\eta_Q = 0.2$ for the first site, $\delta_{iso} = -28.5$ppm, C_Q=1.94MHz, $\eta_Q = 1.0$ for the second and $\delta_{iso} = -31.3$ppm, C_Q=1.72MHz, $\eta_Q = 0.5$ for the third. Using these parameters, the isotropic frequency shifts in the triple-quantum dimension were calculated to give -74.2, -71.4 and -84.9ppm, respectively. These numbers are in the same region as the peaks in the triple-quantum spectrum. Compared with the simulated spectra in Figure 3.25, it is likely that the spectrum contains multiple overlapping well-defined patterns. However, accurate determination of the CSA parameters for this salt requires a three-dimensional experiment that separates the three sites.

Experiments on other samples were also performed (for example, $^{23}Na_2C_2O_4$, $^{23}Na_2SO_4$, $^{87}RbClO_4$ and $^{87}Rb_2SO_4$) and in all of the cases, pure-absorption phase 3QVAS spectra were obtained. The spectra all have an asymmetric triple-quantum dimension, but no clear singularities can be identified to accurately determine CSA

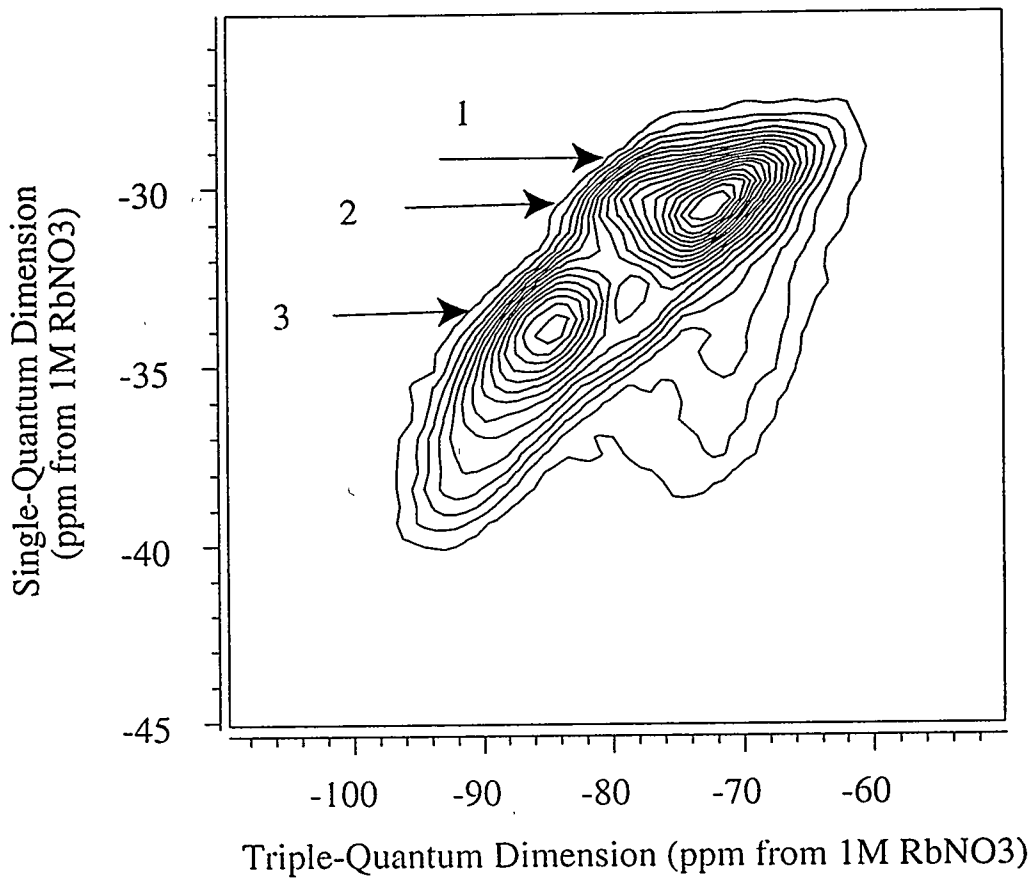

Figure 3.24: 11.7T 3QVAS spectrum of ^{87}Rb in $RbNO_3$.

parameters. This is most likely due to the existence of other anisotropic interactions including dipolar coupling. For MQVAS to be useful, such interactions have to be small enough that they do not obscure the CSA effect.

The next chapter shows that 2D switching-angle spinning (SAS) spectra for quadrupolar nuclei are more sensitive to small variations in Euler angles between the chemical shift and quadrupolar principal axis systems (PAS) [84, 86]. The two-dimensional 3QVAS patterns for $I = \frac{3}{2}$ nuclei may also be used to yield similar information. Figure 3.25 shows the simulated 2D 3QVAS spectra using same chemical shift and quadrupolar parameters. As one can see, the patterns show a significant dependence on the relative orientation of the two tensors, thus providing a promising method for

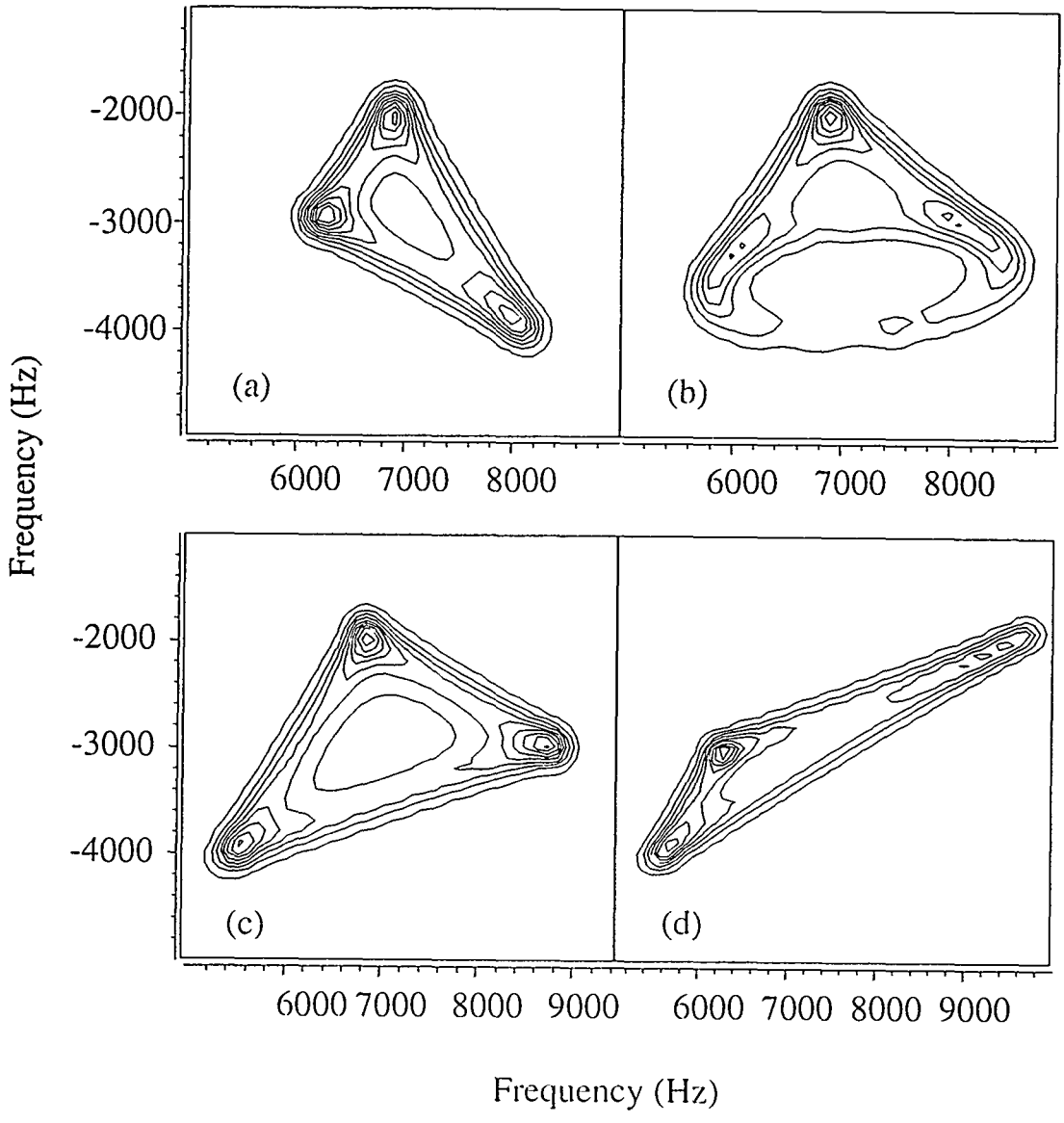

Figure 3.25: Simulated two-dimensional 3QVAS patterns with different Euler angles. The parameters used in the simulations are C_Q=3.0MHz, $\eta_Q = 1.0, \delta_{iso} = 0.0$ppm, $\eta_{CS} = 1.0, I = 3/2, \omega_0 = 150$MHz. The Euler angles are (a) (0°,0°,0°) (b)(0°, 0°, 45°) (c) (0°,0°,90°) (d) (90°,90°,90°).

quantifying the Euler angles.

3.7 Alternatives to DAS and MQMAS

3.7.1 Double Rotation (DOR)

DAS and MQMAS are two-dimensional echo like experiments that reconstruct isotropic NMR spectra for quadrupoles in the indirect dimension. Double rotation (DOR) is a simple experiment that does not involve this second-dimension [87, 88]. However, it is technically more difficult since the sample is spun around two angles simultaneously. The two angles are chosen to be the roots of the second- and fourth-order Legendre polynomials (54.74° and 30.56°). To derive the Hamiltonian under DOR, an extra rotation transformation is involved and Eqn 2.84 is needed.

$$A^Q_{2m}A^Q_{2,-m} = \sum_{l=0,2,4} < l0|22m,-m > a_{l0} \tag{3.89}$$

Notice that even though the other approach that expands the second-rank tensor product (Eqn 2.76-2.82) works too, it is very tedious to use with this extra rotation.

a_{l0} now has a definition different from Eqn 2.85.

$$a_{l0} = \sum_{n,j,k=-l}^{l} D^{(l)}_{n0}(\omega_{r1}t,\theta_1,0)D^{(l)}_{jn}(\omega_{r2}t,\theta_2,0)D^{(l)}_{kj}(\alpha^Q,\beta^Q,\gamma^Q)\sigma_{lk} \tag{3.90}$$

In this equation, ω_{r1} and ω_{r2} are the spinning rates at two spinning angles θ_1 and θ_2. If only the time-independent terms are considered, we have $n = j = 0$ and

$$a_{l0} = d^{(l)}_{00}(\theta_1)d^{(l)}_{00}(\theta_2)\sum_{k=-l}^{l} e^{-ik\alpha^Q}D^{(l)}_{k0}(\beta^Q)\sigma_{lk}. \tag{3.91}$$

Notice that

$$d^{(l)}_{00} = P_l(\cos\theta), \tag{3.92}$$

The frequency shift under DOR can be written as

$$\omega^{2Q} = \omega_{iso}^{2Q} + A_2^Q(\alpha^Q, \beta^Q)P_2(\cos\theta_1)P_2(\cos\theta_2) + A_4^Q(\alpha^Q, \beta^Q)P_4(\cos\theta_1)P_4(\cos\theta_2). \tag{3.93}$$

Since

$$P_2(\cos\theta_1) = 0 \tag{3.94}$$

$$P_4(\cos\theta_2) = 0, \tag{3.95}$$

only the first term in Eqn 3.93 is nonzero (isotropic 2nd-order shift) and high-resolution is achieved.

DOR has been successfully used to study a series of aluminum or oxygen containing materials [89, 90, 75]. The problem with DOR is that it requires sample spinning at two angles at the same time and the outer spinner can only be spun at about 1kHz. Even with rotor synchronization which creates a virtual spinning speed two times as fast as the real spinning speed, the spectra are still congested with sidebands that spectral interpretation is often complicated.

3.7.2 Dynamic-Angle Hopping

Dynamic-angle hopping (DAH) [91] is an interesting two-dimensional experiment that rotates the sample very slowly but totally removes the sidebands in the isotropic dimension. The isotropic dimension is constructed using a similar scheme as DAS and a hopping is also involved. The experiment is an extension of the magic-angle hopping (MAH) experiment [92]. The basic idea is that high-resolution and removal of spinning sidebands are two different goals in NMR and can be dealt with separately. To achieve high-resolution, the sample does not need to be spun very fast (DOR is an example). Fast spinning is often used since slow spinning gives extra sidebands [22, 93]. If the sidebands can be removed through other ways, fast spinning is not needed.

In DAH, high-resolution is achieved by spinning the sample first at 63.43°, and then at 0° ($k = 5$). The sideband is removed however, by applying five pairs of pulses at 63.43°. Since I have chosen not to include a complete description of spinning sideband theories in chapter 2, I will not go any details about how DAH gets rid of the spinning sidebands. The technique does not find much application, because a DAS probe is still required and the large number of RF pulses used may render many samples inaccessible.

Chapter 4

Application of MQMAS to Aluminum-Containing Materials

The use of multiple-quantum magic-angle spinning to study ^{27}Al-containing materials is probably the most important application of this experiment so far. Aluminum, along with oxygen and silicon, is one of the most common nuclei in zeolites, minerals, glasses and other technologically important materials. Solid-state NMR is becoming increasingly important in resolving some structural and quantification problems in these materials [94, 95, 96, 97, 98, 99, 78, 100, 101].

In aluminosilicate and aluminate crystals and glasses, there are three common types of aluminum environments with different aluminum coordination number. The four- and six-coordinated aluminum sites have been identified in a series of glasses [102, 103, 104, 105, 106], even though the static and MAS spectra of ^{27}Al ($I=\frac{5}{2}$) in glasses are often poorly resolved because of disorder and quadrupolar broadening. The four- and six-coordinated aluminum site appear around 60 and 0ppm respectively, whereas the quadrupolar coupling constants for each type of sites may range from 2-3MHz to 10MHz. An NMR peak around 30ppm was also observed in many silicate materials, especially in samples prepared under high-pressure [107, 108, 109, 110, 111]. This peak was attributed to five-coordinated aluminum in analogous to the assignment of the silicon spectra [112], even though the existence and quantification of this site remain controversial [113]. The high-resolution achieved through MQMAS may shine great light on this problem. In this chapter, I will discuss some of the experiments that are performed on aluminosilicate and aluminate samples that lead to a relatively clear picture of these materials. The utility and the limitation of

MQMAS are also discussed.

4.1 Interpretation of MQMAS Spectra

Before going into any detail about our ^{27}Al experiments, the interpretation of MQMAS spectra is to be discussed first. The goal of most solid-state NMR experiments is to extract useful structural and dynamic information about the materials of interest. Such information is strongly coupled to some NMR parameters including quadrupolar coupling constant (C_Q) and isotropic chemical shift (δ_{iso}). For example, it was suggested that the isotropic chemical shift of ^{27}Al or ^{29}Si directly reflects the coordination number of aluminum or silicon [114, 78]. It was also found that the quadrupolar coupling constant (C_Q) for ^{17}O in the Si-O-Si linkage is approximated by [47, 80, 115]

$$C_Q(\angle Si-O-Si) = C_Q(180°)\frac{2\cos(\angle Si-O-Si)}{\cos(\angle Si-O-Si)-1}. \tag{4.1}$$

Thus the measurement of chemical shift and quadrupolar parameters may be essential in discriminating and quantifying aluminum sites with different coordination number.

The extraction of quadrupolar (C_Q and η_Q) and chemical shift parameters (δ_{iso}, δ_{CS}, η_{CS}) may not always be obvious. For instance, the observed DAS and MQMAS shifts are the combination of the isotropic chemical shift and second-order quadrupolar shift. Special treatment needs to be done to separate the shifts from the two sources.

4.1.1 Spectral Simulation

Simulating the experimental NMR lines is by far the most widely used approach in solid-state NMR to get information about the anisotropic interactions. For quadrupolar nucleus, the simulation would ideally include up to 8 independent parameters

$(\delta_{iso}, \delta_{CS}, \eta_{CS}, C_Q, \eta_Q, \alpha, \beta, \gamma)$. The large number of parameters may overfit the data and practically, three parameters (δ_{iso}, C_Q and η_Q) are used in simulations. This approximation neglects CSA, but is proved adequate, especially when fast MAS is performed which minimizes the CSA effect.

The problem with the fitting procedure is that the number of fitting parameters grows up quickly when there are multiple sites in the system. This is one of the reasons that MAS spectra of ^{27}Al are often hard to qualify and quantify. The overlap of the four-, five- and six-coordinated aluminum peaks makes the simulation almost impossible in some cases. High-resolution techniques such as DAS or MQMAS are then useful to differentiate distinct sites in the system and provide initial guess of the NMR parameters for these sites. In the best cases (See Figures 3.9 and 3.11), when distinct sites are resolved in the DAS or MQMAS spectrum, each site can be simulated separately, which greatly reduces the number of parameters in the fitting and increases the accuracy and precision of the simulation.

4.1.2 DAS and MQMAS: Extraction of δ_{iso} and P_Q

It is possible to obtain δ_{iso} and P_Q (defined below) without resorting to the simulation method. As shown in section 3.2, the observed DAS or MQMAS frequency is the combination of the isotropic chemical shift and the isotropic 2nd-order quadrupolar shift.

$$\delta^{DAS} = \delta_{iso} + \delta^{2Q}_{iso} \tag{4.2}$$

$$\delta^{MQMAS} = k_1\delta_{iso} + k_2\delta^{2Q}_{iso} \tag{4.3}$$

To obtain the isotropic chemical shift and the quadrupolar coupling constant, multiple-field experiments are performed. The isotropic chemical shift δ_{iso} is not dependent on the external field strength (in the units of ppm); the second-order quadrupolar

shift, on the other hand, is inversely proportional to the square of the B_0 field.

$$\delta_{iso}^{2Q} = -\frac{3\times 10^6}{40}\frac{(I(I+1)-\frac{3}{4})C_Q^2(1+\frac{\eta_Q^2}{3})}{\omega_0^2 I^2(2I-1)^2} = C\frac{P_Q^2}{\omega_0^2} \tag{4.4}$$

Here,

$$P_Q = C_Q\sqrt{1+\frac{\eta_Q^2}{3}} \tag{4.5}$$

and

$$C = -\frac{3\times 10^6}{40}\frac{(I(I+1)-\frac{3}{4})}{I^2(2I-1)^2}. \tag{4.6}$$

If DAS measurements are done at two separate fields, one gets

$$\delta_1^{DAS} = \delta_{iso} + C\frac{P_Q^2}{\omega_{01}^2} \tag{4.7}$$

$$\delta_2^{DAS} = \delta_{iso} + C\frac{P_Q^2}{\omega_{02}^2}. \tag{4.8}$$

Solving the simultaneous equations gives

$$P_Q = \omega_{01}\omega_{02}\sqrt{\frac{\delta_1^{DAS}-\delta_2^{DAS}}{C(\omega_{02}^2-\omega_{01}^2)}} \tag{4.9}$$

$$\delta_{iso} = \frac{\omega_{01}^2\delta_1^{DAS}-\omega_{02}^2\delta_2^{DAS}}{\omega_{01}^2-\omega_{02}^2}. \tag{4.10}$$

One should notice that to obtain P_Q and δ_{iso}, all we need is two linearly independent equations of P_Q and δ_{iso}. Therefore, one of the equations may come from DAS (or MAS), and the other one from MQMAS. To see this, recall that

$$\delta^{DAS} = \delta_{iso} + C\frac{P_Q^2}{\omega_0^2} \tag{4.11}$$

$$\delta^{MQMAS} = k_1\delta_{iso} + Ck_2\frac{P_Q^2}{\omega_0^2}. \tag{4.12}$$

Site	$\delta^{9.4T}_{MAS}$(ppm)	$\delta^{9.4T}_{3QMAS}$	$\delta^{11.7T}_{MAS}$	$\delta^{11.7T}_{3QMAS}$	δ_{iso}	P_Q(MHz)
T1	58.6±2.0	-34.2±0.2	59.6±1.5	-34.0±0.2	61.0±0.7	2.07±0.50
T2	59.7±2.0	-36.4±0.2	61.8±1.5	-35.7±0.2	63.9±0.6	2.58±0.50
T3	66.1±2.0	-39.1±0.2	67.2±1.5	-38.4±0.2	69.2±0.7	2.34±0.50

Table 4.1: Isotropic shifts and quadrupolar coupling parameters for leucite from 11.7 T and 9.4 T 3QMAS experiments, derived from 3QMAS and MAS peak positions.

If the observed shifts in the single- and triple-quantum spectra are available, one would get

$$P_Q = \omega_0 \sqrt{\frac{k_1 \delta^{DAS} - \delta^{MQMAS}}{C(k_1 - k_2)}} \tag{4.13}$$

$$\delta_{iso} = \frac{k_2 \delta^{DAS} - \delta^{MQMAS}}{k_2 - k_1}. \tag{4.14}$$

Figure 4.1 shows how Eqn 4.13 and Eqn 4.14 can be used to extract both P_Q and δ_{iso} from a single MQMAS experiment. In the two-dimensional ^{27}Al spectrum of leucite at 11.7T, three isotropic peaks are observed in both dimensions. Inserting the observed shifts for each site in both dimension into Eqn 4.13 and Eqn 4.14, the isotropic chemical shift and quadrupolar product for each site can be generated.

To improve the overall accuracy and precision for the measurement of P_Q and δ_{iso}, multiple experiments should be performed at many fields. This opens the possibility of a linear least-square fit of the observed shifts. Since the MQMAS and DAS shifts are scaled differently, preprocessing of the observed shifts is needed before the fitting can be done. To do this, the observed shift is first written in the more general form as follows.

$$\delta^{obs} = k_1 \delta_{iso} + k_2 \omega^{2Q}_{iso} \tag{4.15}$$

For DAS, $k_1 = k_2 = 1$. Dividing both sides of the equation by k_1, we get an equation

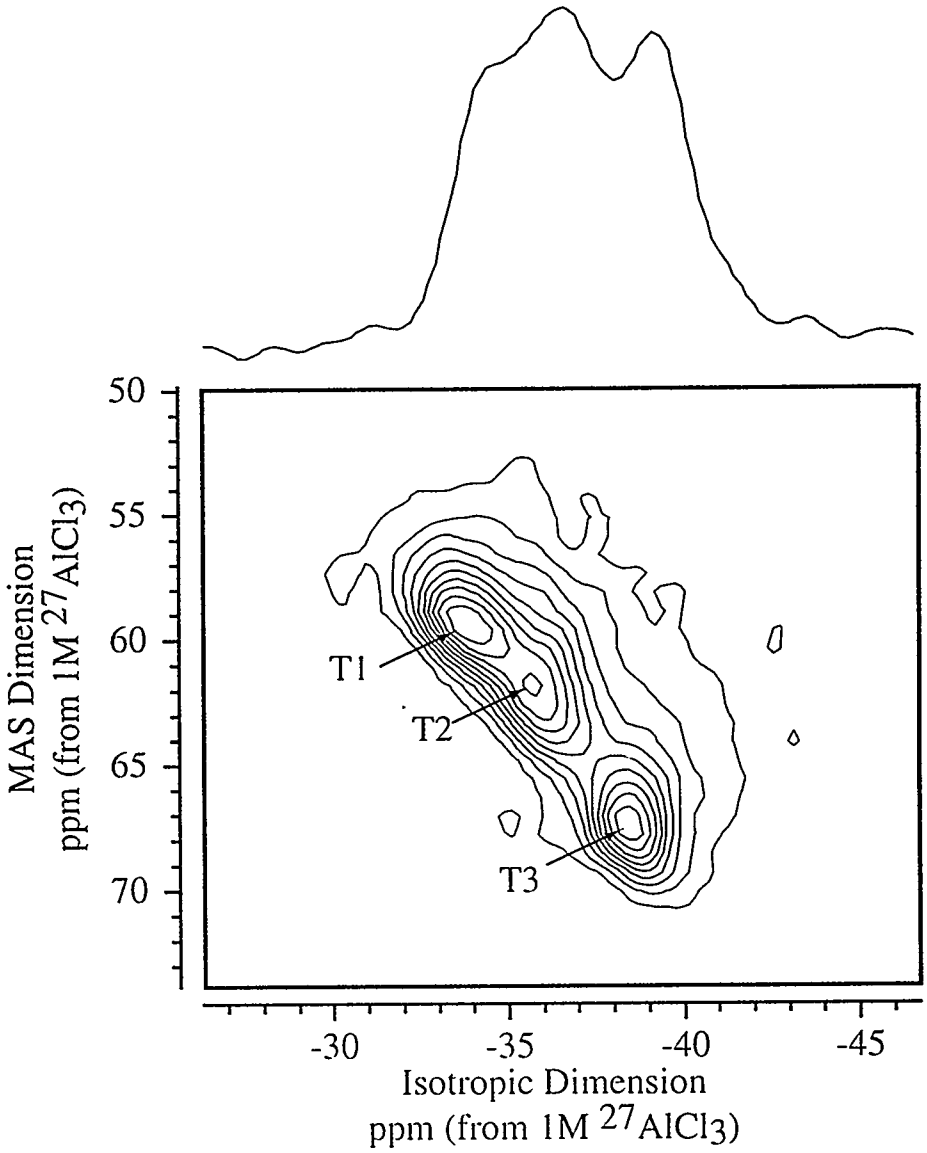

Figure 4.1: Contour plot of ^{27}Al 3QMAS NMR spectrum for leucite. The 1D MQMAS spectrum on top is the projection onto the isotropic dimension.

that can be used for the linear regression:

$$\frac{\delta^{obs}}{k_1} = \delta_{iso} + \frac{k_2}{k_1}\omega_{iso}^{2Q} = \delta_{iso} + \frac{Ck_2}{k_1\omega_0^2}P_Q^2. \tag{4.16}$$

Plotting $\frac{\delta^{obs}}{k_1}$ versus $\frac{Ck_2}{k_1\omega_0^2}$ would give a straight line, whose slope is the square of P_Q, and the interception is the isotropic chemical shift. Figure 4.2 demonstrates this strategy for leucite, where the 9.4T and 11.7T data are combined and used in the fitting. This linear regression gives significant improvement on the overall errors, and the fitting results are reported in table 4.1.

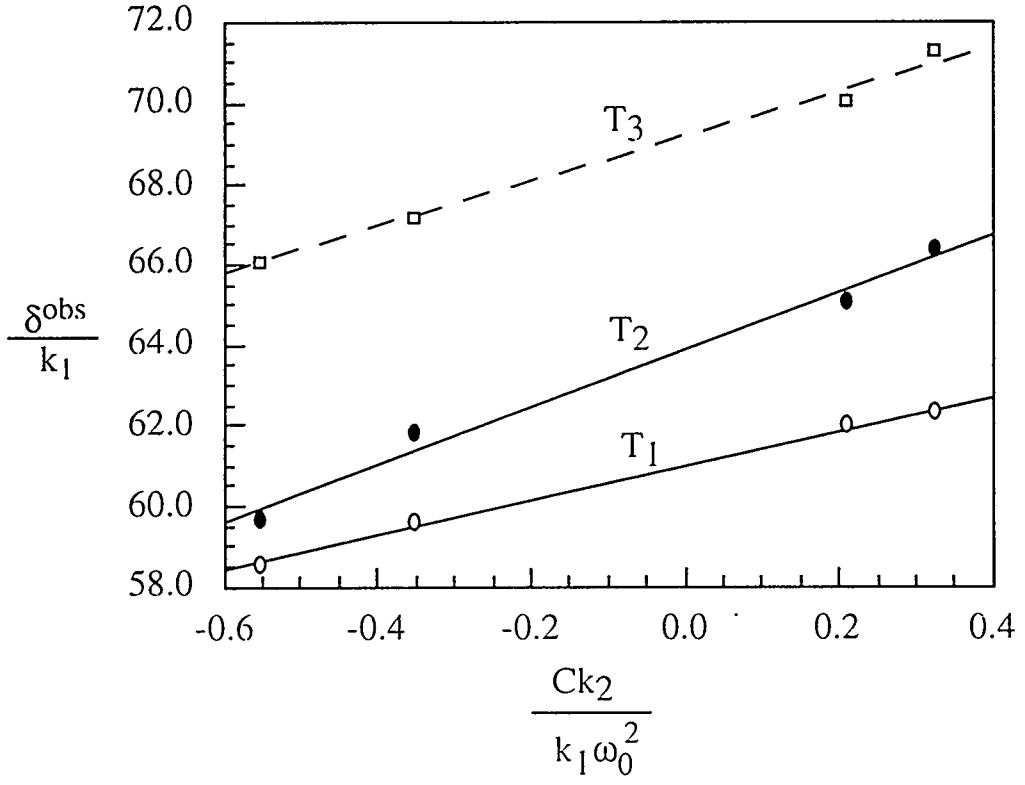

Figure 4.2: Least-square fit of 11.7T and 9.4T MAS and 3QMAS shifts for leucite. The data and fitting results are tabulated in Table 4.1.

It is important to note that it is impossible to extract C_Q and η_Q from only the isotropic shifts in DAS or MQMAS spectra. Such information comes from the simulation of the NMR lineshape. In this respect, MQMAS has a subtle advantage

over DAS. The anisotropic spectrum in DAS (assuming $k = 1$) is a VAS spectrum with sample rotating at 79.19° or 37.38°. The anisotropic spectrum in MQMAS, on the other hand, is a MAS spectrum. Simulating the MAS spectrum gives more accurate isotropic chemical shift and quadrupolar parameters for two reasons. First, the chemical shift anisotropy does not distort the MAS lineshape. Second, at one of the two $k = 1$ DAS angles, the NMR spectrum has a long tail (Figure 3.4), whose intensity is so low that can not be precisely measured in experiments and reproduced by simulation. This long tail, however, determines the magnitude of the quadrupolar coupling constant and introduces significant uncertainties. The MAS spectrum does not have this problem and can often be accurately simulated.

4.1.3 Quantification

Sometimes, not only the NMR lineshapes for each site, but also the quantification for the sites are important. Since MQMAS is not quantitative, the isotropic spectra can seldom be used for quantitative purpose unless all the sites have very similar quadrupolar coupling constants. There has been some work showing that DAS is relatively quantitative, if the T_1 for different sites are similar [116].

A better approach for quantification may be a combination of the high-resolution techniques with the simulation of static or MAS spectra [47]. In this approach, DAS or MQMAS provide initial estimate of the number of sites in the sample, and the chemical shift and quadrupolar parameters for each site. These parameters are then fed to a fitting program to fit the static or MAS spectra. In the case that each site in the sample has well-defined lineshape, this approach is superior to other approaches that use the information from only one technique.

4.2 Experiments

4.2.1 Sample Preparation

The sample of the natural framework silicate mineral leucite ($KAlSi_2O_6$, from the Roman volcanic province) has been previously studied in detail by ^{29}Si MAS NMR [117]. Several samples of crystalline anorthite ($CaAl_2Si_2O_8$, another framework silicate) were prepared by the method described in a detailed study of Si/Al disorder [118]. A glass of this composition was prepared by melting of the oxides at 1650°C for about 1 hour followed by air quenching. Several portions of the glass were then crystallized by reheating at 1400°C for either 4 minutes (sample 1) or 65 hours (sample 2). Powder X-ray diffraction on these samples, and ^{29}Si MAS NMR spectra, showed only anorthite to be present. The latter spectra closely resemble those of Phillips et al. [118] for samples crystallized for 15 minutes and 179 hours, respectively, and thus have a smaller difference in the extent of disorder than expected (presumably because of vagaries of thermal history and nucleation kinetics). A sample of natural kyanite (Al_2SiO_5, locality unknown) was also selected in order to test the relative excitation efficiencies for Al sites with widely varying quadrupolar coupling constants. A glass of composition 40 mole% MgO, 40 mole% B_2O_3, 20 mole% Al_2O_3 was selected because of its large concentrations of four-, five-, and six-coordinated aluminum as determined previously by ^{27}Al MAS NMR, and was also prepared by mixing and melting the oxides.

4.2.2 NMR Spectroscopy

The MAS experiments at 9.4T were performed on a modified Varian VXR-400S spectrometer with a 5mm high-speed MAS probe from Doty Scientific, Inc., with spinning rates of about 11 kHz. At 11.7 T, experiments were performed on a Chemagnetics spectrometer using the same probe or a home-built DAS probe described

in the preceding chapter. Spin-lattice relaxation times (T_1) were measured with the saturation-recovery method, and delay times in 3QMAS experiments were chosen to be at least $3T_1$ to assure nearly complete relaxation. The low efficiency of the triple-quantum excitation, and the two-dimensional data acquisition, resulted in typical total acquisition times for the spectra shown here of 12-24 hours, much longer than times typically required for 1D, single-quantum MAS experiments (typically a few minutes for ^{27}Al). Useful 3QMAS spectra can generally be obtained in somewhat shorter times of a few hours.

The pulse sequence used was the shift-echo 3QMAS sequence and is shown in Figure 3.10. The first and second pulses are solid-state 540° pulses applied with the highest allowable power (50-60kHz). The third pulse is a 180° pulse applied with lower power level and is approximately 15-20μs in duration. The t_1 period was selected to have a dwell time which was equal to the desired t_1 dwell time (after complete processing) multiplied by $\frac{19}{31}$. This factor arises from the scaling of observed shifts (Table 3.1). The MAS t_2 spectral width was usually 6-20 kHz while in the t_1 dimension it was usually 6-15 kHz. Usually 40-100 t_1 points were required to obtain spectra without truncation artifacts. The delay between the second and third pulses was set to values ranging from 1-3 ms (10-30 rotor cycles). In the referencing stage, the offset in the isotropic dimension (the ppm value of the center of the resulting t_1 dimension spectrum) need to be multiplied by $\frac{k-3}{k+1}$ or $-\frac{17}{31}$.

The determination of the isotropic chemical shift (δ_{iso}) and quadrupolar coupling product P_Q was done using the approach described at the beginning of this chapter. When possible, MAS peak shapes in slices of the 2D spectra were fitted with a least-square program (utilizing the CERN MINUIT routines) in which all relevant parameters in the MAS peak shape (C_Q, η_Q, δ_{iso}, integrated intensity, Lorentzian and Gaussian broadening) were allowed to vary. In general, the two methods produced

similar results, although the latter approach may allow η_Q and C_Q to be derived in addition to P_Q.

4.3 Results

4.3.1 Leucite

The leucite MQMAS spectrum has been shown in Figure 4.1 to demonstrate different strategies in giving useful NMR parameters. This mineral has a complex structure with three crystallographically distinct tetrahedral sites (T_1, T_2, T_3). Because of the complexity of the ^{29}Si spectra (as many as 15 overlapping peaks), and the low resolution of ^{27}Al MAS spectrum (Figure 1.3), the fraction of the total Al on each site remains imprecisely known. Models of essentially identical ^{29}Si spectra have yielded fractions of about 0.1, 0.2, 0.4 on T_1, T_2, T_3 respectively, in one model [117], 0.25, 0.50, 0.25 in a second model [119] and 0.50, 0.25, 0.25 in a third [120].

The MAS spectra shown in Figure 4.3 seems to suggest that the fractions are 0.5, 0.25, 0.25, consistent with earlier analysis of ^{27}Al MAS data by others [121]. However, this conclusion is based on the assumption that the quadrupolar coupling constants for each site is so small that the MAS spectrum is a superposition of three Gaussian peaks. This may not be true since intensity in one peak may come from the shoulders in the quadrupolar lineshape of other peaks. The ^{27}Al 2D 3QMAS spectrum of leucite (Figure 1.1) shows 3 partially overlapping peaks corresponding to the three sites. The projection in the isotropic dimension shows considerably better resolution than MAS spectra in Figure 1.3. Compared to the MAS spectra, the 3QMAS data are more definitive in ruling out any influence of second-order quadrupolar coupling on peak shape. Fitting the projection with three Gaussian peaks suggests that the intensities of the three peaks are equal within about a 20% error. Residual broadening, presumably due to the disordered arrangement of second-

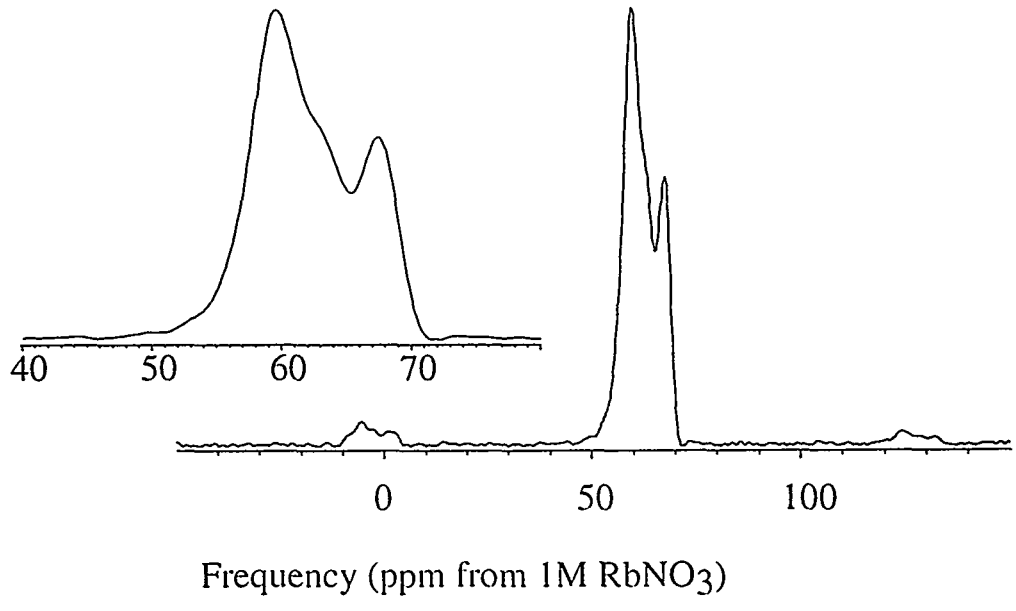

Figure 4.3: ^{27}Al MAS spectra of Leucite. The spectrum was taken with the Hahn-echo sequence. The spectral region 40-80ppm is expanded to show the three partially resolved peaks.

neighbor cations and a resulting distribution of isotropic chemical and quadrupolar shifts, appears to limit the ultimate resolution.

Imperfect site excitation has the potential to be quite significant in 3QMAS experiments, making quantification of intensities complex. Even though a long pulse is capable of transferring coherence from a zero- to a triple-quantum state, the efficiency of this process is highly dependent on C_Q and on the overall RF field strength. An assumption of uniform excitation is thus most likely to be valid if C_Q values for different sites are similar. Exact C_Q values are not known for leucite, but data for isotropic chemical shifts and for P_Q have be extracted and shown in Table 4.1 from the two-dimensional NMR spectra at 9.4T and 11.7T. The chemical shifts agree well with values previously derived from MAS spectra including satellite sidebands, and P_Q data are consistent with previous rough estimates of 1-2MHz [121]. The close similarity of the P_Q values for the three peaks suggests that in this case intensities in the 3QMAS experiment are likely to be quantitative and thus imply site occupancies

that are somewhat discrepant from previous models. Given the disagreements among existing models, however, the significance of their differences with the present data are uncertain.

4.3.2 Kyanite

Kyanite was studied to further assess the quantification of 3QMAS peak intensities. The mineral contains 4 equally populated octahedral Al sites, with C_Q values of 10.0, 9.4, 6.5, and 3.7 MHz. The MAS spectrum is contrasted with the isotropic projection of the 3QMAS spectrum in Figure 4.4. The resolution in the latter is dramatically increased: separation of the peaks in the latter is enhanced by the large range in C_Q, and peaks are much narrower because of the full averaging of the second-order quadrupolar broadening. Even sites with very large C_Q values are excited and observed. However, it is clear that observed intensities are systematically reduced with increasing C_Q, suggesting that caution is required in materials where ranges of C_Q are large or are unknown.

4.3.3 Crystalline Anorthite

Anorthite is an excellent test for ^{27}Al spectral resolution: it has eight crystallographically distinct tetrahedral Al sites, and is fully ordered (natural samples) or nearly so (synthetic samples). C_Q and η_Q values for all sites have been reported from single crystal data, but isotropic chemical shifts are not known because ^{27}Al MAS spectra are completely unresolved. 3QMAS data at 11.7 T for more ordered crystalline anorthite are shown in Figure 4.5. The spectrum is complex, but contains a number of significant, resolvable features. The 9.4T spectrum is essentially the same in overall appearance with slight shifts. Results for the somewhat less ordered crystals are very similar, if perhaps slightly less well-resolved, and have not been

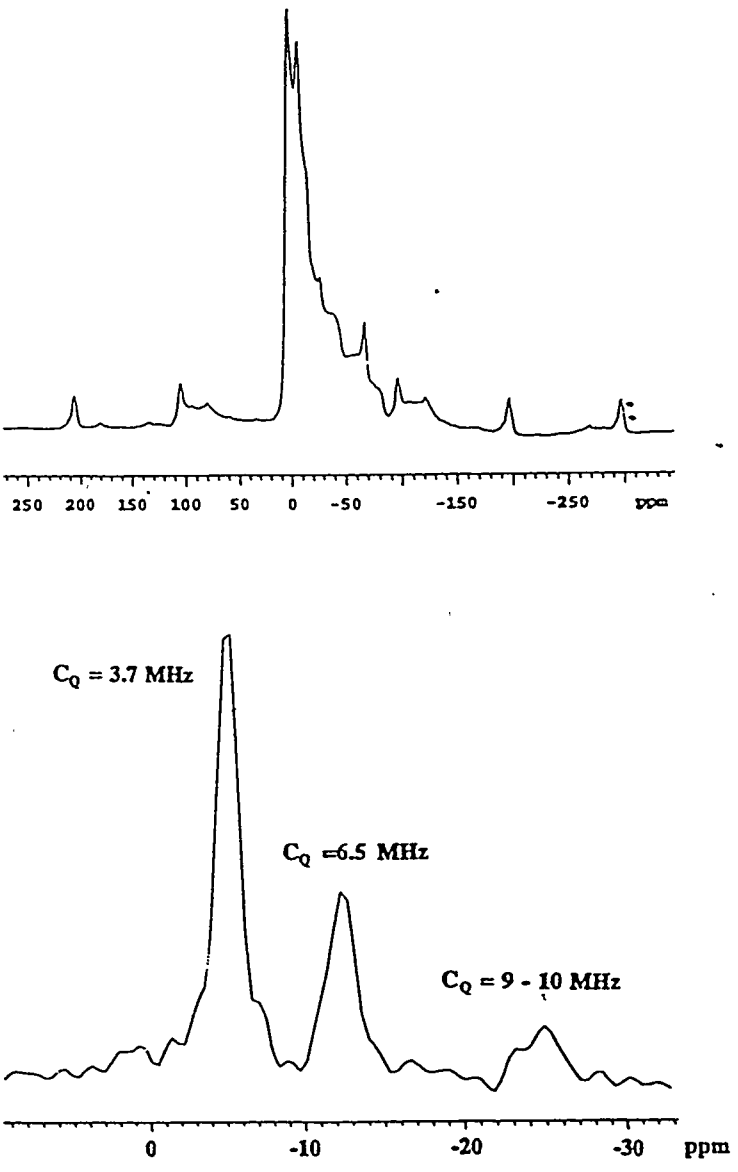

Figure 4.4: (above) ^{27}Al MAS spectrum for kyanite; (below) Isotropic projection of 3QMAS spectrum. Labels indicate P_Q for each site.

analyzed in detail. Both approaches described at the beginning of this chapter are taken to analyze the data. In both, slices through the 2D spectra at the positions of obvious spectral features were taken (Figure 4.6). In the first approach, the peak

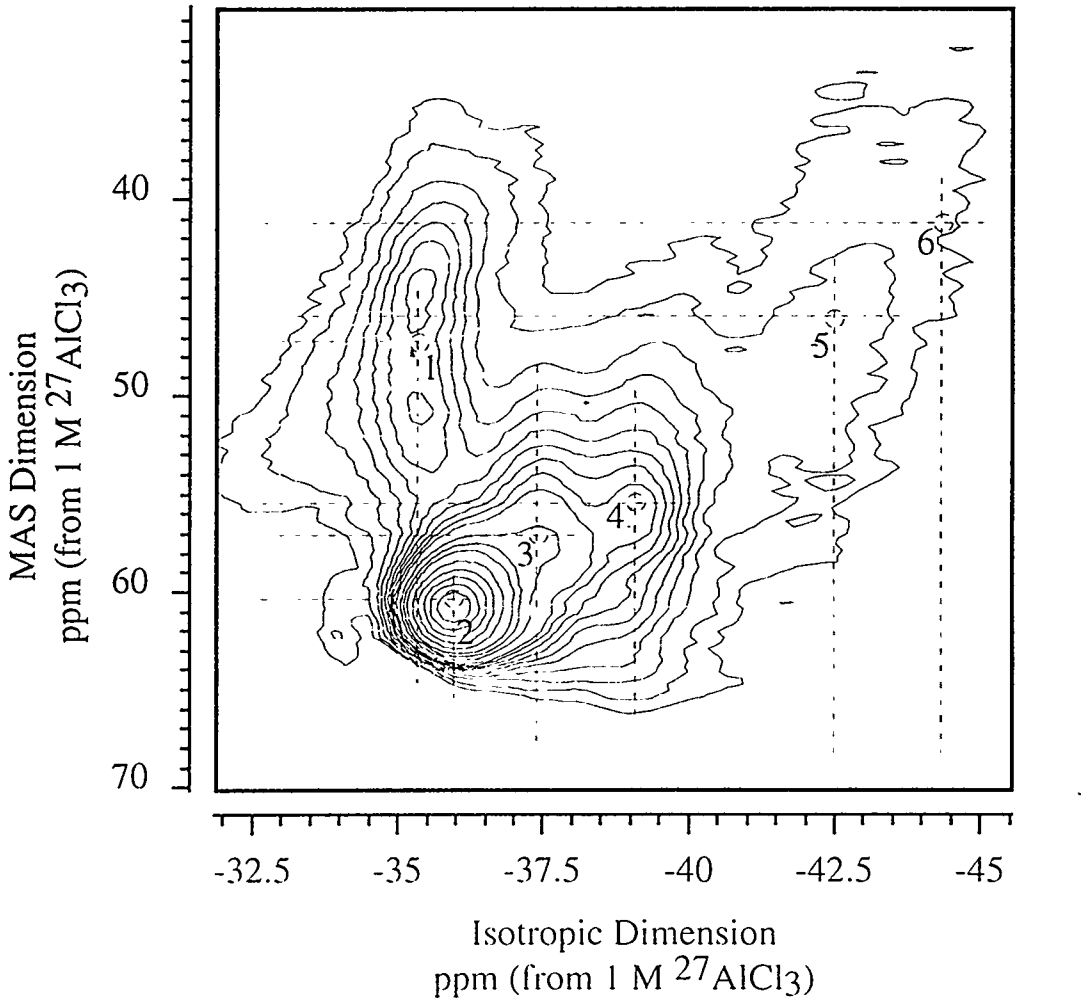

Figure 4.5: Contour plot of ^{27}Al 3QMAS NMR spectrum for crystal anorthite at 11.7T. The number points show the position of singularities, through which slices were taken for simulations.

position in the ω_1 dimension and the center of gravity in the ω_2 (MAS) dimension were determined, and δ_{iso} and P_Q were calculated using Eqn 4.13 and 4.14. Results for the data at 9.4T and 11.7T are shown in Tables 4.2 and 4.3, and are consistent with each other within estimated uncertainties.

Peak	δ_{MAS}(ppm)	δ_{3QMAS}(ppm)	δ_{iso} (ppm)	P_Q(MHz)
1	48.0±3.0	-35.4±0.2	58.4±1.1	5.43±0.50
2	61.0±1.0	-36.0±0.2	63.9±0.4	2.88±0.33
3	58.0±3.0	-37.4±0.2	64.4±1.1	4.26±0.63
4	55.0±3.0	-39.1±0.2	65.2±1.1	5.38±0.50
5	47.0±3.0	-42.5±0.2	66.2±1.1	7.37±0.37
6	40.0±5.0	-44.4±0.2	65.8±1.9	8.54±0.52

Table 4.2: Isotropic shifts and quadrupolar coupling parameters for crystalline anorthite from 11.7T 3QMAS experiments, derived from 3QMAS and MAS peak positions.

Peak	δ_{MAS}(ppm)	δ_{3QMAS}(ppm)	δ_{iso} (ppm)	P_Q(MHz)
1	40.8±2.0	-37.1±0.3	57.7±0.8	5.53±0.21
2	59.0±1.0	-36.2±0.2	63.4±0.4	2.83±0.20
3	56.0±2.0	-37.1±0.3	63.3±0.8	3.64±0.32
4	51.1±3.0	-39.1±0.3	63.8±1.1	4.80±0.36
5	36.6±4.0	-45.6±0.3	65.9±1.5	7.28±0.32
6	25.0±5.0	-49.0±0.3	65.5±1.9	8.56±0.33

Table 4.3: Isotropic shifts and quadrupolar coupling parameters for crystalline anorthite from 9.4T 3QMAS experiments, derived from 3QMAS and MAS peak positions.

MAS peak shapes in slices of the 2D spectra were also simulated as described in the experimental section. For example, the slice projected from -34.5 to -36.5 ppm in the ω_1 dimension (which contains two distinct sites) is shown in Figure 4.6. The simulated spectrum agrees well with all singularities appearing in the ω_2 dimension of the experimental data as expected. One possible limitation of this approach is distortion of the ω_2 dimension (MAS) peak shape due to non-uniform excitation of nuclei in crystallites with different orientation, but we do not expect this problem to be severe in this case. Results of simulations are shown in Table 4.4. The fit allows assignment of at least five features in the spectra to particular crystallographic sites, based on published single crystal data (Table 4.4).

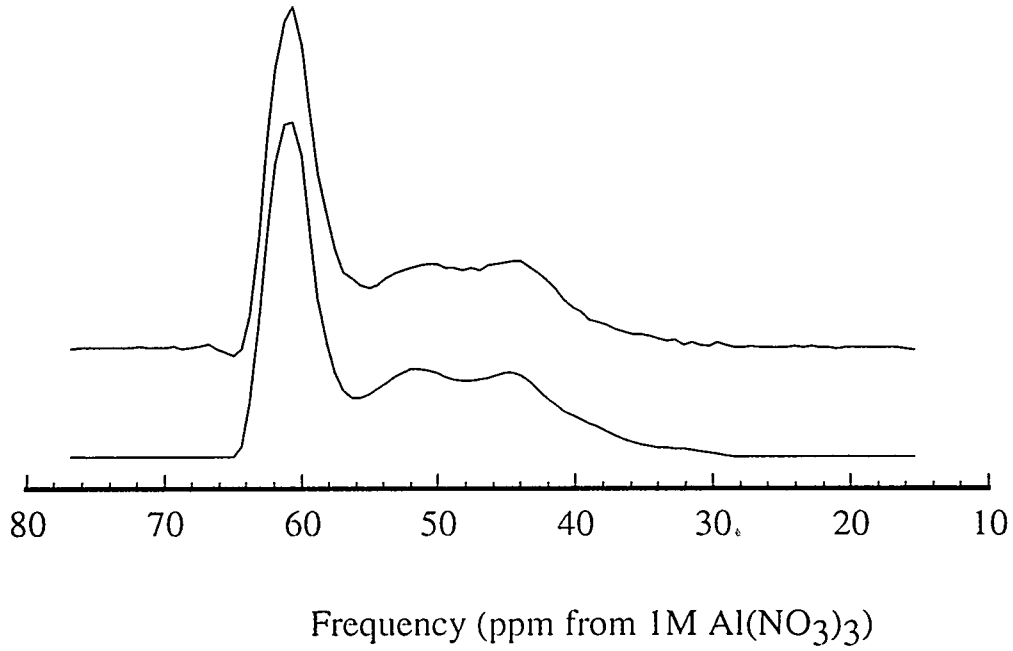

Figure 4.6: MAS Projection from -34.5 to -36.5 ppm in the isotropic dimension of the 11.7 T 3QMAS spectrum of anorthite. The simulation of this slice was fit and the parameters are those for peaks 1 and 2 as shown in Table 4.4.

A sixth feature, at the low frequency side in ω_1, can be simulated with parameters that are closest to those expected for the 0zi0 site, but could probably also be attributed to 0z00 (C_Q= 7.4 MHz) or to m000 (C_Q= 6.3 MHz). In fact, the whole tail of the spectrum in this region could well be comprised of poorly resolved signal from the three peaks with largest C_Q. As noted above for kyanite, peaks for sites with relatively large C_Q are expected to have reduced intensities as well as greater width in the ω_2 dimension, and thus are expected to be relatively difficult to observe with 3QMAS. The broad feature on the high frequency (ω_1) side of the tallest peak is also likely to be due to an unresolved peak, again possibly one of the unassigned peaks with large C_Q. In general, the agreement between the results for δ_{iso} and P_Q of the two approaches to assigning spectral features is excellent.

The estimated isotropic chemical shifts for the five relatively well-constrained sites are plotted in Figure 4.7 as a function of the mean intertetrahedral (Si-O-

Powder Results						
Peak	δ^{obs}_{3QMAS}(ppm)	δ^{pred}_{3QMAS}(ppm)	δ_{iso} (ppm)	C_Q(MHz)	η_Q	P_Q(MHz)
1	-35.3	-37.2	60.6	5.76	0.45	5.95
2	-35.9	-35.8	63.6	2.66	0.53	2.78
3	-37.3	-37.9	64.7	4.39	0.51	4.58
4	-39.1	-39.0	65.6	4.87	0.62	5.17
5	-42.2	-40.3	66.3	6.58	0.70	7.10
6	-44.0	-45.0	66.2	8.19	0.65	8.75

Single Crystal Results and Assignments					
	Single Crystal				
Peak	C_Q(MHz)	η_Q	P_Q (MHz)	site	mean angle
1	5.5	0.42	5.7	$m0i0$	145.4°
2	2.6	0.66	2.8	$mzi0$	137.9°
3	4.4	0.53	4.6	0000	138.0°
4	4.9	0.75	5.3	$mz00$	133.5°
5	6.8	0.65	7.3	$00i0$	131.1°
6	8.5	0.66	9.1	$0zi0$	132.0°

Table 4.4: Results from fitting the MAS projections (slices) out of the 3QMAS NMR spectrum at 11.7T for crystalline anorthite, compared with previous results from single crystal NMR [122] and with mean Si-O-Al bond angles from the x-ray diffraction structure. Uncertainties in fitted C_Q values are about 0.5MHz; in η_Q about 0.2, and in δ_{iso} about 1 to 2 ppm.

Al) angle. As expected from previous MAS NMR studies of both ^{29}Si and ^{27}Al in framework aluminosilicates, δ_{iso} decreases systematically with increasing mean angle. The 3QMAS data fall close to a line previously fitted to data from ordered phases, confirming the accuracy of the new data and of the site assignments. An earlier fit that included data for disordered minerals as well agrees even more closely with the anorthite data. This agreement may be fortuitous, in that bond angle calculations for disordered crystals are based on average long range structure, and thus may be distorted by the lack of data on true local bonding geometry.

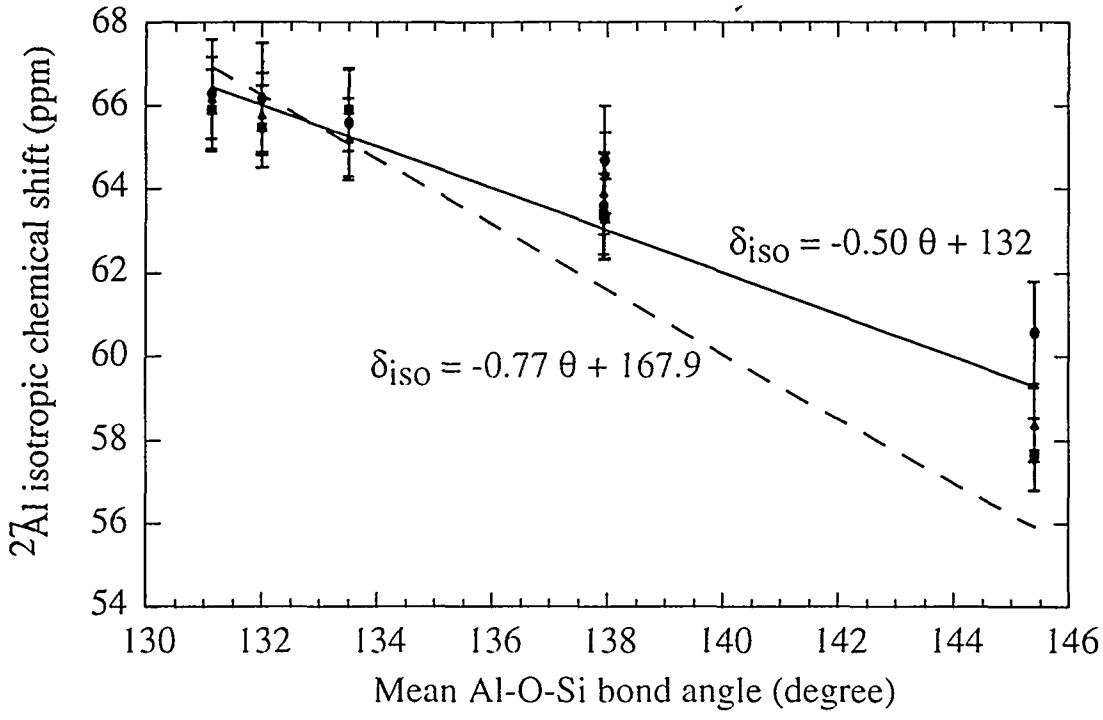

Figure 4.7: Isotropic chemical shifts for anorthite, derived from 3QMAS data, plotted against the mean Si-O-Al angle (θ) at each site. Only six sites are plotted, as data for remaining two are not well constrained by the spectra. Solid circles: results from simulations of slices in 11.7 T spectrum; solid triangles: results from 2D peak positions at 11.7 T; solid squares: results from 2D peak positions at 9.4 T. Solid line is a fit to data for a variety of aluminosilicates (both ordered and disordered) with δ = -0.50θ + 132; dashed line is a fit to data for ordered structures only, with δ = -0.77θ + 167.9 .

4.3.4 Anorthite ($CaAl_2Si_2O_8$) Glass

The 3QMAS spectrum for the glass of anorthite composition is shown in Figure 4.8. As expected from the MAS spectrum, it is broad and unresolved. The peak maximum and the center of mass are shifted by roughly 5 ppm from those of the crystal in both dimensions, suggesting a decrease in the mean chemical shift and/or an increase in the mean C_Q. The much greater overall width is not surprising in light of the disorder in the glass.

In MAS spectra of glasses in which Al is expected to be four-coordinated by oxygen (as in this composition), there is often significant spectral intensity in the

region of isotropic chemical shifts for five- and six-coordinated Al. In the absence of clear, discrete peaks in such spectra, it is generally assumed that such low-frequency tails are the result of second-order quadrupolar broadening. (This is supported by the narrowness of satellite transition sidebands in MAS spectra.) The 2D 3QMAS spectrum confirms this conclusion strongly: in comparison with clearly separated features for AlO_5 and AlO_6 groups as seen in the glass described next (Figure 4.9), there is no detectable intensity at these positions in the $CaAl_2Si_2O_8$ glass. On the other hand, the 2D shapes of the AlO_4 peaks in both glasses are surprisingly similar, perhaps suggesting similar ranges of δ_{iso} and C_Q.

4.3.5 Magnesium Aluminoborate Glass

This material was chosen because it contains sub-equal concentrations of four, five-, and six-coordinated Al, which are clearly seen as partially resolved peaks in ^{27}Al MAS NMR spectra. The 3QMAS spectrum is shown in Figure 4.9, and has three well-separated peaks that can be assigned to the three coordinations. The lack of significant overlap of the 2D peaks indicates that this approach may be very useful for detecting (or excluding) the presence of relatively small concentrations of the higher coordination states, whose presence is likely to be ambiguous in MAS spectra. Estimates of isotropic chemical shifts and quadrupolar products P_Q for these peaks can be made by measuring the positions of the peak maxima in both dimensions as above. For the AlO_6, AlO_5, and AlO_4 peaks respectively, we obtain 4, 31, and 63 ppm for δ_{iso} and 2, 3, and 5 MHz for C_Q. These results are complicated by the likelihood of overlap of signal from sites with varying parameters within each major peak, and uncertainties are at least 2 ppm and 0.5 to 1.0 MHz. The relative population of the above three environments obtained from the total projection of the 2D spectrum is about 1: 2 : 6. As shown before for the kyanite sample, however, the triple quantum

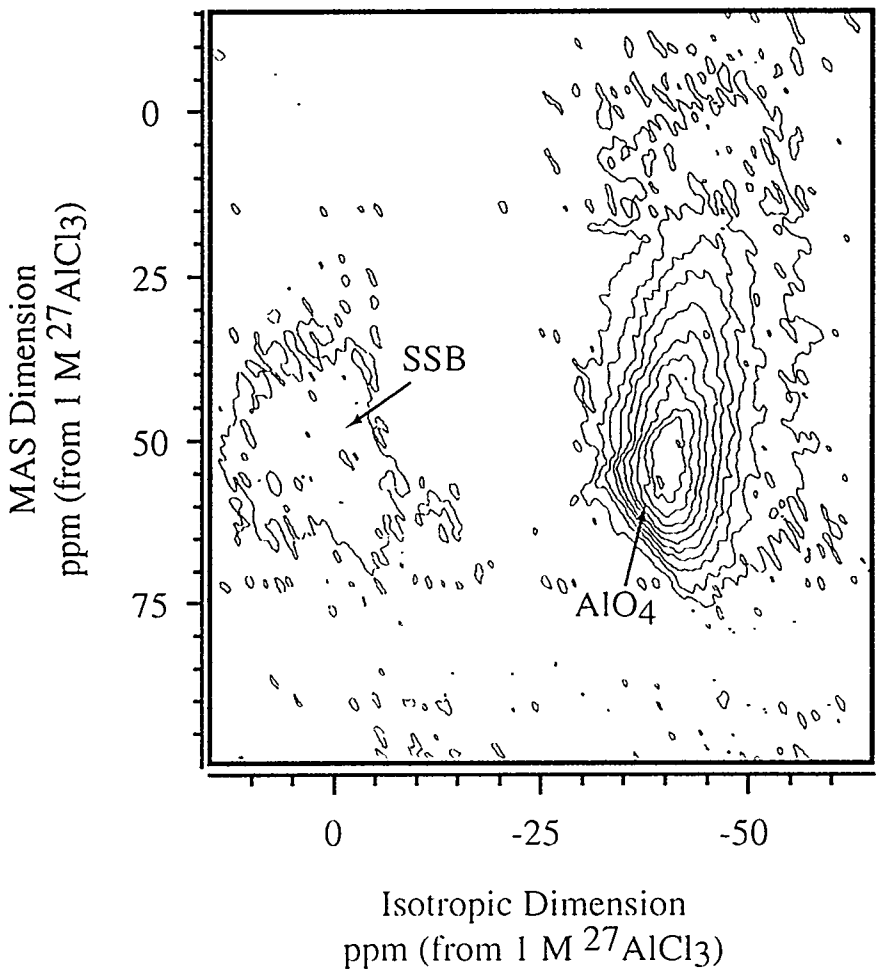

Figure 4.8: Contour plot of ^{27}Al 3QMAS NMR spectrum for $CaAl_2Si_2O_8$ (anorthite composition) glass at 11.7 T. The peak assignable to AlO_4 sites is labeled. Note the absence of peaks at the AlO_5 and AlO_6 regions seen in Figure 4.9. Low-intensity feature to left of main peak is a spinning sideband (SSB).

excitation efficiency for Al sites systematically decreases with increasing P_Q. Thus, the intensity observed for the AlO_4 peak is likely to be underestimated relative to the others.

The 2D spectrum is consistent with ranges of chemical shifts and coupling constants known from crystalline materials. AlO_6 sites generally have δ_{iso} between 1 and 15 ppm and C_Q between 1 and 10 MHz. This would result in 3QMAS peak positions of -1 to -30 ppm in the isotropic dimension and -50 to 12 ppm in the MAS dimension. Values of δ_{iso} for AlO_5 sites typically fall between 30 and 40 ppm, with C_Q between 3 and 10 MHz, giving 3QMAS peak positions ranging from -18 to -40 ppm in the isotropic dimension and -30 to 30 ppm in the MAS dimension. Finally, AlO_4 sites typically have δ_{iso} between 55 and 88 ppm and C_Q between 1 and 10 MHz, resulting in 3QMAS peak positions from -30 to -60 ppm in the isotropic dimension and 0 to 80 ppm in the MAS dimension. Note that in Figure 4.9, each of the labeled peaks falls neatly in the center of the corresponding regions. For the AlO_4 peak we also fitted slices along the ω_2 dimension, as was done for the crystalline phases. Again, for a disordered material results from this procedure are non-unique because each slice contains unresolved intensity from sites with ranges in chemical shift and C_Q. However, this approach does give some estimate of the range of parameters present, about 62 to 75 ppm for δ_{iso} and 4 to 6.5 MHz for C_Q.

4.3.6 Goosecreekite

Goosecreekite is a natural zeolite whose structure is still somewhat controversial. Earlier studies showed that there is only one tetrahedral aluminum site in this zeolite. A recent refinement of the structure, however, showed that two slightly different aluminum sites exist. The MAS spectrum of this sample shows however, only one peak. In this respect, MQMAS would be an ideal technique to resolve this structural

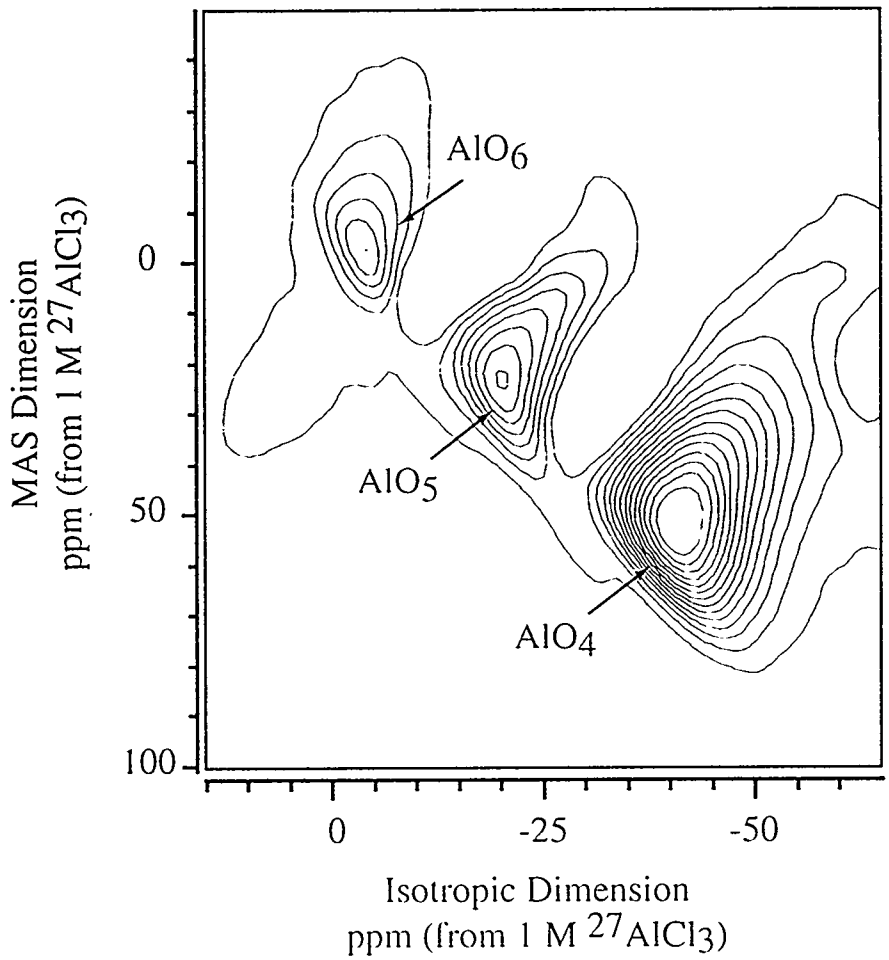

Figure 4.9: Contour plot of ^{27}Al 3QMAS NMR spectrum for a glass of composition 40 mole% MgO, 40 mole% B_2O_3, 20 mole% Al_2O_3. Peaks assignable to AlO_6, AlO_5, and AlO_4 groups are labeled.

problem.

Figure 4.10a shows the ^{27}Al 3QMAS spectrum of goosecreekite taken at 11.7T. The 1D 3QMAS spectrum has only one Gaussian peak (1ppm, FWHM), which is narrower than the MAS spectrum (5ppm, FWHM). The two-dimensional spectrum has already resolved some structures. As one can see, the low frequency side of the isotropic dimension corresponds to a larger quadrupolar coupling constant, and thus a broader MAS dimension. Even though the spectrum can be interpreted as two overlapping peaks with slightly different chemical shifts and quadrupolar coupling constants, the assignment is not unique.

The 5QMAS spectrum in Figure 4.10b, however, shows clearly that there are two distinct aluminum sites in this zeolite. The observed frequency in MAS and 5QMAS can be described by

$$\delta^{MAS} = \delta_{iso} + \delta^{2Q}_{iso} \tag{4.17}$$

$$\delta^{5QMAS} = \frac{85}{37}\delta_{iso} - \frac{50}{37}\delta^{2Q}_{iso}. \tag{4.18}$$

Using the shifts in the single-quantum and multiple-quantum dimensions, isotropic shifts and quadrupolar coupling constants for both sites can be extracted, using the strategy developed at the beginning of this chapter. The results are listed in Table 4.5.

site	δ^{MAS}(ppm)	δ^{3QMAS}(ppm)	δ^{5QMAS}(ppm)	δ_{iso}(ppm)	P_Q(MHz)
1	55.9	-33.8	137.5	58.4	2.7
2	55.2	-32.8	141.7	59.3	3.4

Table 4.5: Isotropic chemical shifts and quadrupolar coupling products for goosecreekite.

The use of quintuple-quantum coherence to enhance the resolution of ^{27}Al spectra was well-studied by Amoureux in a series of aluminum-phosphate zeolites [79].

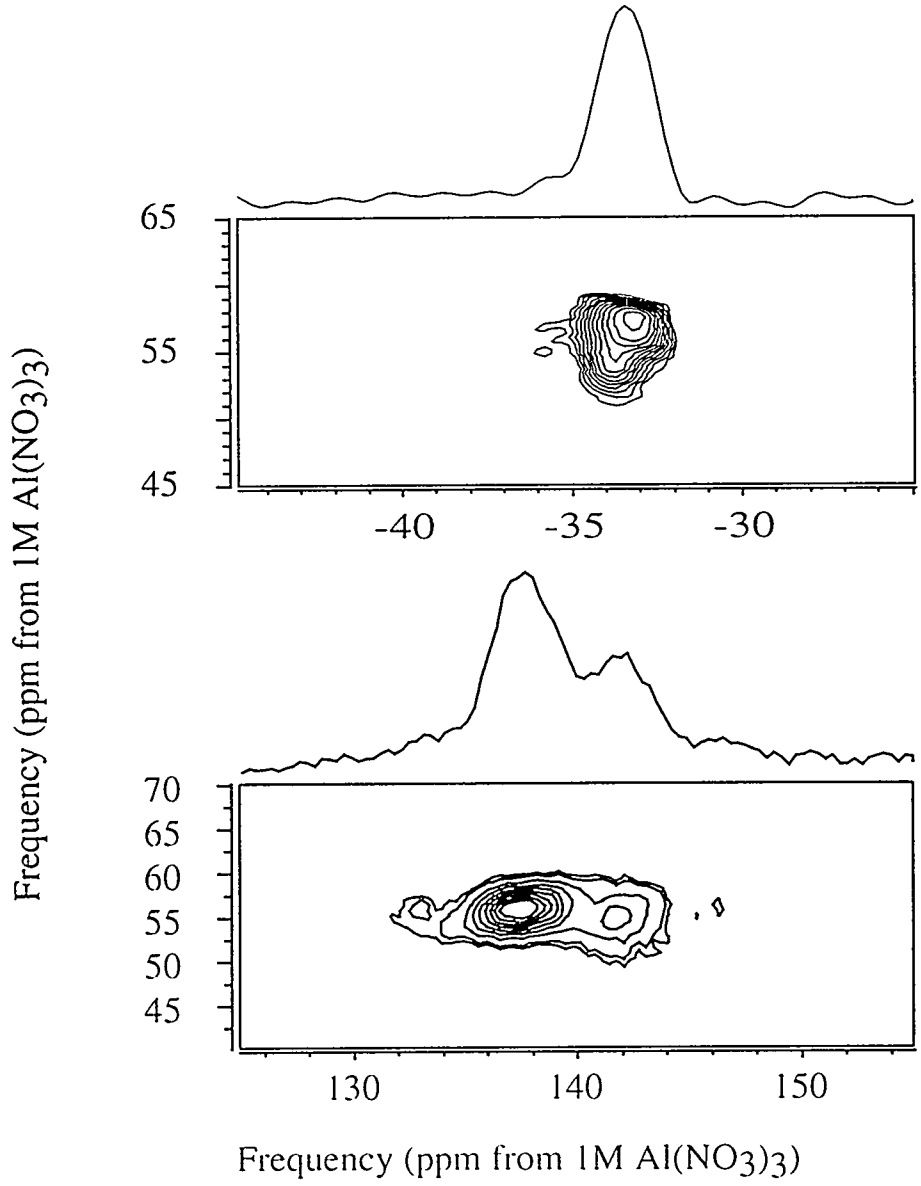

Figure 4.10: 11.7T 3QMAS(b) and 5QMAS(a) spectra of goosecreekite. Notice that even the 3QMAS spectrum resolves two sites.

However, in all of the samples he studied and our goosecreekite sample, the quadrupolar coupling constants are relatively small. The question of excitation for large coupling constants is a future problem in the utilization of this higher-order multiple-quantum coherence.

4.4 ^{17}O 3QMAS

Before concluding this chapter, I will include some initial results on the application of 3QMAS to the study of oxygen sites in silicate crystals. Oxygen is the most important element in various types of materials and has been extensively studied by MAS and by DAS [47, 81, 95, 75, 96, 97, 100, 101, 123, 124, 125]. Because of its low resonance frequency and low natural abundance, isotopic enrichment is often needed in most of the studies.

Oxygen sites in silicate and aluminosilicate materials are roughly classified into two types: the bridging and the non-bridging oxygens. The bridging oxygen connects two framework atoms (silicon or aluminum), whereas the non-bridging oxygen has charge compensating cations (often alkaline or alkaline earth cations) as nearest neighbors. The quadrupolar coupling constants for the bridging oxygens range from 4-7MHz, which are larger than those for the non-bridging oxygens (2.5-3.5MHz). This large difference in quadrupolar coupling constants induces different quadrupolar shifts that the bridging and non-bridging oxygens are at least partially separated in a DAS or MQMAS spectrum.

Figure 4.11 shows the 3QMAS spectra of two minerals larnite (Ca_2SiO_4) and forsterite(Mg_2SiO_4). Corresponding DAS spectra revealed 4 peaks for larnite, and 3 sites for forsterite [75]. The 3QMAS spectra of larnite gives only two resolved peaks. The three forsterite peaks are however, all resolved. In both samples, only non-bridging oxygens exist so all of the sites are expected to be excited. For another

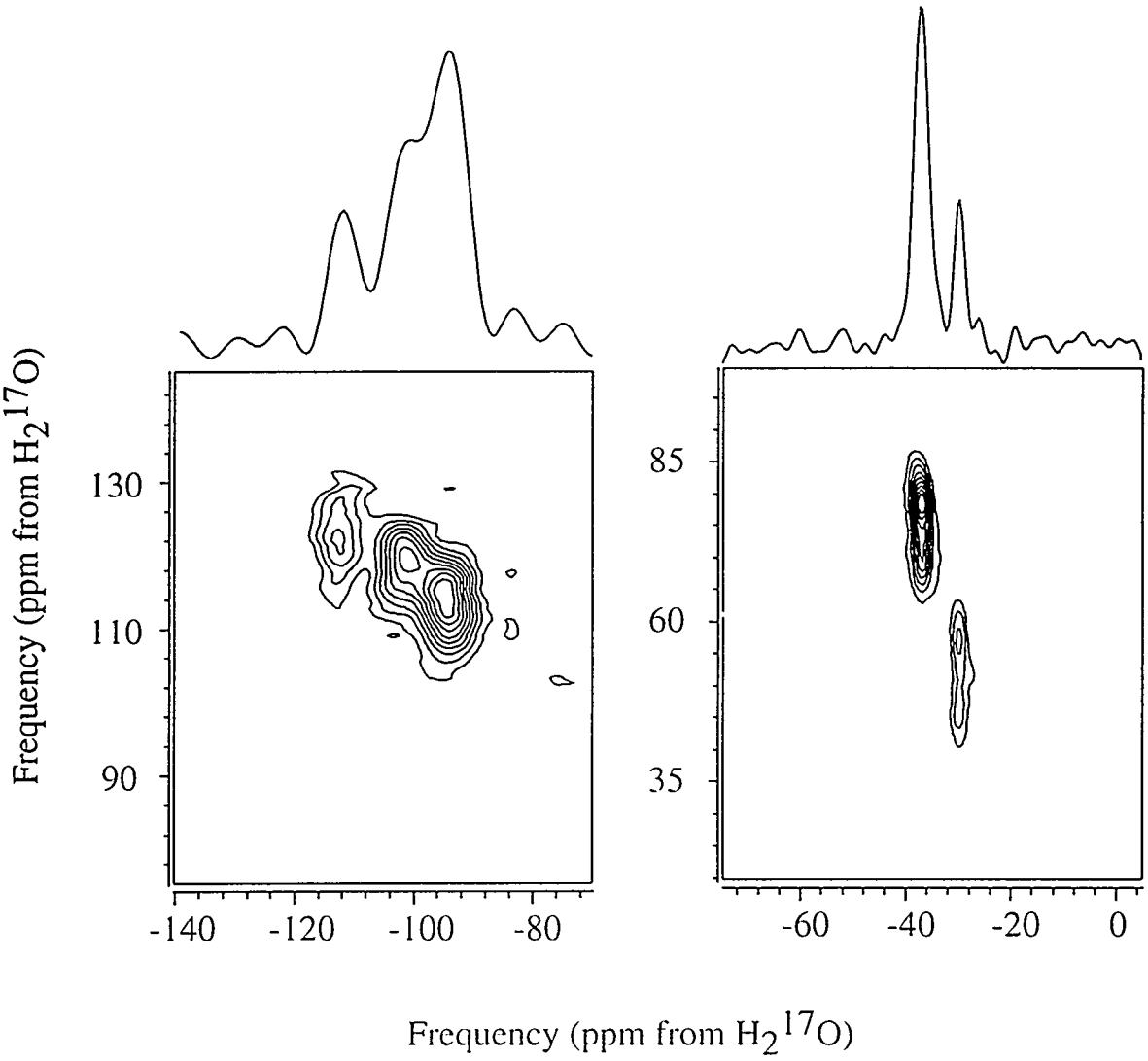

Figure 4.11: 11.7T ^{17}O 3QMAS of larnite (left) and forsterite (right).

sample enstatite, where bridging oxygen sites also exist, we were not able to excite the bridging oxygens using a relatively low power (30-40kHz). However, 3QMAS experiments on bridging oxygens have been performed in many groups, and their results suggest that such experiments are feasible when the enrichment level is high (20-40%) and when the spin-lattice relaxation time is short (less than 1 second) [56, 116, 126, 127]. More importantly, oxygen sites in Si-O-Si and Si-O-Al linkages are often well-separated. It is also interesting that when T_1 is short, 3QMAS actually gives better S/N than DAS. Based on these preliminary works, it is quite promising to use 3QMAS for the study of a series of technologically important materials, including multi-component oxides, zeolites and supported oxide catalysts.

4.5 Conclusions

Multiple-quantum magic-angle spinning (MQMAS) spectra can provide enhanced resolution for ^{27}Al in aluminosilicate and aluminate materials, both crystalline and amorphous, although resolution in the isotropic dimension may still be limited by disorder and other less well understood mechanisms of residual broadening. Additional information on NMR parameters may be obtainable because the two dimensional spectra provide some separation of chemical shift and quadrupolar effects, both from simple peak position data and from fitting of MAS peak shapes in slices of the spectra. MQMAS signal can be obtained even from sites with quadrupolar coupling constants as large as 9MHz, but intensity is systematically reduced with increasing C_Q. We have derived new data for isotropic chemical shifts for five or six of the eight sites in crystalline anorthite, which agree reasonably well with previous correlation with structure. In glasses, the separation between peaks for Al in different coordination states is excellent, and provides a new and sensitive test for the presence of AlO_5 and AlO_6 sites in glasses dominated by AlO_4, although absolute quantification may

remain difficult.

Chapter 5

Correlation Spectroscopy with MQMAS

Up to now, we have only considered the NMR spectra under single-spin interactions (chemical shift and/or quadrupolar interactions). To interpret NMR spectra of networks of spins, connectivity among different spins is to be established. Heteronuclear correlation (HETCOR) as a means of mapping out the spin topology, is proved powerful to correlate the chemical shifts of directly coupled spins and elucidate the structure of heteronuclear coupling networks [5]. HETCOR in the solid-state has been limited to pairs of spin-$\frac{1}{2}$ nuclei in the past, due to the lack of high-resolution for quadrupolar nuclei. With the development of DAS and MQMAS, we demonstrate in this chapter that true high-resolution HETCOR spectra are equally obtainable for quadrupolar nuclei.

5.1 Heteronuclear Correlation (HETCOR)

Heteronuclear correlation spectroscopy is a routine method in liquid-state NMR and represents only a special experiment among a series of two-dimensional correlation methods [5, 8]. The key of the experiment is coherence transfer between two types of coupled heterospins. In weakly coupled systems, coherence transfer between two spins occurs only if there is a non-varnishing dipolar- or J-coupling between the spin pair. Since the magnitude of dipolar and J-couplings is inversely proportional to the third power of the distance between the two spins, only those spins that are in spatial proximity show significant couplings and induce coherence transfer. As a result, the appearance of cross-peaks in 2D HETCOR spectra serves as a proof of spatial proximity between the coupling partners. The spectrum is thus a visu-

alization of the topology of the spin system in a direct and informative way. This detailed information about the spin system is often essential for the determination of the structure of large molecules [128] and complicated materials [129].

It is worth describing cross-polarization (CP) [13, 130] here before we go into any details about HETCOR. Cross-polarization is the most widely used technique in the solid-state to achieve heteronuclear coherence transfer and signal enhancement. Dipolar coupling, whose magnitude often exceeds that of the J-coupling by an order of magnitude, is the basis of the coherence transfer process. The simplest CP scheme, as shown in Figure 5.1, starts by applying a $\frac{\pi}{2}$ pulse along the rotating frame y-

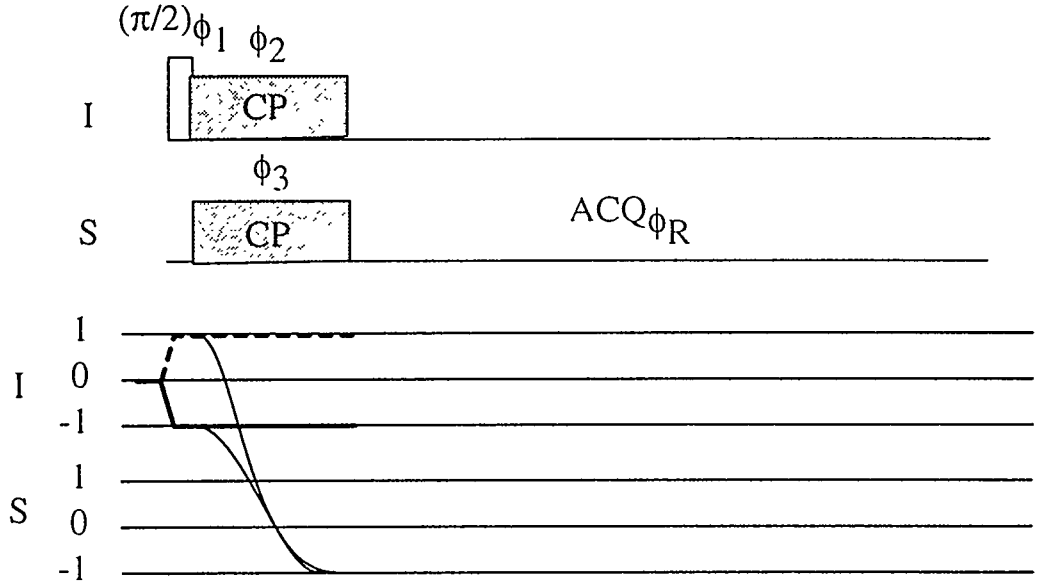

Figure 5.1: Cross-Polarization between two spins I and S.

axis on one type of the spins (usually the more abundant spin type that serves as magnetization source and is termed as I-spin). This pulse generates single-quantum coherence on the I-spins, which is subsequently locked along the rotating frame x-axis by applying a long pulse along the x-axis. If a long pulse is also applied to the S-spins (the less abundant spin type that borrows magnetization from I-spins), and

the magnitude of the RF field fulfills the Hartmann-Hahn condition

$$\gamma_I B_{1I} = \gamma_S B_{1S}, \tag{5.1}$$

the precession frequencies of the two types of spins are equal and the flip-flop terms in the dipolar Hamiltonian are now zero-energy process. This greatly enhances the energy transfer process between two types of spins and the net result is often that the rare spin (S-spin) magnetization is amplified significantly. For instance, When cross-polarization (CP) is applied to a ^{1}H–^{13}C system, a gain of a factor of 3–4 in ^{13}C polarization can be achieved. The signal to noise (S/N) ratio is often boosted by more than an order of magnitude, since ^{1}H has shorter T_1 than ^{13}C that fast repetition can be used with CP. Currently, cross-polarization magic-angle spinning (CPMAS), which combines cross-polarization with magic-angle spinning, is the single most routine experiment performed in most solid-state NMR laboratories.

Cross-polarization between two quadrupolar nuclei or a spin-$\frac{1}{2}$ and a quadrupolar nuclei suffers a number of difficulties. First, the rotating frame Hamiltonian is dominated by the large first-order quadrupolar interaction, which is highly anisotropic that the quadrupolar coupling constant depends on the crystalline orientations.

$$C_Q^{eff} = \frac{C_Q}{2}(3\cos^2\beta^Q - 1 + \eta_Q \sin^2\beta^Q \cos 2\alpha^Q) \tag{5.2}$$

Here, C_Q^{eff} is the effective quadrupolar coupling constant and $(\alpha^Q, \beta^Q, \gamma^Q)$ are the Euler angles between the quadrupolar principal axis frame (PAS) and the lab frame. The differences in the quadrupolar coupling constants complicate the Hartmann-Hahn matching condition for cross-polarization [69, 70]. For instance, when $C_Q^{eff} \ll \omega_1$, the Hartmann-Hahn condition is the same as that of a spin-$\frac{1}{2}$ pair.

$$\gamma_I B_{1I} = \gamma_S B_{1S} \tag{5.3}$$

However, when $C_Q^{eff} \gg \omega_1$, the Hartmann-Hahn condition needs to be modified to include a constant factor dependent on the spin quantum number of the quadrupolar

nucleus.

$$\gamma_I B_{1I} = (S + \frac{1}{2})\gamma_S B_{1S} \tag{5.4}$$

In a powder sample, it is often the case that neither of the above two conditions are fulfilled and the effective quadrupolar coupling constant C_Q^{eff} is comparable to the RF strength (ω_1). The spin dynamics is far more complicated (see the discussions in chapter 3 on spin locking) that no single intuitive formulus exists for the whole sample.

The matching condition in a rotating sample is further complicated by two facts. First, the dipolar interactions that mediate the CP transfer are averaged to zero over a rotor period (the instantaneous dipolar coupling, instead, still exists and induces coherence transfer), reducing the efficiency of cross-polarization (CP). Second, the effective coupling constant for a quadrupolar spin is no longer constant and fluctuates periodically. As a result, there exists no unique matching condition that all of the spins with different crystalline orientations fulfill. This suggests that CP spectra involving quadrupolar nuclei are often not quantitative. Nevertheless, the fact that only spin pairs with non-varnishing dipolar couplings give rise to coherence transfer and therefore cross-peaks in 2D HETCOR spectra is still valid. This means that HETCOR experiment between quadrupolar and spin-$\frac{1}{2}$ nuclei would in principle, provides similar information on the spin coupling network compared to the correlation for spin-$\frac{1}{2}$ pairs.

A simple HETCOR sequence is constructed by incorporating the CP sequence with a simple one pulse experiment on S-spins. As shown in Figure 5.2, a $\frac{\pi}{2}$ pulse applied to the I-spins brings the I-spin magnetization into the x-y plane of the laboratory frame. The magnetization evolves under the I-spin Hamiltonian for a variable time t_1, during which the I-spin resonance frequencies are encoded into the resultant magnetization. Through cross-polarization, this magnetization on the I-spin is

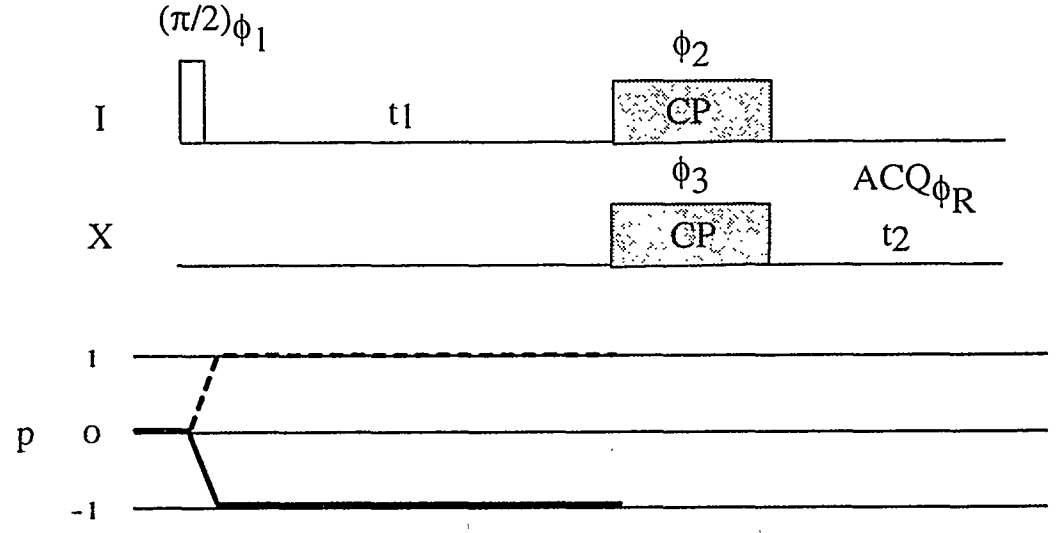

Figure 5.2: Pulse sequence and coherence pathway for a traditional HETCOR experiment. Notice that only the coherence pathway on *I* spin is shown.

transferred into S-spin magnetization, which continues to evolve under the S-spin Hamiltonian and is recorded with quadrature detection. The two frequency domains after two-dimensional Fourier transformation are the I- and S-spin chemical shifts, with cross-peaks appearing between the resonances of dipolar coupled heteronuclear spins. Magic-angle spinning is usually applied during the whole experiment to enhance the spectral resolution in both dimensions.

5.2 HETCOR with Quadrupoles

Figure 5.3 is an example of regular two-dimensional HETCOR spectrum between a spin-$\frac{1}{2}$ and a quadrupolar nucleus. The $^{23}Na/^{31}P$ HETCOR spectrum is taken on sodium trimetaphosphate ($Na_3P_3O_9$), which was prepared by heating NaH_2PO_4 at 550° for 3 hours and slowly cooling the sample down to room temperature [43]. X-ray diffraction (XRD) shows that the sample is well-crystallized and of the correct phase. MAS NMR spectra on ^{23}Na and ^{31}P confirm the conclusion that there are two distinct types of ^{23}Na and ^{31}P sites in this compound. The two phosphorus peaks, -18.7 and

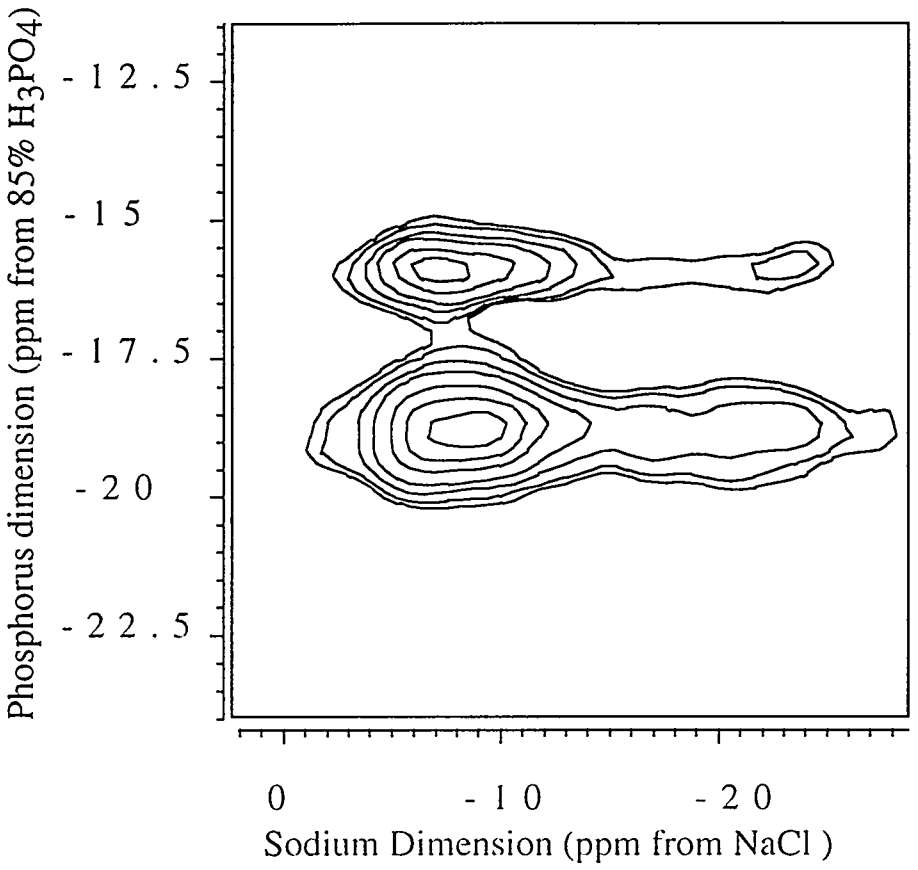

Figure 5.3: A conventional two-dimensional ^{23}Na-^{31}P HETCOR spectrum of $Na_3P_3O_9$ collected at 11.7T. The sample is spinning at 5kHz and the contact time is 5msec.

-15.5 ppm away from a 85% H_3PO_4 standard (0.0ppm), are the general and mirror sites respectively. The ^{23}Na spectrum, broadened to about 4kHz by second-order quadrupolar interaction, can be deconvoluted into two quadrupolar powder patterns, with isotropic chemical shifts at -6.2 and -22.1 ppm with respect to solid NaCl at 0.0 ppm.

The existence of four cross-peaks between the two ^{31}P and ^{23}Na resonances suggests that each ^{31}P site is near to both ^{23}Na sites. Similarly, each ^{23}Na site is also near to both ^{31}P sites. This qualitatively agrees to the crystal structure of $Na_3P_3O_9$ that all of the sodium and phosphorus positions are interconnected (through oxygen atoms).

Notice that the HETCOR experiment is performed by transferring coherence from the lower gyromagnetic ratio quadrupolar nucleus (^{23}Na) to the higher gyromagnetic ratio spin-$\frac{1}{2}$ nucleus (^{31}P). This is the reversed case of most CP experiments. For cross-polarization between spin-$\frac{1}{2}$ and quadrupolar nuclei, unless ^{1}H or ^{19}F is involved or the quadrupolar nucleus is of very low abundance, CP from spin-$\frac{1}{2}$ nucleus to quadrupolar nucleus does not enhance the signal to noise ratio [42, 70, 131, 132]. Two reasons account for this anomaly: (1), CP between quadrupolar and spin-$\frac{1}{2}$ nuclei is often inefficient; (2), spin-$\frac{1}{2}$ nuclei often have long spin-lattice relaxation times (T_1) which preclude rapid signal averaging. Therefore CP is better used as a spectral editing method, rather than a signal-enhancing technique. On the contrary, like in the current case, CP from quadrupolar spins enhances sensitivity of the spin-$\frac{1}{2}$ nucleus.

Due to the complex spin dynamics during cross-polarization, it is not easy to retrieve exact distance information from the HETCOR experiment. Also, the resolution in the quadrupolar dimension is low. The resolution problem is less severe for $Na_3P_3O_9$, where the two sodium sites are separated by their chemical shifts. For more interesting materials with complex structures and overlapping resonances, it is important to have liquid-like resolution in the quadrupolar dimension. As shown in the next section, high-resolution is achievable for quadrupoles in both dimensions of a HETCOR spectrum, when DAS or MQMAS is applied to the regular HETCOR experiment.

5.3 High-Resolution HETCOR

True high-resolution correlation between quadrupolar and spin-$\frac{1}{2}$ nuclei can be achieved by correlating the dynamic-angle spinning (DAS) or multiple-quantum magic-angle spinning (MQMAS) spectrum of a quadrupolar nucleus with the magic-angle

spinning (MAS) spectrum of the nearby spin-$\frac{1}{2}$ nucleus. Like DAS and MQMAS, both approaches reconstruct the isotropic quadrupolar dimension by breaking up the t_1 evolution time into two parts. The anisotropic resonance frequency of each spin is rendered to have opposite signs during the two separated t_1 time periods of the evolution. When the ratio between the two times are well-selected, anisotropies arising from CSA and the second-order quadrupolar interaction are removed and an echo is formed at the end of t_1 evolution.

In Figure 5.4, we compare the experimental schemes and coherence pathways of DAS/HETCOR and MQMAS/HETCOR. For DAS/HETCOR, a DAS experiment is performed first on ^{23}Na before the sodium magnetization is transferred to ^{31}P through cross-polarization. The experiment proposed by Jarvi et al. chose the (79.19°,37.38°) angle pair with $k = 1$. The sample stays at 79.19° and 37.38° for an equal amount of time ($\frac{t_1}{2}$), which creates a DAS echo at the end of the t_1 period due to the refocusing of the second-order quadrupolar interaction. Cross-polarization is then performed at 0° to maximize the CP efficiency. This results in a second rotor axis reorientation that brings the spinner axis to the direction of the static field. After CP, another reorientation of the rotor axis is needed to allow data acquisition at the magic-angle. Including the final hop during recycle delay that brings the spinner axis back to 79.19°, a total of 4 hops are required for each single scan that takes about 120-150msec. Representative spectrum of DAS/HETCOR can be found in the paper by Jarvie and Mueller [43]. Notice that a static-coil hopping probe is a priori for this type of experiment, since pulsing at 0° is needed.

The number of hops in DAS/HETCOR can be decreased to 3 by choosing the $k = 5$ DAS angle pair. This however, still requires a hopping DAS probe. The MQMAS/HETCOR experiment, which does not involve reorientation of spinner axis, relieves the requirement of a static-coil hopping DAS probe. It starts by excit-

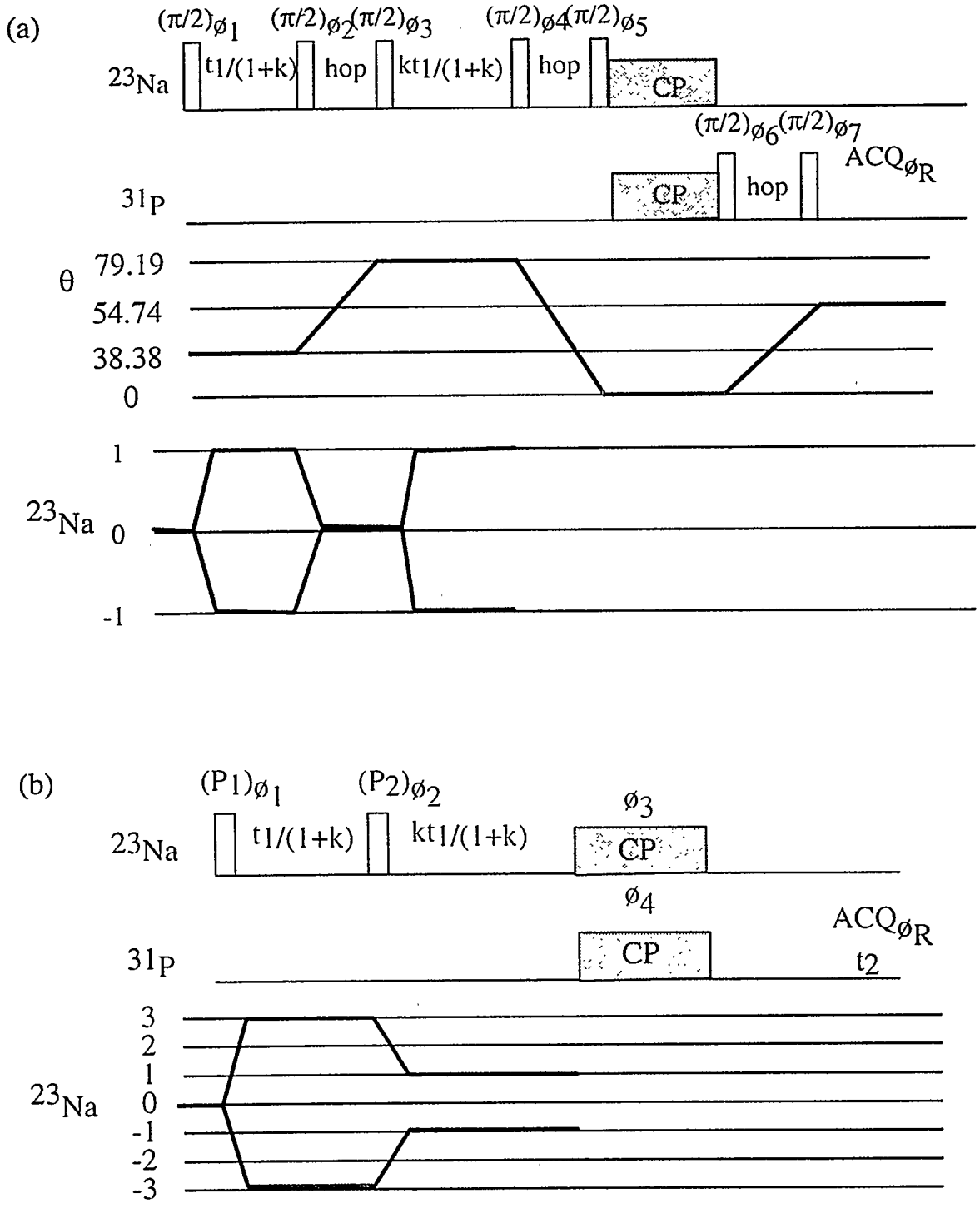

Figure 5.4: Comparison of DAS/HETCOR and MQMAS/HETCOR pulse sequences and coherence transfer pathways.

ing the triple-quantum coherence on ^{23}Na. As described in earlier chapters, the excitation is most efficiently performed by applying a single strong RF pulse near to the sodium resonance frequency. The triple-quantum coherence is then allowed to evolve for $\frac{t_1}{1+k}$ and then another strong pulse (reconversion pulse) transfers the triple-quantum coherence to single-quantum coherence, which evolves for $\frac{kt_1}{1+k}$ before cross-polarization is done at the magic-angle. The subsequent detection period is the same as in DAS/HETCOR.

The 96-step phase cycle for MQMAS/HETCOR is given in Table 5.1. Mirror image coherence transfer pathways are retained during the two separated t_1 period, leading to two-dimensional pure-absorption lineshapes. The phase cycle has incorporated CYCLOPS and spin-temperature alternation to remove possible artifacts due to imperfections of hardware setting. A separate dataset that shifts the phase of ϕ_3 by 90° is needed to allow for pure-absorption spectra.

	MQMAS/HETCOR cosine											
ϕ_1	0°	60°	120°	180°	240°	300°						
ϕ_2	0°	0°	0°	0°	0°	0°	90°	90°	90°	90°	90°	90°
	180°	180°	180°	180°	180°	180°	270°	270°	270°	270°	270°	270°
ϕ_3	0°											
ϕ_4	0°	0°	0°	0°	0°	0°	0°	0°	0°	0°	0°	0°
	0°	0°	0°	0°	0°	0°	0°	0°	0°	0°	0°	0°
	90°	90°	90°	90°	90°	90°	90°	90°	90°	90°	90°	90°
	90°	90°	90°	90°	90°	90°	90°	90°	90°	90°	90°	90°
	180°	180°	180°	180°	180°	180°	180°	180°	180°	180°	180°	180°
	180°	180°	180°	180°	180°	180°	180°	180°	180°	180°	180°	180°
	270°	270°	270°	270°	270°	270°	270°	270°	270°	270°	270°	270°
	270°	270°	270°	270°	270°	270°	270°	270°	270°	270°	270°	270°
ϕ_r	0°	180°	0°	180°	0°	180°	180°	0°	180°	0°	180°	0°
	90°	270°	90°	270°	90°	270°	270°	90°	270°	90°	270°	90°
	180°	0°	180°	0°	180°	0°	0°	180°	0°	180°	0°	180°
	270°	90°	270°	90°	270°	90°	90°	270°	90°	270°	90°	270°

Table 5.1: Phase cycles for MQMAS/HETCOR

The utility of the MQMAS/HETCOR experiment is well-demonstrated in Figure 5.5 on $Na_3P_3O_9$. Experimental conditions are chosen to closely mimick the regular HETCOR experiment (Figure 5.3). For example, the sample is spun at 5kHz in both cases, and the contact time is set to 5msec in both experiments. As expected, the ^{23}Na dimension contains two isotropic peaks (3ppm, FWHM) at -5.0 and -24 ppm. These numbers are different from those observed in DAS/HETCOR due to the different field strengths and scaling factors. Again, four distinct cross-peaks are observed, confirming the conclusion of a fully coupled $^{23}Na/^{31}P$ spin network. Analogous to the fact that DAS/HETCOR has many advantages over DAS, MQMAS/HETCOR has similar advantages over DAS/HETCOR. For example, the most important one is that technically, MQMAS/HETCOR is much simpler because dynamic-angle spinning probe is not a prerequisite. To perform CP at 0°, a static-coil DAS probe is required, which is not available currently from most NMR probe venders. As a comparison, our MQMAS/HETCOR experiment was done on a doubly-tuned MAS probe, which is available in most modern solid-state NMR labs.

The technical simplification of MQMAS also gives another advantage that makes MQMAS/HETCOR a preferred technique to study a wider range of zeolitic and glassy materials that contain nuclei with short spin-lattice relaxation times (for instance, ^{27}Al and ^{11}B). As an example, Chmelka et al. showed that regular $^{1}H/^{27}Al$ HETCOR experiment is able to discriminate acidic sites in zeolite catalysts. Incorporating MQMAS to this experiment is natural and would enhance the ^{27}Al dimension resolution by an order of magnitude. Another example shown by Amoureux recently demonstrates that MQMAS can be combined with CP for spectral editing [15]. In his study, the connectivity among the different ^{19}F and ^{27}Al sites are studied in aluminum phosphate zeolites. MQMAS/HETCOR in this case may lead to a direct mapping of the connectivity topology. More importantly, MQMAS/HETCOR with

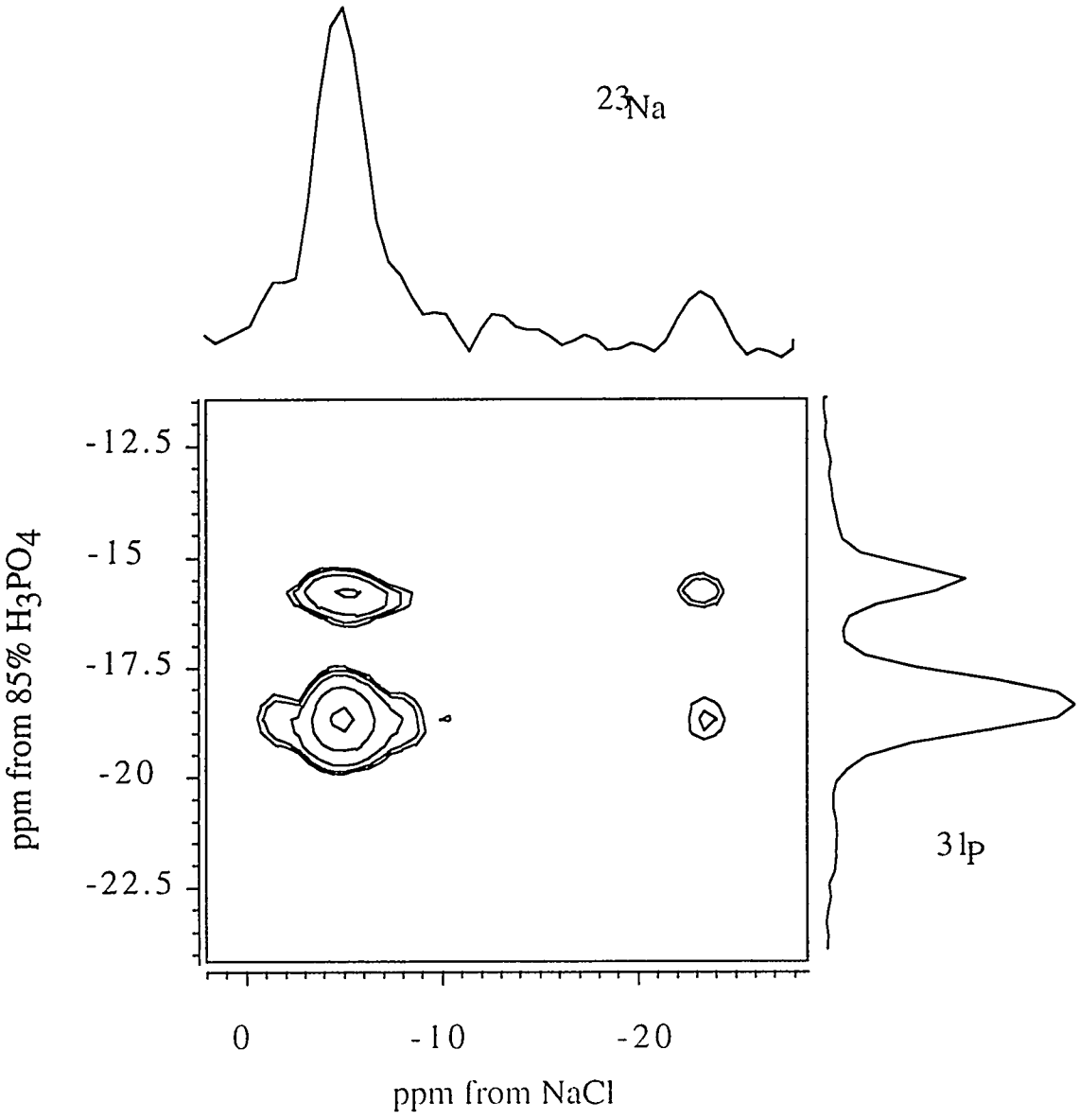

Figure 5.5: Two-dimensional ^{23}Na-^{31}P MQMAS/HETCOR spectrum of $Na_3P_3O_9$ collected at 11.7T. The sample is spinning at 5kHz and the contact time is 5msec.

$^{27}Al/^{29}Si$ spin pair can potentially be used to study a whole spectrum of minerals and zeolites. In all of these cases, DAS/HETCOR would fail due to short T_1 for ^{27}Al.

Another potential advantage of MQMAS/HETCOR experiment for spin-$\frac{3}{2}$ is that the resolution in the quadrupolar dimension may be better than that observed in the DAS/HETCOR experiment for two reasons: (1), the DAS linewidth for ^{23}Na is determined by homonuclear dipolar interaction, which is not averaged out efficiently in DAS and often gives larger linewidth than MQMAS. For example, the ^{23}Na linewidth in DAS/HETCOR is about 800Hz (FWHM), whereas that in the MQMAS/HETCOR spectrum is only 400Hz. (2), the scaling factors of the chemical and quadrupolar shifts in MQMAS is larger than 1 (or smaller than -1). This better resolution is crucial, for example, in differentiating sodium sits in sodium phosphate and silicate glasses [133].

The disadvantage of MQMAS/HETCOR is again associated with the inefficiency of excitation and reconversion pulses. Compared with the DAS/HETCOR spectrum (which is not quantitative either), the intensity of the low frequency ^{23}Na site is much lower than the site population expected from XRD. Even though simulations show that low frequency site with larger quadrupolar coupling constant has one-quarter of intensity of the other site due to different excitation and reconversion efficiencies, it is not clear how much of the discrepancy can be attributed to this effect. Cross-polarization, as discussed earlier, introduces extra problems that are hard to quantify. Because of this, MQMAS/HETCOR and DAS/HETCOR experiments should both be considered as qualitative, rather than quantitative.

It is worth noting that different multiple-quantum excitation and reconversion schemes can be combined with HETCOR to better quantify the MQMAS/HETCOR spectra. While this partially solves the quantification problem, it is very likely that the problem will still exist. Even though there is a scheme that claims quantitat-

ive MQMAS excitation and reconversion [63], the validity of it is still limited to high excitation power and small variations in the quadrupolar coupling constants for different sites.

5.4 Conclusion

In summary, high-resolution HETCOR spectra involving quadrupolar nuclei can be obtained by correlating DAS or MQMAS spectrum of the quadrupolar nucleus with the MAS spectrum of the spin-$\frac{1}{2}$. The two resultant techniques are complementary to each other that provide qualitative characterization of the spin coupling networks. These techniques would have direct application to sodium phosphate glasses, where the characterization of site distribution and connectivity network is essential to the understanding of local ordering in amorphous materials. With the new resolution and spectral editing capabilities, detailed inspection of local microstructure in various classes of technologically important materials is possible.

Chapter 6

Switching-Angle Spinning of Quadrupoles

One of the major goals in the other chapters of this thesis is to determine the isotropic chemical shift (δ_{iso}) and the quadrupolar coupling parameters (C_Q and η_Q). The anisotropic chemical shift interaction that a quadrupolar nucleus also experiences is only briefly discussed. The chemical shift anisotropy, however, like the quadrupolar interaction, contains valuable information about the local geometry around the nucleus and is the major structural probe for spin-$\frac{1}{2}$ nuclei. This chapter is concerned primarily with the extraction of the full chemical shift parameters and the relative orientation between the CSA tensor and the quadrupole tensor.

6.1 Overview

Study of coexistent interaction tensors by NMR can be dated back to the early sixties [134, 135]. There are at least two major reasons that such a study is crucial. First, the NMR spectra can not be well-understood or reproduced by theoretical calculations if only one of the interactions is assumed to be dominating; second, in the case of coexisting dipolar and chemical shift tensors, the dipolar tensor is often coaxial with the intermolecular vector. Knowing the relative orientation between the chemical shift and the dipolar tensors allows a direct mapping of the chemical shift tensor to the molecular frame [136]. In the case of coexisting chemical shift and quadrupolar tensors, mapping the quadrupolar tensor frame onto the chemical shift tensor frame may lead to a better picture of the relationship between the quadrupolar interaction and the molecular structure.

The most accurate method for the study of coexisting chemical shift and quad-

rupolar tensors is the single-crystal method [137]. By carefully reorienting the single crystal sample in the static magnetic field, the change of the NMR peaks is recorded and analyzed. Good agreement between experimental data and fittings can often be achieved. The method, while being accurate, is tedious and sometimes impossible since the growth of the single-crystal may be nontrivial.

Simulating the static NMR spectra is another approach that was used by Bray et al. in 1969 [134] and by Cheng et al. in 1990 [85] for the study of ^{51}V and ^{87}Rb, respectively. The simulation involves at least 8 parameters, and multiple-field or multiple-nuclear experiments are often required; thus, the technique is not very powerful, especially in cases where multiple sites exist in the sample. For example, the result obtained by Cheng et al. on $RbClO_4$ (one Rb site) is consistent with the DAS and MQMAS results; however, their results on Rb_2SO_4 and Rb_2CrO_4 (multiple sites) are much less accurate and are inconsistent with the data from high-resolution techniques [24].

Simulating the MAS spectra [138, 139] has the similar problem as simulating the static spectra. The advantage is, however, that some small interactions (for instance, dipolar coupling) may be averaged out by MAS and do not affect the NMR lineshape. This may be a disadvantage as well, since chemical shift interaction is also averaged and its effect on the spectra is only reflected by the sideband intensity.

The above two techniques, while being less accurate, are quite simple and straightforward. Another interesting approach is to simulate the whole MAS spectra, including the satellite transitions [140, 141]. This type of spectra often has enough information to constrain the simulation, and determination of very small chemical shift anisotropies has been reported. The experiment may, however, be difficult and requires well-calibrated hardware. Since the spectra may cover up to a 1MHz frequency range, a single experiment does not suffice to excite the whole spectral range. In this

case, multiple spectra are recorded with different carrier frequencies. The resultant spectra have to be scaled and combined carefully to give the final spectrum.

The major problem with the previous simulation method is that the spectra are not sensitive enough to small or intermediate chemical shift interaction. A natural extension is then to exploit a second dimension. This idea has been applied to the coexisting dipolar and chemical shift tensors, where a separated local field(SLF) NMR technique maps out both interactions and their relative orientation to each other in two separate frequency domains [8]. I would like to demonstrate in this chapter that it is equally possible to extract quadrupolar and chemical shift tensor orientation through a two-dimensional switching-angle spinning (SAS) experiment.

6.2 Theory

6.2.1 Coexisting Tensors

In this section, only the coexistence of chemical shift and quadrupolar tensors is considered, even though the basic theory is applicable to other coexisting tensors. As discussed in chapter two, the quadrupolar and chemical shift interactions are characterized by two and three parameters respectively. These parameters are C_Q and η_Q for quadrupolar interaction and $\delta_{iso}, \delta_{CS}$ and η_{CS} for CSA. These parameters are defined in the principal axis frame (PAS) of each interaction and the two frames are related to each other through a general rotation (Figure 6.1). We will assume that the three Euler angles between the two frames are ϕ, θ and ψ.

Calculating the powder NMR spectra under spinning condition involves an ensemble average over all the crystallites. We can specify each crystallite by giving the three Euler angles $(\alpha^Q, \beta^Q, \gamma^Q)$ between the quadrupolar PAS and the rotor frame. The frequency shift for this crystallite has contributions from the chemical shift in-

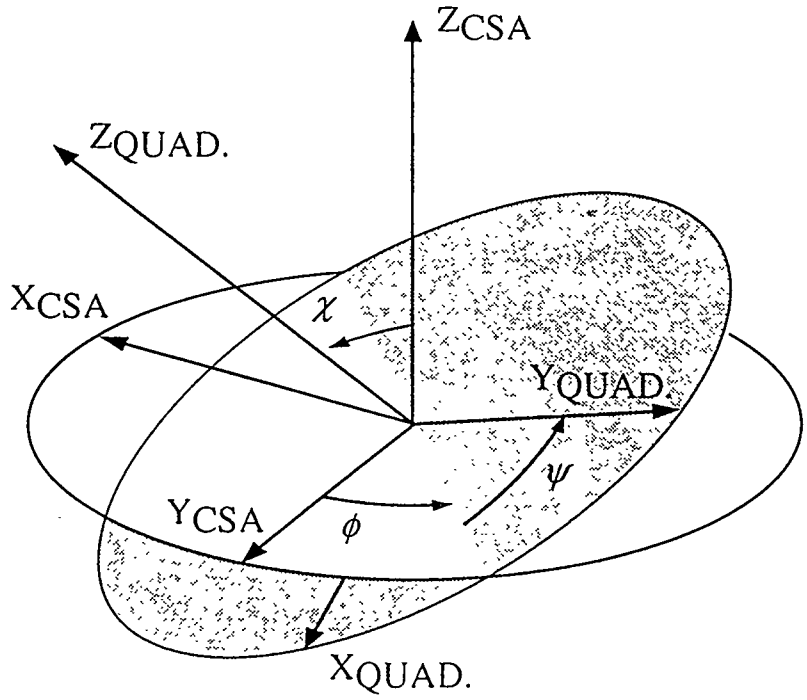

Figure 6.1: A schematic representation of the quadrupolar and chemical shift principle axis systems (PAS) with a relative orientation characterized by the Euler angles ϕ, χ and ψ.

teraction and the quadrupolar interaction.

$$\Omega = \omega^{CS} + \omega^{2Q} \tag{6.1}$$

Eqn 2.60 and Eqn 2.66 can be used to calculate the relevant terms in the above equation. For the quadrupolar shift, the quadrupolar tensor is first transformed into the rotor frame, and then to the laboratory frame. This is exactly the same as what we did in chapter 2 and the final result is Eqn 2.77. For the chemical shift interaction, however, an extra rotation from its PAS to the quadrupolar PAS is needed.

$$CSA\ PAS \xrightarrow{\phi,\chi,\psi} QI\ PAS \xrightarrow{\omega_r t,0,0} Rotor\ Frame \xrightarrow{\omega_r t,0,0} Lab\ Frame \tag{6.2}$$

Eqn 2.68 needs to be modified to include this rotation.

$$A_{20}^{CS} = \sum_{k=-2}^{2} D_{k0}^{(2)}(\omega_r t, 0, 0) \sum_{l=-2}^{2} \sum_{n=-2}^{2} D_{nl}^{(2)}(\alpha, \beta, \gamma) D_{lk}^{(2)}(\phi^Q, \chi^Q, \psi^Q) \rho_{2n}^{CS}. \tag{6.3}$$

Exact expansion of this equation is tedious and complicated, but the final chemical shift would have the following format.

$$\omega^{CS} = \omega_{iso} + A_2^{CS}(\alpha, \beta, \gamma, \phi^Q, \chi^Q) P_2(\cos\theta) \tag{6.4}$$

6.2.2 Switching-Angle Spinning

The experimental scheme of switching-angle spinning (SAS) [142, 143] is shown in Figure 6.2, together with the pulses applied. The experiment is in fact, similar to a DAS experiment for quadrupoles (Figure 3.7). The difference is, however, that the two angles (θ_1, θ_2) are not one of the DAS angle pairs. Most often, the experiment is used to correlate the isotropic and anisotropic chemical shift spectra of a spin-$\frac{1}{2}$ nucleus. For this reason, one of the spinning angles is chosen to be the magic-angle to give high-resolution in one dimension. In our experiment, we also keep the magic-angle as one of the angles, since MAS narrows the quadrupolar lineshape by an order of magnitude. Different from the spin-half case, both dimensions of an SAS spectrum of a quadrupolar nucleus do not have high-resolution.

This two-dimensional SAS experiment can be viewed as mapping the resonance frequencies of a powder sample onto a two-dimensional frequency plane, whereas a 1D experiment maps those frequencies onto a one-dimensional axis. Since the sample is spinning at two different angles during the two time periods, the resonance frequencies in the two dimensions for a single crystallite are different. The two-dimensional map then reflects the correlation between these frequencies. More specifically, the intensity of the resulting SAS spectrum is proportional to the probability that a nuclear spin having NMR frequency ω_1 at θ_1 and ω_2 at θ_2.

For a powder sample, the NMR frequency as a function of orientation is not single valued. Hence, for one-dimensional spectra there is overlap of signals corresponding to crystallites with different orientations. When the NMR frequencies are sampled

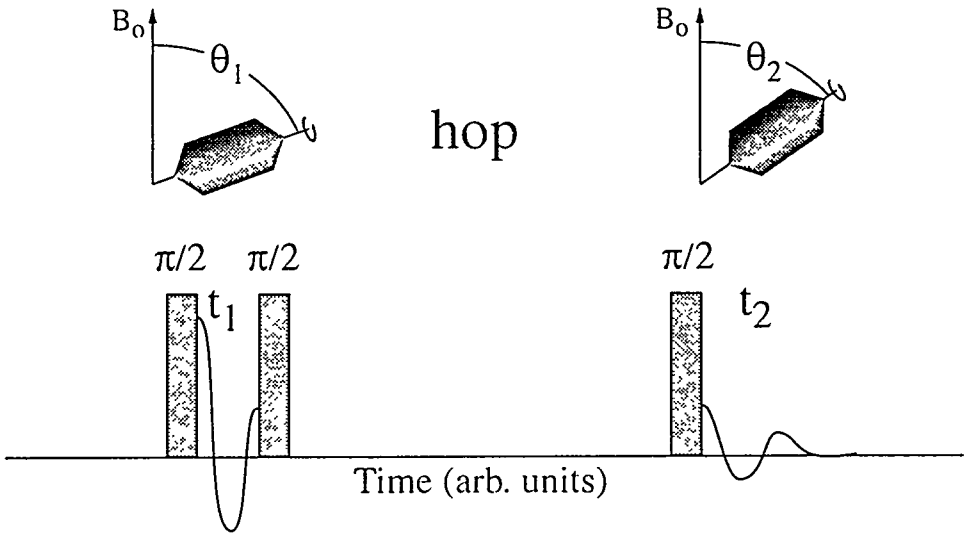

Figure 6.2: A schematic representation of the switching-angle spinning (SAS) experiment. As the sample is spinning about θ_1 relative to the magnetic field, a 90° RF-pulse is applied. The magnetization evolves in the plane transverse to the magnetic field for a time t_1 until another RF-pulse stores the magnetization along the field axis. The spinning axis is then changed to θ_2. A final RF-pulse places the magnetization back into the transverse plane where it is detected. The experiment is repeated with t_1 incremented by a dwell time.

for two times in an SAS experiment, under different spinning conditions, the relative contributions of chemical shift and quadrupolar interaction are different for the two dimensions. The resulting spectra thus have less overlapping and better reflect the relative orientation between the two tensors.

The two-dimensional SAS spectra can be simulated by calculating the following integration over all crystallites.

$$I(\omega_1,\omega_2) = \int_0^{2\pi}\int_0^{\pi} \delta(\omega_1,\Omega_1(\alpha^Q,\beta^Q))\delta(\omega_1,\Omega_1(\alpha^Q,\beta^Q))\sin\beta^Q d\alpha^Q d\beta^Q \qquad (6.5)$$

Here, Ω_1 and Ω_2 are the resonance frequencies in Eqn 6.1, and Dirac δ-function is used. To see how the SAS spectra depend on the quadrupolar parameters, Figure 6.3 shows the calculated spectra with different spinning angles and quadrupolar asymmetric parameters (η_Q). For the simulation, θ_2 has been set to the magic-angle, and only θ_1 is varied. The spectra suggest that SAS technique is very sensitive to η_Q and

produces well-defined two-dimensional lineshapes.

6.3 Experiment

All samples used in the experiment were obtained from commercial sources, typically with a stated purity of 99.8%. The ^{23}Na and ^{87}Rb NMR spectra were acquired at 4.2T (^{23}Na, 49.1 MHz; ^{87}Rb 60.8 MHz), 9.4T (^{23}Na, 105.9 MHz; ^{87}Rb 130.9 MHz) or 11.7T (^{23}Na, 132.3 MHz; ^{87}Rb 163.6 MHz), with a Nalorac Quest, Bruker AM-400 or a Chemagnetics CMX-500 spectrometer, respectively. A home-built NMR probe based on the design of Eastman et al. [72], capable of fast reorientation of the spinning axis, and employing a Doty Scientific (Columbia, SC) 5 mm fast MAS stator was used [73]; except for the ^{23}Na NMR spectra acquired at 4.2T, using a static-coil DAS probe based on the design of Mueller et al. [23]. A Whedco (Ann Arbor, MI) high torque stepping motor and motor controller were used to reorient the rotor axis in typically 40ms. The spinning axis was initially set to 54.74° using the ^{81}Br NMR signal of KBr. The pulse sequence we used are similar to the DAS sequence and same phase cycle was used. To ensure selective excitation of the central transition, 90° RF pulses were typically longer than 10μs. Generally, 128 and 512 points were acquired in t_1 and t_2, respectively, with 32 scans per t_1 value. However, the experimental parameters depended greatly on sample and field strength. During processing, the t_1 dimension was zero filled to 256 points and 100Hz Gaussian line-broadening was applied in both dimensions. Dilute aqueous solutions of $RbNO_3$ and NaCl were used as external standards. Unlike DAS or MQMAS, no shear transformation is needed in this case. The simulations were performed on a Silicon Graphics (Mountain View, CA) R4000 workstation using a program written in FORTRAN. A two-dimensional spectrum with 128 points in both dimensions takes approximately three seconds to calculate.

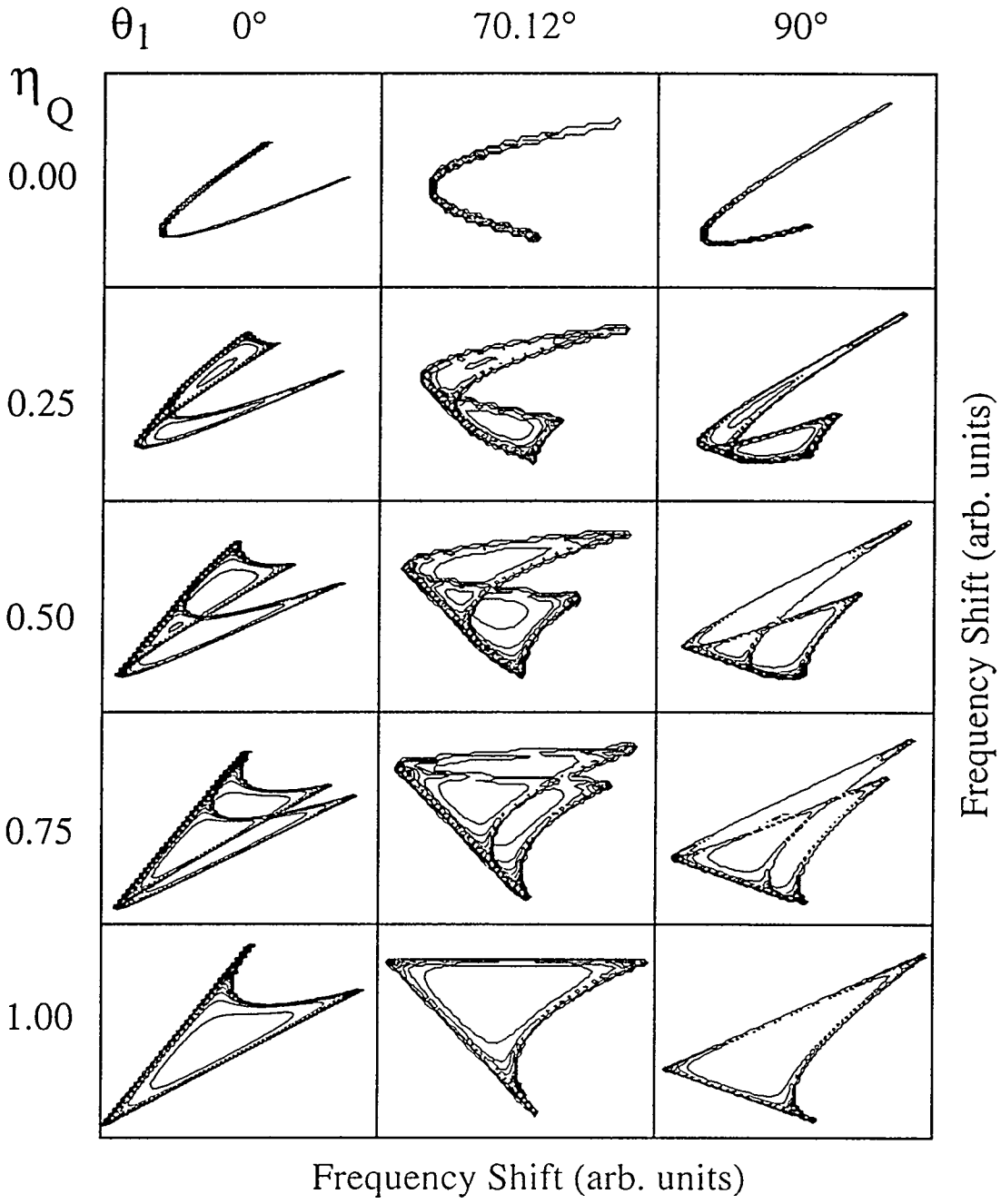

Figure 6.3: Simulated two-dimensional SAS spectra, considering only the quadrupolar interaction, as a function of θ_1 and the quadrupolar asymmetry parameter, η_Q. θ_2 is 54.74°. The horizontal dimension is the MAS dimension.

6.4 Results

As a test of the technique and the simulation program, a sample was chosen that had been studied previously and contains one crystallographically distinct sodium site that has negligible chemical shift anisotropy [41]. In Figure 6.4, the experimental and simulated ^{23}Na SAS NMR spectra of Na_2SO_4 acquired with θ_1 and θ_2 equal to 80° and 54.74°, respectively, are shown. The magic-angle was chosen to minimize the CSA

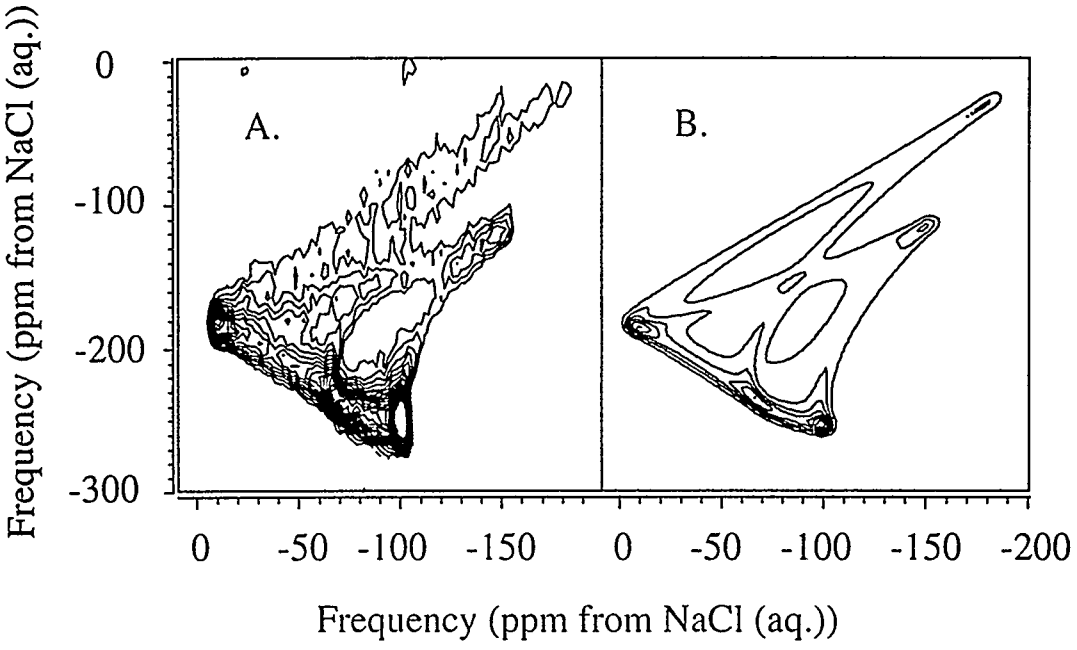

Figure 6.4: (A) Experimental and (B) simulated two-dimensional ^{23}Na SAS NMR spectra of Na_2SO_4 acquired at 4.2T with $\theta_1 = 80°, \theta_2 = 54.74°$. The simulated spectrum corresponds to $C_Q = 2.6$MHz, $\eta_Q = 0.6$, and $\delta_{iso} = 4$ppm. No chemical shift anisotropy was included in the simulation. The horizontal dimension is the MAS dimension.

effect in this dimension; the other angle was chosen to be near to 90° to minimize the sideband intensity. The simulated spectrum yields $C_Q = 2.6$MHz, $\eta_Q = 0.6$, and $\delta_{iso} = 4$ppm, consistent with previously reported values. The projection of the ω_2 dimension corresponds to an MAS spectrum and is consistent with an MAS spectrum acquired separately, as well as with a simulation of the one-dimensional

spectrum calculated using the same parameters as above. For simple systems, the quadrupolar parameters are obtainable using the SAS technique, with an accuracy equal to or greater than that obtained from one-dimensional magic-angle spinning spectra.

Many two-dimensional spectra were calculated to determine the effects of a small anisotropic chemical shift (δ_{CS}) on SAS spectra. For I=$\frac{3}{2}$ and a moderate C_Q (3MHz) at a resonance frequency of 100 MHz, a δ_{CS} of less than 10ppm is difficult to detect. However, a δ_{CS} of 15ppm can cause discernible changes in the spectral features. The effect of the chemical shift anisotropy on the two-dimensional lineshape depends on the relative orientation of the two principle axis systems and is more significant when the two principle axis systems are not coincident, especially when V_{ZZ} and δ_{ZZ} are not parallel.

Shown in Figure 6.5 is a ^{87}Rb SAS NMR spectrum of Rb_2SO_4 acquired at 9.4T; also shown separately are the spectra of the individual sites and the corresponding simulations. Rb_2SO_4 has two rubidium sites that are resolved with θ_1 equal to 90°. The spectrum is however, not resolved at the magic-angle. Thus the correlation of spectra at two angles by SAS could lead to the determination of quadrupolar parameters for both sites.

In a separated MAS spectrum acquired with the sample spinning at 10kHz, spinning sidebands are still apparent due to the large quadrupolar interactions and result in the intensity of the two sites overlapping in the one-dimensional MAS spectrum (not shown here). In the SAS spectrum the signal is spread into a two-dimensional frequency plane yielding greater resolution and nearly complete separation of the two sites. The simulations of the SAS spectrum yield C_Q =5.3 and 2.6MHz, η_Q= 0.1 and 1.0, δ_{iso}= 16 and 40ppm for the two sites, respectively. These results are consistent with those obtained by Baltisberger from field-dependent DAS measurements

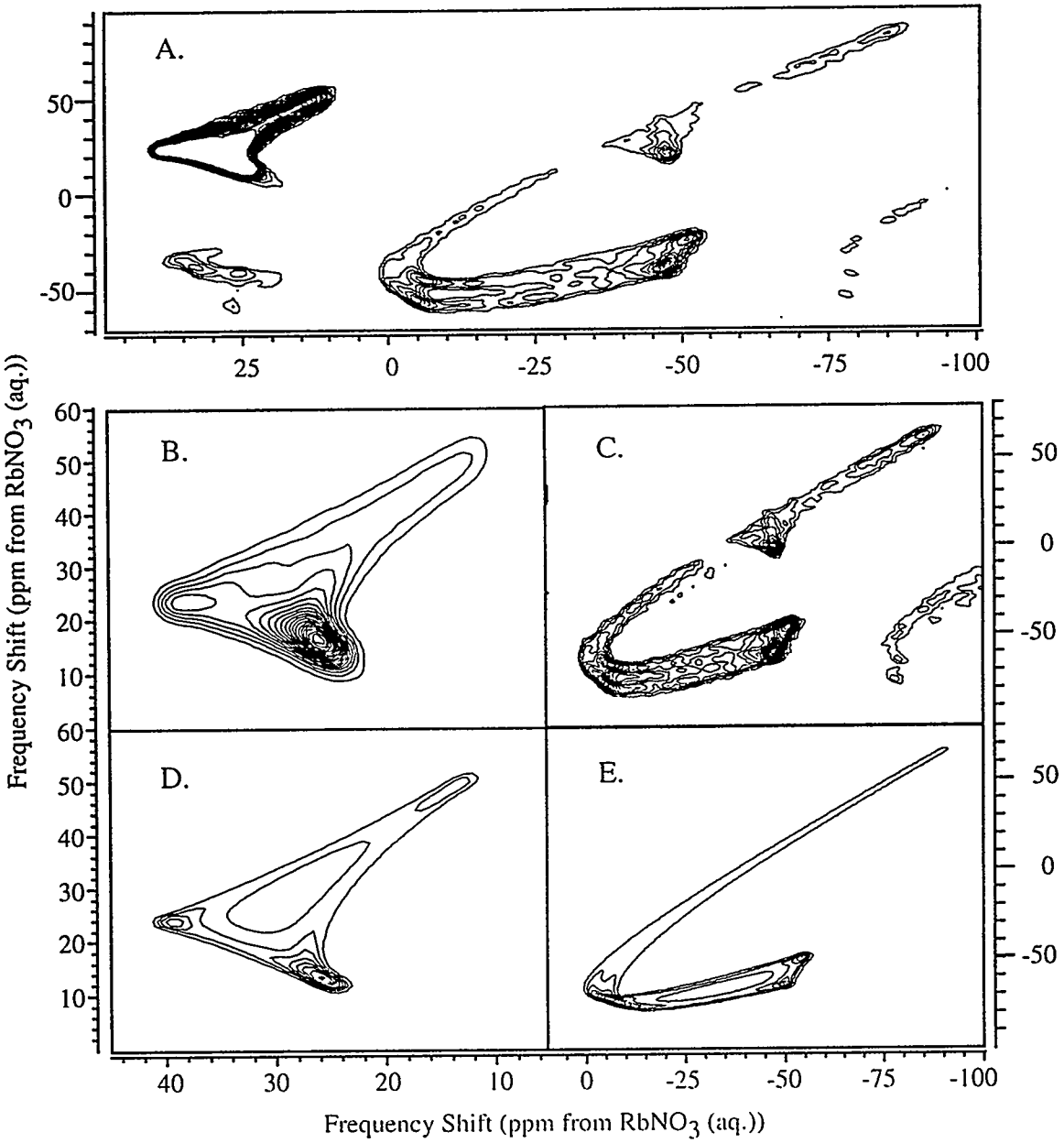

Figure 6.5: Experimental and simulated two-dimensional ^{87}Rb SAS NMR spectra of R_2SO_4 acquired at 9.4T with $\theta_1 = 90°, \theta_2 = 54.74°$. The simulated spectra were calculated for $C_Q = 5.3$ and 2.6MHz, $\eta_Q = 0.1$ and 1.0, and $\delta_{iso} = 16$ and 40ppm, respectively. The horizontal dimension is the MAS dimension. (A). SAS spectrum with 2-sites (Contour levels: 1%-20%, 1% increments). (B) and (D): Experimental and simulated spectra for site I with $C_Q = 2.6$MHz (Contour level: 5%-100%, 5% increments). (C) and (E): Experimental (Contour levels: 0.5%-10%, 0.5% increments) and simulated (Contour levels: 5%-100%, 5% increments) spectra for site II with $C_Q = 5.3$MHz.

[24], by Fernandez from simulating MAS spectra [139], and for the C_Q = 2.6 MHz site by Cheng et al. [85] from measurements of static powder samples. Although, Cheng et al. [85] reported much different values for the C_Q= 5.3 MHz site. Overlap between the two sites in the one-dimensional MAS spectrum complicates the accurate determination of these parameters using one-dimensional techniques.

The discrepancy between the simulated and experimental spectra shown in Figure 6.5 may be due to the anisotropic chemical shifts of both sites. The anisotropic chemical shifts have been reported by Fernandez et al. [139] from simulations of one-dimensional MAS spectra to be 12 and 35ppm for the C_Q=2.6 and 5.3MHz sites, respectively. The relative orientation of the principle axis systems was also reported, though with large uncertainties. While in some cases a better agreement between the experimental and simulated SAS spectra is obtained by including anisotropic chemical shifts, simulations incorporating their results do not match the experimental spectrum better than simulations neglecting the anisotropic chemical shift. This opens the question of how accurate the chemical shift parameters can be determined by one-dimensional NMR when the chemical shift anisotropy is relatively small. Further refinements of the two-dimensional SAS spectra are needed to accurately determine the small anisotropic chemical shifts and the relative orientation of the principle axis systems.

In Figure 6.6, the ^{87}Rb SAS NMR spectrum and projections of Rb_2CrO_4 acquired at 11.7T with θ_1 and θ_2 equal to 70.12° and 54.74°, respectively, are shown. One-dimensional MAS spectrum of this sample was shown in chapter 3 and the magnitude of CSA was estimated there to be around 110ppm (δ_{CS} = −110ppm). The two-dimensional SAS lineshape results from the combination of quadrupolar and chemical shift interactions. The projection above the contour plot is indistinguishable from a MAS spectrum of the central-transition measured independently. Both

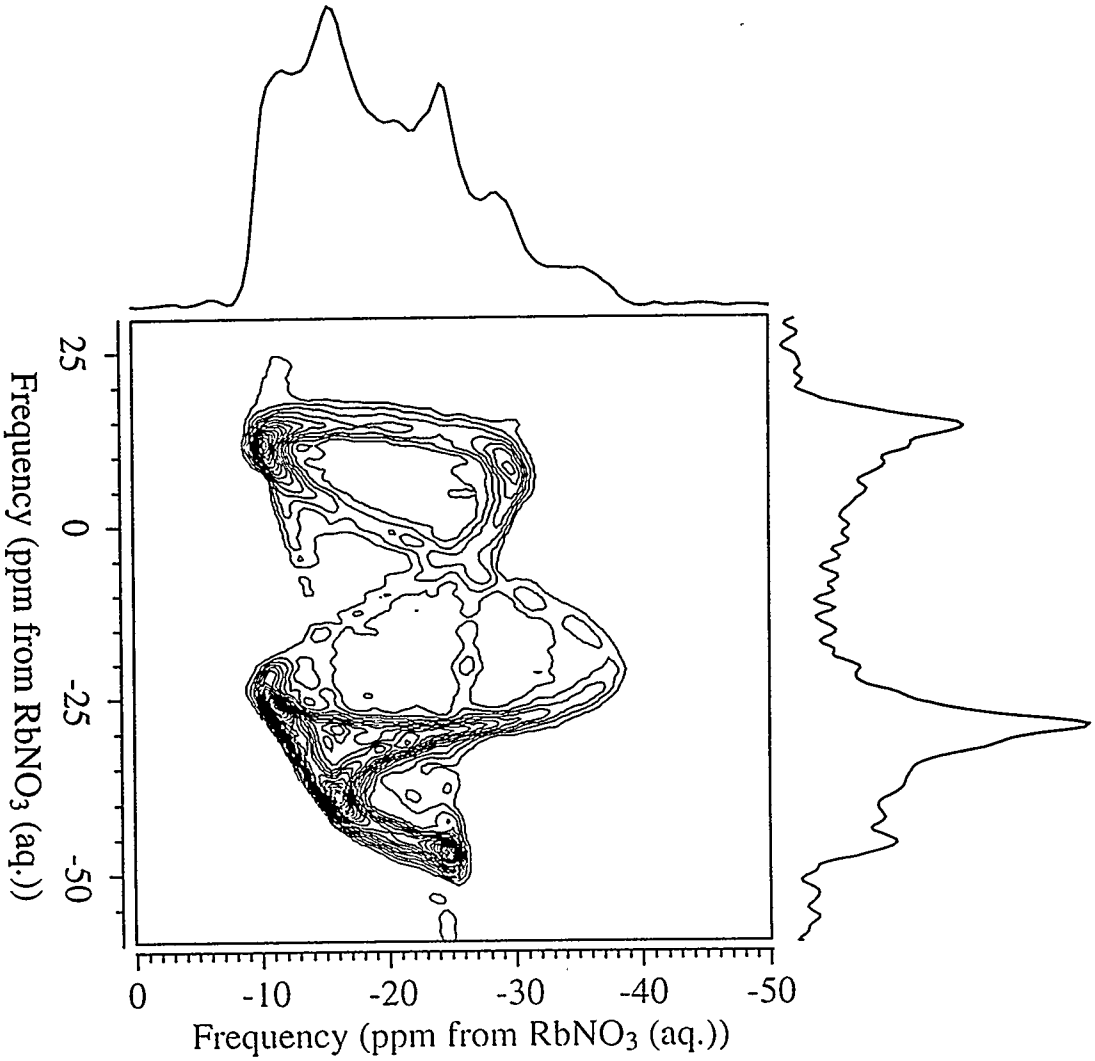

Figure 6.6: Experimental two-dimensional ^{87}Rb SAS NMR spectrum and projections of Rb_2CrO_4 acquired at 11.7 T with $\theta_1 = 70.12°, \theta_2 = 54.74°$. The horizontal dimension is the MAS dimension. The projections in both dimensions are also shown.

one-dimensional projections have structure; however the two-dimensional lineshape contains more detail. While Rb_2CrO_4 has two rubidium sites, the site with the smaller quadrupolar interaction is selectively observed. The MAS spectrum of Rb_2CrO_4 at 11.7 T has more structure than if only the quadrupolar interaction was present. Both the centerband and spinning sidebands are affected, since the spinning speed is not fast enough to completely average the anisotropic chemical shift. The MAS spectra of Rb_2CrO_4 at various fields were simulated using the parameters determined from the SAS experiments, and reproduce most of the features in the centerband and sidebands of the experimental spectra.

In Figure 6.7, the ^{87}Rb SAS NMR experimental and simulated spectra of Rb_2CrO_4, obtained with $\theta_1 = 70.12°$ and $\theta_2 = 54.74°$ acquired at 4.2, 9.4 and 11.7T are shown. The differences among the three measured spectra reflect the dependence of the chemical shift and quadrupolar interactions on magnetic field strength. The smaller the magnetic field, the smaller the chemical shift interaction is relative to the quadrupolar interaction. Note that the spectrum acquired at the lowest field, 4.2T, appears similar to spectra in Figure 6.3 calculated considering only the quadrupolar interaction. All the simulated spectra in Figure 6.7 were calculated using the following parameters, $C_Q = 3.5$MHz, $\eta_Q = 0.3$, $\delta_{iso} = -7$ppm, $\delta_{CS} = -110$ppm, $\eta_{CS} = 0$, $\chi = 70°$, $\psi = 0°$. ϕ is undefined because, in this case the chemical shift interaction is axially symmetric ($\eta_{CS} = 0$). The fact that the same parameters fit the spectra acquired at three field strengths rigorously demonstrates the precision of the technique. The quadrupolar coupling constant, quadrupolar asymmetry parameter and isotropic chemical shift are all consistent with the values determined using field-dependent DAS measurements by Baltisberger et al. [24].

To determine the sensitivity of the spectra to the chemical shift parameters, spectra were calculated with δ_{CS} and η_{CS} varied separately by ± 15 ppm and from 0 to

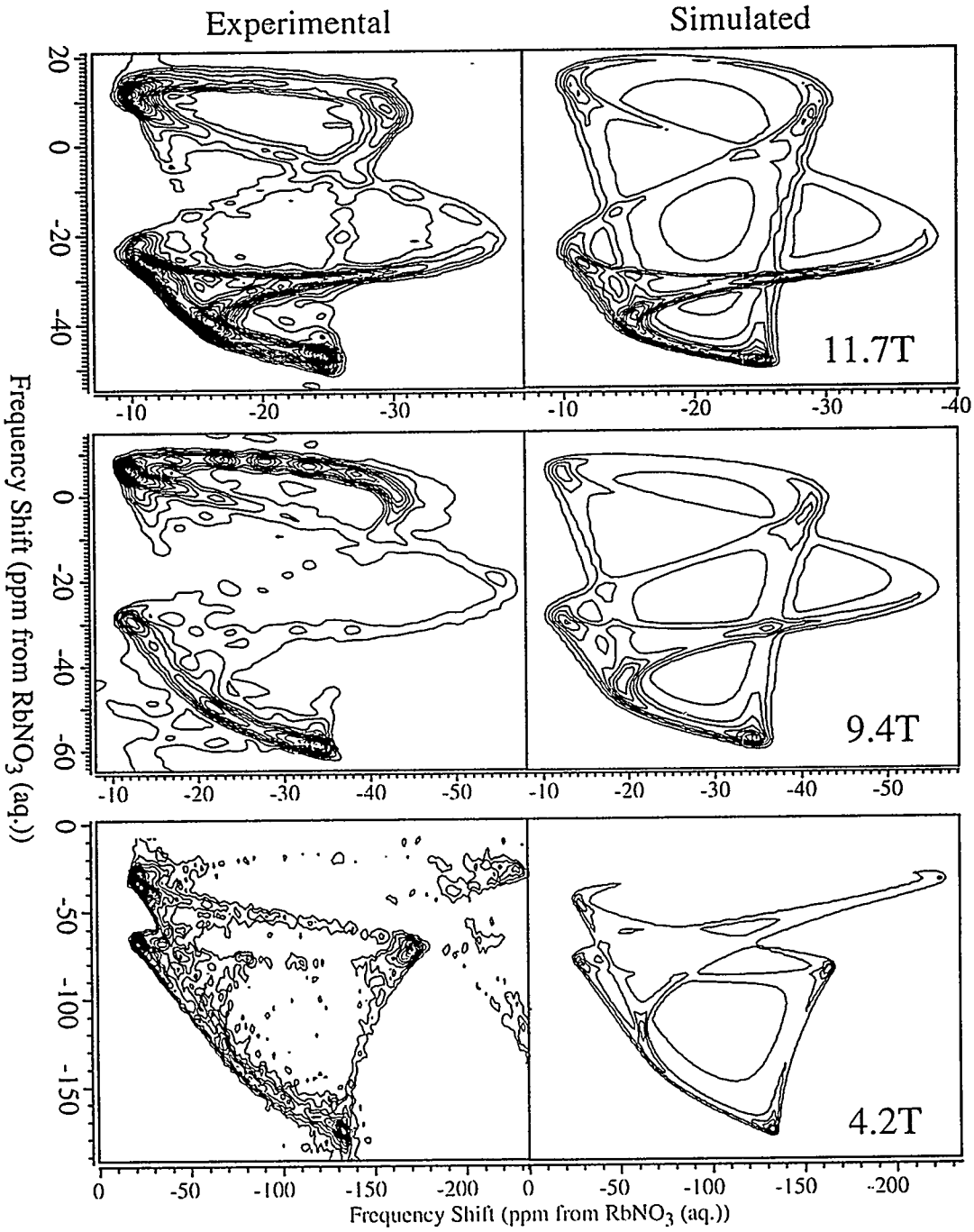

Figure 6.7: Experimental and simulated two-dimensional ^{87}Rb SAS NMR spectra of Rb_2CrO_4 measured at 4.2T, 9.4T, and 11.7T with $\theta_1 = 70.12°, \theta_2 = 54.74°$. The same parameters were used for the simulated spectra at all three fields strengths, and are $C_Q = 3.5$MHz, $\eta_Q = 0.3, \delta_{iso} = -7$ppm, $\delta_{CS} = -110$ppm, $\eta_{CS} = 0, \chi = 70°, \psi = 0°$. The horizontal dimension is the MAS dimension.

0.15, respectively, with all the remaining parameters identical to those used for the simulations shown in Figure 6.7. From simulated spectra such as those presented in Figure 6.8, the uncertainty in δ_{CS} and η_{CS} is determined to be $\pm$15ppm and less than 0.15, respectively. To determine the sensitivity of the simulated spectra on χ, ψ and η_Q the spectra presented in Figure 6.9 were calculated with parameters identical to those in Figure 6.7 except that χ, ψ and η_Q were varied separately by $\pm$5°, from 0 to 15°, and $\pm$0.1 respectively. The simulated spectra calculated with ψ equal to +15° or -15° are equivalent. From simulations such as those shown in Figure 6.9, conservative error estimates for χ, ψ and η_Q are $\pm$5°, $\pm$15°, and $\pm$0.1, respectively. Considering the greater accuracy in determining β compared to γ, and similar results reported by Fernandez et al. [139], one might suspect that this is a general trend. Further experiments on other systems can be performed to clarify this point.

Thus, the chemical shift and quadrupolar interaction parameters and the relative orientation between the principle axis systems are determined with the following accuracy: $C_Q = 3.5 \pm 0.2$MHz, $\eta_Q = 0.3 \pm 0.1$, $\delta_{iso} = -7$ ppm, $\delta_{CS} = -110 \pm 15$ ppm, $\eta_{CS} = 0 \pm 0.15$, $\chi = 70° \pm 5°$, $\psi = 0° \pm 15°$, with ϕ undefined. These results differ significantly from those determined from one-dimensional NMR spectra of powder samples reported by Cheng et al. [85].

6.5 Conclusion

NMR has the potential to characterize the local atomic environment in materials and can be used to determine structure property relationships, location and distribution of substitution species, and motion and diffusion of atoms, as well as other technologically important properties in inorganic solids. With NMR, an experimentalist has the unprecedented advantage of being able to manipulate the Hamiltonian of the system under study using radio frequency pulses and sample spinning, among

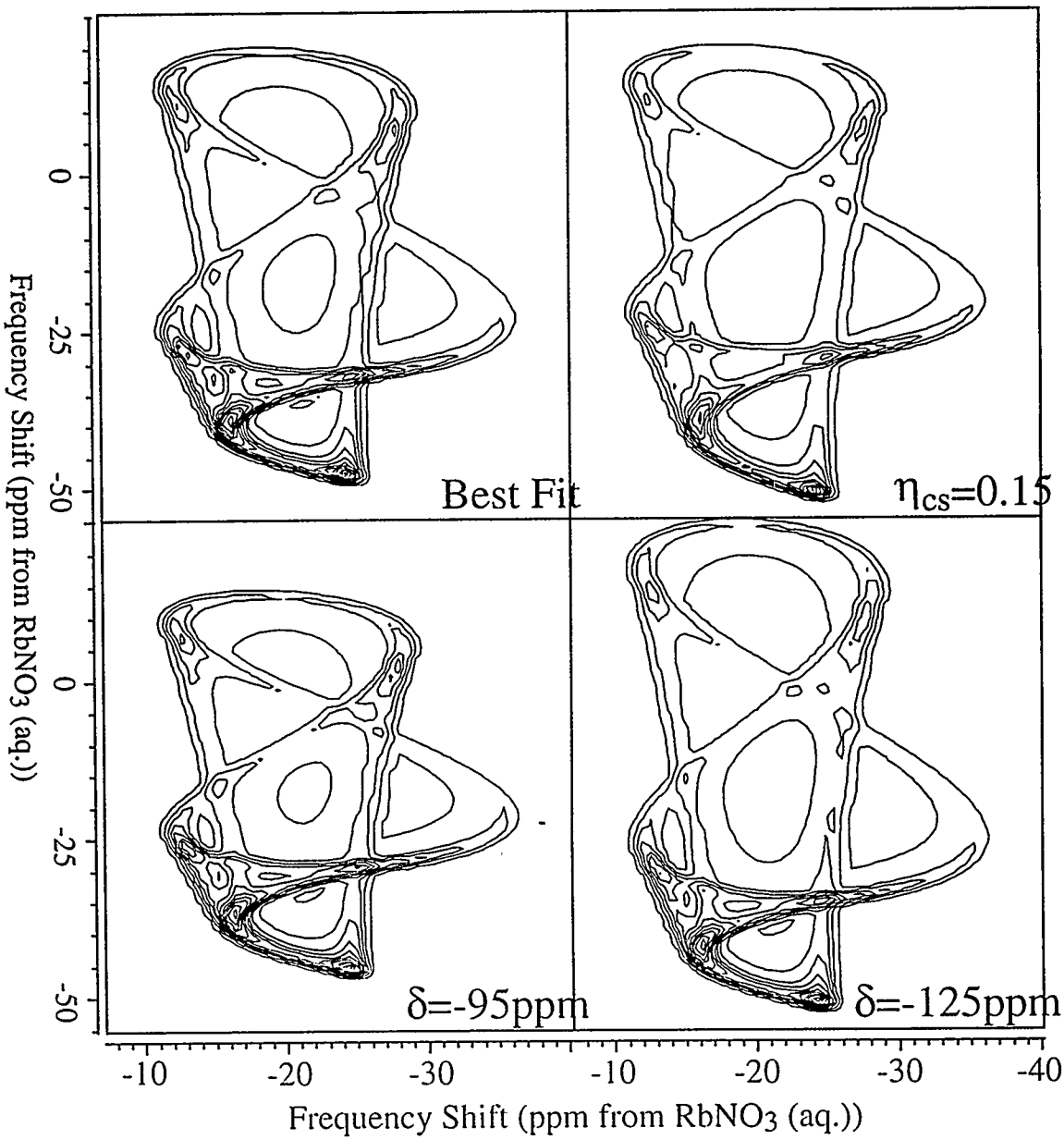

Figure 6.8: Simulated two-dimensional ^{87}Rb SAS NMR spectra of Rb_2CrO_4 at 11.7T with $\theta_1 = 70.12°, \theta_2 = 54.74°$. The same parameters ($C_Q = 3.5$MHz, $\eta_Q = 0.3, \delta_{iso} = -7$ppm, $\delta_{CS} = -110$ ppm, $\eta_{CS} = 0, \chi = 70°, \psi = 0°$) were used for all the simulated spectra except where noted. The horizontal dimension is the MAS dimension.

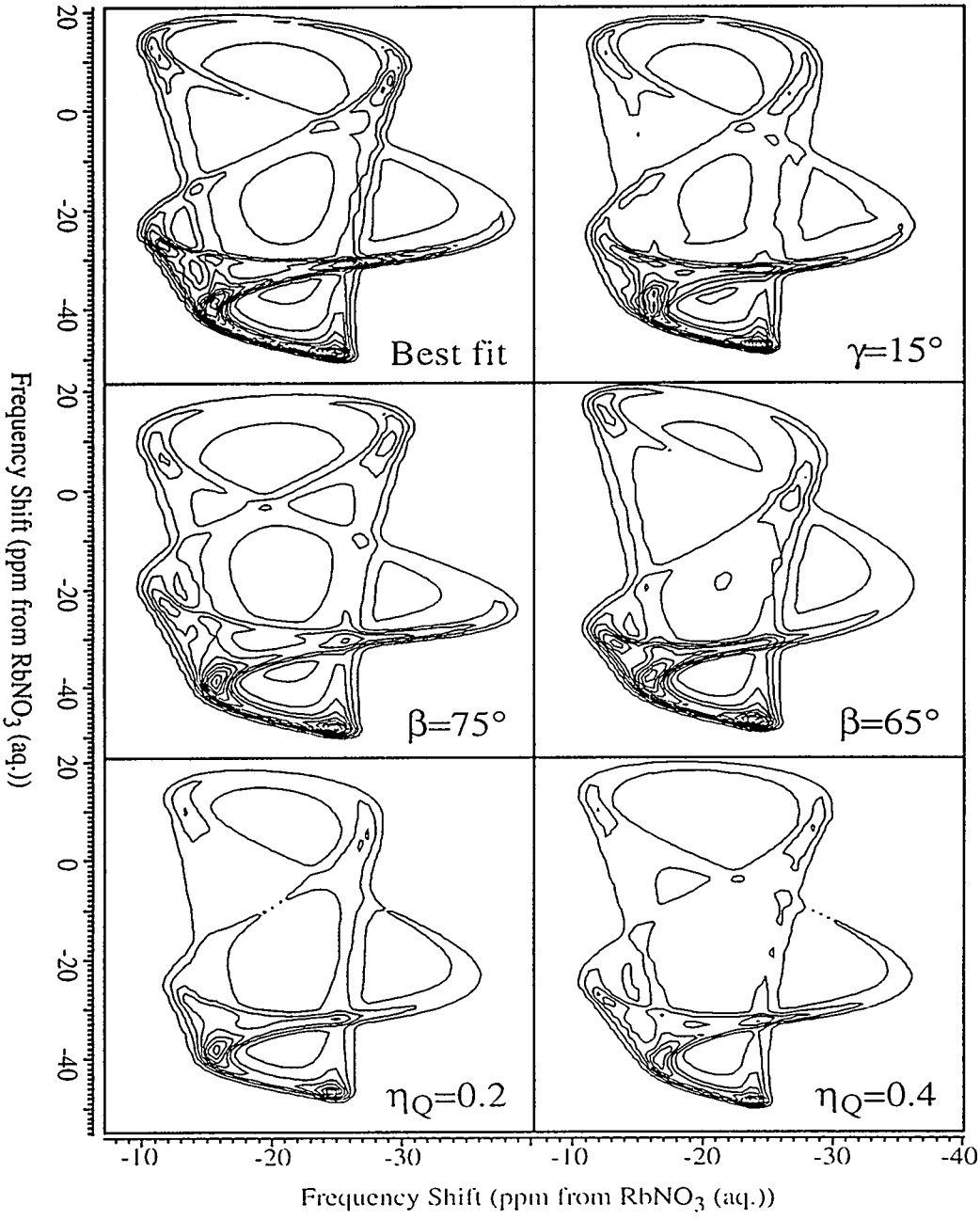

Figure 6.9: Simulated two-dimensional ^{87}Rb SAS NMR spectra of Rb_2CrO_4 at 11.7T with $\theta_1 = 70.12°, \theta_2 = 54.74°$. The same parameters ($C_Q = 3.5$MHz, $\eta_Q = 0.3, \delta_{iso} = -7$ppm, $\delta_{CS} = -110$ ppm, $\eta_{CS} = 0, \beta = 70°, \gamma = 0°$) were used for all the simulated spectra except where noted. The horizontal dimension is the MAS dimension.

other techniques. The combination of these methods with multi-dimensional NMR techniques enables the direct correlation and/or deconvolution of multiple interactions. These ideas have been used in this chapter to correlate the quadrupolar and chemical shift interactions and to determine the quadrupolar and chemical shift tensor elements, as well as the relative orientation between the two principal axis systems for a rubidium site in R_2CrO_4. Extension of these methods to a three-dimensional experiment by incorporating a purely isotropic dimension will be applicable to systems with multiple atomic sites and those with a distribution of isotropic shifts such as glasses. In this case, variable-angle correlation spectroscopy can be incorporated with SAS to simplify the technical requirement of the experiment [86, 144].

Appendix A

A Short Review on MQMAS

This appendix gives a review on MQMAS, which after being proposed by Frydman [3], received considerable and extensive attention in the past years. Our contribution at Berkeley, as described in the preceding chapters, represents a very small fraction of the problems and applications come with this technique. While much of the work from other groups has been mentioned before, a review here makes this thesis a more complete reference.

A.1 History

Multiple-quantum NMR on half-integer quadrupoles has been studied for more than two decades. Most experiments were performed on single-crystals and the results served as a nice demonstration of creation and detection of multiple-quantum coherences in the solid-state [64, 65, 145, 146, 147]. The difficulties that hinder the application to powder samples is a general belief that the excitation and reconversion of the multiple-quantum coherences are inefficient for powder samples.

Amoureux was probably the first to explicitly derive the second-order quadrupolar Hamiltonian associated to symmetric multiple-quantum transitions ($m \leftrightarrow -m$) for powder samples under spinning condition [20]. The results showed that the dependence of this Hamiltonian on the spinner axis is different to that of the central transition only by some constant factors. The magnified chemical shift differences were the primary driving force of his study. The possibility of using multiple-quantum coherences to enhance the resolution of a quadrupolar NMR spectrum was not realized until Frydman [3] proposed the MQMAS experiment two years later.

Research interests on MQMAS then fall into two groups, aiming at technique development and application respectively. The questions that the first group of people are interested in include the efficient acquisition of MQMAS spectra and extending MQMAS to include other features for better spectral interpretation; the latter group concerns more about systematic studies of interesting materials in the solid-state.

A.2 Technique Development

Three types of questions are among the primary goals of the first group. The first one involves data acquisition, processing and spectral interpretation. Due to the similarities between DAS and MQMAS, much of the DAS variations were directly applied to MQMAS, making this discipline somewhat mature now. The second problem is about the excitation of multiple-quantum coherence and its reconversion to observable single-quantum coherence. This turns out as a difficult problem that remains unsolved. The third direction is toward the utilization of MQMAS principles to other experiments for spectral editing and characterization.

A.2.1 Data Acquisition

The first MQMAS spectrum presented by Frydman [3] is a 1D spectrum. Acquisition of pure-absorption phase two-dimensional MQMAS spectra was the topic of a subsequent paper [51] and also the topic of many other publications [48, 49]. In principle, this problem is the same as the acquisition problem with DAS and all of the DAS solutions [46, 50] are equally applicable here. For example, the z-filter technique used by Mueller [46] to give pure-absorption phase DAS spectra was used by Amoureux [48] and Wimperis [49] to acquire pure-absorption MQMAS spectra. It is worth noting that this solution, which was shown not optimal for the DAS case [50], is not optimal for MQMAS either. A simple redefinition of the isotropic dimension

with possible use of whole-echo acquisition for DAS is superior to the z-filter method. Even though it was claimed that z-filter gives slightly less spectral distortion, the 2-4 fold sacrifice in sensitivity may act as the killing factor for an MQMAS experiment.

The whole-echo method, which gives better sensitivity and has been primarily applied in DAS for ^{23}Na, ^{87}Rb and ^{17}O, may not be a good choice for nuclei such as ^{27}Al, ^{11}B even though they sometimes show long spin-spin relaxation times. The possible problem with this improvement is that the spin-spin relaxation time for different sites might be different and whole-echo acquisition makes the spectra less quantitative. The decision on whether or not this modification should be used must be left to the experimenter.

Mossiot pointed out that data acquisition with rotor synchronization yields spectra without sidebands and gives better MAS dimension lineshapes [148]. The acquisition method is also more sensitive, due to the smaller spectral width one needs to cover in the high-resolution dimension. His result shows that when the spectra have a lot of sidebands, unsynchronized acquisition may give centerband pattern quite different from perfect quadrupolar lineshape and lead to errors in estimating the quadrupolar parameters. The downside of the experiment is that fast spinning ($>$ 10kHz) is a priori since the spectral width is now coupled with the spinning speed and a slow spinning speed means a small spectral window that may not cover all the different sites.

Recently there have been many papers about the avoidance of shearing transformation [49, 55]. These papers do not make significant improvement on the old acquisition scheme. The modified experiment still requires intensive manipulation of the time-domain data that most NMR softwares do not provide directly.

A.2.2 Spectral Interpretation

Without high-resolution techniques such as DAS, DOR and MQMAS, δ_{iso}, C_Q and η_Q are determined primarily by simulating the quadrupolar lineshape. With DAS and DOR, lineshape simulation is avoidable if experiments are performed at more than one field strengths. Since C_Q and η_Q are often coupled together, only the quadrupolar product P_Q can be derived and two experiments with different fields suffice to the determination of P_Q and δ_{iso}. Even though, lineshape simulation is still preferred since it gives better quantification, and it derives C_Q and η_Q separately.

Interpretation of MQMAS spectra requires a bit more effort since the chemical and second-order quadrupolar shifts are scaled differently other than DAS and DOR. Multiple-field experiments are not necessary but preferred. Different spectral interpretation methods have been shown in Chapter 4. For more complicated cases that the observed DAS shift is not available, multiple-field experiment or spectral simulation is still the right choices.

As described in detail in chapter 3, MQMAS usually gives narrower lines than DAS due to the removal of homonuclear dipolar couplings. The broadening due to heteronuclear dipolar coupling can however be overcome by decoupling. The scaling of the observed frequency in MQMAS spectra gives MQMAS better or worse resolution (compared to DAS), depending on the spin quantum numbers and the transitions observed.

MQMAS and DAS sideband patterns are very similar [45, 83]. The sidebands are not integer multiples of the spinning rate away from the centerband. This is due to the scaling factors introduced in the shearing procedure.

A.2.3 Excitation and Reconversion Pulses

The conventional way of exciting triple-quantum coherence is to use a pair of 90° pulses, separated by a short period of time inversely proportional to the magnitude of the quadrupolar interaction. The conversion from the triple-quantum coherence back to single-quantum coherence is achieved by a single 90° pulse. This scheme was not efficient to excite sites experiencing large quadrupolar interactions [3]. Most of the MQMAS applications use other excitation methods.

Using single long pulse for excitation of triple-quantum coherence can be dated back to late seventies [65, 146]. Amoureux first showed that a simple single strong pulse is equally effective for the creation of triple-quantum coherence and reconversion of this coherence to single-quantum coherence in a spinning sample [149]. The method was separately worked out by Griffin et al. later [68]. Except for the spin-locking method proposed by Griffin [63] for spin-$\frac{3}{2}$ nuclei, this simple excitation scheme seems to be the most efficient one, and is used widely now. How to choose the lengths of the pulses to achieve best efficiency was the topic of many subsequent publications [58, 67].

There seem to be some inconsistencies in literature on how to choose the excitation and reconversion pulse durations. For example, Amoureux [67] suggests that excitation pulses of 240°, 180°, 120° and 90° should be used for I=3/2, 5/2, 7/2 and 9/2 nuclei, respectively; Griffin et al. [68] showed, however, that a 540° pulse is efficient for I=3/2 nuclei; our experiments also suggests that 540° pulse is efficient. The discrepancy comes mainly from the different experimental conditions and conventions that different research groups used. In the simulations performed by Amoureux, relatively high RF power is assumed (100-200kHz), whereas most of our experiments were performed with a much lower power level (30-60kHz). When the power level is low, longer pulse is needed to gain better excitation efficiency (See Figure 3.14

to 3.16). In addition, some factors (field strength, frequency offset, second-order quadrupolar interaction and the spinning speed) that affect the excitation efficiency are not well-studied. While each of these factors may not greatly change the result, their combined effect may be significant and needs further study. Another factor that contributes to the seemingly controversial results is the different conventions used by different groups. Notice that the pulse lengths reported by Amoureux are liquid-state pulse lengths, which are different from solid-state pulse lengths by a constant factor dependent on the spin quantum number. If converted into solid-state pulse lengths, the numbers they reported should read as 480° for I=3/2, 540° for I=5/2, 480° for I=7/2 and 450° for I=9/2. These results are not very different from the solid-state pulse lengths reported by us and Griffin.

The conversion of the triple-quantum coherence back to single-quantum coherence is less effective than the excitation process [58, 67]. A single solid-state 180° pulse is often the most appropriate pulse length.

An interesting question with MQMAS is that even though the excitation and reconversion are not very efficient, the MQ-filtered MAS dimension still resembles the quadrupolar lineshape under MAS. This surprising result was explained by Frydman [58] using a very simple model. The effect is attributed to sample spinning, which renders the excitation much less orientation-dependent. A more rigorous treatment through simulation is still not available. Such a treatment is important to the full understanding of the excitation process. Currently, most simulations treat the spin ensemble as a whole and report only the ensemble averaged results. The results, while applicable in reality, lack physical intuition. It may be insightful to classify spins with different orientations into many groups and see how each group of spins are affected by different excitation schemes. The results may be more intuitive and may lead to better excitation methods.

An alternative excitation scheme that utilizes spin-locking pulses was proposed by Griffin et al. [63]. According to their reports, the excitation method gives better quantification than the single-pulse method. The tenet of the method is that even for crystallites with large quadrupolar coupling constants, under MAS and spin-locking condition, the effective quadrupolar coupling constants go through 2 or 4 zero-crossings [69, 70]. The single-quantum coherence is transferred into multiple-quantum coherence during spin-locking period. While the results shown in the paper are promising, it is not clear why a better quantification is necessarily achievable, since the spin-locking efficiency for half-integer nuclei is orientation-dependent and inefficient too. Answer to this question also requires a careful look at the response of each spin to RF pulses.

There are at least two other groups that work on the application of shaped pulses for excitation. However, their results are not positive compared to the simple single pulse excitation and reconversion mechanisms. It is also worth noting that when the excitation field strength exceeds some limit, further increase in B_1 does not necessarily lead to improved excitation efficiency. This conclusion is not well tested, since in most NMR laboratories, very high RF power (>200kHz) is still not available.

A.2.4 Extensions

Examples of utilizing quintuple-quantum coherence to enhance spectral resolution for spin-$\frac{5}{2}$ nuclei was first demonstrated by Amoureux [79]. 5QMAS gives better resolution than 3QMAS, but has primarily been applied to ^{27}Al in zeolites with small quadrupolar coupling constants [15, 79, 150]. Excitation of quintuple-quantum coherence is often difficult, thus this spectral enhancement method is only applicable to sites with very small quadrupolar coupling constants (2-3MHz).

An interesting extension of MQMAS is to use it for the measurement of chemical

shift anisotropy (CSA) [45]. For spin-$\frac{3}{2}$ nuclei, chemical shift effect is magnified by a factor of greater than 2 in the multiple-quantum isotropic dimension, and the second-order quadrupolar interaction is scaled down. CSA dominates the isotropic dimension sideband pattern when it is relatively large. Simulation of the isotropic dimension gives CSA parameters, even though the method does not provide detailed information about the relative orientation between the CSA and QI tensors. Another method that performs multiple-quantum experiment at 30.56° or 70.12° removes second-order quadrupolar interaction totally, and allows the direct determination of CSA parameters [45]. The method however is limited to samples with moderate CSA of many kilohertz.

Combining MQMAS with Cross-polarization (CP) was recently presented by Amoureux et al. [15]. CP was performed on $^{19}F/^{27}Al$ pair and the resultant spectra suggested that fluorine is connected to only one type of the aluminum sites. The result is promising for spectral editing, but special care must be taken to interpret the CP/MQMAS spectra.

In the above CP experiment, ^{19}F single-quantum coherence was first transferred to ^{27}Al single-quantum coherence, which was then stored as z-magnetization. Triple-quantum excitation was performed on this magnetization. The coherence transfer is somewhat inefficient since a z-filter is used. It is not clear if it is experimentally feasible to transfer the ^{19}F single-quantum coherence directly to ^{27}Al triple-quantum coherence. Early experiments on ^{2}H give positive signs even though ^{2}H usually has smaller quadrupolar coupling constant [147].

In Chapter 5, we showed another CP based experiment---MQMAS/HETCOR [151]. The experiment allows the registry of high-resolution HETCOR spectra for quadrupoles and maps out the spin network directly. The experiment was demonstrated on $^{23}Na/^{31}P$ pairs, but by no means should be limited to those systems.

A.3 Application

A.3.1 ^{27}Al

About half of the MQMAS applications by now involves aluminum [60, 61, 79, 150, 152, 153]. The high abundance and high resonance frequency makes it very suitable for MQMAS studies. Also, aluminum is one of the most important nuclide in zeolites, minerals, glasses and other interesting materials. In zeolites, it was demonstrated that MQMAS is able to differentiate aluminum sites with slightly different environments. The resolution is usually good enough compared to DOR, and could be further improved by exciting the quintuple-quantum coherences. In most of the zeolitic materials studied so far, the quadrupolar coupling constants are small (2-5MHz). MQMAS was also applied to the study of alumina catalysts. Once again, the quadrupolar coupling constants are not too large. A systematic study of aluminum in aluminosilicate and aluminate minerals has been presented in detail in chapter 4. The result there suggest that when C_Q is large, the spectra are no longer quantitative. Two different methods of retrieving quadrupolar parameters were also discussed there. It was shown that MQMAS is often able to differentiate aluminum sites with different coordination numbers, which is important in understanding the microstructure of glassy materials.

A.3.2 ^{23}Na

Most of the ^{23}Na work were performed on model compounds to demonstrate the efficiency of different experimental schemes. It was found that MQMAS is often efficient for ^{23}Na as most sites have small quadrupolar coupling constants [58]. Sodium sites with small differences in chemical shifts and/or quadrupolar coupling constants are differentiable from each other with MQMAS. The technique has been utilized

to separate two strongly overlapping resonances from distinct sites in glasses and to detect impurities in Na_2HfO_3 [57].

A.3.3 ^{11}B

Even though ^{11}B sites usually have small C_Q values, published MQMAS results on this nuclide is surprisingly rare. In principle, ^{11}B spectra are easy to obtain. As a very positive example, Hwang et al. presented a series of ^{11}B spectra of B_2O_3 and B_2S_3 glasses that up to 8 boron peaks were identified in a single spectrum [62]. The superior resolution offered by MQMAS would greatly contribute to the understanding of borate or borosilicate glasses.

A.3.4 ^{17}O

Compared to the wide application of DAS to ^{17}O, MQMAS of ^{17}O is somewhat limited. According to our calculation, 3QMAS and 5QMAS are both not adequate to resolve multiple-sites with varying Si-O-Si bond angles. The conclusion seems to find more support in the past year [127]. Our experiment on zeolite Y yielded at the most two peaks whereas DAS gives 3 well-resolved peaks. For non-bridging oxygen, however, MQMAS is as powerful as DAS in resolving overlapping peaks.

It is clear that non-bridging and bridging oxygen sites usually gives different peaks in the isotropic dimension [116, 126, 127]. Same conclusion is also true for oxygen in Si-O-Si and Si-O-Al fragments [56]. Based on the high-resolution available from MQMAS, kinetics of ^{17}O labeling [116] has been studied to show that Si-O-Si and Si-O-Al have different reactivity. Such an effect was first observed in ZSM-5 zeolite through ^{18}O labeling [154], and recently received more interests in other areas.

A.3.5 Less Common Quadrupolar Nuclides

MQMAS on ^{87}Rb [45, 51], ^{45}Sc [45], ^{55}Mn [3] were also performed. The results serves as demonstration of the potential applicability of MQMAS to a series of other nuclei. My experience with nuclides such as ^{65}Ga and ^{93}Nb is however, negative. The large quadrupolar coupling constants are the major problem with the experiment, even though homonulcear dipolar coupling may introduce extra complications.

Bibliography

[1] K. T. Mueller, B. Sun, G. C. Chingas, J. W. Zwanziger, T. Terao, and A. Pines. Dynamic-Angle Spinning of Quadrupolar Nuclei. *J. Magn. Reson.*, 86:470, 1990.

[2] A. Llor and J. Virlet. Towards High-Resolution NMR of More Nuclei in Solids: Sample Spinning with Time-Dependent Spinner Axis Angle. *Chem Phys. Lett.*, 152:248, 1988.

[3] L. Frydman and J. S. Harwood. Isotropic Spectra of Half-integer Quadrupolar Spins for Bidimensional Magic-Angle Spinning NMR. *J. Am. Chem. Soc.*, 117:5367, 1995.

[4] A. Abragam. *Principles of Nuclear Magnetism.* Clarendon Press, Oxford, England, 1961.

[5] R. R. Ernst, G. Bodenhausen, and A. Wokaun. *Principles of Nuclear Magnetic Resonance in One and Two Dimensions.* Oxford University Press, New York, 1991.

[6] C. P. Slichter. *Principles of Magnetic Resonance* Springer-Verlag, Berlin, 1990.

[7] M. Mehring. *Principles of High Resolution NMR in Solids.* Springer-Verlag, Berlin, 1983.

[8] K. S. Rohr and H. W. Spiess. *Multidimensional Solid-State NMR and Polymers.* Academic Press. London. 1994.

[9] G. Engelhardt. *High-Resolution Solid-State NMR of Silicates and Zeolites.* John Wiley & Sons. New York. 1987.

[10] R. N. Zare. *Angular Momentum: Understanding Spatial Aspects in Chemistry and Physics.* John Willey & Sons. New York, 1988.

[11] J. J. Sakurai. *Advanced Quantum Mechanics.* Addison-Wesley Publishing Inc., Redwood City, California, 1985.

[12] C. C. Tannoudji, B. Diu, and F. Laloe. *Quantum Mechanics.* John Wiley & Sons, Paris, 1977.

[13] A Pines, M. G. Gibby, and J. S. Waugh. Proton-Enhanced NMR of Dilute Spins in Solids. *J. Chem. Phys.*, 59:569, 1973.

[14] E.O. Stejskal, J. Schaefer, and J.S. Waugh. Magic-Angle Spinning and Polarization Transfer in Proton-Enhanced NMR. *J. Magn. Reson.*, 28:105, 1977.

[15] M. Pruski, D. P. Lang, C. Fernandez, and J. P. Amoureux. Multiple-Quantum Magic-Angle Spinning NMR with Cross-Polarization: Spectral Editing of High-Resolution Spectra of Quadrupolar Nuclei. *Solid State NMR*, 7:327, 1997.

[16] J. E. Roberts, S. Vega, and R. G. Griffin. Two-Dimensional Heteronuclear Chemical Shift Correlation Spectroscopy in Rotating Solids. *J. Am. Chem. Soc.*, 106:2506, 1984.

[17] A. Samoson. Satellite Transition High-Resolution NMR of Quadrupolar Nuclei in Powders. *Chem Phys. Lett.*, 119:29, 1985.

[18] G. Kunath, P. Losso, S. Steuernagel, H. Schneider, and C. Jager. ^{27}Al satellite Transition Spectroscopy (satras) of Polycrystalline Aluminium Borate $9Al_2O_3{\cdot}2B_2O_3$. *Solid State NMR*, 1:261, 1992.

[19] C. Jager. *NMR Basic Principles and Progress*, vol. 32, page 133. Springer-Verlag, Berlin Heidelberg, 1991.

[20] J. P. Amoureux. High-Resolution Solid-State NMR for Spin 3/2 and 9/2 - the Multi-Quantum Transitions Method. *Solid State NMR*, 2:83, 1993.

[21] M. M. Maricq and J. S. Waugh. NMR in Rotating Solids. *J. Chem. Phys.*, 70:3300, 1979.

[22] J. Herzfeld and A.E. Berger. Sideband Intensities in NMR Spectra of Samples Spinning at the Magic Angle. *J. Chem. Phys.*, 73:6021, 1980.

[23] K. T. Mueller. *Dynamic-Angle Spinning and Double Rotation of Quadrupolar Nuclei*. PhD thesis, University of California at Berkeley, 1991.

[24] J. H. Baltisberger, S. L. Gann, E. W. Wooten, T. H. Chang, K. T. Mueller, and A. Pines. Rb-87 Dynamic-Angle Spinning NMR Spectroscopy of Inorganic Rubidium Salts. *J. Am. Chem. Soc.*, 114:7489, 1992.

[25] F. Dyson. Time Ordering Operator. *Phys. Rev.*, 75:468, 1949.

[26] N. C. Nielsen, H. Bildsoe, and H. J. Jakobsen. Finite rf Pulse Excitation in MAS NMR of Quadrupolar Nuclei. Quantitative Aspects and Multiple-Quantum excitation. *Chem Phys. Lett.*, 191:205, 1992.

[27] N. C. Nielsen, H. Bildsoe, and H. J. Jakobsen. Multiple-Quantum MAS Nutation NMR Spectroscopy of Quadrupolar Nuclei. *J. Magn. Reson.*, 97:149, 1992.

[28] B. Bloembergen, E. M. Purcell, and R. V. Pound. *Phys. Rev.*, 73:679, 1948.

[29] J. Haase, K. D. Park, K. Guo, H. K. C. Timken, and E. Oldfield. Nuclear Magnetic Resonance Spectroscopic Studies of Spin-Lattice Relaxation of Quadrupolar Nuclei in Zeolites. *J. Phys. Chem.*, 195:6996, 1991.

[30] J. Haase and E. Oldfield. Spin-echo Behavior in Nonintegral-Spin Quadrupolar Nuclei in Inorganic Solids. *J. Magn. Reson. Series A*, 101:30, 1993.

[31] G. Bodenhausen, H. Kogler, and R. R. Ernst. Selection of Coherence-Transfer Pathways in NMR Pulse Experiments. *J. Magn. Reson.*, 58:370, 1984.

[32] A. D. Bain. Coherence levels and coherence pathways in NMR. A Simple Way to Design Phase Cycling Procedures. *J. Magn. Reson.*, 56:418, 1984.

[33] J. Keeler. *Multinuclear Magnetic Resonance in Liquids and Solids-Chemical Applications*, page 103. Kluwer Academic Publishers, Netherlands, 1990.

[34] D.J. States, R.A. Haberkorn, and D.J. Ruben. A Two-Dimensional Nuclear Overhouser Experiment with Pure Absorption Phase in Four Quadrants. *J. Magn. Reson.*, 48:286, 1982.

[35] E. R. Andrew, A. Bradbury, and R. G. Eades. Nuclear Magnetic Resonance Spectra from a Crystal Rotated at High speed. *Nature*, 182:1659, 1958.

[36] E. R. Andrew, A. Bradbury, and R. G. Eades. Removal of dipolar broadening of Nuclear Magnetic Resonance Spectra of Solids by Specimen Rotation. *Nature*, 183:1802, 1959.

[37] S. Vega, E. T. Olejniczak, and R. G. Griffin. Rotor frequency lines in the Nuclear Magnetic Resonance Spectra of Rotating Solids. *J. Chem. Phys.*, 80:4832, 1984.

[38] D. W. Alderman, M. S. Solum, and D. M. Grant. Methods for Analyzing Spectroscopic Lineshapes. NMR Solid Powder Patterns. *J. Chem. Phys.*, 84:3717,

1986.

[39] Z. Zheng, Z. Gan, N.K. Sethi, D.W. Alderman, and D.M. Grant. An Efficient Simulation of Variable-Angle Spinning Lineshapes for the Quadrupolar Nuclei with Half-integer Spin. *J. Magn. Reson.*, 95:509, 1991.

[40] S. Ganapathy, S. Shore, and E. Oldfield. Variable-Angle Sample-Spinning NMR Spectroscopic Studies of Non-integral Spin Quadrupolar in Solids: Analysis of Spinning-Sidebands for the Case $\eta = 0$. *Chem Phys. Lett.*, 169:301, 1990.

[41] S. Ganapathy, S. Schramm, and E. Oldfield. Variable-Angle Spinning High-Resolution NMR of Solids. *J. Chem. Phys.*, 77:4360, 1982.

[42] J. H. Baltisberger, S. L. Gann, P. J. Grandinetti, and A. Pines. Cross-Polarization Dynamic-Angle Spinning Nuclear Magnetic Resonance of Quadrupolar Nuclei. *Mol. Phys.*, 81:1109, 1994.

[43] T. P. Jarvie, R. M. Wenslow, and K. T. Mueller. High-Resolution Solid-State Heteronuclear Correlation NMR for Quadrupolar Nuclei. *J. Am. Chem. Soc.*, 117:570, 1995.

[44] C. Dean, T. W. Hambley, and M. R. Snow. Structures of Phase IV Rubidium Nitrate, $RbNO_3$, and Phase II Cesium Nitrate, $CsNO_3$. *Acta Cryst.*, 40:1512, 1984.

[45] S. H. Wang, Z. Xu, Baltisberger J. H., L. M. Bull, J. F. Stebbins, and A. Pines. Multiple-Quantum Magic-Angle Spinning and Dynamic-Angle Spinning NMR Spectroscopy of Quadrupolar Nuclei. *Solid State NMR*, 8:1, 1997.

[46] K. T. Mueller, E. W. Wooten, and A. Pines. *J. Magn. Reson.*, 92:620, 1991.

[47] P. J. Grandinetti, J. H. Baltisberger I. Farnan, J. F. Stebbins, U. Werner, and A. Pines. Solid-State ^{17}O Magic-Angle and Dynamic-Angle Spinning NMR Study of the SiO_2 Polymorph Coesite. *J. Phys. Chem.*, 99:12341, 1995.

[48] J. P. Amoureux, C. Fernandez, and S. Steuernagel. z-filter in MQMAS NMR. *J. Magn. Reson. Series A*, 12:116, 1996.

[49] S. P. Brown, S. J. Heyes, and S. Wimperis. Two-Dimensional MAS Multiple-Quantum NMR of Quadrupolar Nuclei. Removal of Inhomogeneous Second-Order Broadening. *J. Magn. Reson. Series A*, 119:280, 1996.

[50] P. J. Grandinetti, J. H. Baltisberger, A. Llor, Y. K. Lee, U. Werner, M. A. Eastman, and A. Pines. Pure-Absorption-Mode Lineshapes and Sensitivity in Two-Dimensional Dynamic-Angle Spinning NMR. *J. Magn. Reson. Series A*, 103:72, 1993.

[51] D. Massiot, B. Touzo, D. Trumeau, J. P. Coutures, J. Virlet, P. Florian, and P. J. Grandinetti. Two-Dimensional Magic-Angle Spinning Isotropic Reconstruction Sequences for Quadrupolar Nuclei. *Solid State NMR*, 6:73, 1996.

[52] K. Nagayama, P. Bachmann, K Wuthrich, and R. R. Ernst. *J. Magn. Reson.*, 31:133, 1978.

[53] A. Bax, R. H. Griffey, and B. L. Hawkins. *J. Magn. Reson.*, 55:301, 1983.

[54] A. C. Kolbert, M. H. Levitt, and R. G. Griffin. *J. Magn. Reson.*, 85:42, 1989.

[55] S. P. Brown and S. Wimperis. Two-Dimensional Multiple-Quantum MAS NMR of Quadrupolar Nuclei. Acquisition of Whole Echo. *J. Magn. Reson.*, 124:279, 1997.

[56] P. J. Dirken, S. C. Kohn, M. E. Smith, and E. R. H. van Eck. Complete Resolution of Si-O-Si and Si-O-Al Fragments in an Aluminosilicate Glass by ^{17}O Multiple Quantum Magic Angle Spinning NMR Spectroscopy. *Chem Phys. Lett.*, 266:568, 1997.

[57] J. V. Hanna, M. E. Smith, and H. J. Whitfield. Multiple Quantum Magic Angle Spinning NMR detection of Impurity Phase in Na_2HfO_3. *J. Am. Chem. Soc.*, 118:5772, 1996.

[58] A. Medek, J. S Harwood, and L. Frydman. Multiple-Quantum Magic-Angle Spinning NMR: A New Method for the Study of Quadrupolar Nuclei in Solids. *J. Am. Chem. Soc.*, 117:12779, 1995.

[59] C. Jager, P. Hartmann, G. K. Fandrei, O. Hirsch, P. Rehak, J. Vogel, M. Feike, H. W. Spiess, K. Herzog, and B. Thomas. Novel Oppertunities of Structural Investigations of Glasses by 2D NMR, Multiple Quantum NMR and ^{27}Al MAS NMR Lineshape Analysis. *Ber. Bunsenges. Phys. Chem.*, 100:1560, 1996.

[60] J. H. Baltisberger, Z. Xu, J. F. Stebbins, S. H. Wang, and A. Pines. Triple-Quantum Two-Dimensional ^{27}Al Magic-Angle Spinning Nuclear Magnetic Resonance Spectroscopic Study of Aluminosilicate and Aluminate Crystals and Glasses. *J. Am. Chem. Soc.*, 118:7209, 1996.

[61] J. Rocha, A. P. Esculcas, C. Fernandez, and J. P. Amoureux. Two-Dimensional Triple-Quantum ^{27}Al MAS NMR Spectroscopic Study of the High-Temperature Phase Transformation of Microporous VPI-5. *J. Phys. Chem.*, 100:17889, 1996.

[62] S. H. Hwang, C. Fernandez, J. P. Amoureux, J. Cho, S. W. Martin, and M. Pruski. Quantitative Study of the Short Range Order in B_2O_3 and B_2S_3 by MAS and Two-Dimensional Triple-Quantum MAS ^{11}B NMR. *Solid State NMR*, 8:109, 1997.

[63] G. Wu, D. Rovnyak, and R. G. Griffin. Quantitative Multiple-Quantum Magic-Angle-Spinning NMR Spectroscopy of Quadrupolar Nuclei in Solids. *J. Am. Chem. Soc.*, 118:9326, 1996.

[64] S. Vega. Fictitious Spin 1/2 Operator Formalism for Multiple Quantum NMR. *J. Chem. Phys.*, 68:5518, 1978.

[65] A. Wokaun and R. R. Ernst. Selective Excitation and Detection in Multilevel Spin System: Application of Single Transition Operators. *J. Chem. Phys.*, 67:1752, 1977.

[66] E. R. Johnston. Density Matrix Theory for Calculating Magnetization Transfer and Dynamic LineShape Effects. *Concepts in Magn. Reson.*, 7:219, 1995.

[67] J. P. Amoureux, C. Fernandez, and L. Frydman. Optimized Multiple-Quantum Magic-Angle Spinning NMR Experiments on Half-Integer Quadrupoles. *Chem. Phys. Lett.*, 259:347, 1996.

[68] G. Wu, D. Rovnyak, B. Q. Sun, and R. G. Griffin. High-Resolution Multiple Quantum MAS NMR Spectroscopy of Half-Integer Quadrupolar Nuclei. *Chem. Phys. Lett.*, 249:210, 1996.

[69] A. J. Vega. MAS NMR Spin locking of Half-Integer Quadrupolar Nuclei. *J. Magn. Reson.*, 96:50, 1991.

[70] A. J. Vega. MAS Spin-locking of Half-Integer Quadrupolar Nuclei. *J. Magn. Reson.*, 96:50, 1992.

[71] S. M. De Paul, M. Ernst, J. S. Shore, J. F. Stebbins, and A. Pines. Cross-Polarization from Quadrupolar Nuclei to Silicon Using Low-Radio-Frequency Amplitudes during Magic-Angle Spinning. *J. Phys. Chem.*, 101:3240, 1997.

[72] M. A. Eastman, P. J. Grandinetti, Y. K. Lee, and A. Pines. Double-Tuned Hopping-Coil Probe for Dynamic-Angle-Spinning NMR. *J. Magn. Reson.*,

98:333, 1992.

[73] F. D. Doty and P. D. Ellis. Design of High Speed Cylindrical NMR Sample Spinners. *Rev. Sci. Instr.*, 52:1868, 1981.

[74] D. Massiot, I. Farnan, N. Gautier, D. Trumeau, P. Florian, and P. J. Grandinetti. ^{69}Ga,^{71}Ga Solid State Static, MAS and DAS NMR Study of β-Ga_2O_3. *J. Chim. Phys.*, 92:1847, 1995.

[75] K. T. Mueller, Y. Wu, B. F. Chmelka, J. Stebbins, and A. Pines. High-Resolution Oxygen-17 NMR of Solid Silicates. *J. Am. Chem. Soc.*, 113:32, 1990.

[76] K. T. Mueller, G. C. Chingas, and A. Pines. NMR Probe for Dynamic-Angle Spinning. *Rev. Sci. Instr.*, 62:1445, 1991.

[77] M. Hanaya and R. K. Harris. Effect of ^{1}H-Decoupling in Two-Dimensional Multiple-Quantum MAS NMR Spectroscopy of ^{23}Na in a Hydrous Layered Silicate. *Solid State NMR*, 8:147, 1997.

[78] J. F. Stebbins. *Structure, Dynamics and Properties of Silicate Melts*, vol. 32, page 191. BookCrafters, Inc., Chelsea, Michigan, 1995.

[79] C. Fernandez and J. P. Amoureux. 2D Multiquantum MAS-NMR Spectroscopy of Al-27 in Aluminaphosphate Molecular Sieves. *Chem. Phys. Lett.*, 242:449, 1995.

[80] I. Farnan, P. J. Grandinetti, J. H. Baltisberger, J. F. Stebbins, U. Werner, M. A. Eastman, and A. Pines. Quantification of the Disorder in Network-Modified Silicate Glasses. *Nature*, 358:31, 1992.

[81] P. Florian, K. E. Vermillion, P. J. Grandinetti, and J. F. Stebbins. Cation Distribution in Mixed Alkali Disilicate Glasses. *J. Am. Chem. Soc.*, 118:3493, 1996.

[82] J. H. Baltisberger. *Advances and Applications of Dynamic-Angle Spinning Nuclear Magnetic Resonance*. PhD thesis, University of California at Berkeley, 1993.

[83] P. J. Grandinetti, Y. K. Lee, J. H. Baltisberger, B. Q. Sun, and A. Pines. Sideband Patterns in Dynamic-Angle Spinning. *J. Magn. Reson. Series A*, 102:195, 1993.

[84] J. S. Shore, S. H. Wang, R. E. Taylor, A. T. Bell, and A. Pines. Determination of Quadrupolar and Chemical Shielding Tensors Using Solid-State Two-Dimensional NMR Spectroscopy. *J. Chem. Phys.*, 105:9412, 1996.

[85] J. T. Cheng, J. C. Edwards, and P. D. Ellis. Measurement of Quadrupolar Coupling Constants, Shielding Tensor Elements, and the Relative Orientation of Quadrupolar and Shielding Tensor Principal Axis Systems for Rubidium-87 and Rubidium-85 Nuclei in Rubidium Salts by Solid-State Nuclear Magnetic Resonance. *J. Phys. Chem.*, 94:553, 1990.

[86] A. Medek, J. R. Sachleben, P. Beverwyk, and L. Frydman. Multi-Rank NMR Studies of Half-integer Quadrupolar Nuclei in Solids by Three-Dimensional Dynamic-Angle Correlation Spectroscopy. *J. Chem. Phys.*, 104:5374, 1996.

[87] A. Samoson, E. Lippmaa, and A. Pines. High-Resolution Solid State NMR, Averaging of Second-Order Effects by Means of a Double-Rotor. *Mol. Phys.*, 65:1013, 1988.

[88] A. Samoson and E. Lippmaa. Synchronized Double-Rotation NMR Spectroscopy. *J. Magn. Reson.*, 84:410, 1989.

[89] R. Jelinek, B.F. Chmelka, Y. Wu, M.E. Davis, J.G. Ulan, R. Gronsky, and A. Pines. Adsorption Effects in Aluminophosphate Molecular Sieves Studied by ^{27}Al Double-Rotation NMR. *Catal. Lett.*, 15:65, 1992.

[90] R. Jelinek, B.F. Chmelka, Y. Wu, P.J. Grandinetti, A. Pines, P.J. Barrie, and J. Klinowski. Study of the Aluminophosphates $AlPO_4$-21 and $AlPO_4$-25 by ^{27}Al Double-Rotation NMR. *J. Am. Chem. Soc.*, 113:4097, 1991.

[91] S. L. Gann, J. H. Baltisberger, and A. Pines. Dynamic-Angle Spinning without Sidebands. *Chem. Phys. Lett.*, 242:171, 1993.

[92] Z. Gan. High-Resolution Chemical Shift and Chemical Shist Anisotropy Correlation in Solids Using Slow Magic-Angle Spinning. *J. Am. Chem. Soc.*, 114:8307, 1992.

[93] J. P. Amoureux, C. Fernandez, and F. Lefebvre. Side-band Analysis in Variable-Angle Sample-Spinning (VASS) NMR for the Central Transition of Quadrupolar Nuclei (Half-Integer Spin). *Magn. Reson. in Chem.*, 28:5, 1990.

[94] J. M. Thomas and J. Klinowski. *Advances in Catalysis*, vol. 33, page 199. Academic Press, Inc., 1985.

[95] S. Schramm, R. J. Kirkpatrick, and E. Oldfield. Observation of High-Resolution Oxygen-17 NMR Spectra of Inorganic Solids(I). *J. Am. Chem. Soc.*, 105:2483, 1983.

[96] H. C. Timken, G. L. Turner, J. P. Gilson, L. B. Welsh, and E. Oldfield. Solid-State Oxygen-17 Nuclear Magnetic Resonance Spectroscopic Studies of Zeolites and Related Systems(II). *J. Am. Chem. Soc.*, 108:7231, 1986.

[97] H. C. Timken, N. Janes, G. L. Turner, S. L. Lambert, L. B. Welsh, and E. Oldfield. Solid-State Oxygen-17 Nuclear Magnetic Resonance Spectroscopic Studies of Zeolites and Related Systems. *J. Am. Chem. Soc.*, 108:7236, 1986.

[98] S. Schramm and E. Oldfield. High-Resolution Oxygen-17 NMR of Solids. *J. Am. Chem. Soc.*, 106:2502, 1984.

[99] L. B. Alemany, D. Massiot, B. L. Sherriff, M. E. Smith, and F. Taulelle. Observation and Accurate Quantification of ^{27}Al MAS NMR Spectra of Some Al_2SiO_5 Polymorphs Containing Sites with Large Quadrupole Interactions. *Chem Phys. Lett.*, 177:301, 1991.

[100] E. Oldfield and R.J. Kirkpatrick. High-Resolution Nuclear Magnetic Resonance of Inorganic Solids. *Sciences*, 227:1537, 1985.

[101] E. Oldfield, H. Kyung, C. Timken, B. Montez, and R. Ramachandran. High-Resolution Solid-State NMR of Quadrupolar Nuclei. *Nature*, 318:163, 1985.

[102] R. J. Kirkpatrick, R. Oestrike, C. A. Weiss, K. A. Smith, and E. Oldfield. High-Resolution ^{27}Al and ^{29}Si NMR Spectroscopy of Glasses and Crystals along the Join $CaMgSi_2O_6$-$CaAl_2SiO_6$. *Am. Miner.*, 71:705, 1986.

[103] C. I. Merzbacher, B. L. Sherriff, J. S. Hartman, and W. B. White. A High-Resolution ^{29}Si and ^{27}Al NMR study of Alkaline Earth Aluminosilicate. *J. of Non-Cryst. Solids*, 124:194, 1990.

[104] R. Oestrike, W. H. Yang, R. J. Kirkpatrick, R. L. Hervig, A. Navrotsky, and B. Montez. High-Resolution ^{23}Na, ^{27}Al and ^{29}Si NMR Spectroscopy of Framework Aluminosilicate Glasses. *GeoChim. Cosmochim. Acta*, 51:2199, 1987.

[105] G. Engelhardt, N. Nofz, K. Fockel, F. G. Wihsmann, M Magi, A. Samosen, and E. Lippmaa. Structural Studies of Calcium Aluminosilicate Glasses by High-Resolution Solid State ^{29}Si and ^{27}Al Magic Angle Spinning Nuclear Magnetic Resonance. *Phys. Chem. Glass.* 26:157, 1985.

[106] S. F. Dec, J. J. Fitzgerald, J. S. Frye, M. P. Shatlock, and G. E. Maciel. Observation of Six-coordinate Aluminum in and Alusite by Solid-State ^{27}Al MAS NMR. *J. Magn. Reson.*, 93:403, 1991.

[107] B. C. Bunker, R. J. Kirkpatrick, R. K. Brow, G. L. Turner, and C. Nelson. Local Structure of Alkaline-Earth Boroaluminate Crystals and Glasses: II. ^{11}B and ^{27}Al MAS NMR Spectroscopy of Alkaline-Earth Boroaluminate Glasses. *J. Am. Ceram. Soc.*, 74:1430, 1991.

[108] B. T. Poe, P. F. McMillan, C. A. Angell, and R. K. Sato. Al and Si Coordination in SiO_2-Al_2O_3 Glasses and Liquids: A Study by NMR and IR Spectroscopy and MD Simulations. *Chem. Geol.*, 96:333, 1992.

[109] S. H. Risbud, R. J. Kirkpatrick, A. P. Taglialavore, and B. Montez. Solid-State NMR Evidence of 4-, 5-, and 6-fold Aluminum Sites in Roller-Quenched SiO_2-Al_2O_3 Glasses. *J. Am. Ceram. Soc.*, 70:10, 1987.

[110] R. K. Sato, P. F. McMillan, P. Dennison, and R. Dupree. High-Resolution ^{27}Al and ^{29}Si MAS NMR Investigation of SiO_2-Al_2O_3 Glasses. *J. Phys. Chem.*, 95:4484, 1991.

[111] R. K. Sato, P. F. McMillan, P. Dennison, and R. Dupree. A Structural Investigation of High-Alumina Content Glasses in CaO-Al_2O_3-SiO_2 System via Raman and MAS NMR. *Phys. Chem. Glass.* 32:149, 1991.

[112] J. F. Stebbins. NMR Evidence for Five-coordinated Silicon in a Silicate Glass at Atmospheric Pressure. *Nature*, 351:638, 1991.

[113] M. Schmucker and H. Schneider. A new Approach on the Coordination of Al in Non-Crystalline Gels and Glasses of the System Al_2O_3-SiO_2. *Ber. Bunsenges. Phys. Chem.*, 100:1550, 1996.

[114] G. Engelhardt and H. Koller. *NMR Basic Principles and Progress*, vol. 31, page 1. Springer-Verlag, Berlin Heidelberg, 1991.

[115] J. Neuefeind and K. D. Liss. Bond Angle Distribution in Amorphous Germania and Silica. *Ber. Bunsenges. Phys. Chem.*, 100:1341, 1996.

[116] Z. Xu and J. F. Stebbins. ^{17}O Static, MAS, DAS and MQMAS of Stilbite. *Solid State NMR*, in press.

[117] J. B. Murdoch, J. F. Stebbins, I. S. Carmichael, and A. Pines. *Phys. Chem. Miner.*, 15:370, 1988.

[118] B. L. Philips, R. J. Kirkpatrick, and M. A. Carpenter. *Am. Miner.*, 77:484, 1992.

[119] S. C. Kohn, C. M. Henderson, and R. Dupree. *Am. Miner.*, 80:705, 1995.

[120] I. W. Brown, C. M. Cardile, K. J. Mackenzie, M. J. Ryan, and R. H. Meinhold. *Phys. Chem. Miner.*, 15:78, 1987.

[121] B. L. Philips, R. J. Kirkpatrick, and A. Putnis. *Phys. Chem. Miner.*, 16:591, 1989.

[122] B. L. Phillips, R. J. Kirkpatrick, and A. Putnis. *Phys. Chem. Miner.*, 16:591, 1989.

[123] S. Yang, K. D. Parka, and E. Oldfield. Oxygen-17 Labeling of Oxides and Zeolites. *J. Am. Chem. Soc.*, 111:7278, 1989.

[124] T. J. Bastow and S. H. Stuart. ^{17}O NMR in Simple Oxides. *Chem. Phys.*, 143:459, 1990.

[125] S. B. Alder, J. A. Reimer, J. Baltisberger, and U. Werner. Chemical Structure and Oxygen Dynamics in $Ba_2In_2O_5$. *J. Am. Chem. Soc.*, 116:675, 1994.

[126] Z. Xu, J. V. Oglesby, and J. F. Stebbins. Disorder among Network Modifier Cations in Silicate Glasses: New Constraints from Triple-Quantum Oxygen-17 NMR. *Am. Miner.*, in press.

[127] Z. Xu and J. F. Stebbins. ^{17}O Static, MAS, DAS and MQMAS of Stilbite. *Solid State NMR*, in press.

[128] J. N. Evans. *Biomolecular NMR Spectroscopy.* Oxford University Press, New York, 1995.

[129] M. Feike, R. Graf, I. Schnell, C. Jager, and H. W. Spiess. Structure of Crystalline Phosphates from P-31 Double-Quantum NMR Spectroscopy. *J. Am. Chem. Soc.*, 118:9631, 1996.

[130] D. Michel and F. Engelke. *NMR Basic Principles and Progress*, vol. 32, page 69. Springer-Verlag, Berlin Heidelberg, 1993.

[131] S. L. Gann, J. H. Baltisberger, E. W. Wooten, H. Zimmermann, and A .Pines. Cross-Polarization and Dynamic-Angle Spinning of ^{17}O in L-Alanine. *Bull. of Magn. Reson.*, 16:68, 1995.

[132] J. C. Edwards and P. D. Ellis. Cross-Polarization for Quadrupolar Nuclei-Proton to Molybdenum-95. *Magn. Reson. in Chem.*, 28:59, 1990.

[133] R. J. Kirkpatrick and R. K. Brow. Nuclear Magnetic Resonance Investigation of Structures of Phosphate and Phosphate-Containing Glasses: A Review. *Solid State NMR*, 5:9, 1995.

[134] J. F. Baugher, P. C. Taylor, T. Oja, and P. J. Bray. Nuclear Magnetic Resonance Powder Patterns in the Presence of Completely Asymmetric Quadrupole and Chemical Shift Effects: Application to Metavanadates. *J. Chem. Phys.*, 50:4914, 1969.

[135] Jr. Jones, W.H., T.P. Graham, and R.G. Barnes. Nuclear Magnetic Resonance Lineshapes Resulting from the Combined Effects of Nuclear Quadrupole and Anisotropic Shift Interactions. *Phys. Rev.*, 132:1898, 1963.

[136] M. Linder, A. Hohener, and R. R. Ernst. Orientation of Tensorial Interactions Determined from Two-Dimensional NMR Powder Spectra. *J. Chem. Phys.*, 73:4959, 1980.

[137] T. Vosegaard, J. Skibsted, H. Bildsoe, and H. J. Jakobsen. Quadrupolar Coupling and Anisotropic Shielding from Single-Crystal NMR of the Central Transition for Quadrupolar Nuclei. ^{87}Rb NMR of $RbClO_4$ and Rb_2SO_4. *J. Magn. Reson.*, 122:111, 1996.

[138] P. Bodart, C. Fernandez, and J. P. Amoureux. Refinement of Solid-State MAS NMR Spectra of Quadrupolar Nuclei- Application to the Analysis of some V-51 Compounds. *Magn. Reson. Imag.*, 12:333, 1994.

[139] C. Fernandez, J. P. Amoureux, and P. Bodart. Electronic Shieldings and Electric Field Gradients in Rubidium Sulfate Studied by Rb-87 MAS NMR. *J. Magn. Reson. Series A*, 113:205, 1995.

[140] J. Skibsted, N. C. Nielsen, H. Bildsoe, and H. J. Jakobsen. ^{51}V MAS NMR Spectroscopy: Determination of Quadrupolar and Anisotropic Shielding Tensors, Including the Relative Orientation of Their Principal-Axis Systems. *Chem Phys. Lett.*, 188:105, 1992.

[141] J. Skibsted, N. C. Nielsen, H. Bildsoe, and H. J. Jakobsen. Magnitude and Relative Orientation of ^{51}V Quadrupole Coupling and Anisotropic Shielding Tensors in Metavanadates and KV_3O_8 from ^{51}v MAS NMR Spectra. ^{23}Na Quadrupole Coupling Parameters for α- and β-$NaVO_3$. *J. Am. Chem. Soc.*, 115:7351, 1993.

[142] A. Bax, N. M. Szeverenyi, and G. E. Maciel. Chemical Shift Anisotropy in Powdered Solids Studied by 2D FT NMR with Flipping of the Spinning. *J. Magn. Reson.*, 55:494, 1983.

[143] T. Terao, T. Fujii, T. Onodera, and A. Saika. *Chem. Phys. Lett.*, 107:145, 1984.

[144] L. Frydman, G. C. Chingas, Y. K. Lee, P. J. Grandinetti, M. A. Eastman, G. A. Barrall, and A. Pines. Variable-Angle Correlation Spectroscopy in Solid-State Nuclear Magnetic Resonance. *J. Chem. Phys.*, 97:4800, 1992.

[145] S. Vega and A. Pines. Operator Formalism for Double Quantum NMR. *J. Chem. Phys.*, 66:5624, 1977.

[146] S. Vega and Y. Naor. Triple-Quantum NMR on Spin Systems with I=3/2 in Solids. *J. Chem. Phys.*, 75:75, 1981.

[147] S. Vega, T. W. Shattuck, and A. Pines. Double-Quantum Cross-Polarization NMR in Solids. *Phys. Rev. A*, 22:638, 1980.

[148] D. Massiot. Sensitivity and Lineshape Improvements of MQMAS by Rotor-Synchronized Data Acquisition. *J. Magn. Reson. Series A*, 122:240, 1996.

[149] C. Fernandez and J. P. Amoureux. Triple-Quantum MAS-NMR of Quadrupolar Nuclei. *Solid State NMR*. 5:315, 1996.

[150] P. Sarv, C. Fernandez, J. P. Amoureux, and K. Keskinen. Distribution of Tetrahedral Aluminum Sites in ZSM-5 Type Zeolites - an Al-27 (Multiquantum) Magic Angle Spinning NMR Study. *J. Phys. Chem.*, 100:19223, 1996.

[151] S. H. Wang, S. M. De Paul, and L. M. Bull. High-Resolution Heteronuclear Correlation Between Quadrupolar and Spin-1/2 Nuclei Using Multiple-Quantum Magic-Angle Spinning. *J. Magn. Reson. Series A*, 125:364, 1997.

[152] C. Fernandez, J. P. Amoureux, L. Delmotte, and H. Kessler. Crystallographic Site Probing in the Triclinic Cha-like $AlPO_4$ by Al-27 2D Quintuple-Quantum NMR. *Microporous Materials*. 6:125, 1996.

[153] J. Rocha, Z. Lin, C. Fernandez, and J. P. Amoureux. Multiple-Quantum Al-27 MAS NMR Spectroscopy of Microporous Aluminum Methlphosphonate β-AlMePO. *Chem. Commun.*, 100:2513, 1996.

[154] R. von Ballmoos and W. M. Meier. Oxygen-18 Exchange between Zeolite ZSM-5 and Water. *J. Phys. Chem.*, 86:2698, 1982.